

1/2

**CONSOLIDATED UNDRAINED-TRIAXIAL BEHAVIOR
OF A SAND-BENTONITE MIXTURE
AT ELEVATED TEMPERATURE**

by

BRIAN E. LINGNAU

A Thesis
Submitted to the Faculty of Graduate Studies
in Partial Fulfillment of the Requirements for the Degree of
DOCTOR OF PHILOSOPHY

Department of Civil Engineering
University of Manitoba
Winnipeg, Manitoba

© Copyright June 1993.

CONSOLIDATED UNDRAINED-TRIAXIAL BEHAVIOR
OF A SAND-BENTONITE MIXTURE AT
ELEVATED TEMPERATURE

BY

BRIAN E. LINGNAU

A Thesis submitted to the Faculty of Graduate Studies of the University of Manitoba in partial fulfillment of the requirements for the degree of

DOCTOR OF PHILOSOPHY

© 1993

Permission has been granted to the LIBRARY OF THE UNIVERSITY OF MANITOBA to lend or sell copies of this thesis, to the NATIONAL LIBRARY OF CANADA to microfilm this thesis and to lend or sell copies of the film, and UNIVERSITY MICROFILMS to publish an abstract of this thesis.

The author reserves other publications rights, and neither the thesis nor extensive extracts from it may be printed or otherwise reproduced without the author's permission.

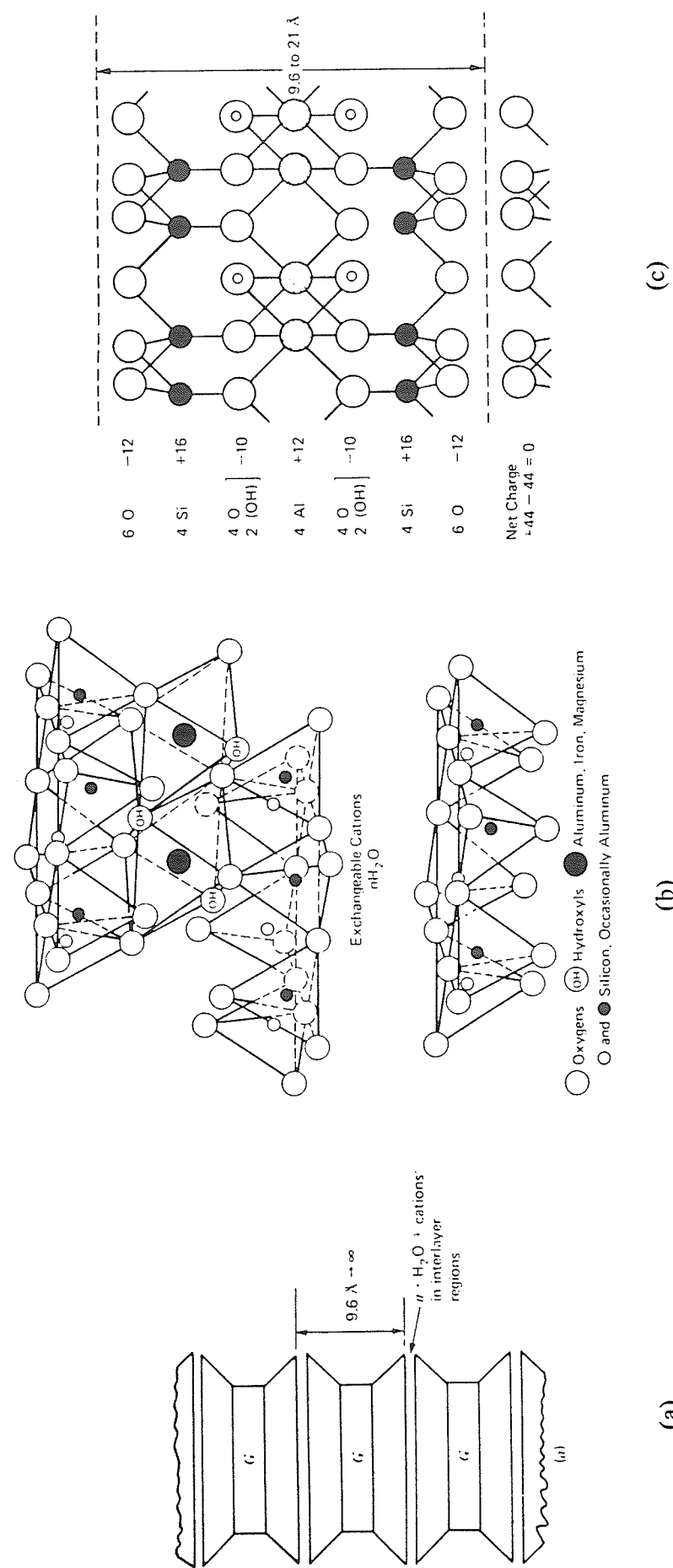


FIGURE 2.1 Structure of montmorillonite: (a) schematic representation; (b) molecular interpretation; (c) charge distribution. (after Mitchell 1976)

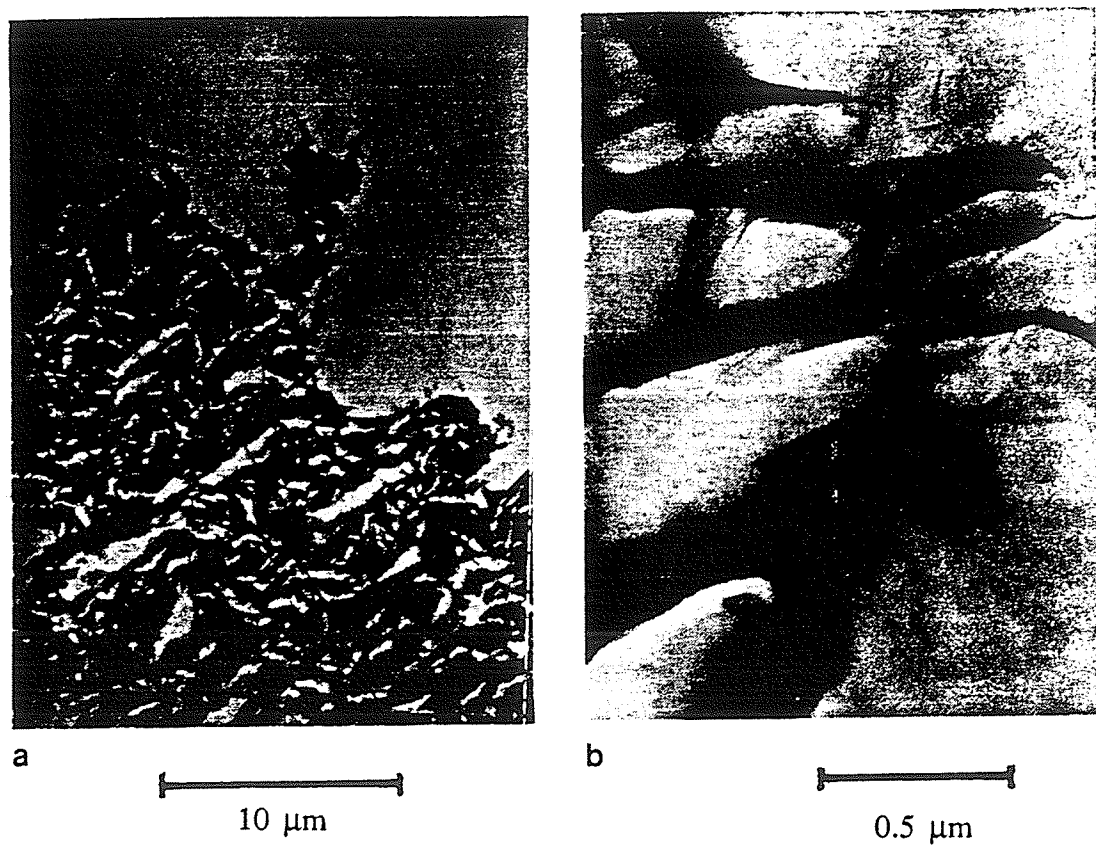


FIGURE 2.2 Bentonite clay autoclaved at 150°C for 0.3 years: (a) general view displaying the microstructural pattern (b) close view of smectite folds and titania inclusion (after Pusch and Güven 1990)

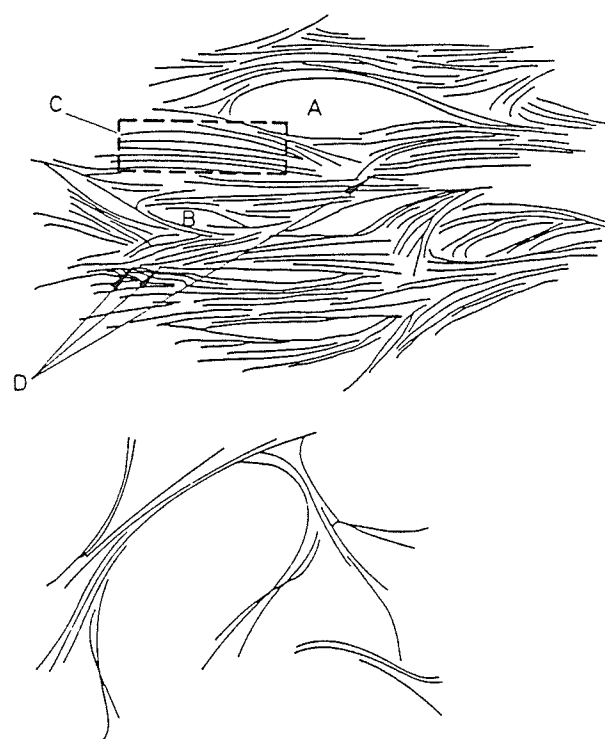


FIGURE 2.3 Schematic image of the microstructure of Na bentonite clay. Upper: dense clay with larger voids (A), smaller pores (B), interlamellar space in stacks (C), and interface of adjacent stacks (D). Lower: expanded, soft clay gel. (after Pusch and Güven 1990)

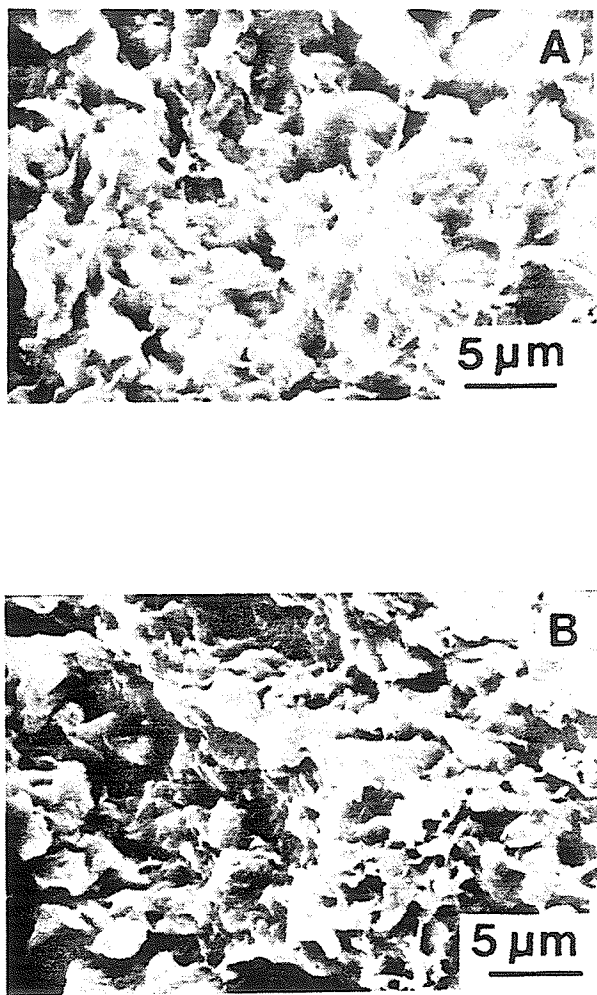


FIGURE 2.4 Scanning electron micrographs of bentonite: (a) isothermal bentonite material (b) after exposure to steam. (after Oscarson and Dixon 1990a)

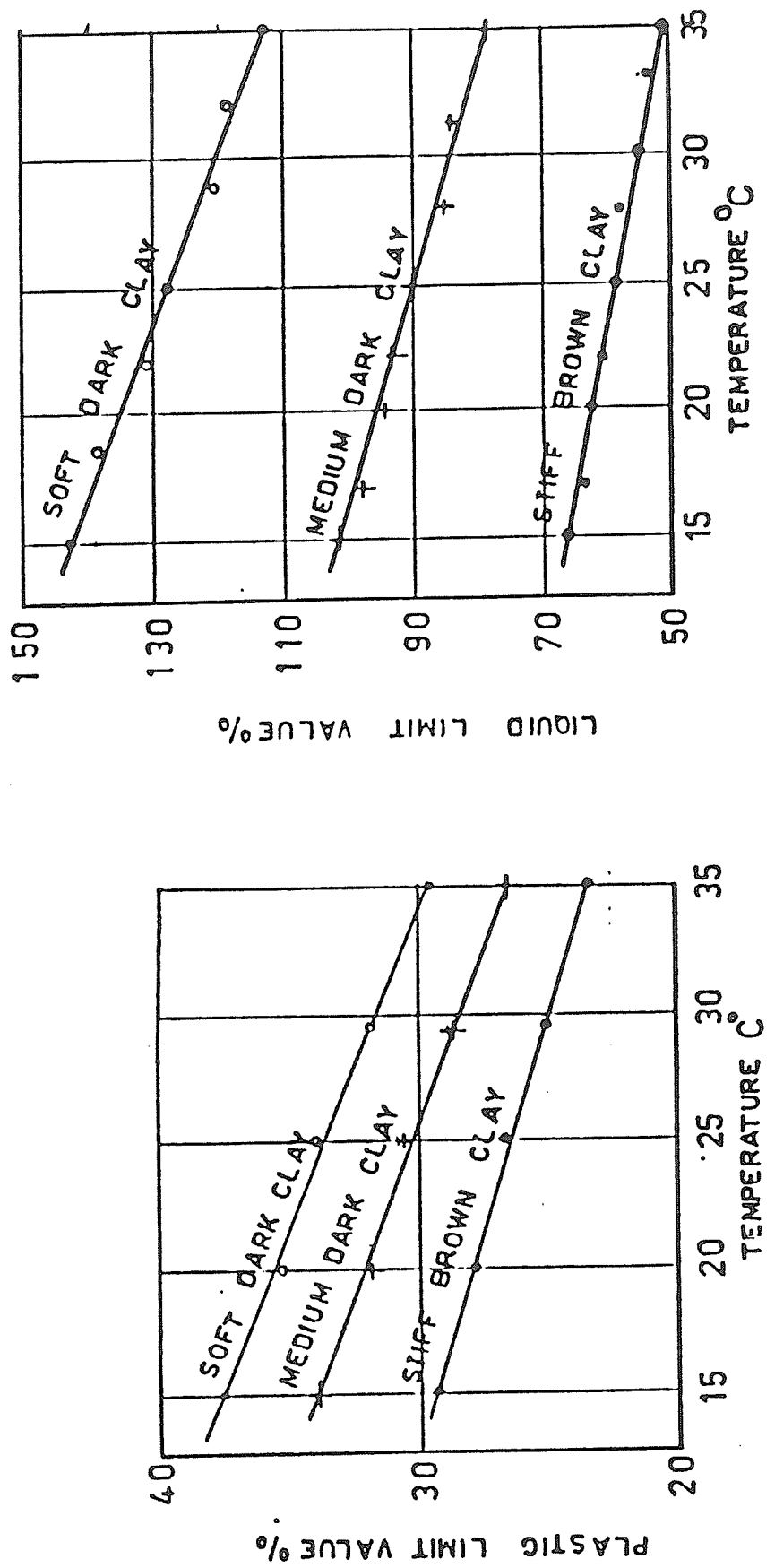


FIGURE 2.5 Atterberg limits of high plasticity clay as a function of temperature: (a) plastic limit; and (b) liquid limit.
(after Youssef and El Ramli 1961)

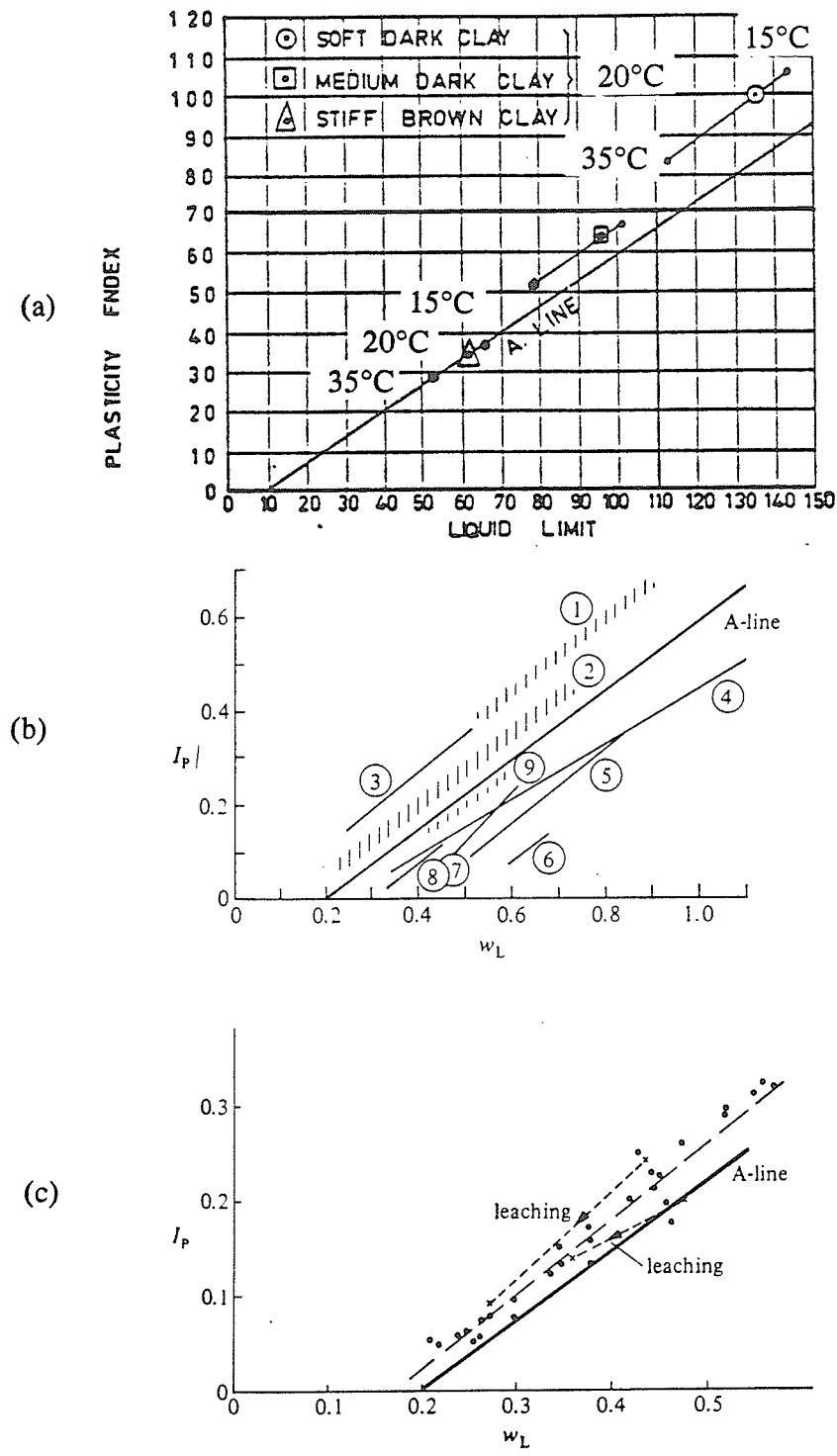


FIGURE 2.6 Relation between liquid limit w_L and plasticity index I_p (a) and Temperature (after Youssef and El Ramli 1961); (b) typical soils: 1, gumbo clays; 2, glacial clays; 3, clay (Venezuela); 4, organic silt and clay; 5, organic clay; 6, kaolin; 7, organic silt and clay; 8, micaceous sandy silt; 9, kaolin-type clays (after Casagrande, 1947). (c) Norwegian marine clays (data from Bjerrum, 1954, 1967).

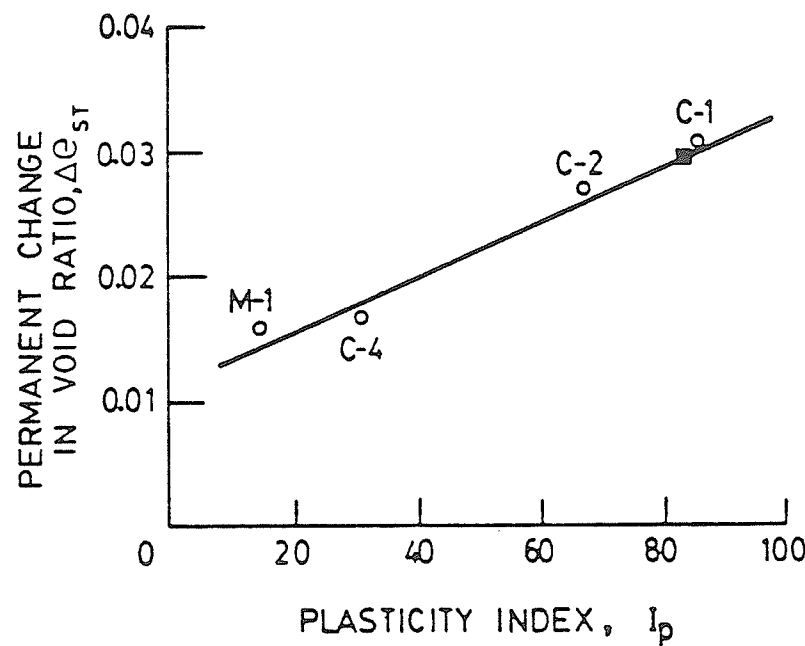


FIGURE 2.7 Deformation response of four marine clays to a temperature cycle of 25°C-50°C-25°C.
 C1: Deep water 4000m, $w_L = 113$, CH.
 C2: Deep water 4000m, $w_L = 93$, CH.
 C4: Shallow water 400m, $w_L = 56$, CH.
 M1: Deep water 4000m, $w_L = 45$, ML, Carbonates = 59%
 (after Demars and Charles 1982)

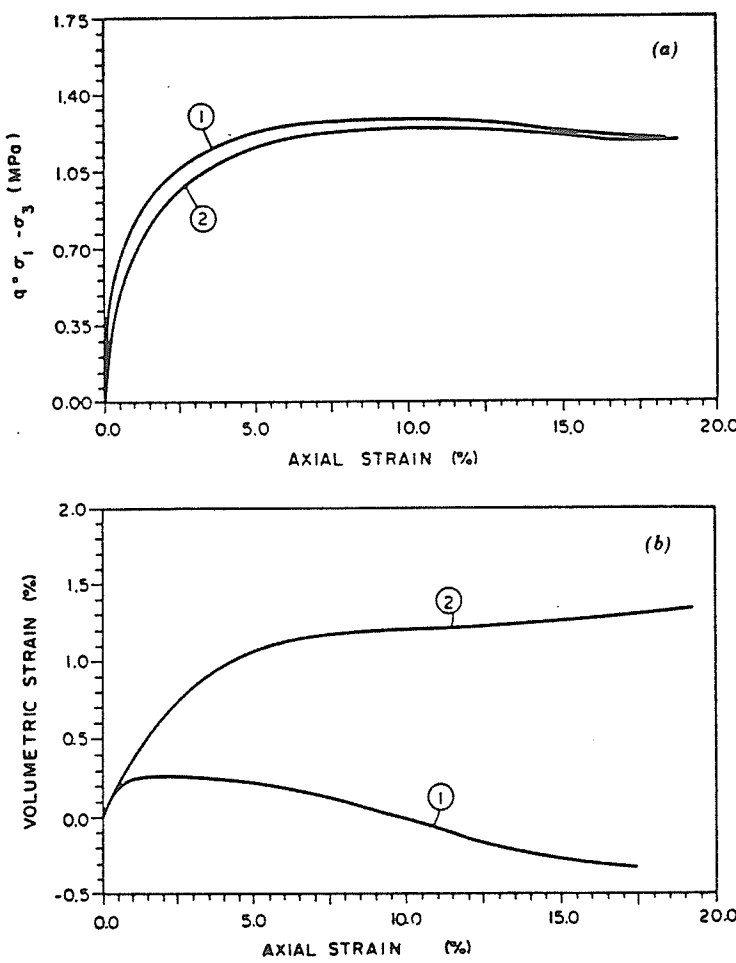


FIGURE 2.8 Drained triaxial compression tests on Pontida silty clay at room and high temperature at confining stress of 0.5 MPa (OCR = 5.0); 1 at 23°C, 2 at 98°C: (a) deviatoric stress versus axial strain; and (b) volumetric strain versus axial strain. (after Hueckel and Baldi 1990)

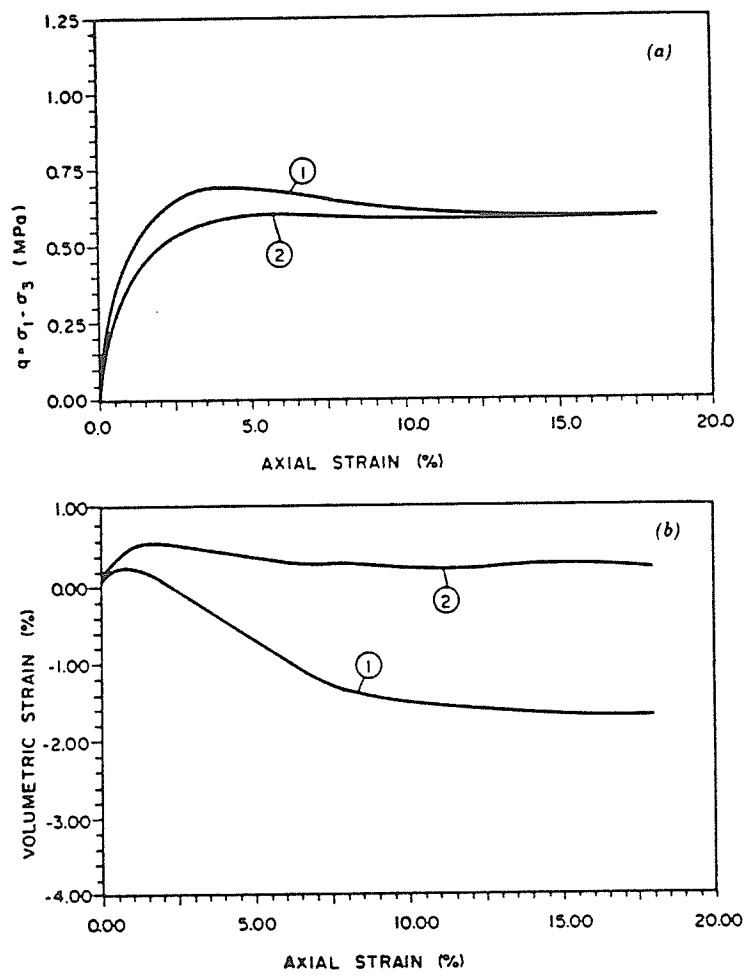


FIGURE 2.9 Drained triaxial compression tests on Pontida silty clay at room and high temperature at confining stress of 0.2 MPa (OCR = 12.5); 1 at 23°C , 2 at 95°C : (a) deviatoric stress versus axial strain; and (b) volumetric strain versus axial strain. (after Hueckel and Baldi 1990)

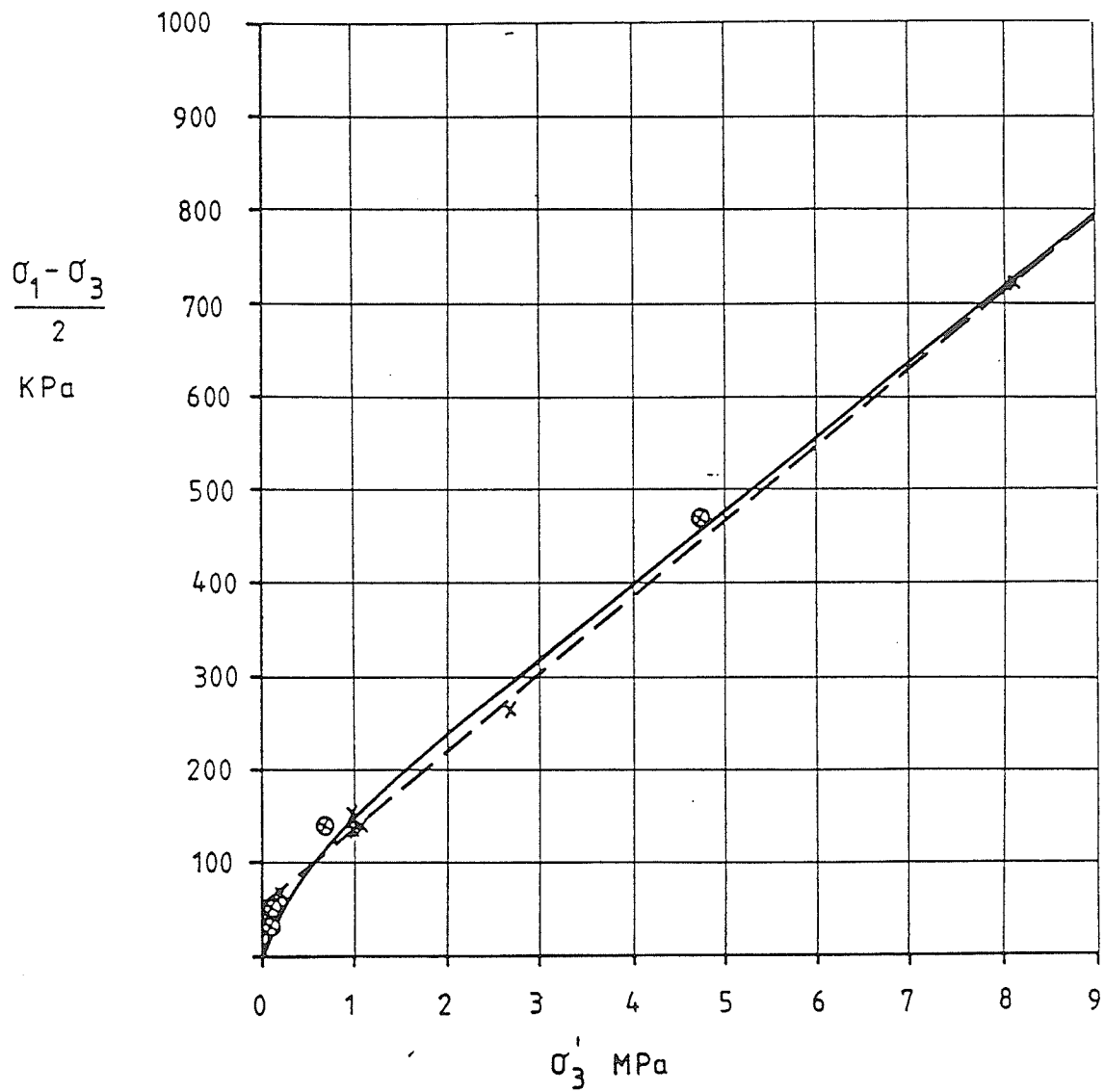


FIGURE 2.10 Failure stresses in the triaxial tests. Notice the different scales of the axes.

- X temperature = 22°C
- ⊗ temperature = 60°C
- failure envelope
- Mohr-Coulomb failure envelope
- (after Börgesson *et al.* 1990)

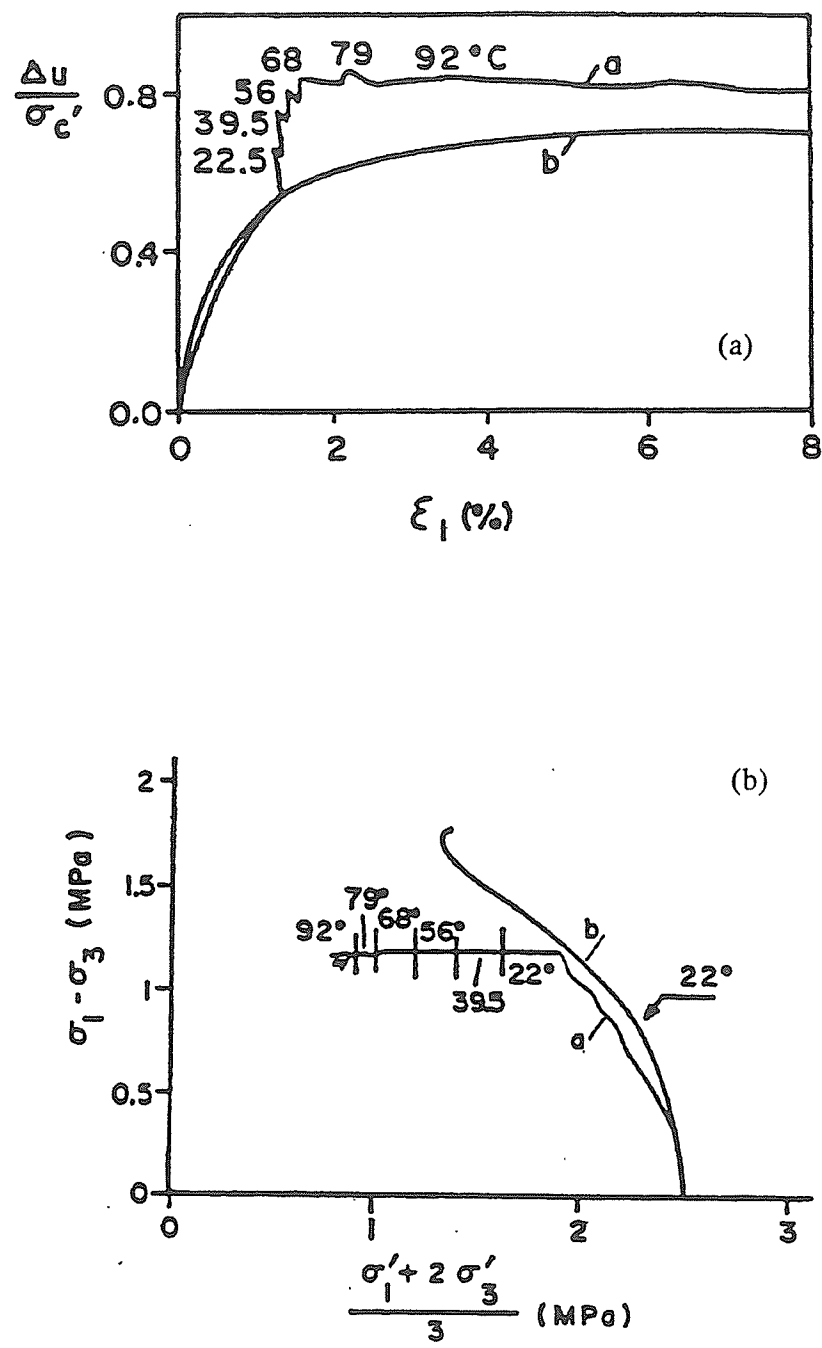


FIGURE 2.11 Pontida silty clay. Undrained heating test: (a) pore pressure generation (b) effective stress path. (after Hueckel and Pellegrini 1991)

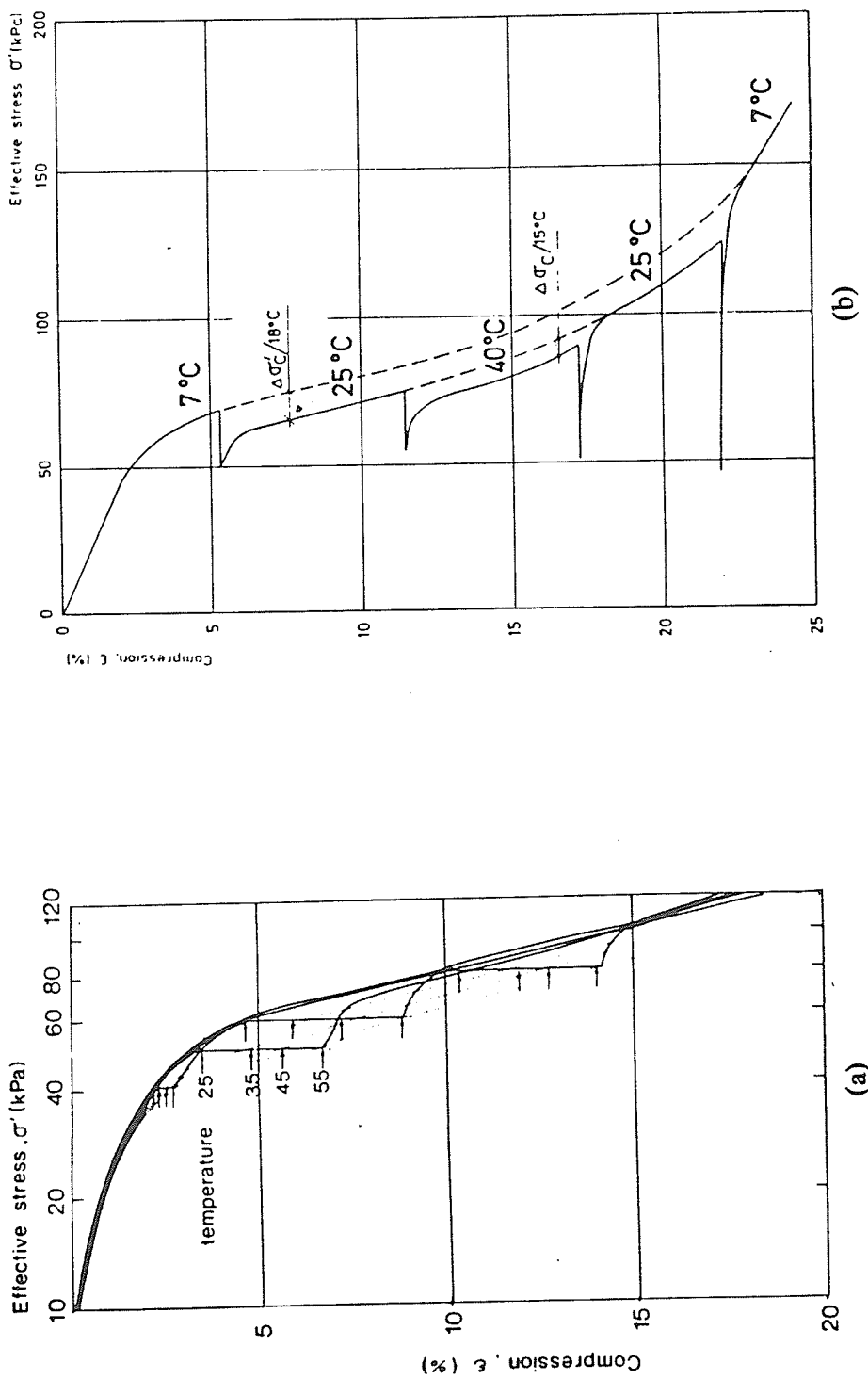


FIGURE 2.12 Oedometer tests on high plastic sensitive marine clays: (a) incremental load tests where the temperature was increased at 40, 50, 60, and 80 kPa, respectively (b) constant rate of strain tests with varying temperature. Clay from Bäckebol. (after Tidfors and Sällfors 1989)

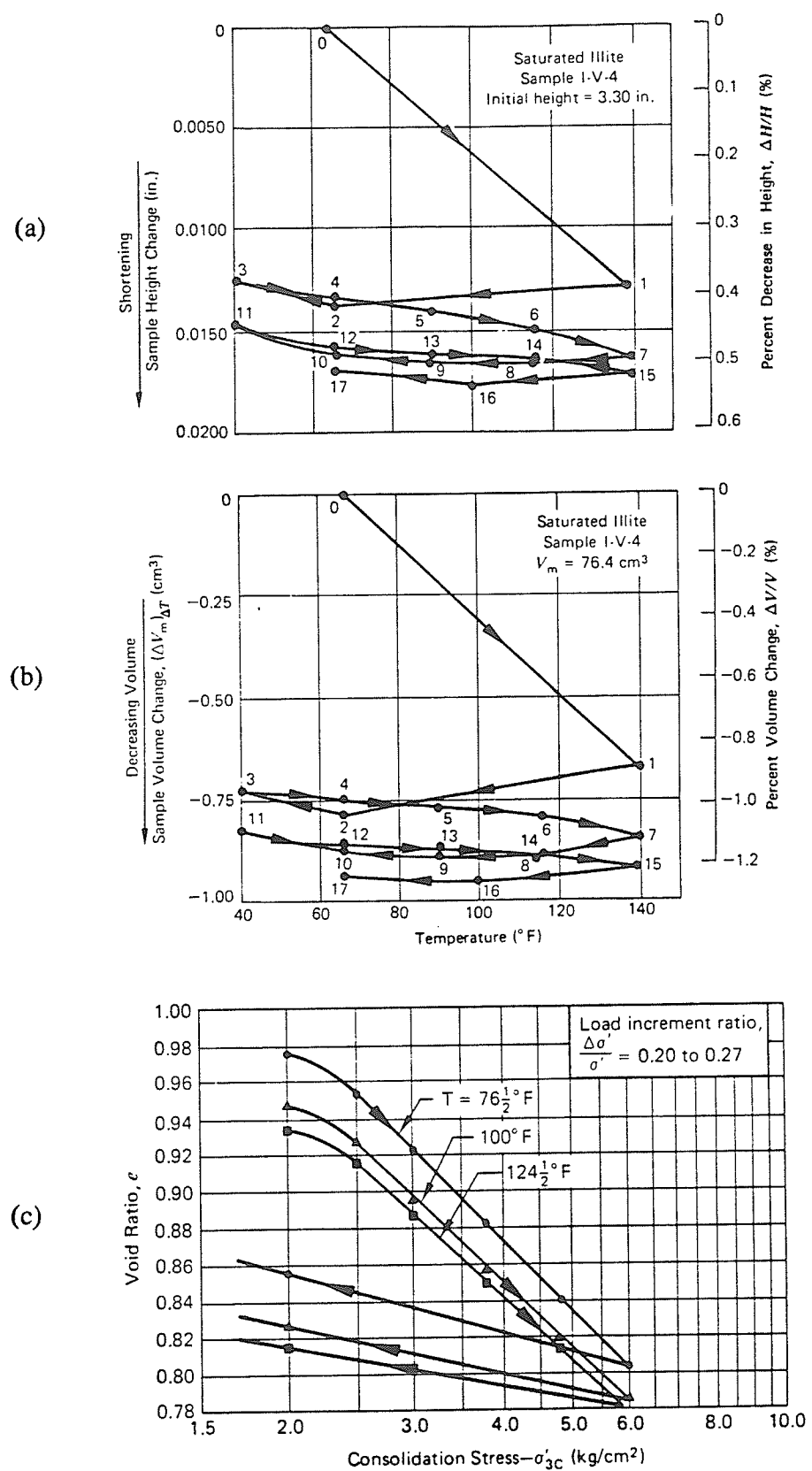


FIGURE 2.13 Effects of temperature variations on saturated illite:
(a) on height (b) on volume change (c) on isotropic consolidation (after Mitchell 1976)

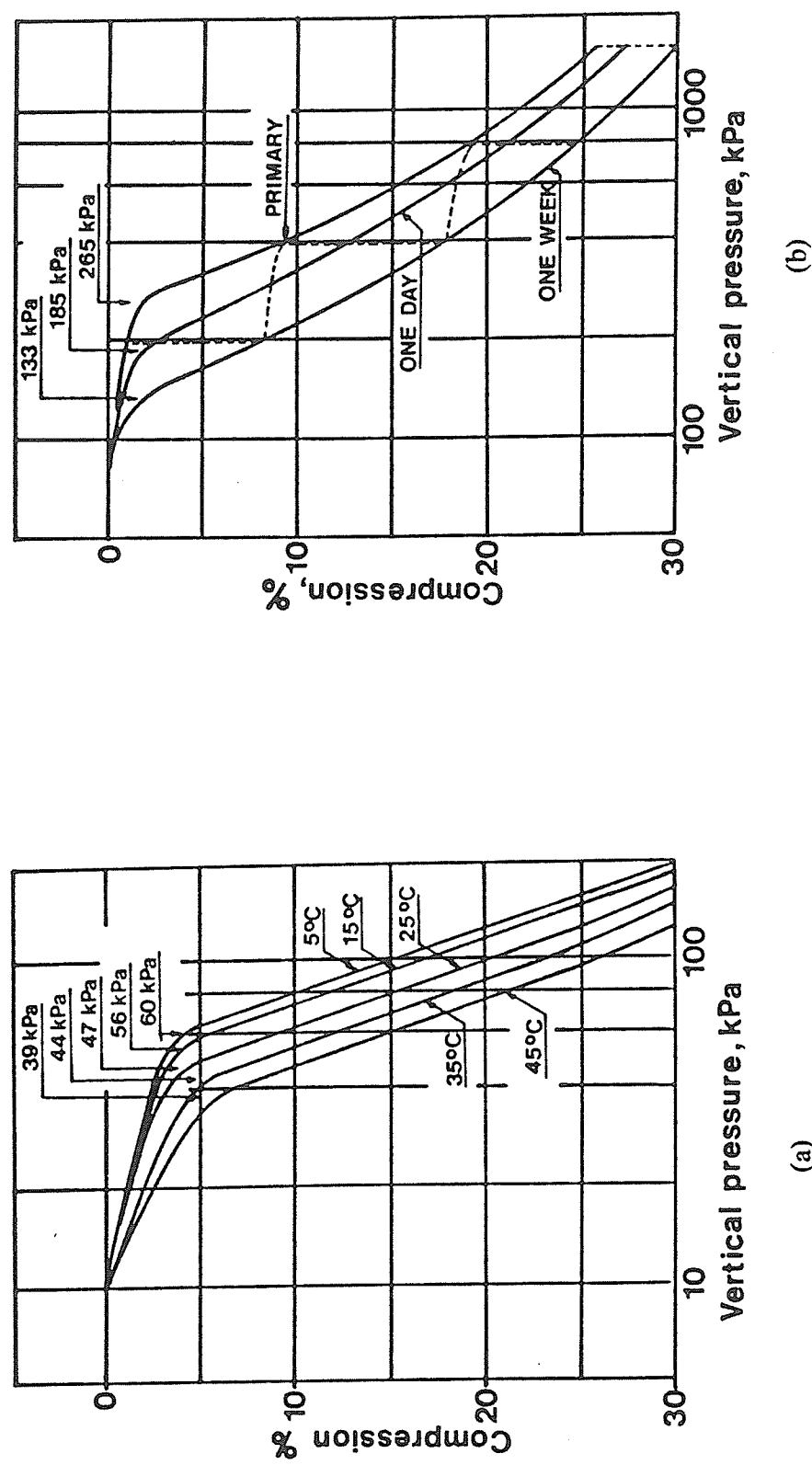


FIGURE 2.14 Oedometer tests on clay: (a) 'identical undisturbed' samples of high plastic marine clay at different temperatures (b) preconsolidation pressure evaluated from primary compression, 1 day and 7 days of loading. (after Eriksson 1989)

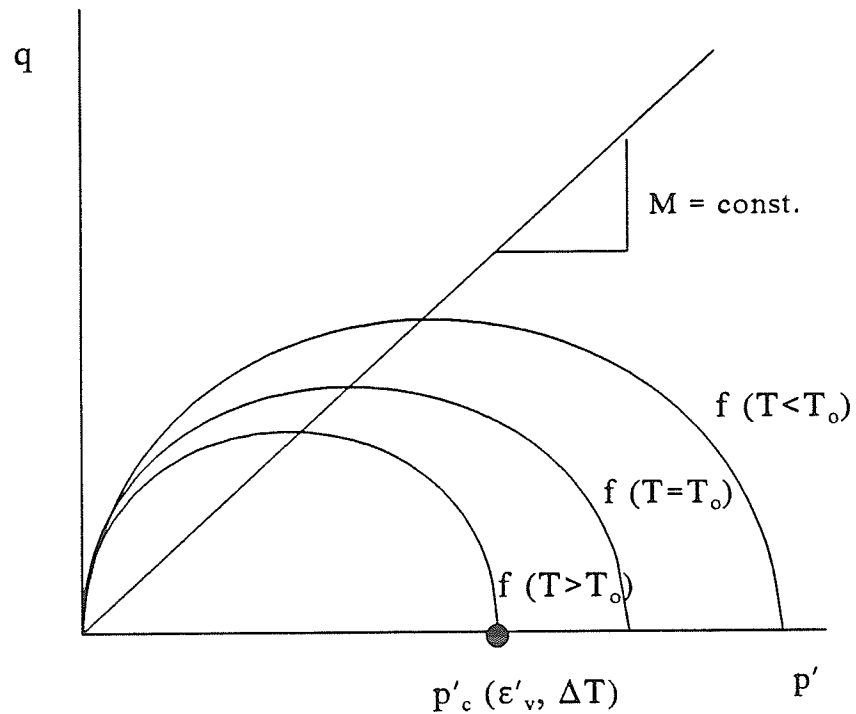


FIGURE 2.15 Schematic of the yield surface sensitivity to temperature. (after Hueckel and Pellegrini 1991)

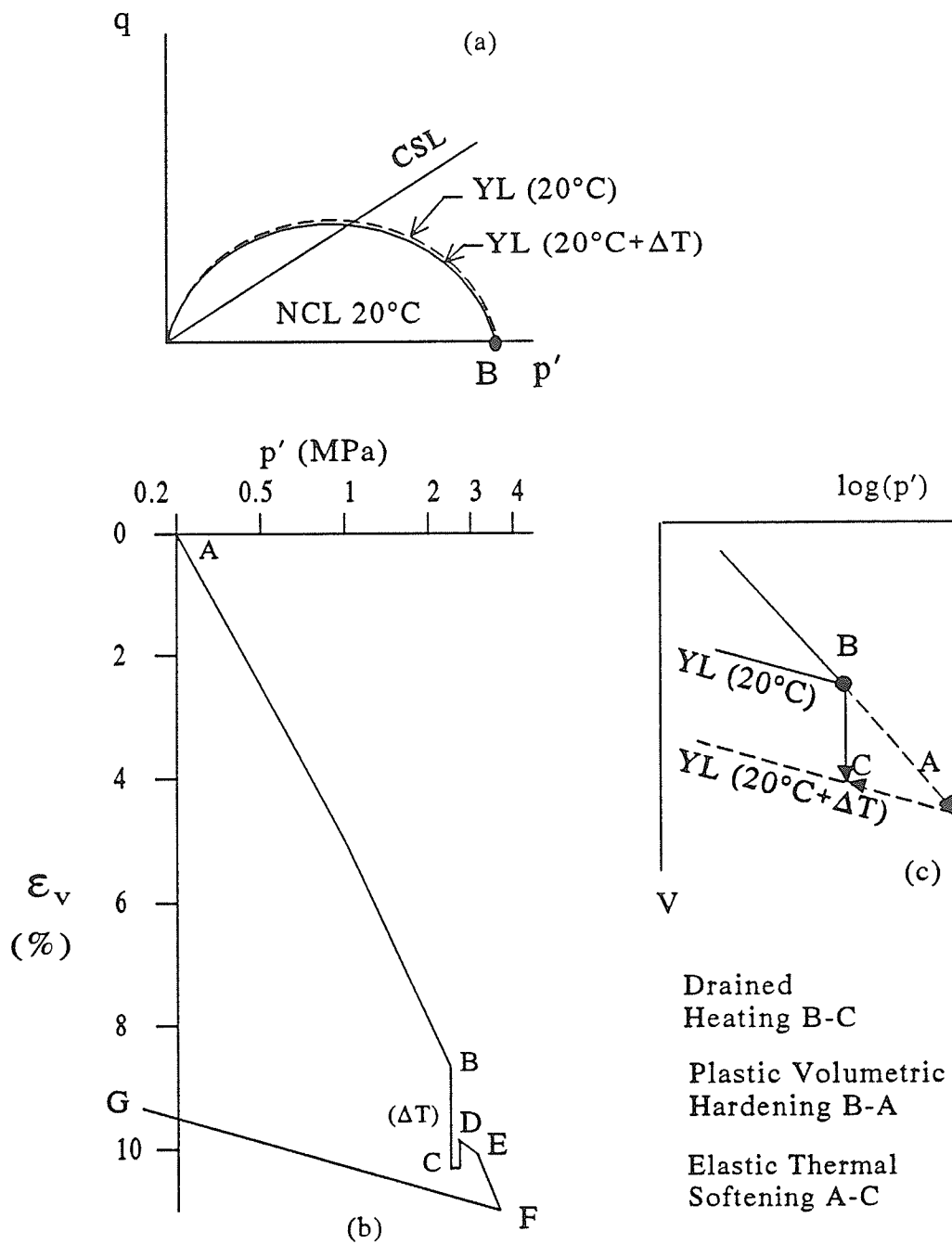


FIGURE 2.16 Yield locus response to drained heating at constant p' : (a) q - p' stress space interpretation (b) V - $\log p'$ space, thermomechanical cycle on Pontida silty clay (after Hueckel and Baldi 1990) (c) yield locus interpretation using concepts of plastic volumetric hardening and thermal (elastic) softening

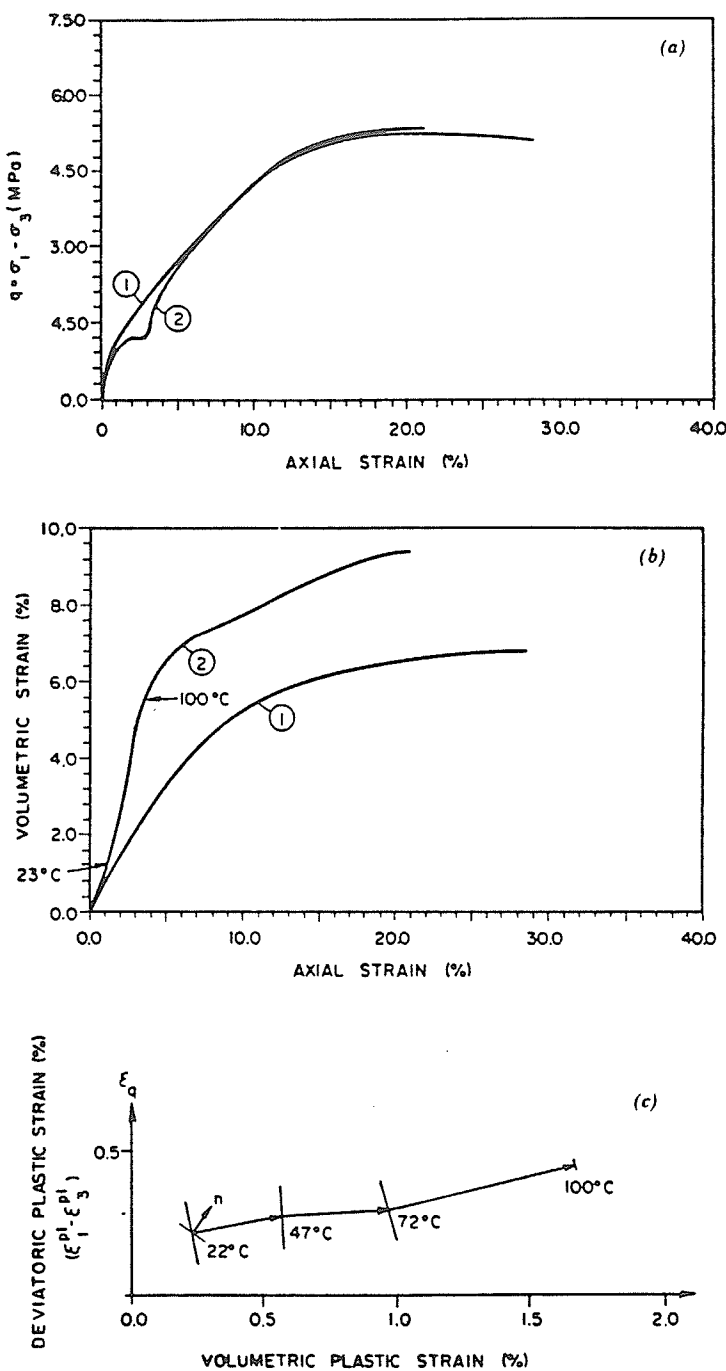


FIGURE 2.17 Triaxial drained compression of normally consolidated specimens of Pontida silty clay 1: at room temperature, 2: at room temperature up to $q = 1.2$ MPa, followed by heating up to 100°C and then by further triaxial compression at high temperature—arrows indicate onset and end of heating: (a) stress deviator versus axial strain; (b) volumetric strain versus axial strain; and (c) thermoplastic strain increment vector during heating—vector n shows plastic strain rate at room temperature in triaxial loading at this stress state. (after Hueckel and Baldi 1990)

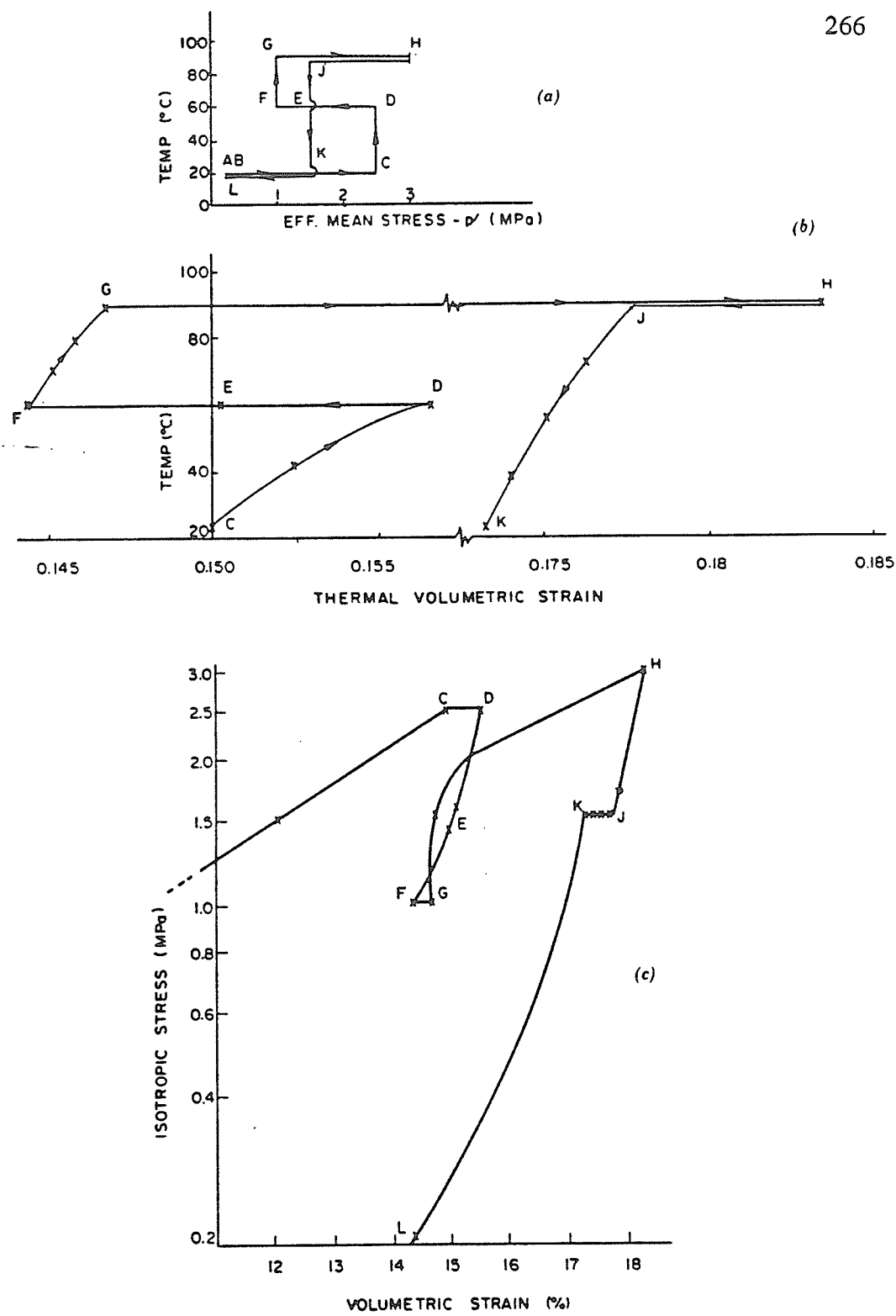


FIGURE 2.18 Thermomechanical drained loading cycle on Pontida clay: (a) temperature versus effective mean normal stress; (b) temperature versus volumetric strain; and (c) isotropic effective stress versus volumetric strain. (after Hueckel and Baldi 1990).

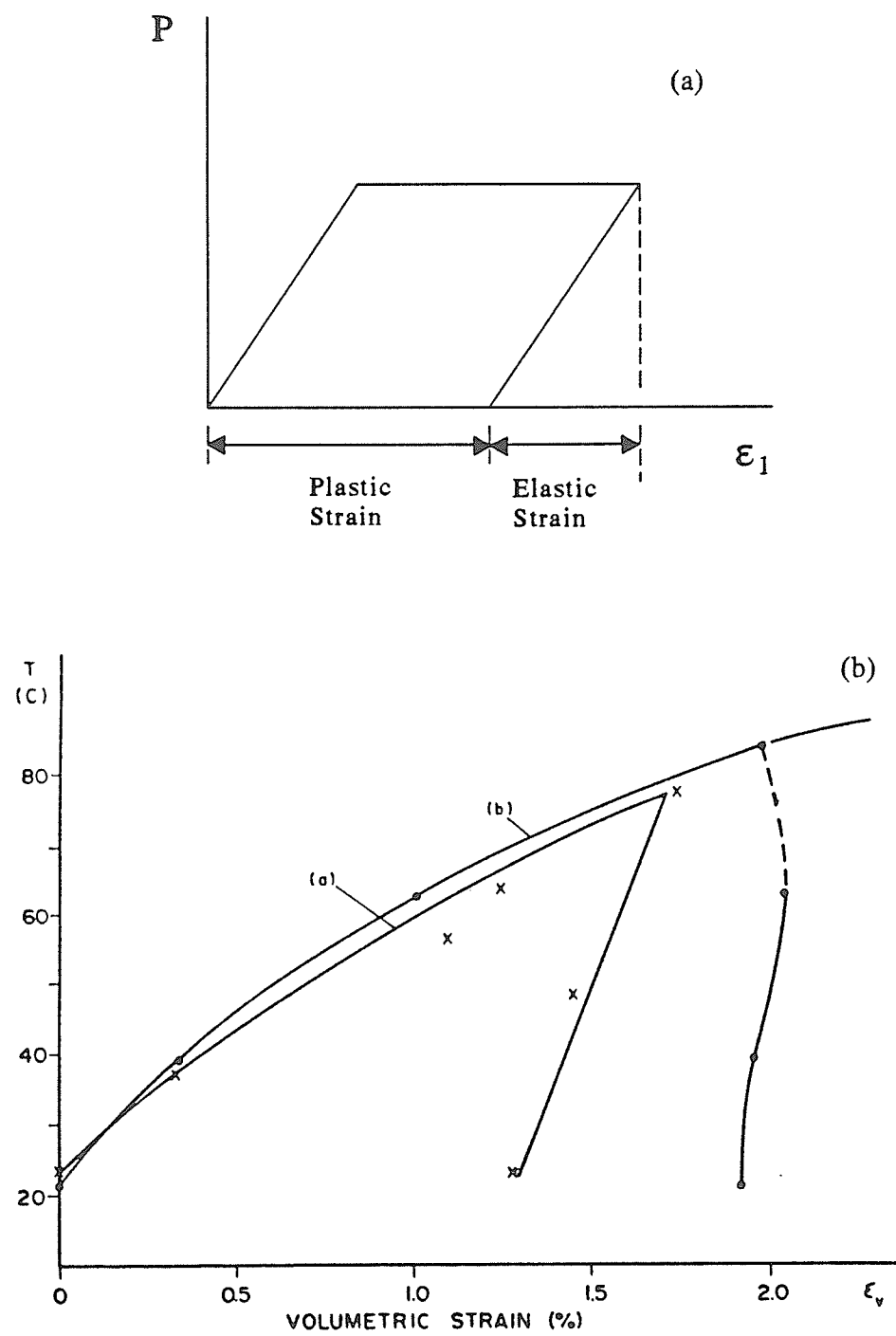


FIGURE 2.19 Interpretation of thermal strains: (a) classical elastic and plastic strains; (b) volumetric strain versus temperature at constant isotropic effective stress. Drained test: (1) at 2.0 MPa on Pontida clay; and (2) at 6 MPa on Boom clay. (after Hueckel and Baldi 1990)

Yield Surfaces of Pure Aluminum

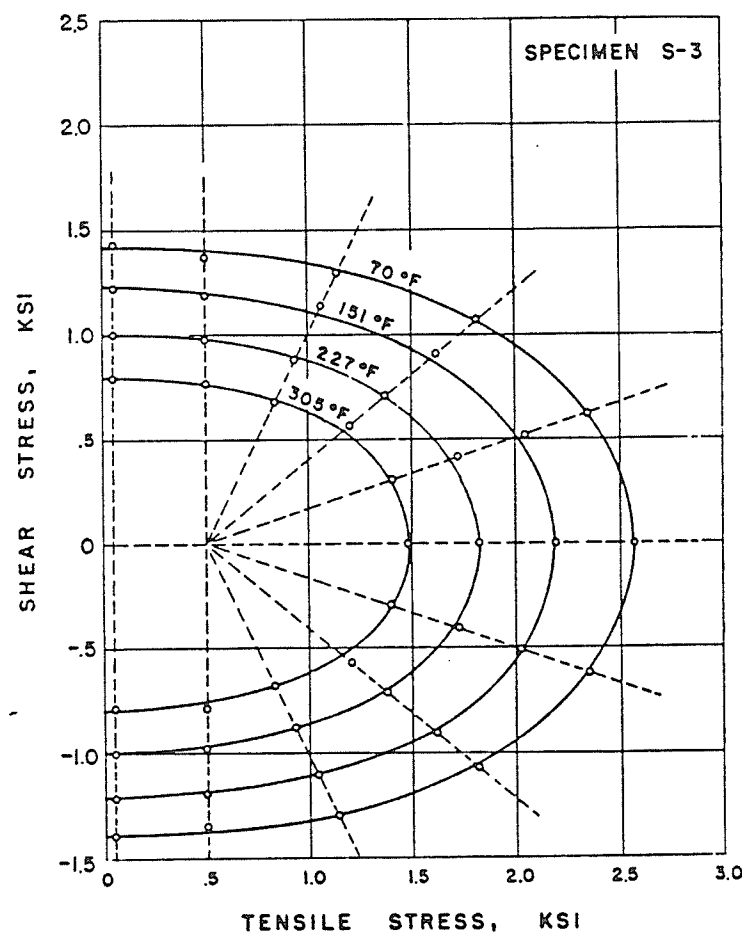


FIGURE 2.20 Initial yield surfaces for pure aluminum at elevated temperature.
(after Phillips 1968)

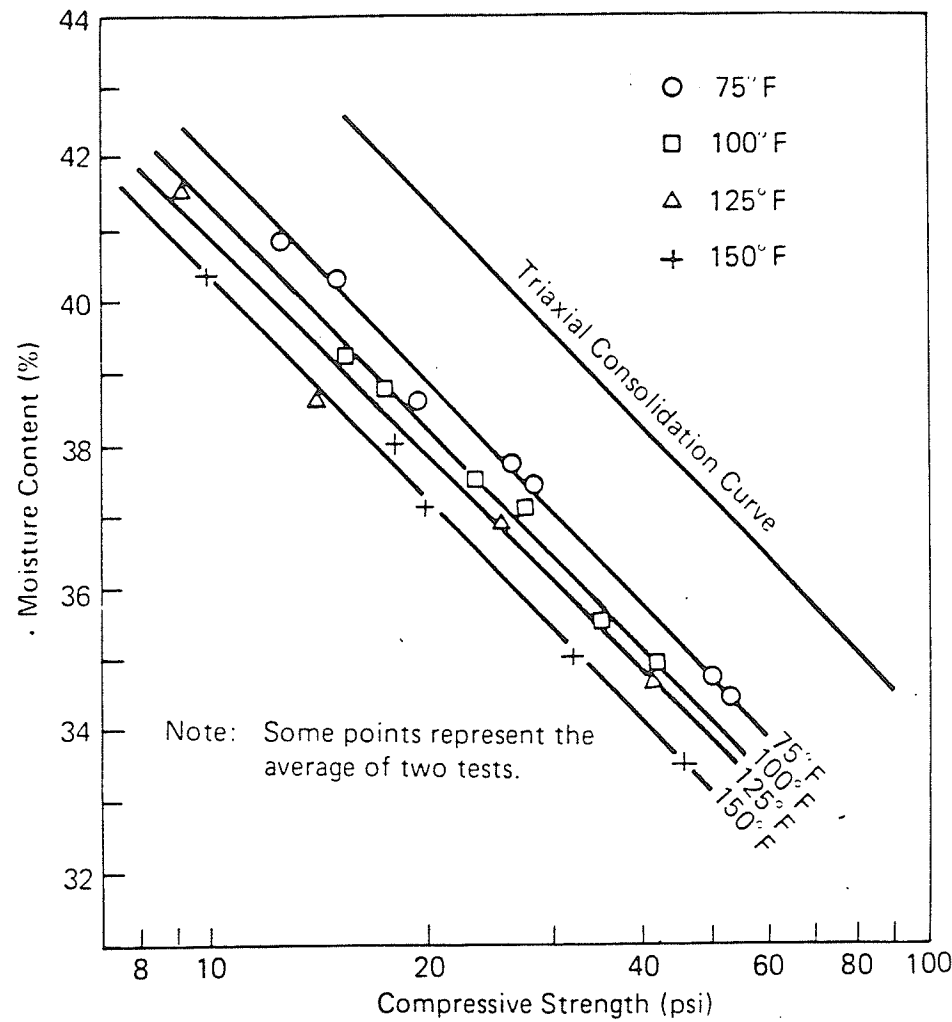


FIGURE 2.21 Effect of temperature on the undrained strength of kaolinite in unconfined compression. (after Sherif and Burrous 1969)

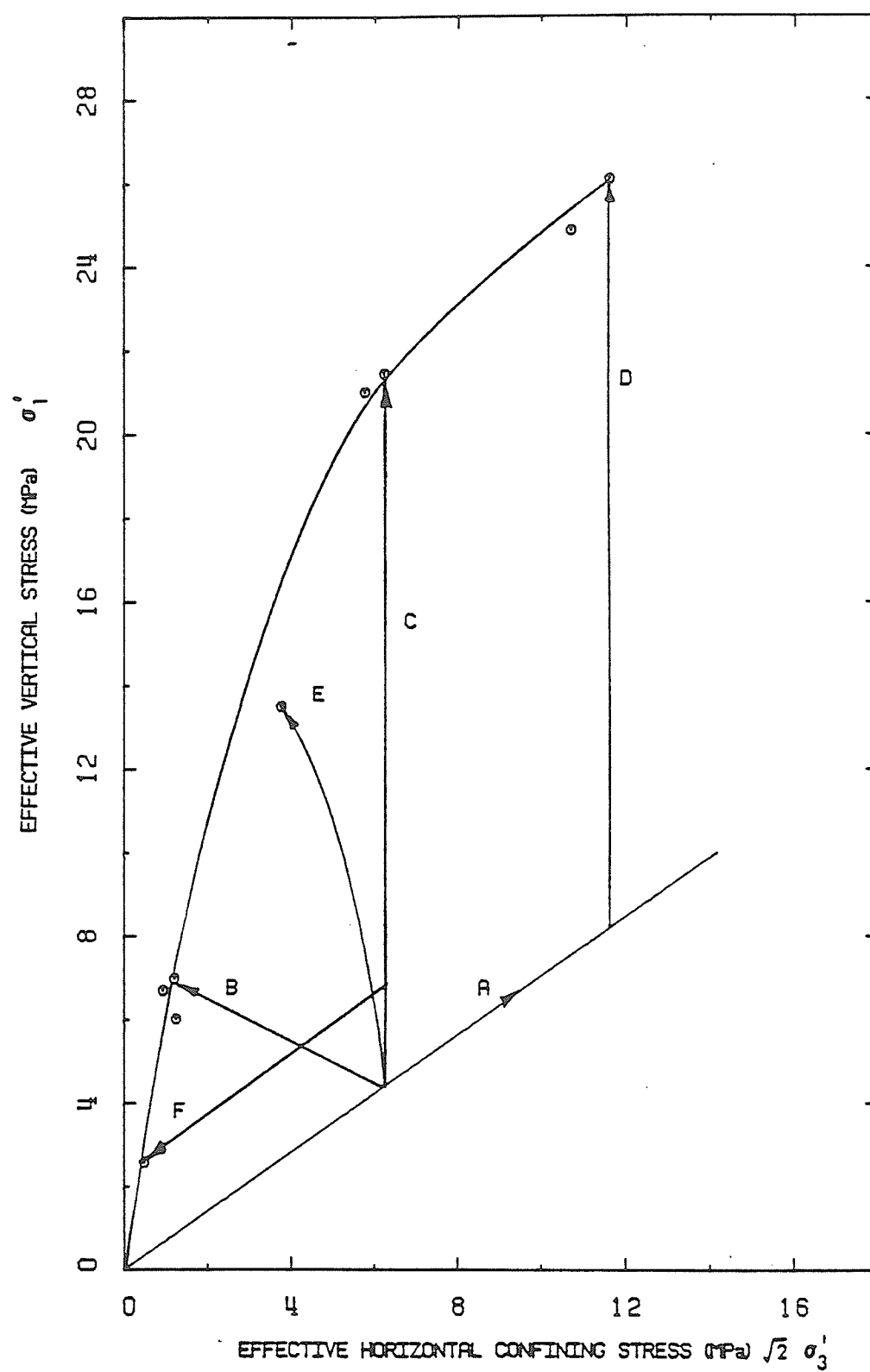


FIGURE 2.22 Stress paths used in high temperature high pressure triaxial testing of Athabasca oil sand. (after Agar 1984)

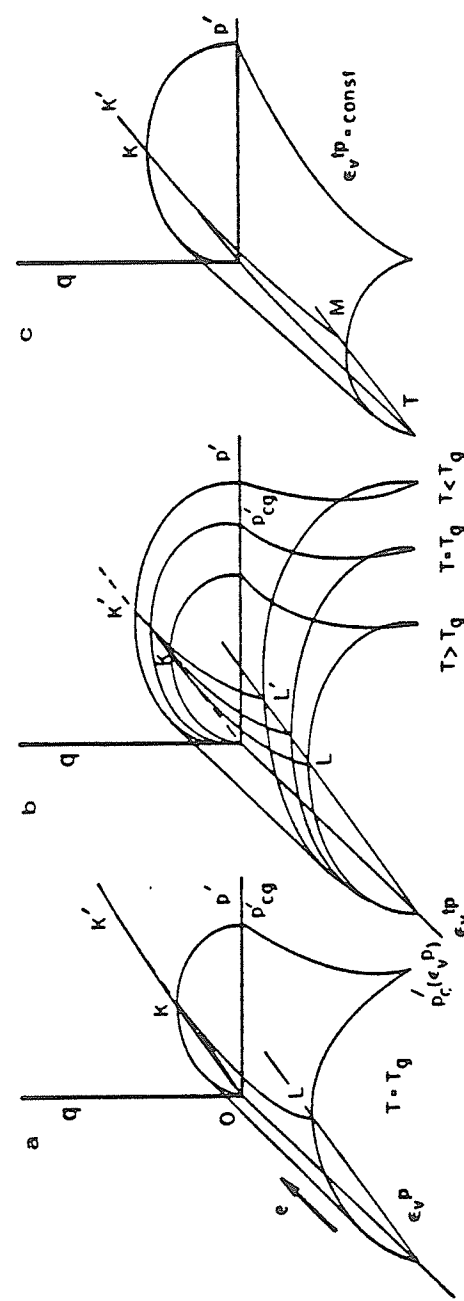


FIGURE 2.23 Cam clay representation of yield surface: (a) room temperature; (b) at variable thermoplastic volumetric strain, ϵ_v^p , and variable temperature, ΔT ; and (c) at constant ϵ_v^p and variable ΔT (thermoelastic process). (after Hueckel and Baldi 1990)

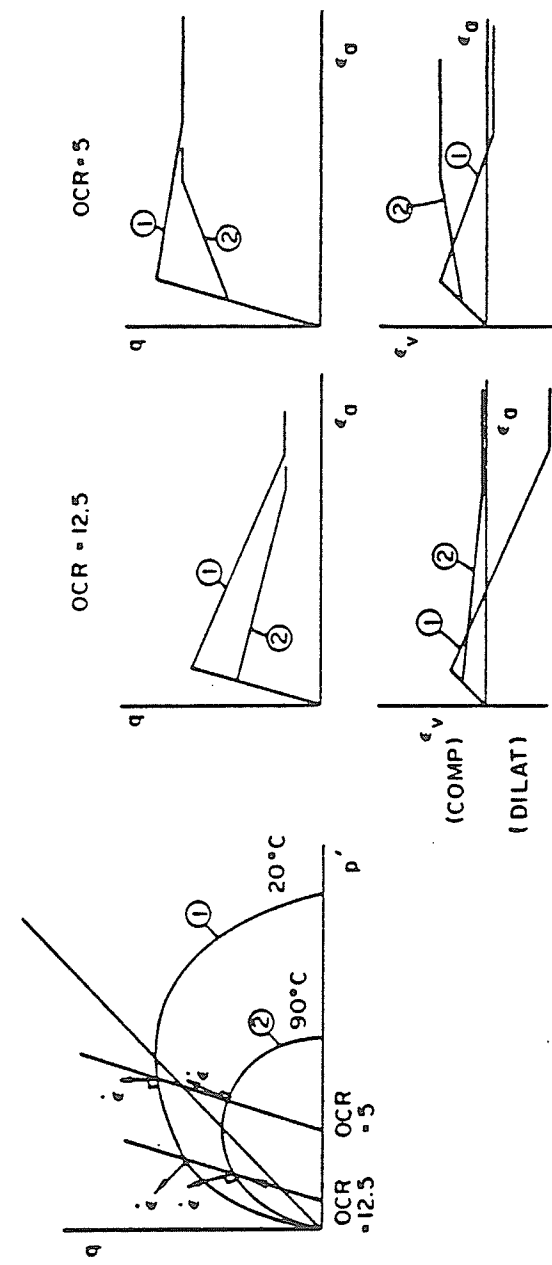


FIGURE 2.24 Two stress paths and theoretical response at room temperature and at 90°C, according to an associative flow rule. (after Hueckel and Baldi 1990)

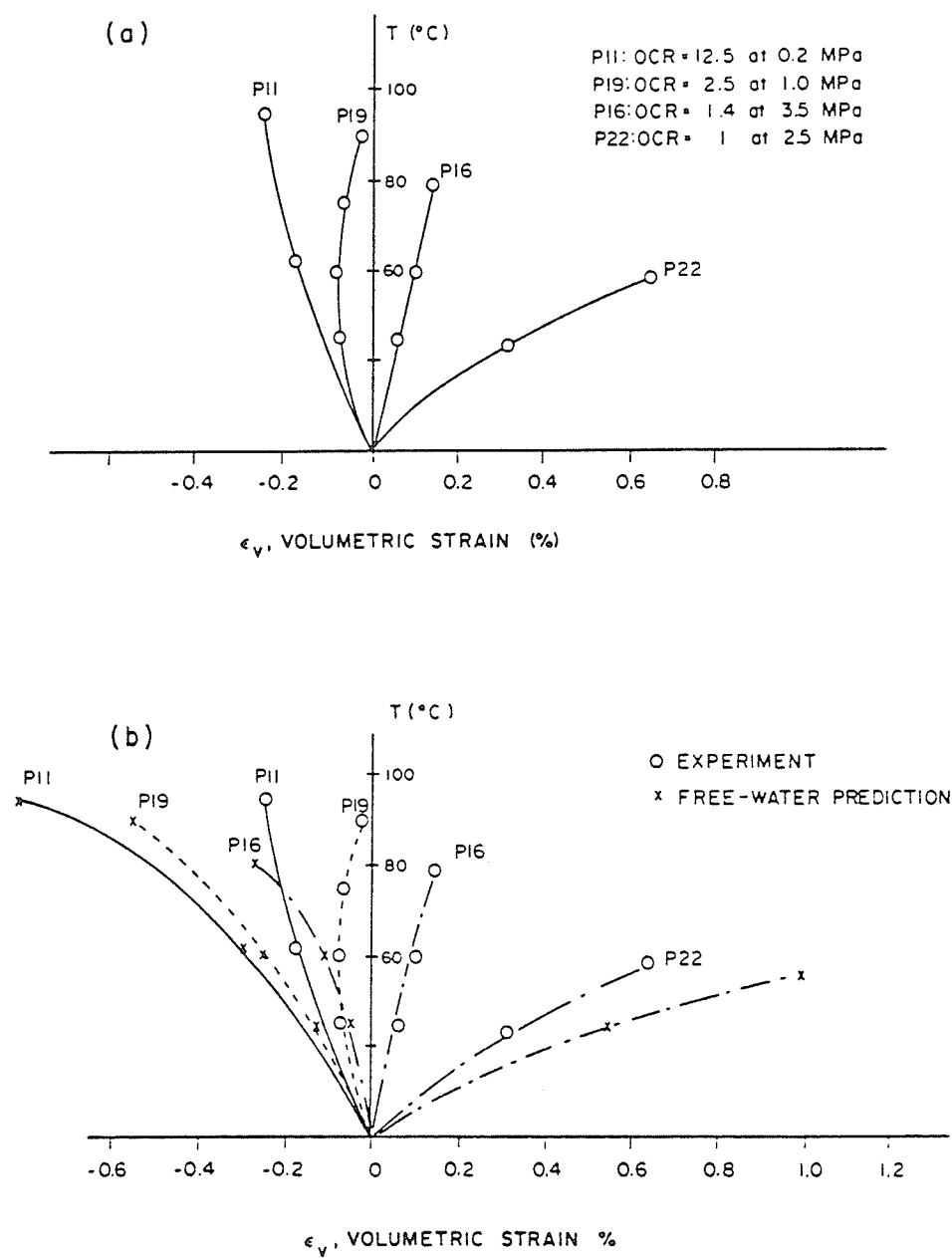


FIGURE 2.25 Triaxial tests on Pontida clay: (a) volumetric strain during heating under constant isotropic effective stress conditions, calculated from measured axial strain; (b) volumetric skeleton strain-comparison between measured strain and the free-water prediction. (after Hueckel and Baldi 1990)

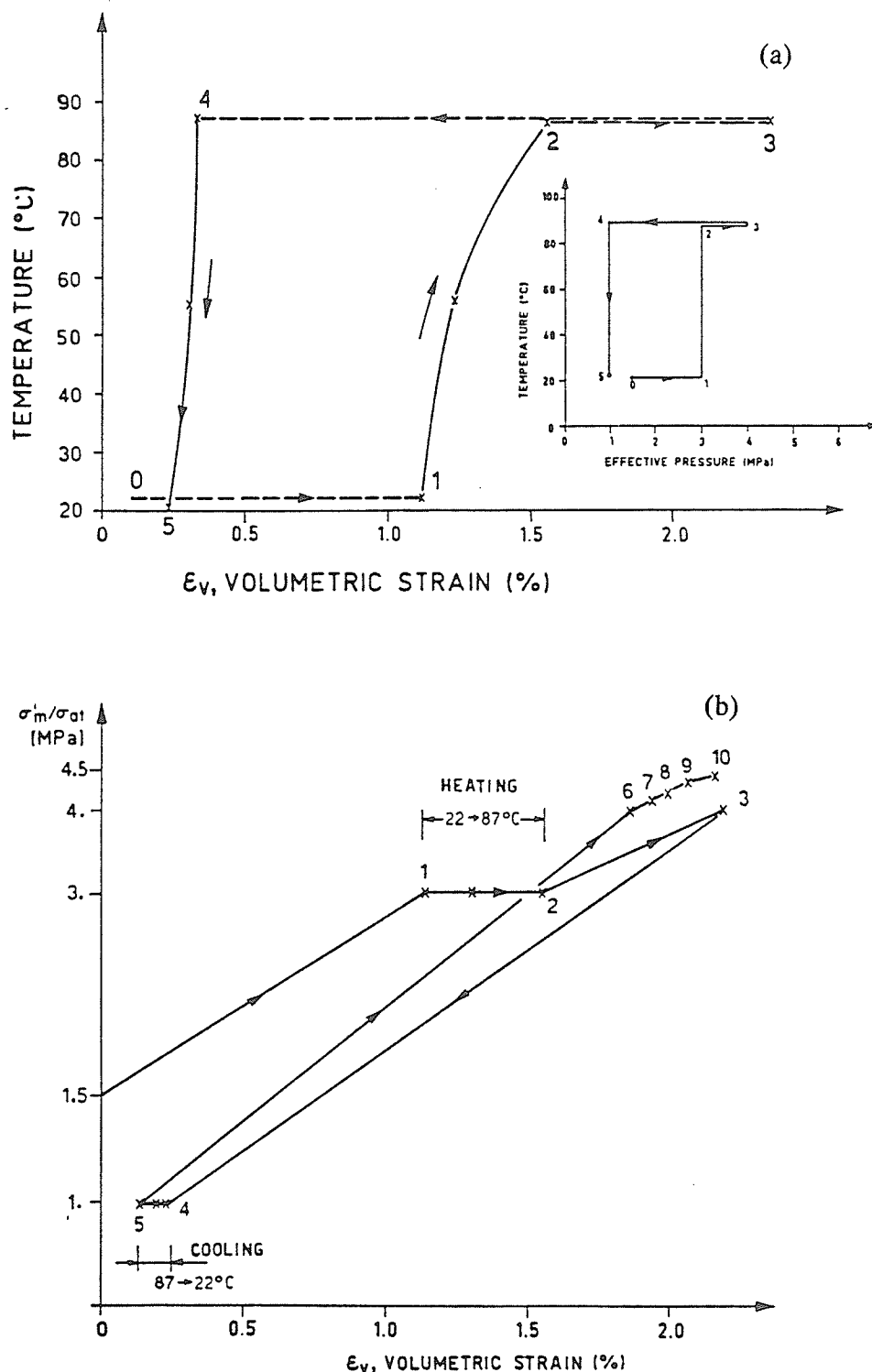


FIGURE 2.26 Thermomechanical cycle of loading on overconsolidated Boom clay:
 (a) strain variation with temperature and pressure loading (inset);
 (b) stress-strain response. (after Baldi *et al.* 1987)

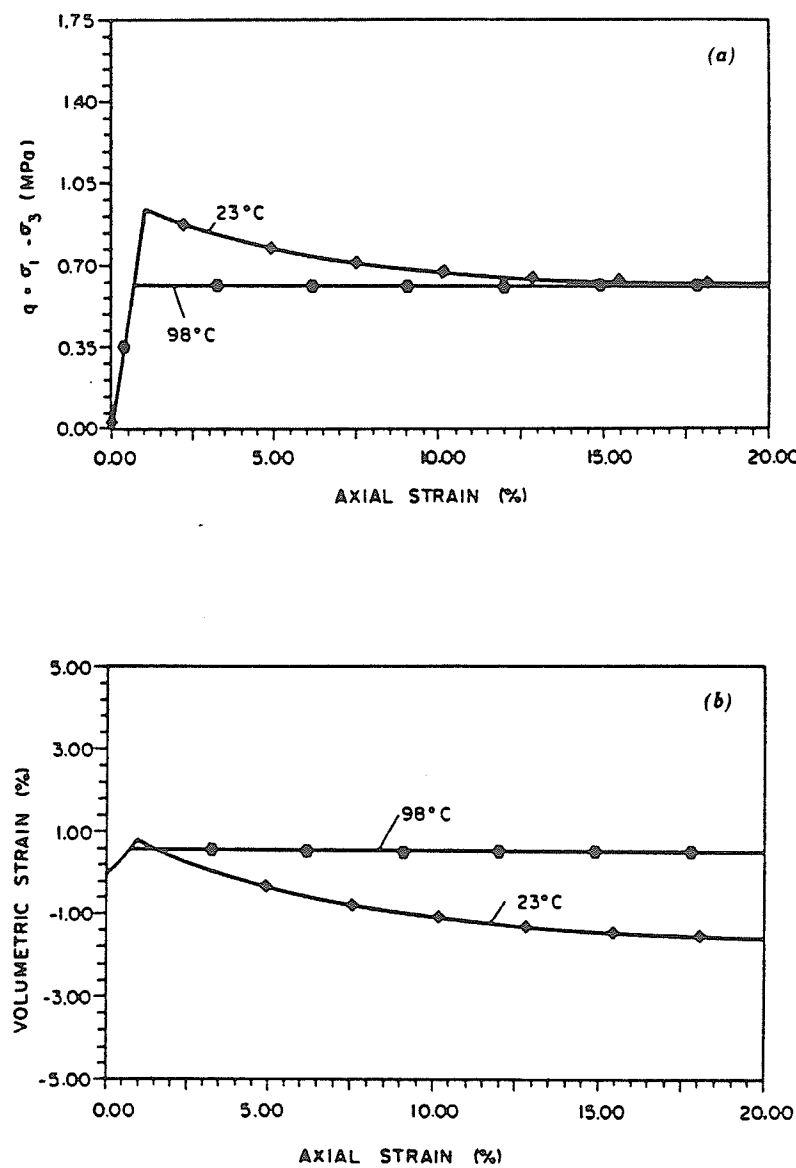


FIGURE 2.27 Numerical simulation of drained triaxial tests until failure, from Borsetto *et al.* (1987): (a) stress difference versus axial strain; and (b) volumetric versus axial strain. (after Hueckel and Baldi 1990)

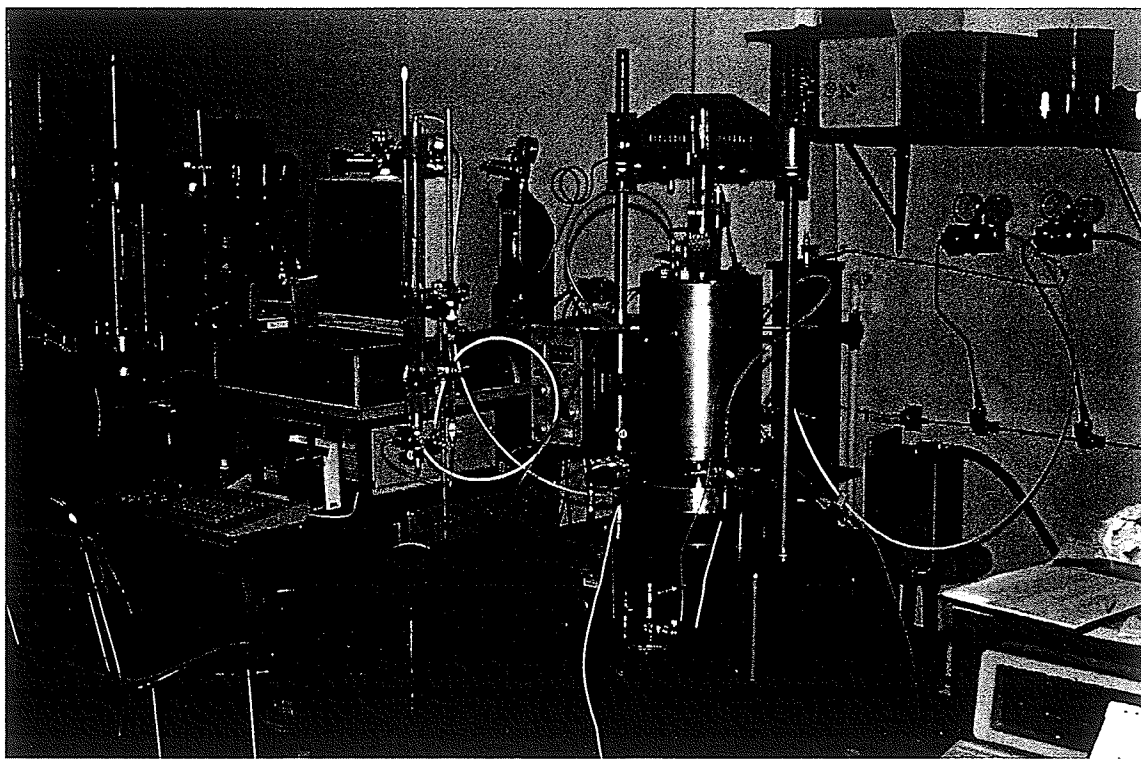
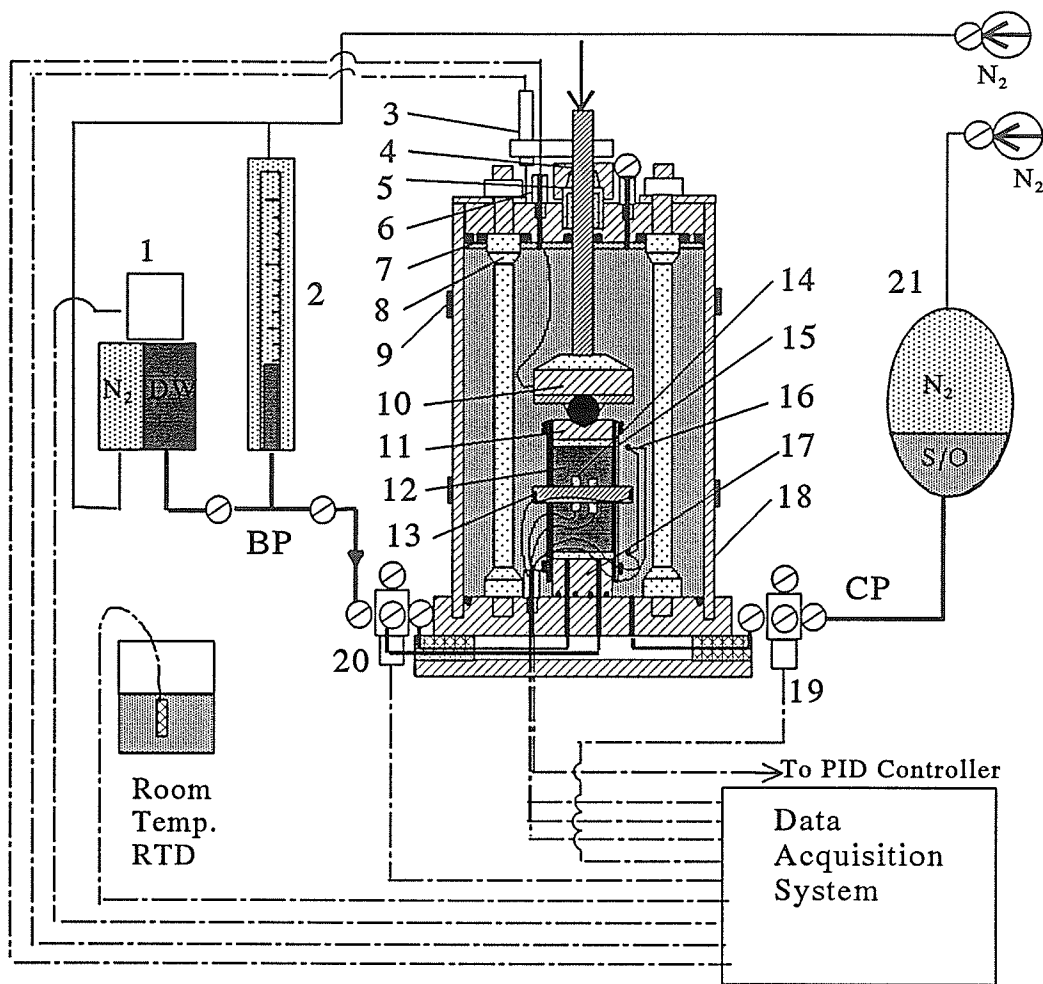


FIGURE 3.1 Ambient Temperature, High Pressure Triaxial Apparatus



LEGEND:

- | | |
|-----------------|---------------------------------|
| 1. DPT | 16. Thermocouple |
| 2. Burette | 17. Pedestal |
| 3. LVDT | 18. Sleeve |
| 4. Piston | 19. Pressure Transducer (Cell) |
| 5. Piston Clamp | 20. Pressure Transducer (BP) |
| 6. Bulkhead | 21. Accumulator |
| 7. U-Cup Seal | BP Back Pressure |
| 8. Tie Rod | CP Cell Pressure |
| 9. Heater Band | DW De-aired Water |
| 10. Load Cell | PID Proportional/Integral/Diff. |
| 11. Top Cap | S/O Silicone Oil |
| 12. Specimen | ← Regulator |
| 13. LSG | ○ On/Off Valv |
| 14. RTD | |
| 15. Membrane | |

FIGURE 3.2 Schematic diagram of High Temperature, high Pressure (HITEP) Cell

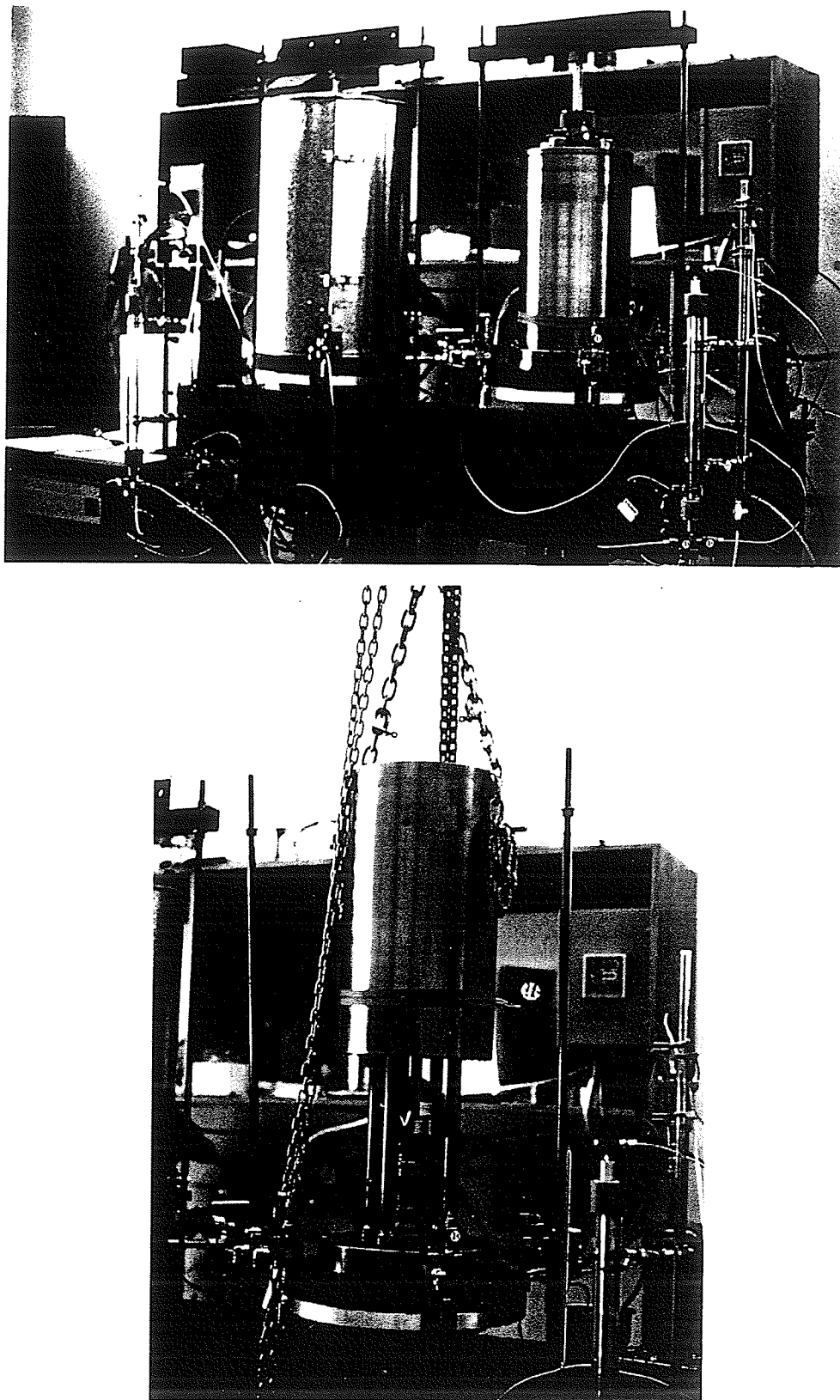
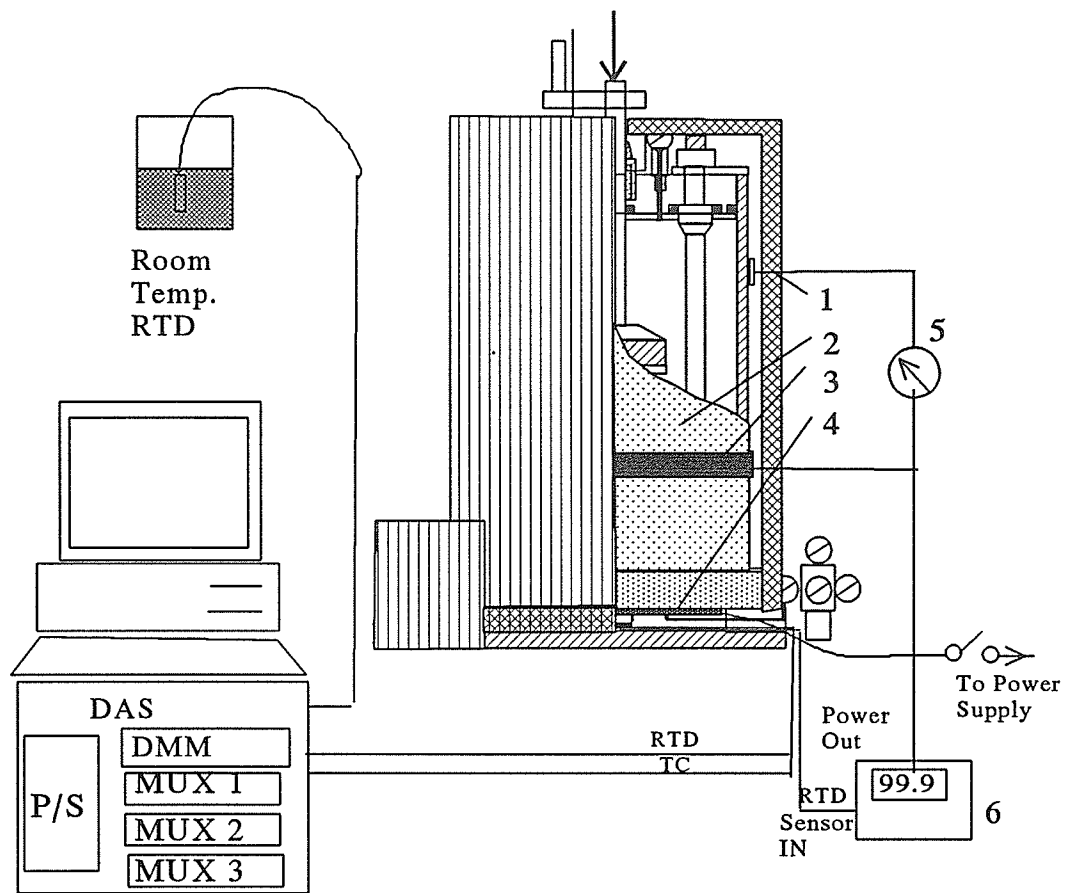


FIGURE 3.3 High Temperature, High Pressure (HITEP) triaxial cell: (a) with and without insulating jacket; (b) with sleeve lifted.



LEGEND:

1. Insulation
2. Sleeve
3. Heater Band
4. Base Heater
5. Rheostat
6. PID Temperature Controller

DAS	Data Acquisition System
DMM	Digital Multimeter
MUX 1	Multiplexer
MUX 2	
MUX 3	
P/S	Power Supply
RTD	Resistance Thermal Device
TC	Thermocouple

FIGURE 3.4 Schematic diagram of Temperature Control System (TCS) for HITEP cell

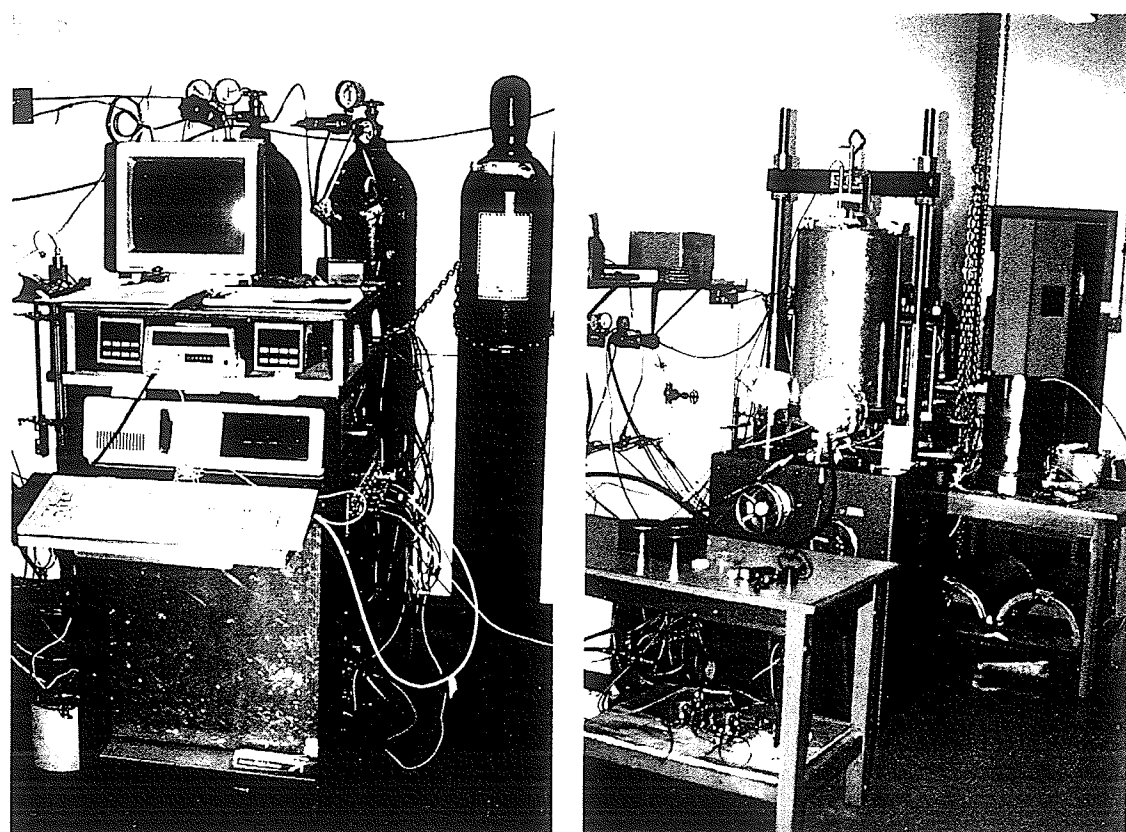


FIGURE 3.5 The complete HITEP apparatus: (a) temperature controllers and data acquisition system; (b) loading frame (background) and pressure control system (foreground)

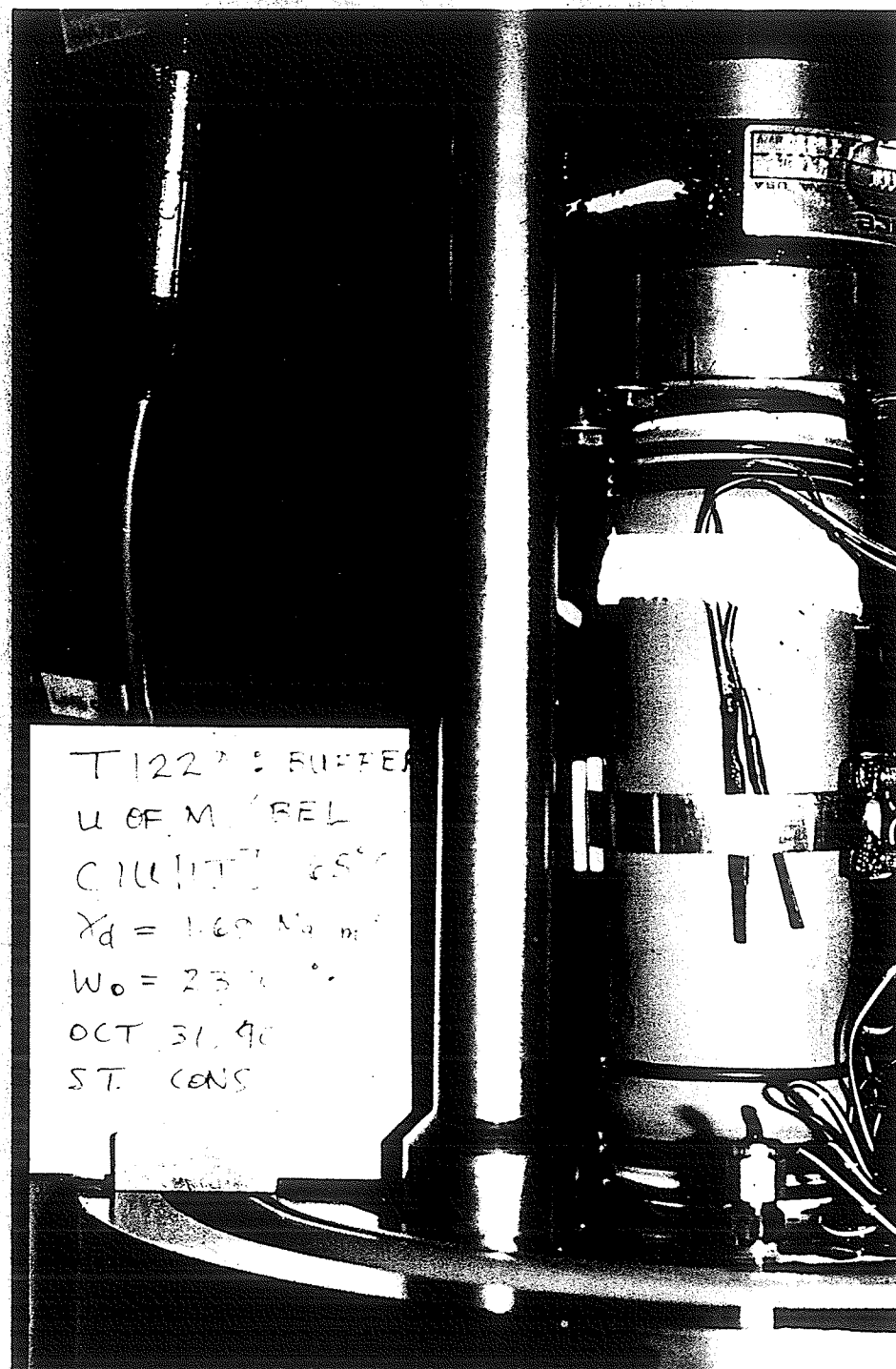
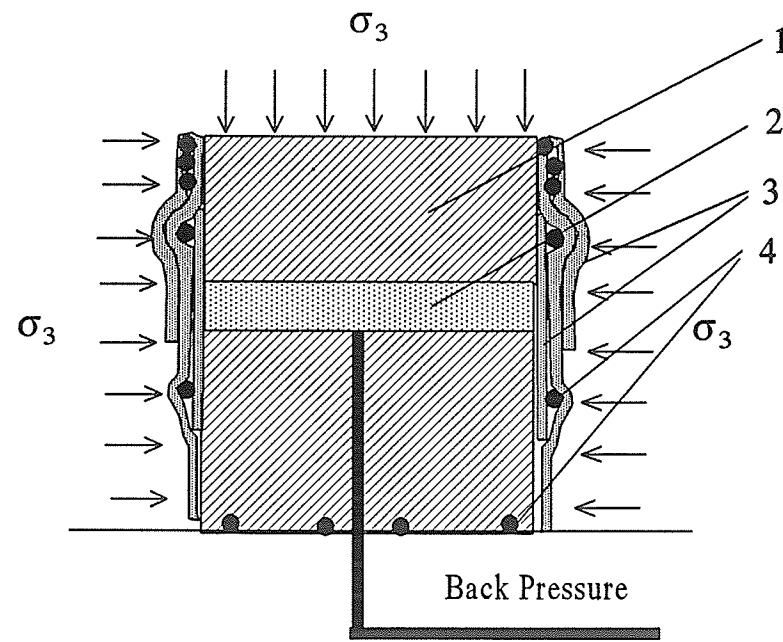


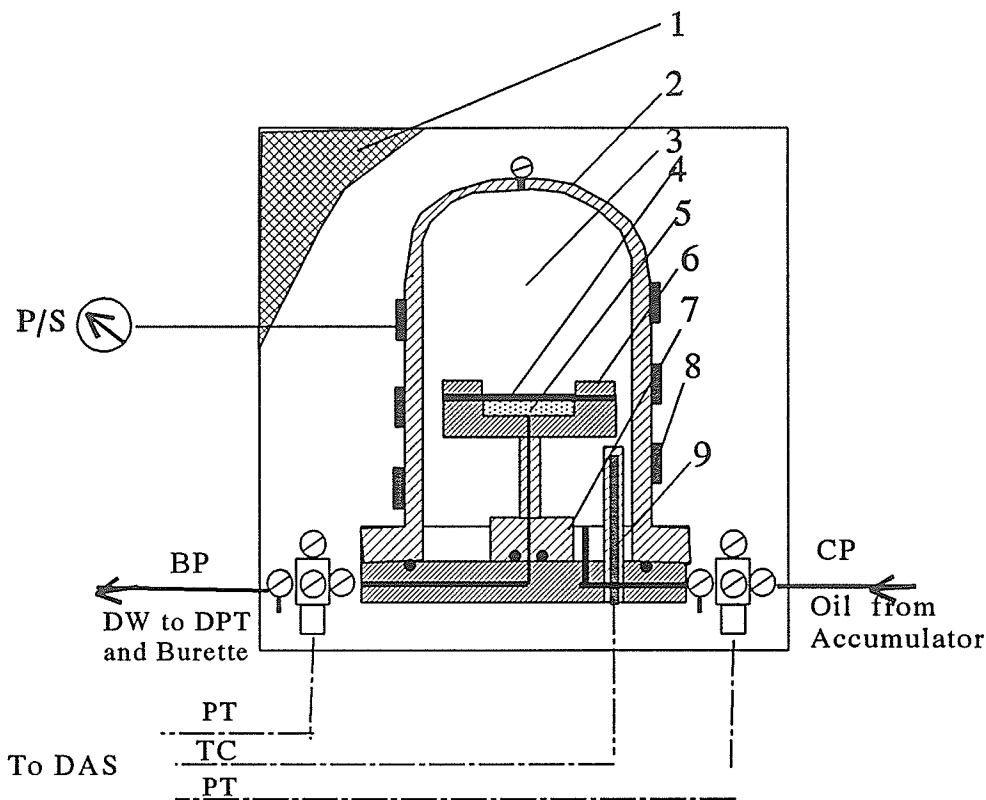
FIGURE 3.6 Buffer specimen before consolidation. Lateral strain guage and RTD shown.



LEGEND:

1. Top Cap
2. Porous Stone
3. Silicone Membranes
4. Viton O-rings

FIGURE 3.7 Leakage apparatus in HITEP cell



LEGEND:

1. Insulation
2. Pressure Vessel
3. Oil
4. Silicone Membrane
5. Porous Stone
6. Clamp Ring
7. Pedestal
8. Band Heater
9. Sheath

- | | |
|------------|-------------------------|
| BP | Back Pressure |
| CP | Cell Pressure |
| DAS | Data Acquisition System |
| DW | De-aired Water |
| P/S | Power Supply |
| TC | Thermocouple |
| PT | Pressure Transducer |
| (Rheostat) | Rheostat |

FIGURE 3.8 Schematic diagram of membrane diffusion cell

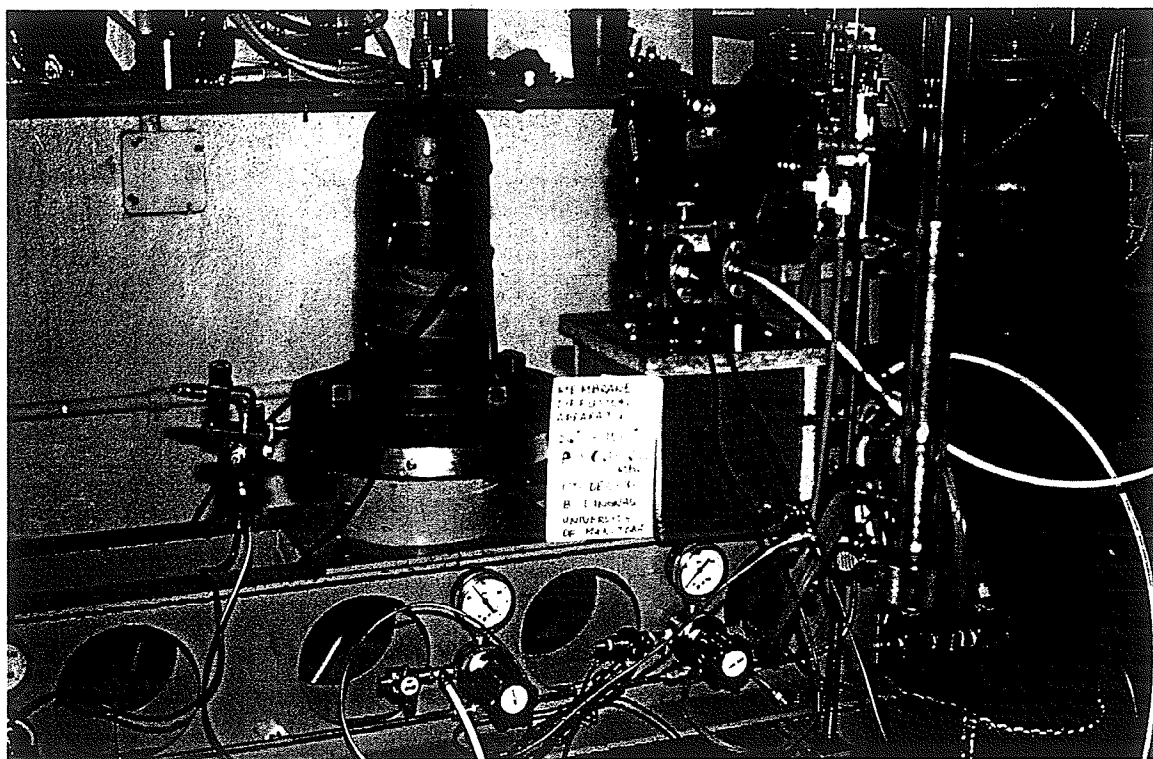


FIGURE 3.9 Membrane diffusion apparatus

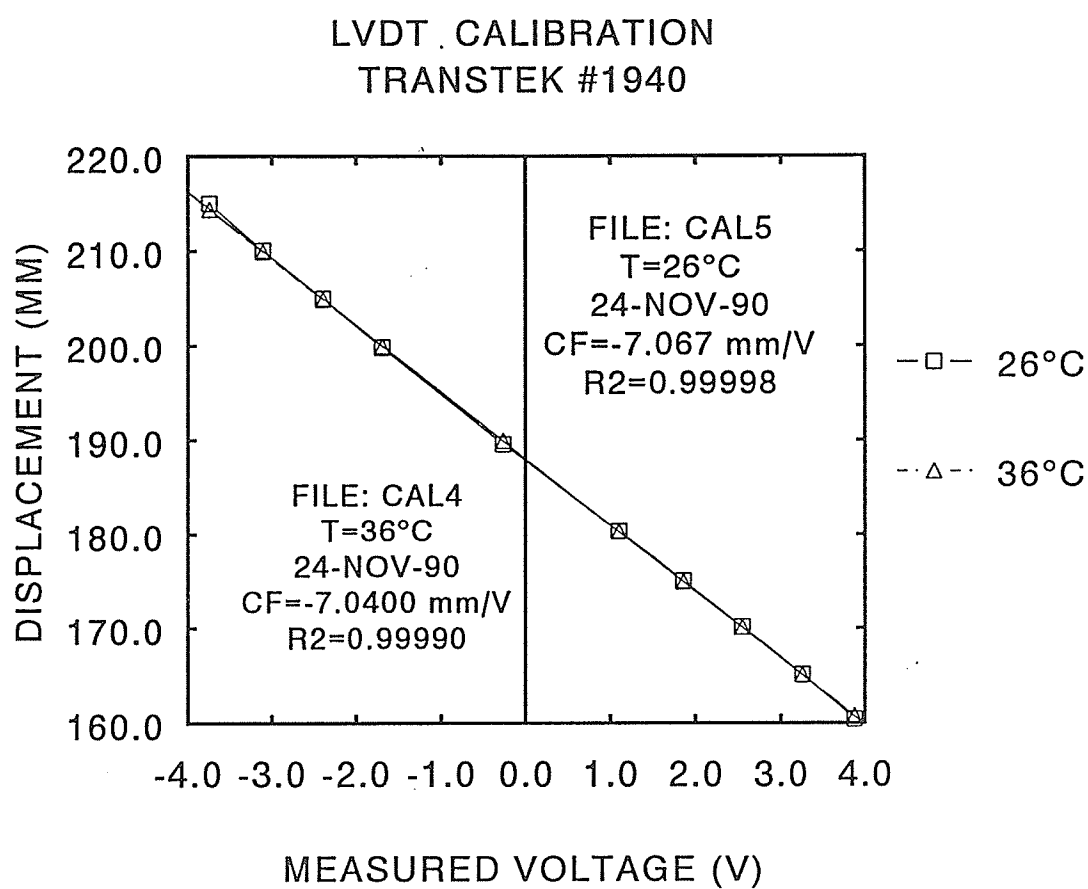


FIGURE 3.10 LVDT calibration at 26°C and 36°C

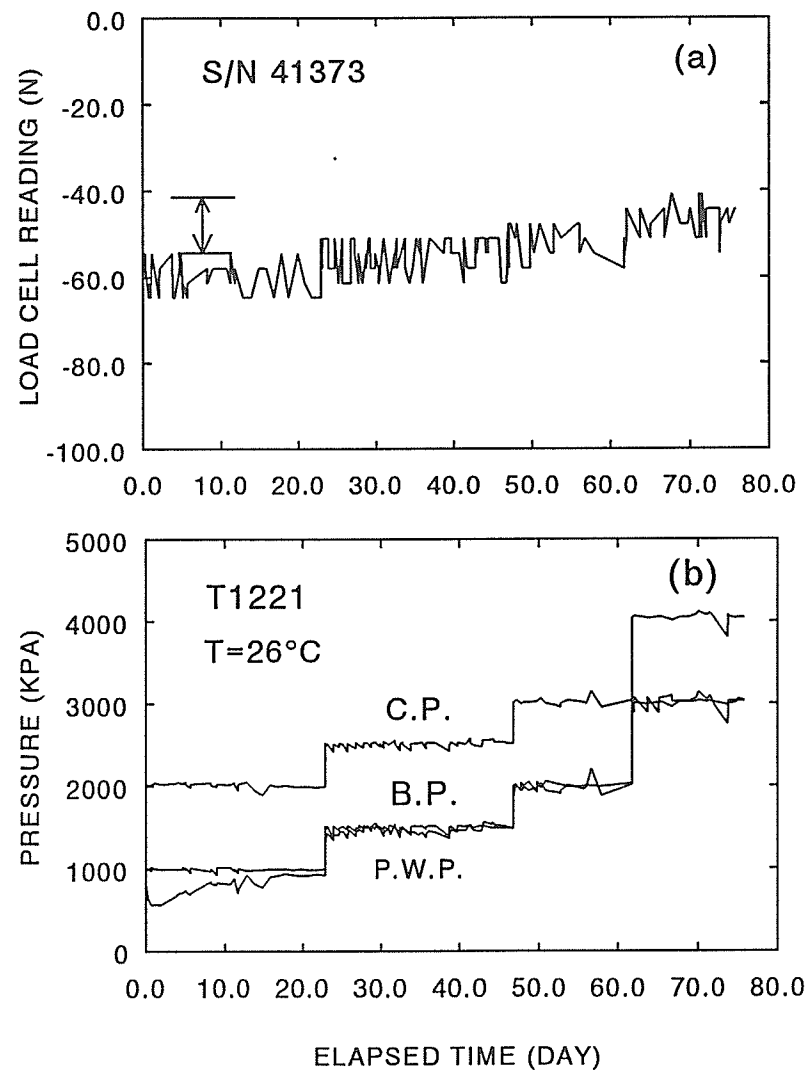


FIGURE 3.11 Pressure dependency of a load cell in HITEP test T1221: (a) load versus elapsed time; (b) pressure versus elapsed time

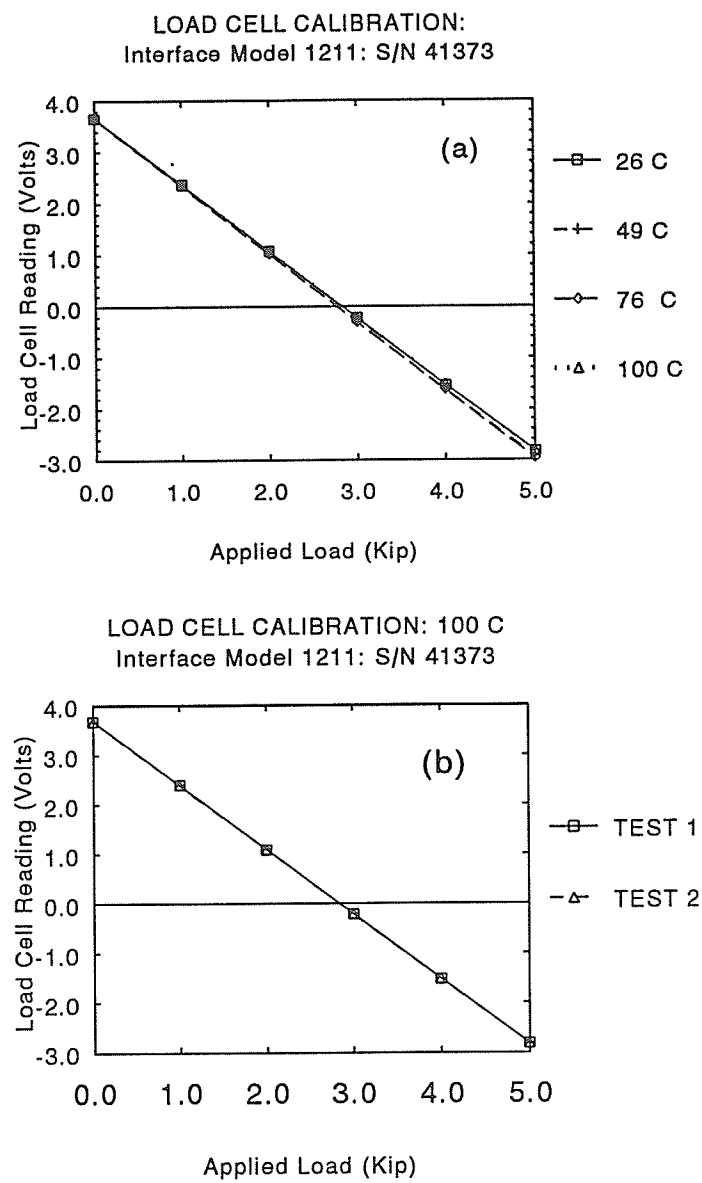


FIGURE 3.12 Temperature dependency of a load cell: (a) output versus applied load at different temperatures; (b) repeatability of output versus applied load at 100°C

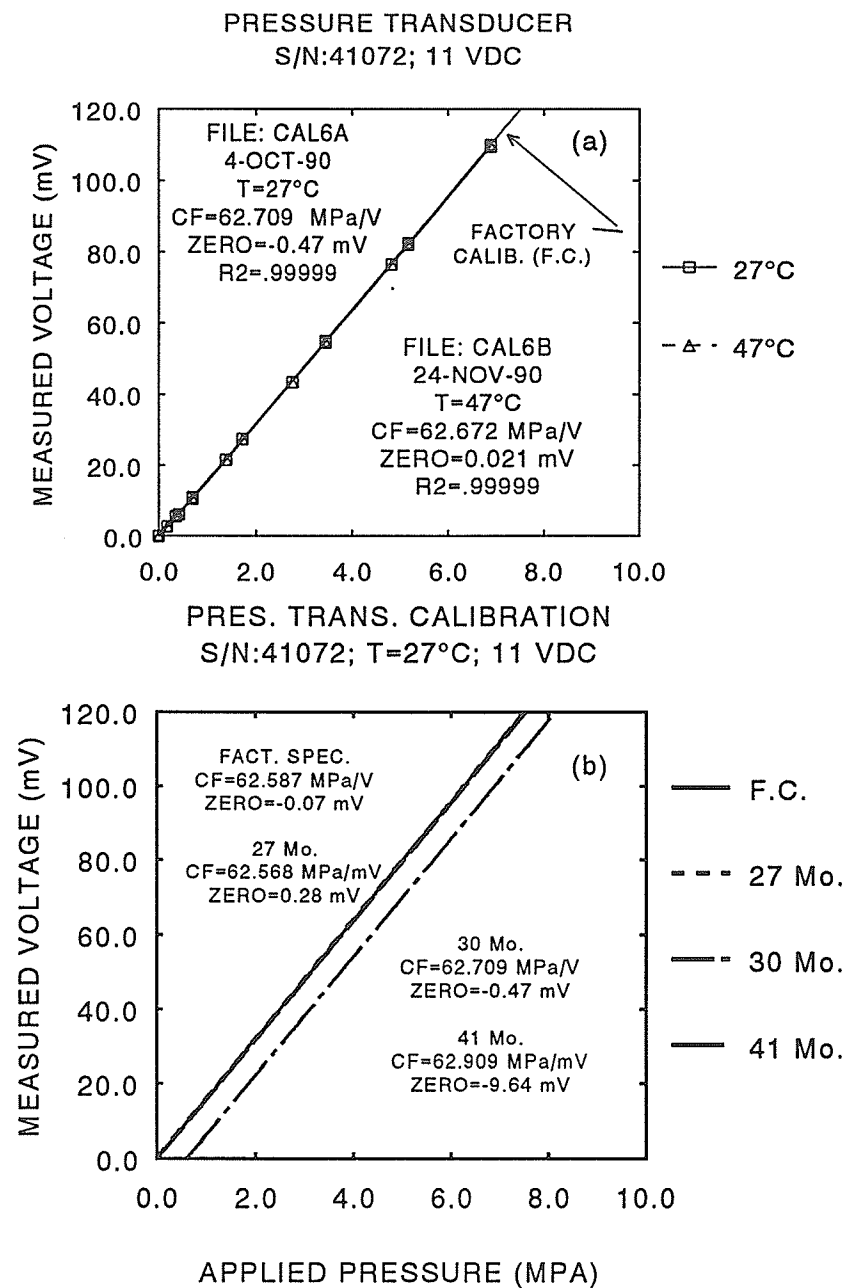


FIGURE 3.13 Pressure transducer calibrations: (a) effect of elevated temperature; (b) effect of continuous use

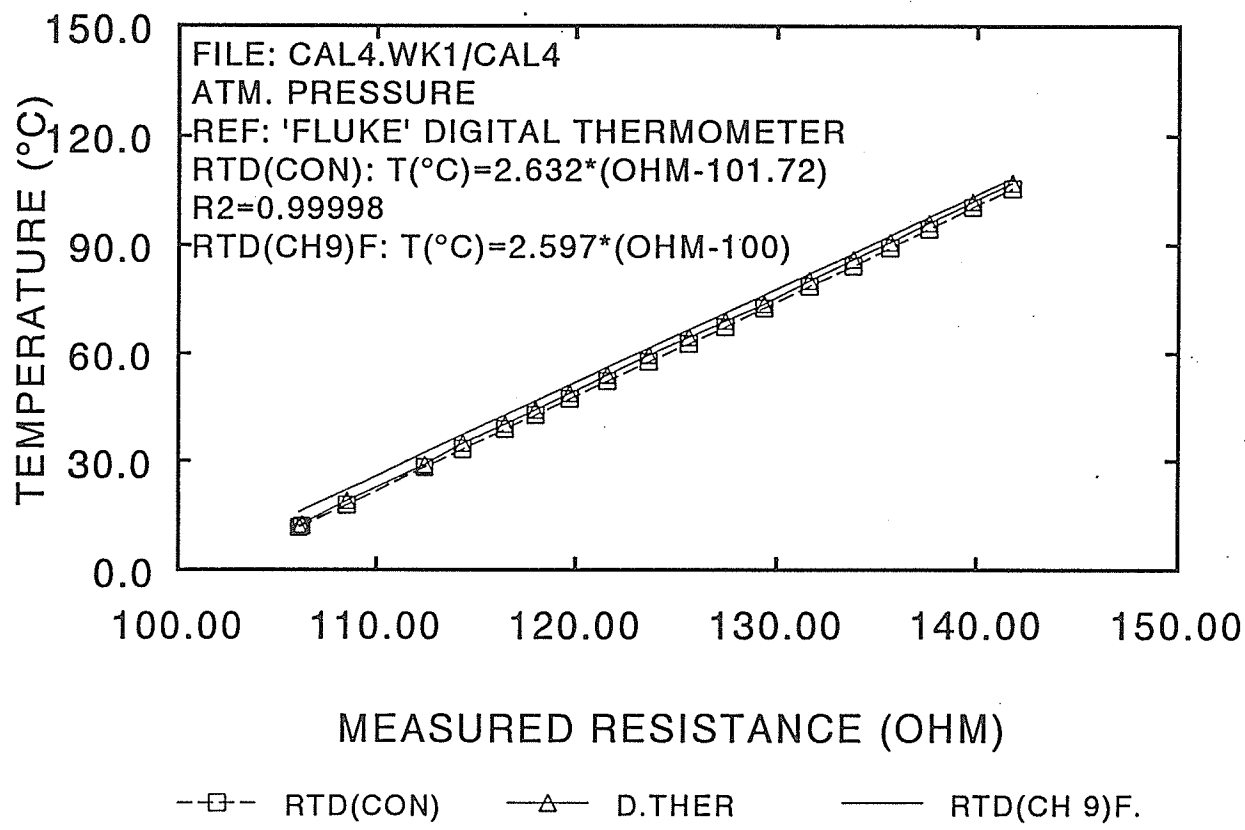


FIGURE 3.14 RTD calibrations compared to a digital thermometer (D.THER)

T1228: DPT CALIBRATION CHECK
S/N C101152;

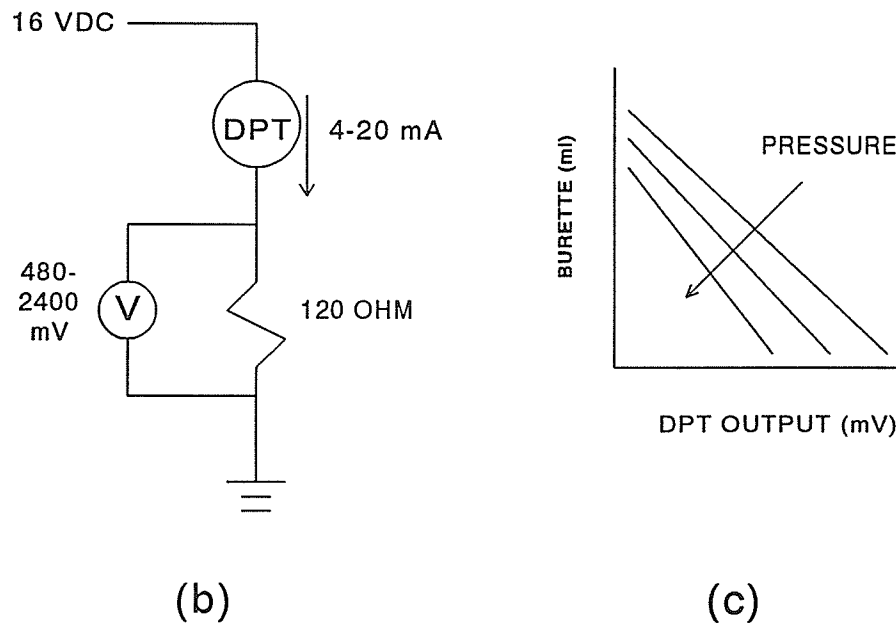
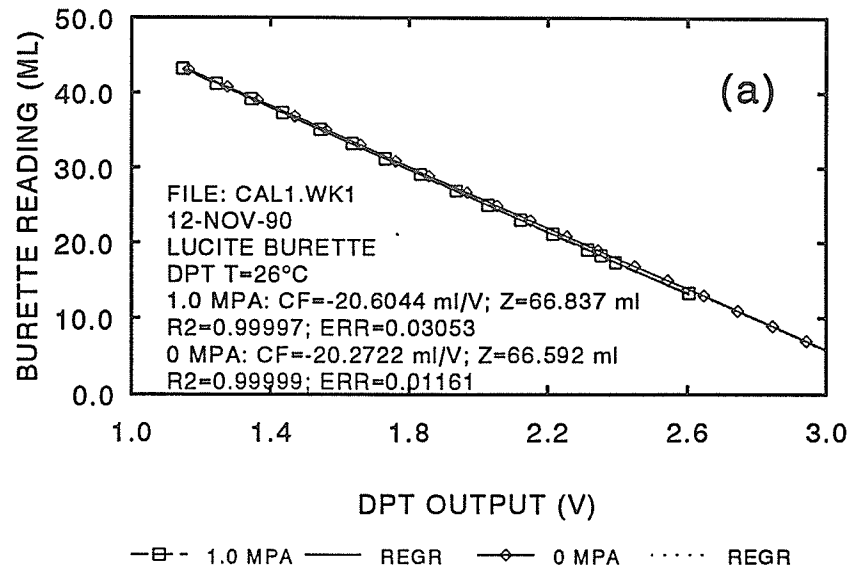


FIGURE 3.15 Volume change measurement: (a) system response including DPT, burette, fittings, water and data acquisition; (b) DPT signal conversion (Amps to Volts); (c) system response simplified

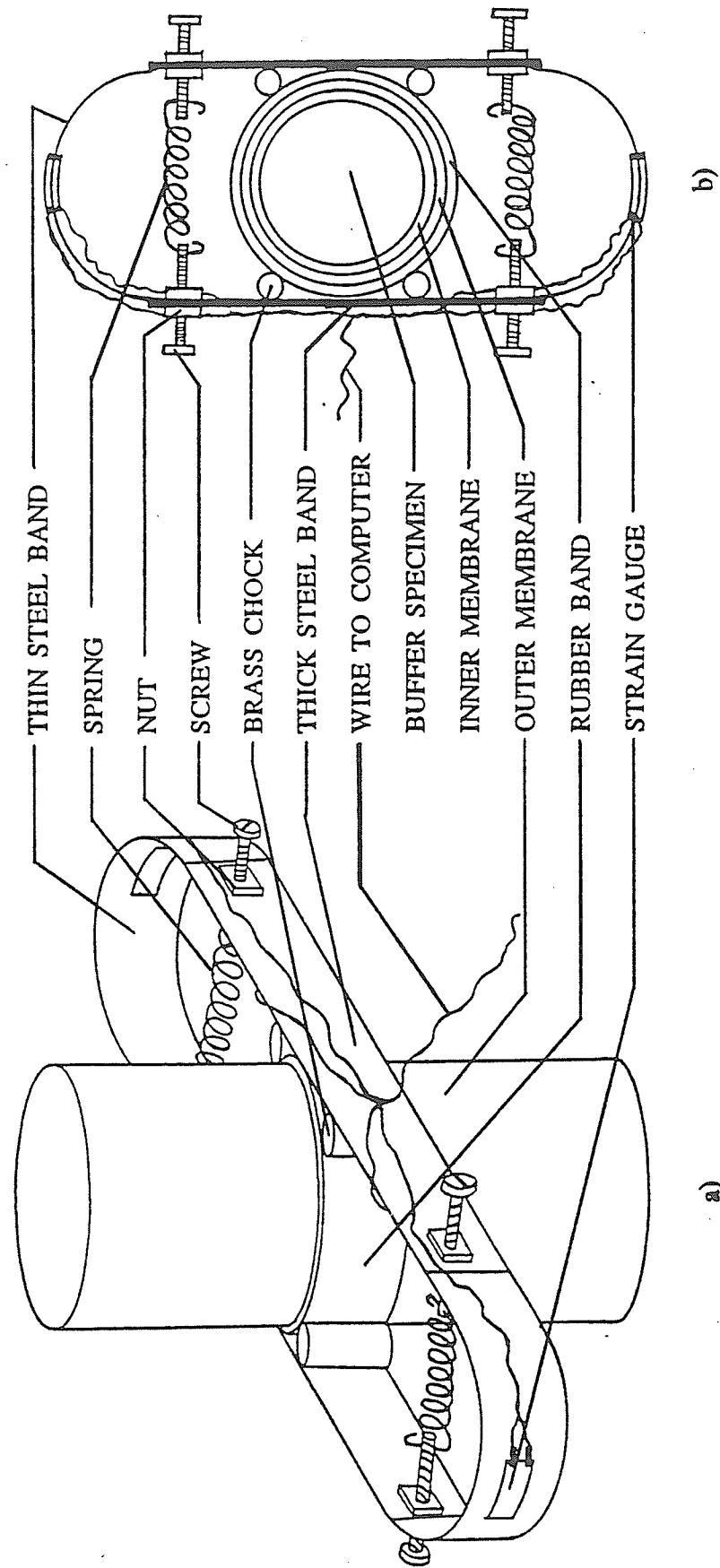


FIGURE 3.16 Lateral Strain Gauge (LSG): (a) isometric view; (b) plan view

LATERAL STRAIN GAGE CALIBRATION

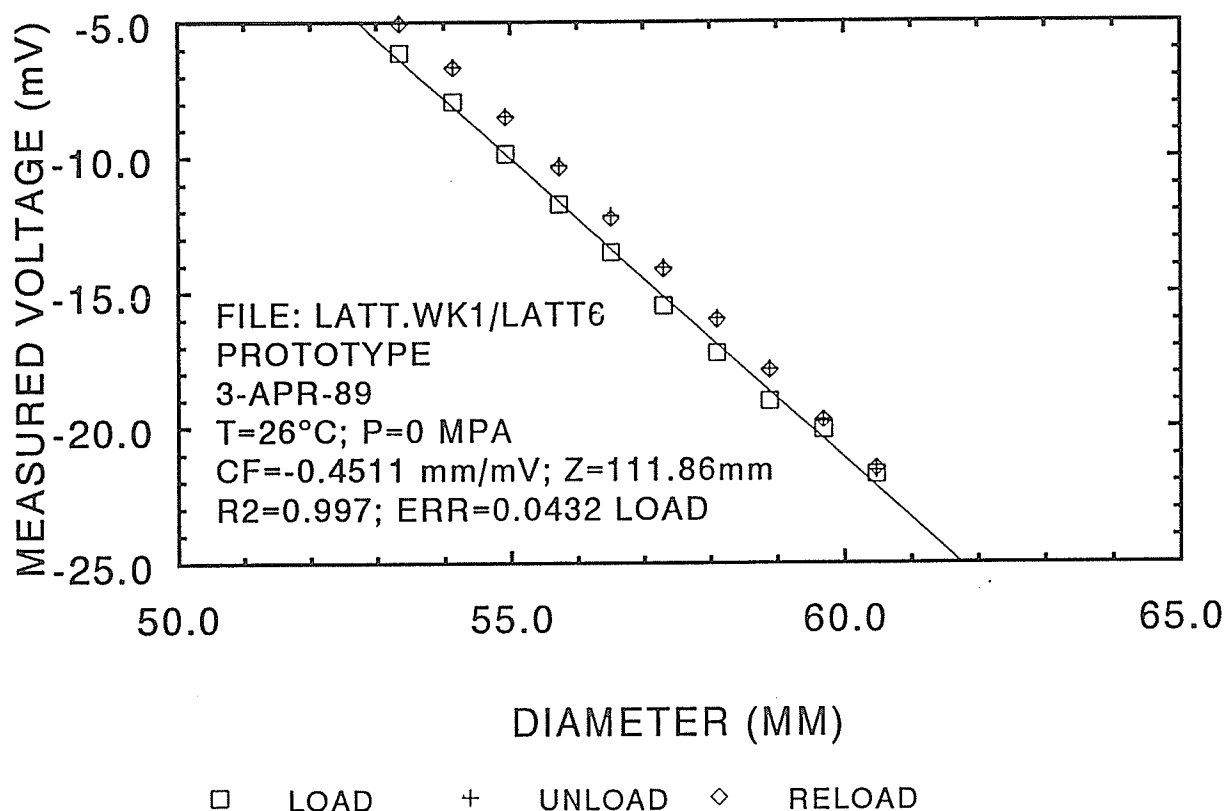


FIGURE 3.17 Calibration of the Lateral Strain Gauge (LSG)

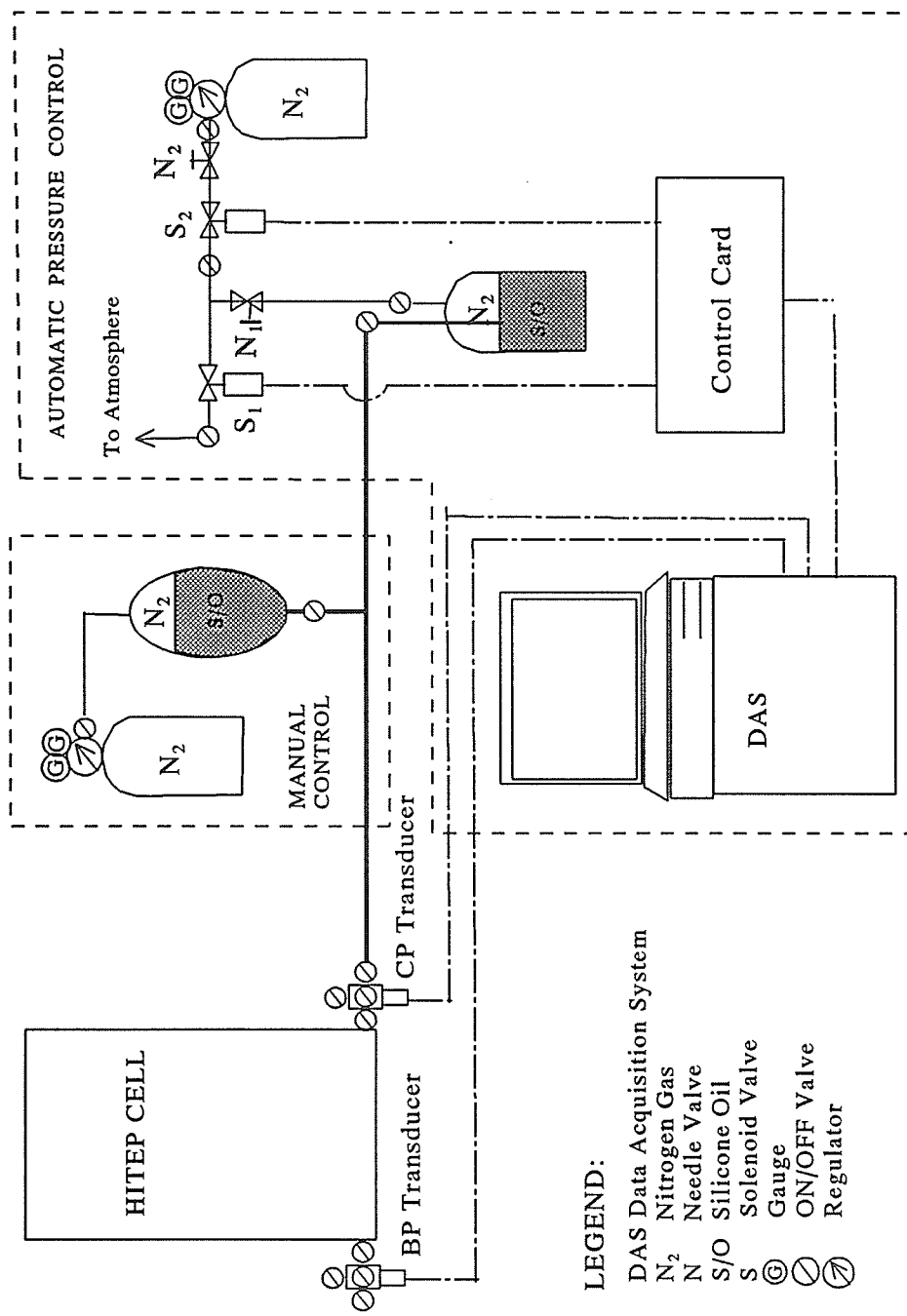


FIGURE 3.18 Schematic diagram of the Pressure Control System (PCS)

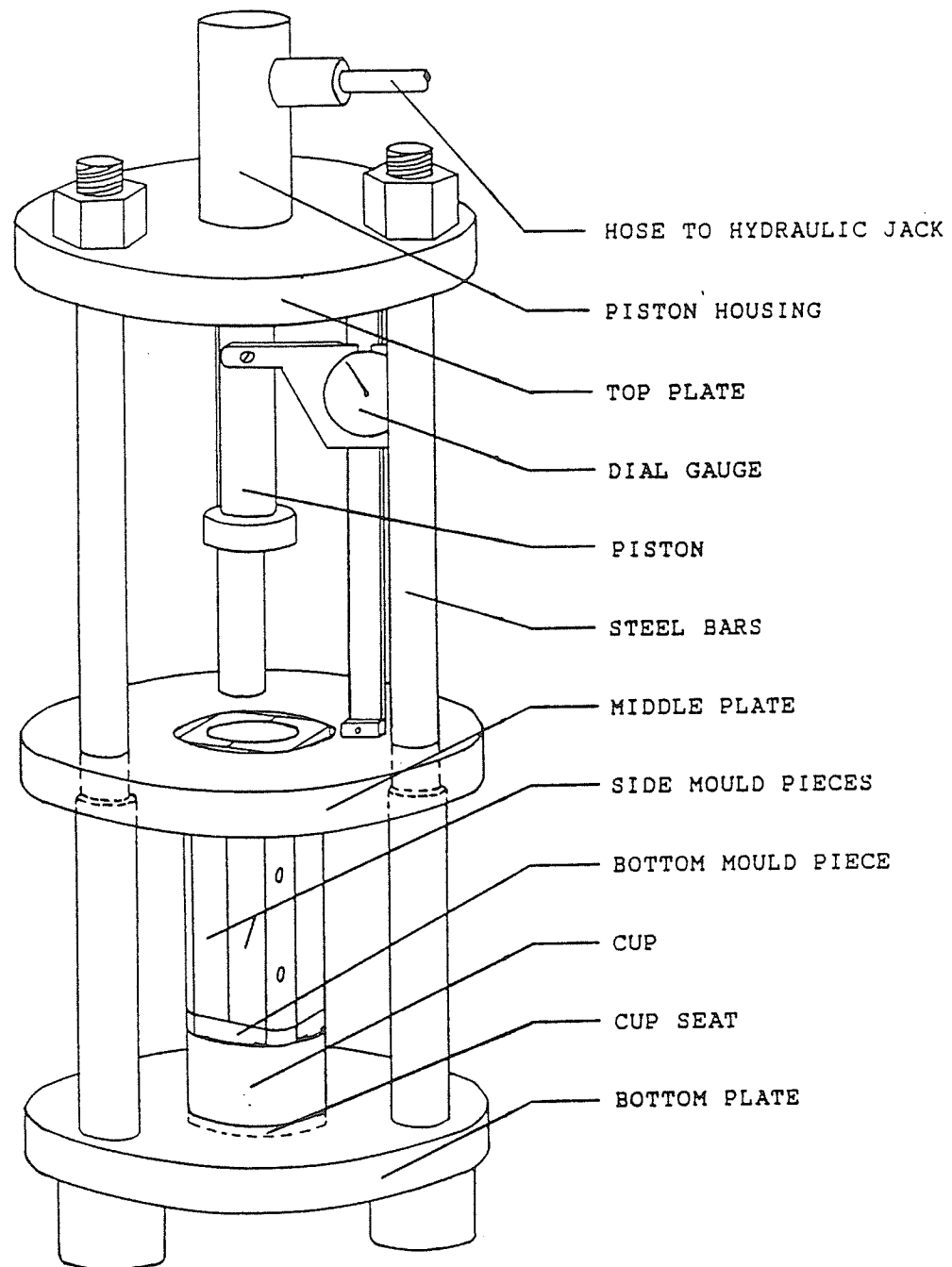


FIGURE 3.19 Specimen forming apparatus

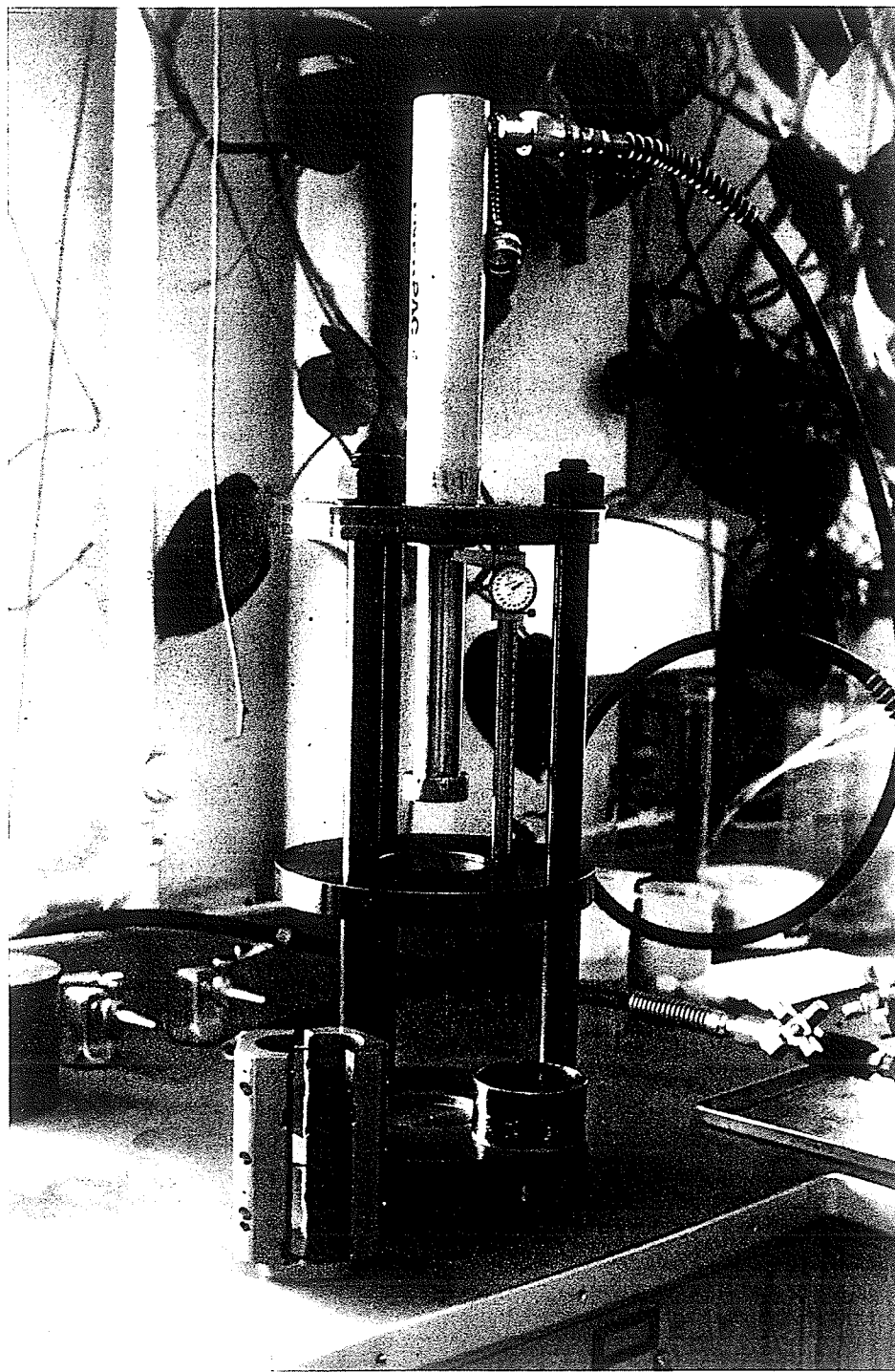


FIGURE 3.20 Specimen compaction mold (foreground) and compaction frame (background)

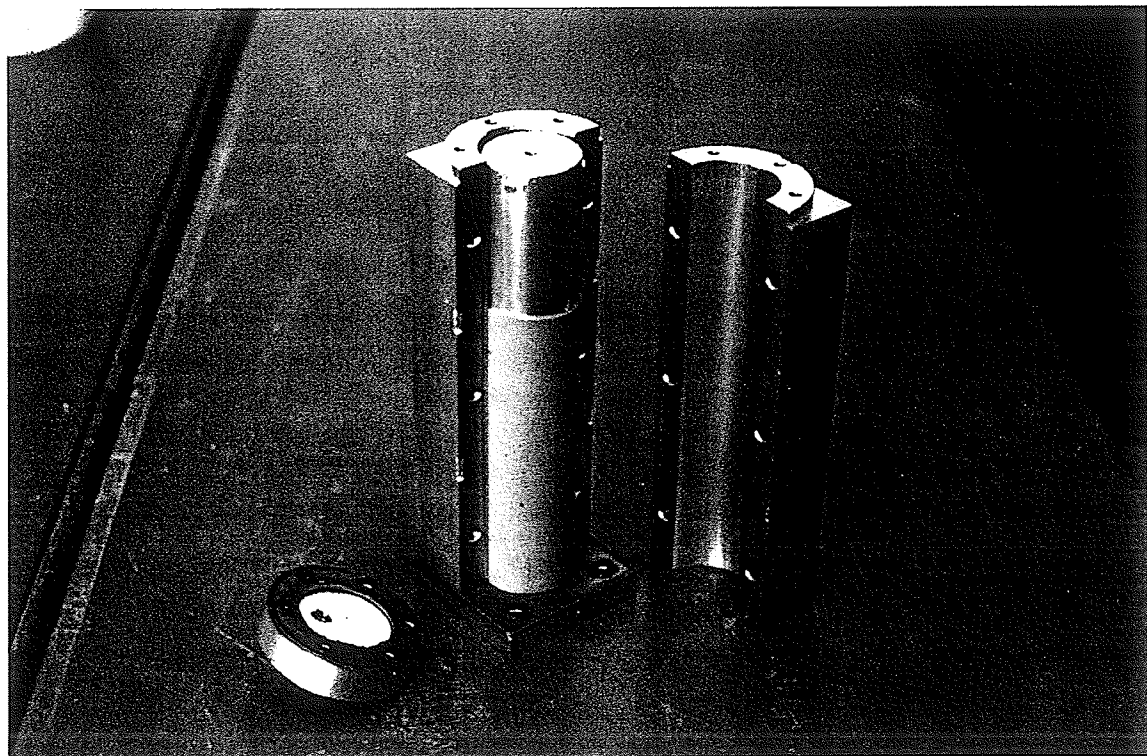


FIGURE 3.21 Improved split mold for forming membranes under pressure and vacuum

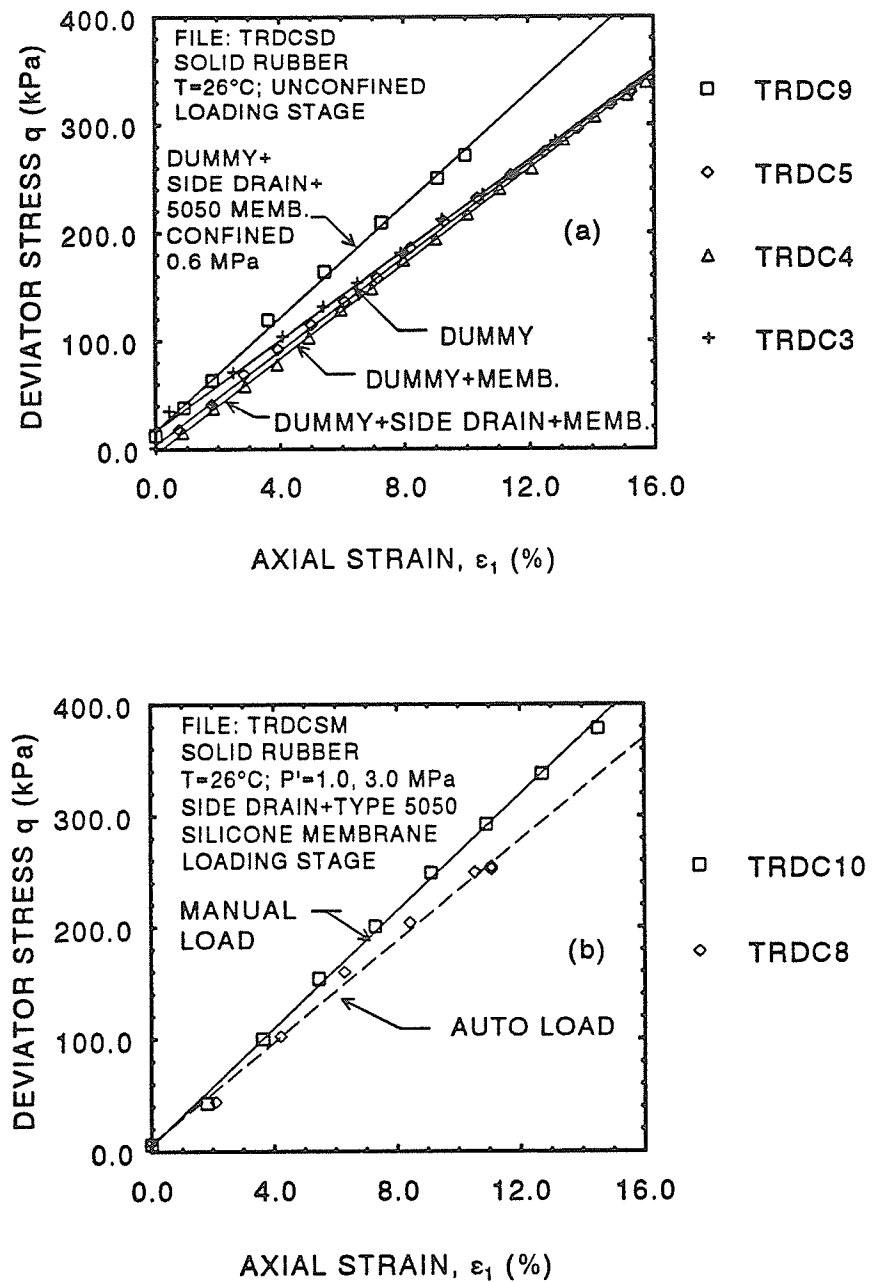


FIGURE 3.22 Rubber dummy tests: (a) effect of confining pressure; (b) effect of test procedure.

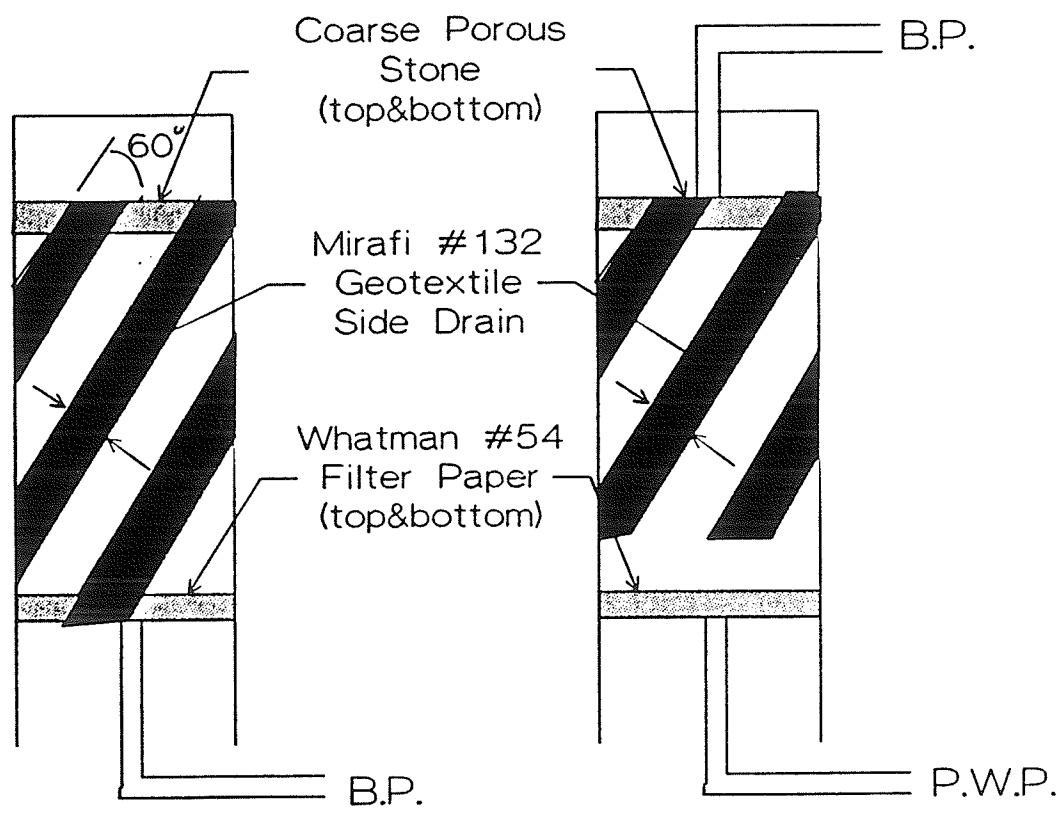


FIGURE 3.23 Basic drainage conditions for buffer

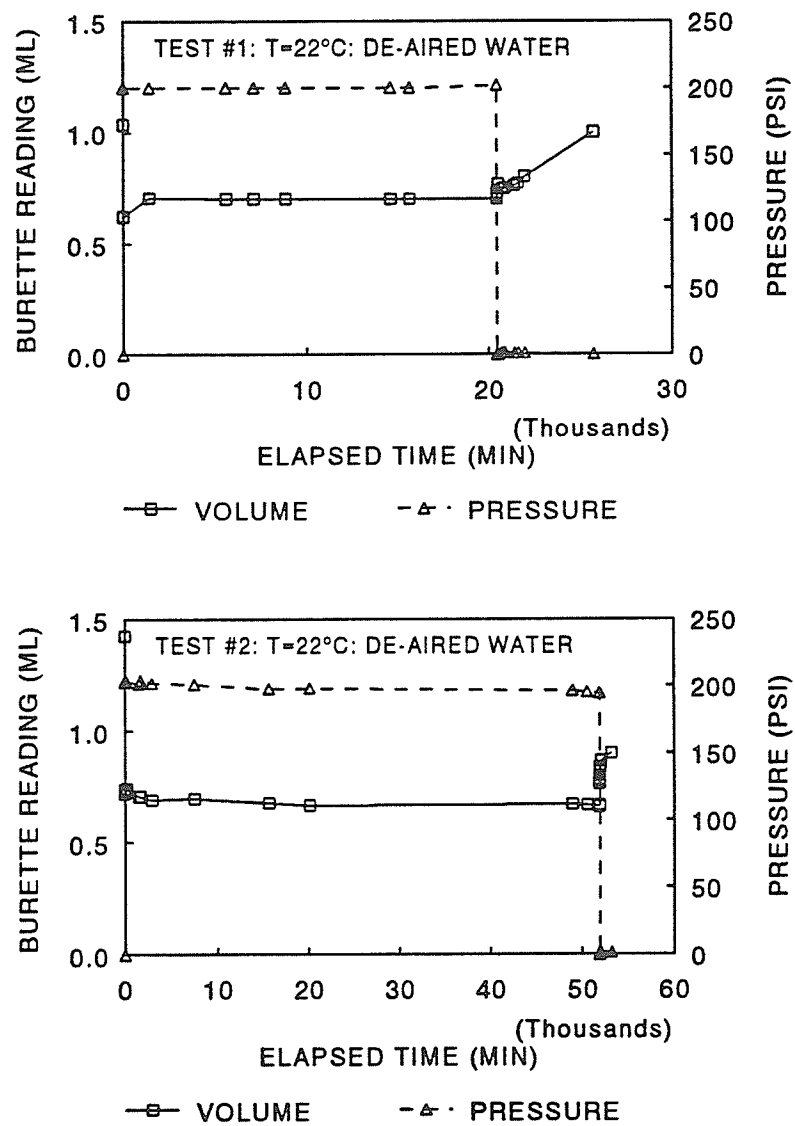


FIGURE 3.24 Pressure-volume-time response of the back-pressure burettes

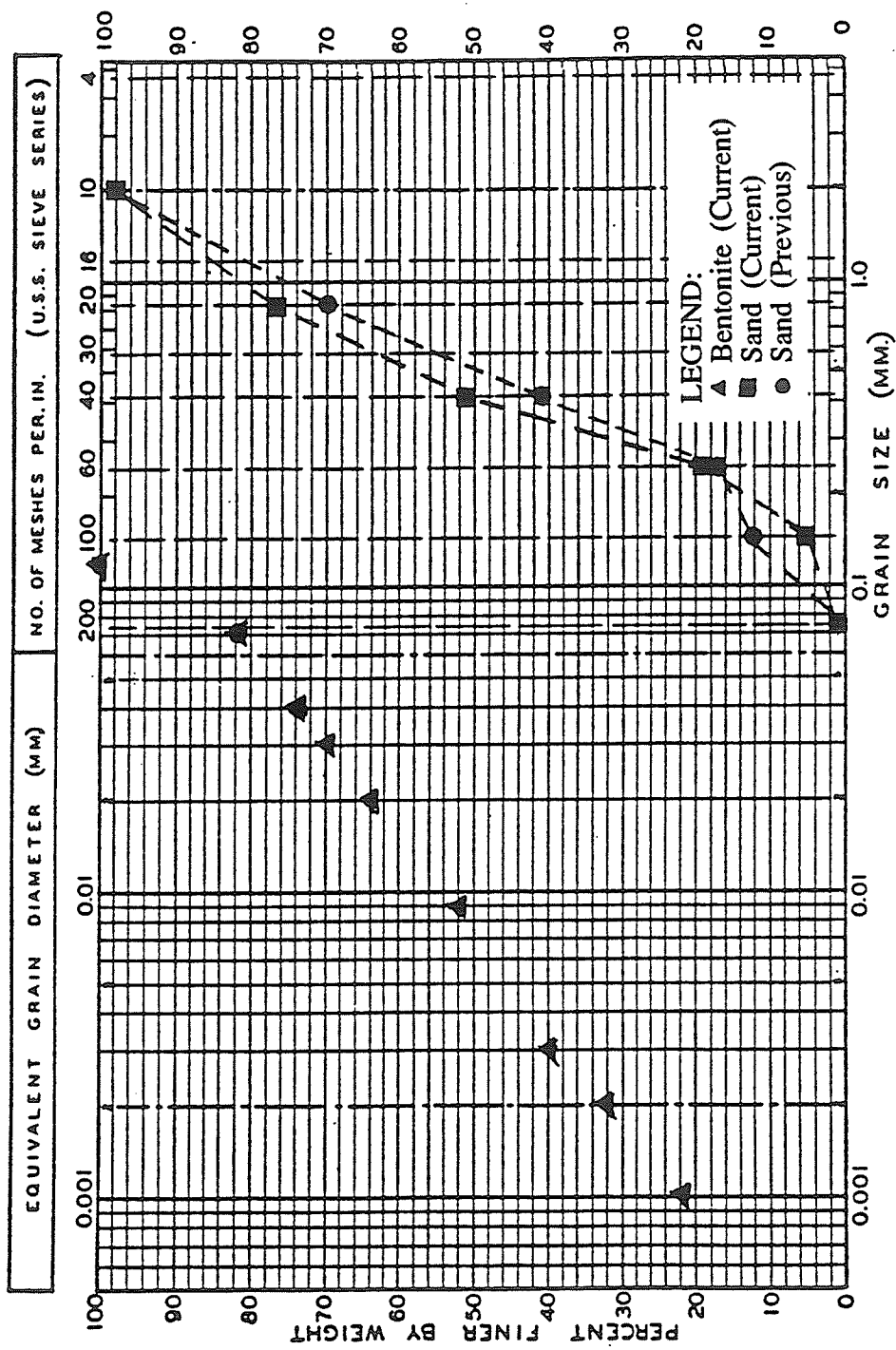


FIGURE 4.1 Sieve analysis of blended sand used in buffer specimens.
(after Dixon and Woodcock 1986)

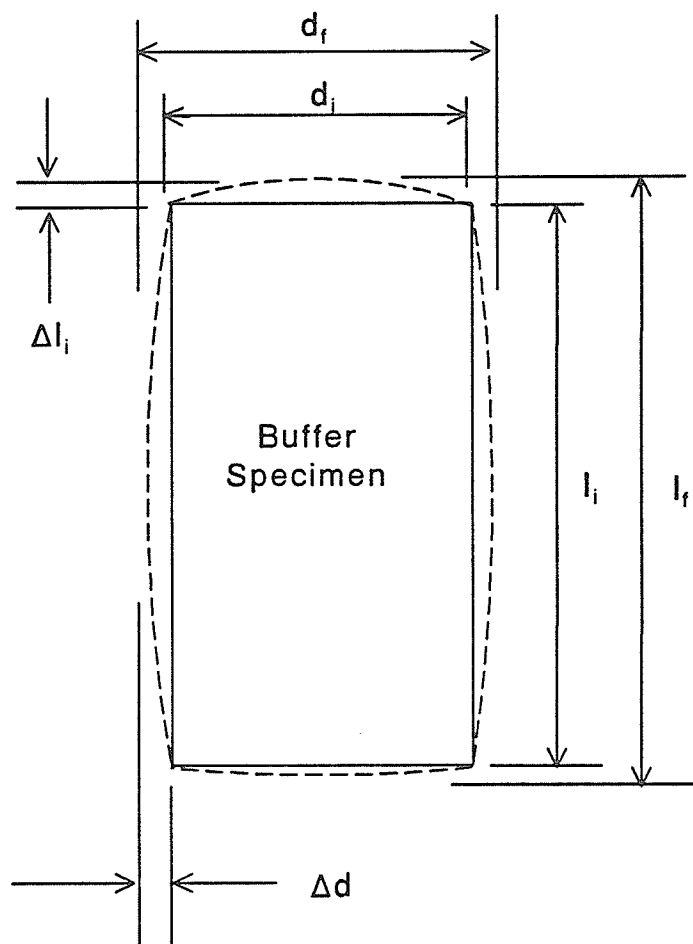


FIGURE 5.1 Bulging of compacted buffer specimens following removal from split mold

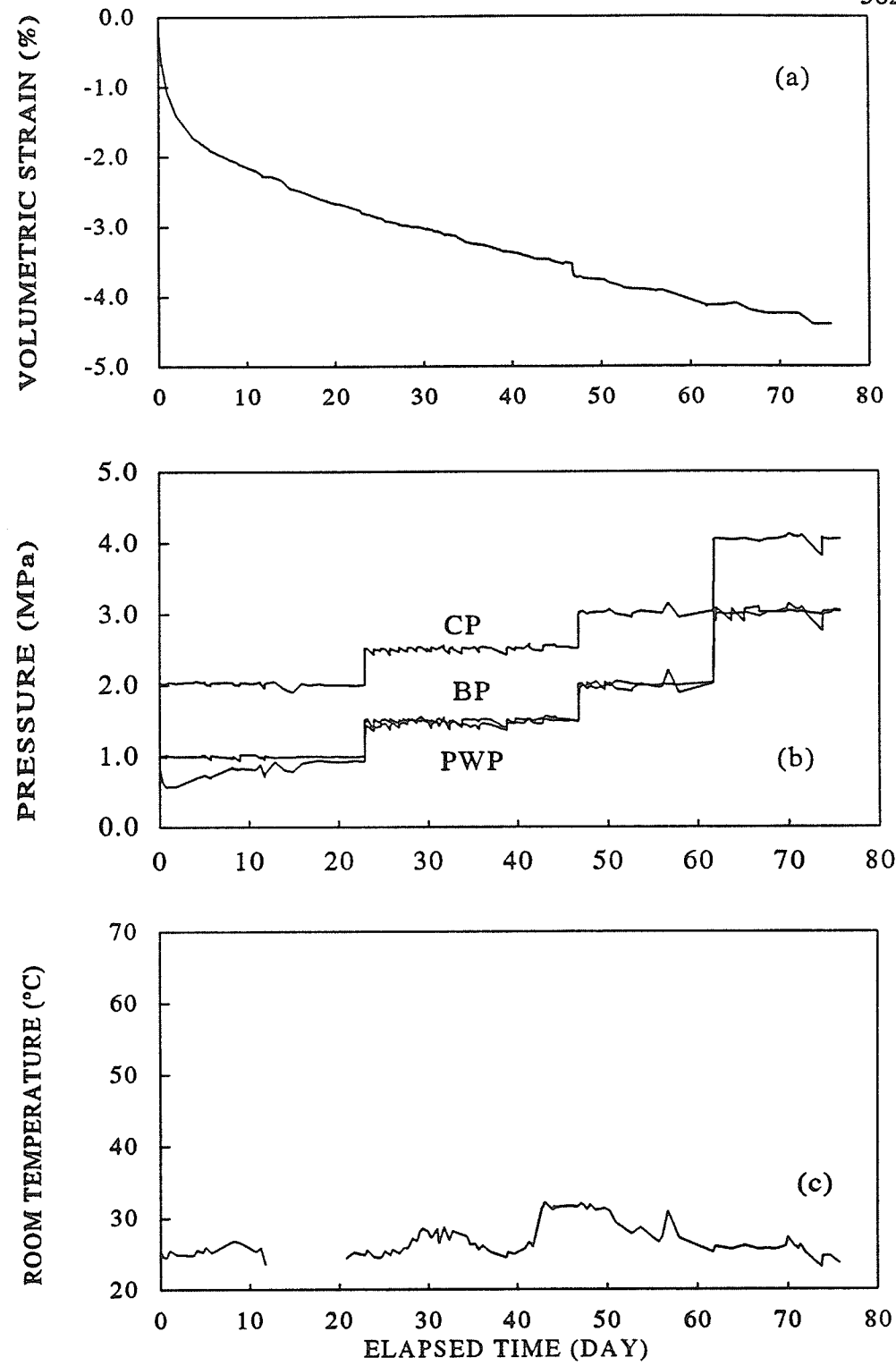


FIGURE 5.2 Consolidation results from CIU(TXC) test T1221: (a) volumetric strain versus elapsed time; (b) pressure versus elapsed time; and (c) temperature versus elapsed time

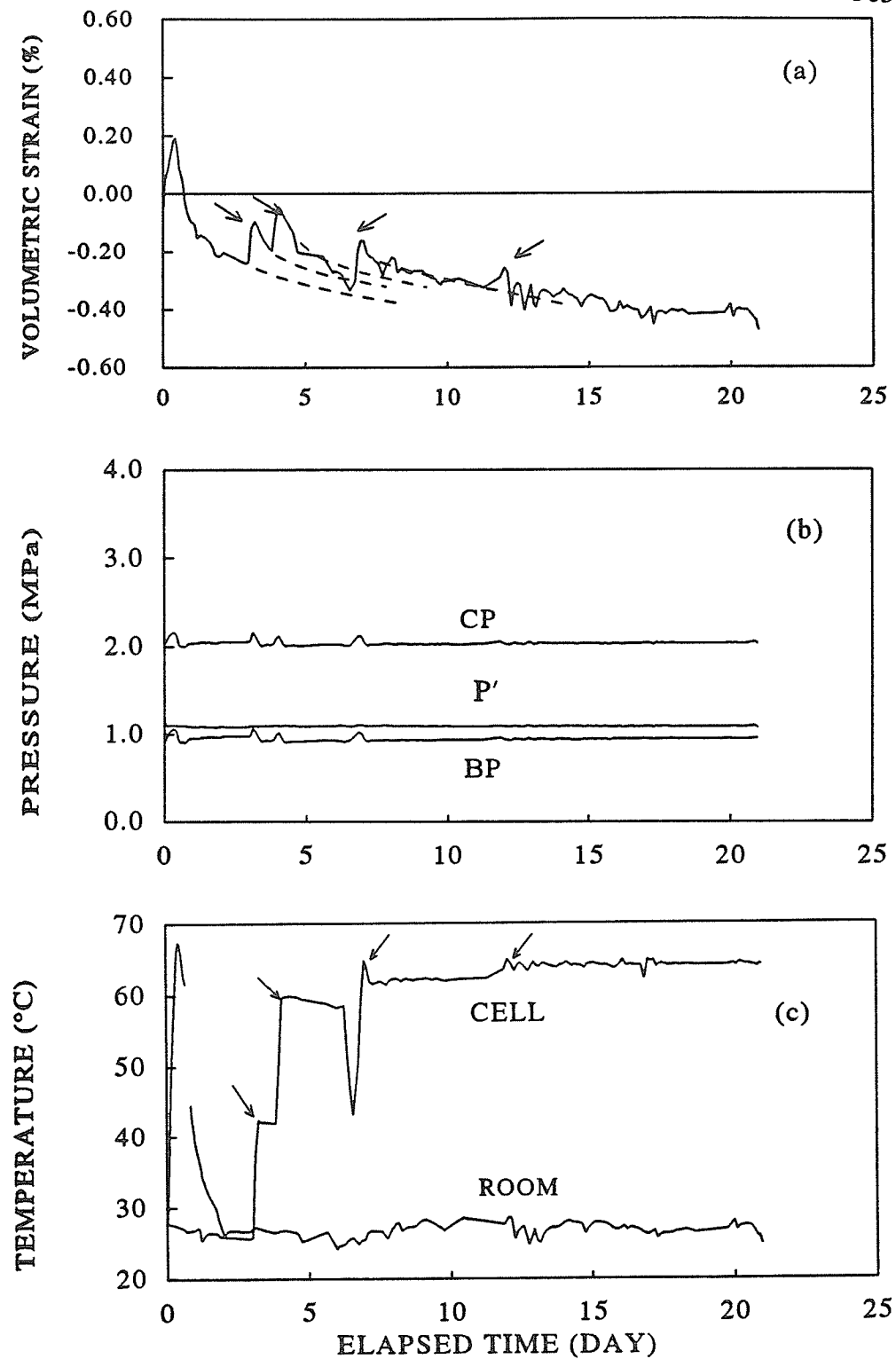


FIGURE 5.3 Consolidation results from CIU(TXC) test T1220: (a) volumetric strain versus elapsed time; (b) pressure versus elapsed time; and (c) temperature versus elapsed time

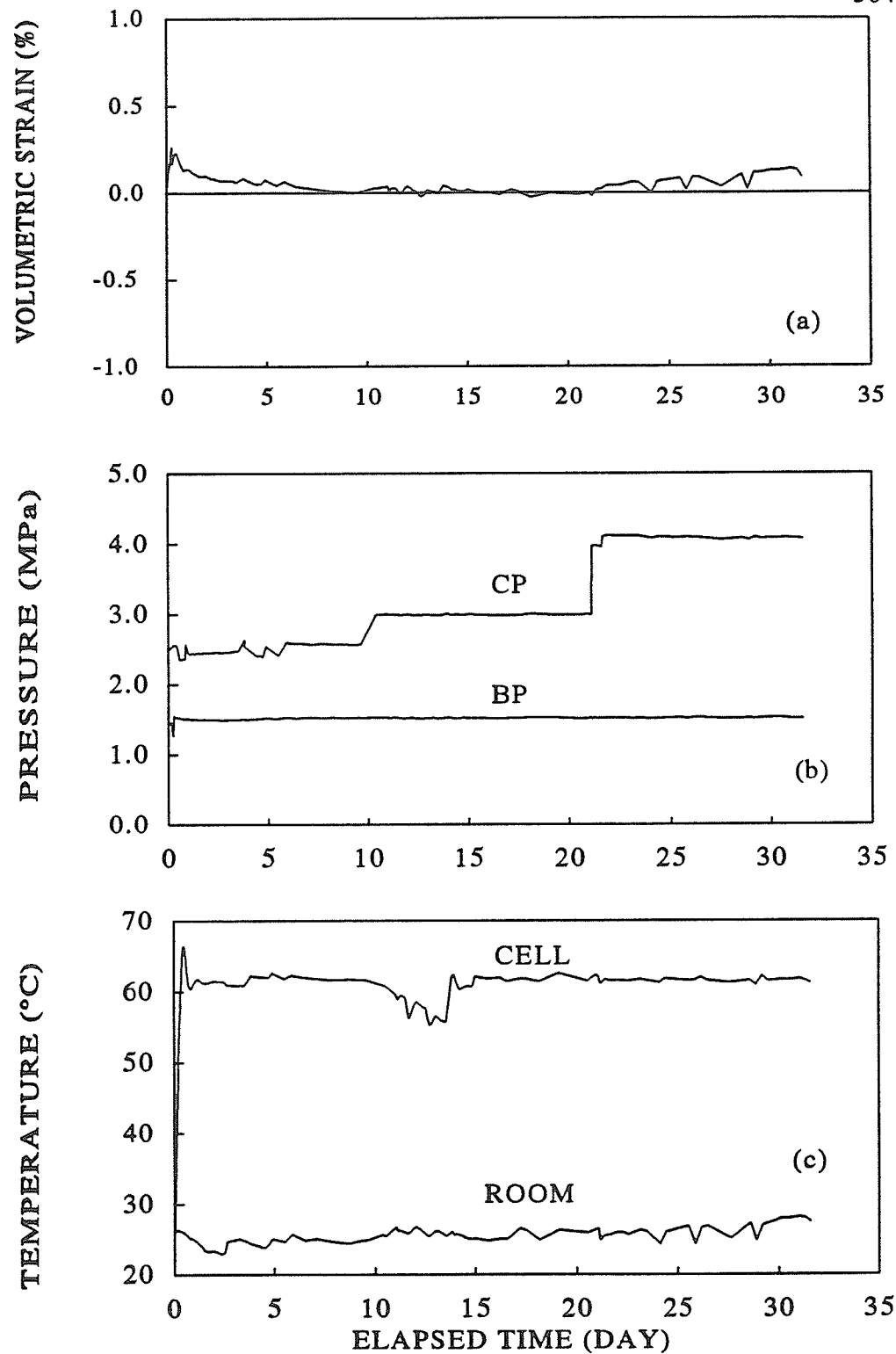


FIGURE 5.4

Consolidation results from CIU(TXC) test T1222: (a) volumetric strain versus elapsed time; (b) pressure versus elapsed time; and (c) temperature versus elapsed time

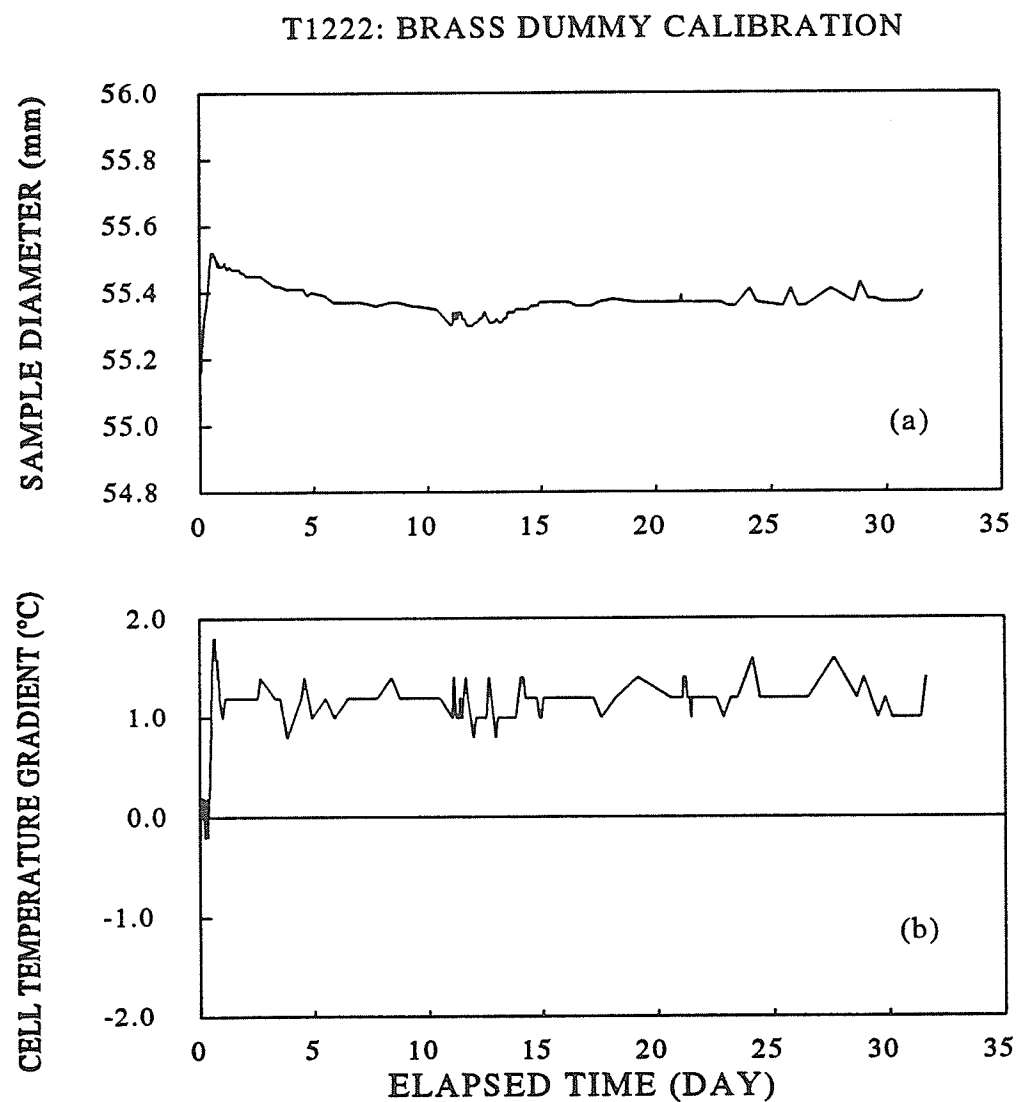


FIGURE 5.5 Consolidation results from CIU(TXC) test T1222: (a) lateral strain gauge readings versus elapsed time; and (b) temperature vs. elapsed time

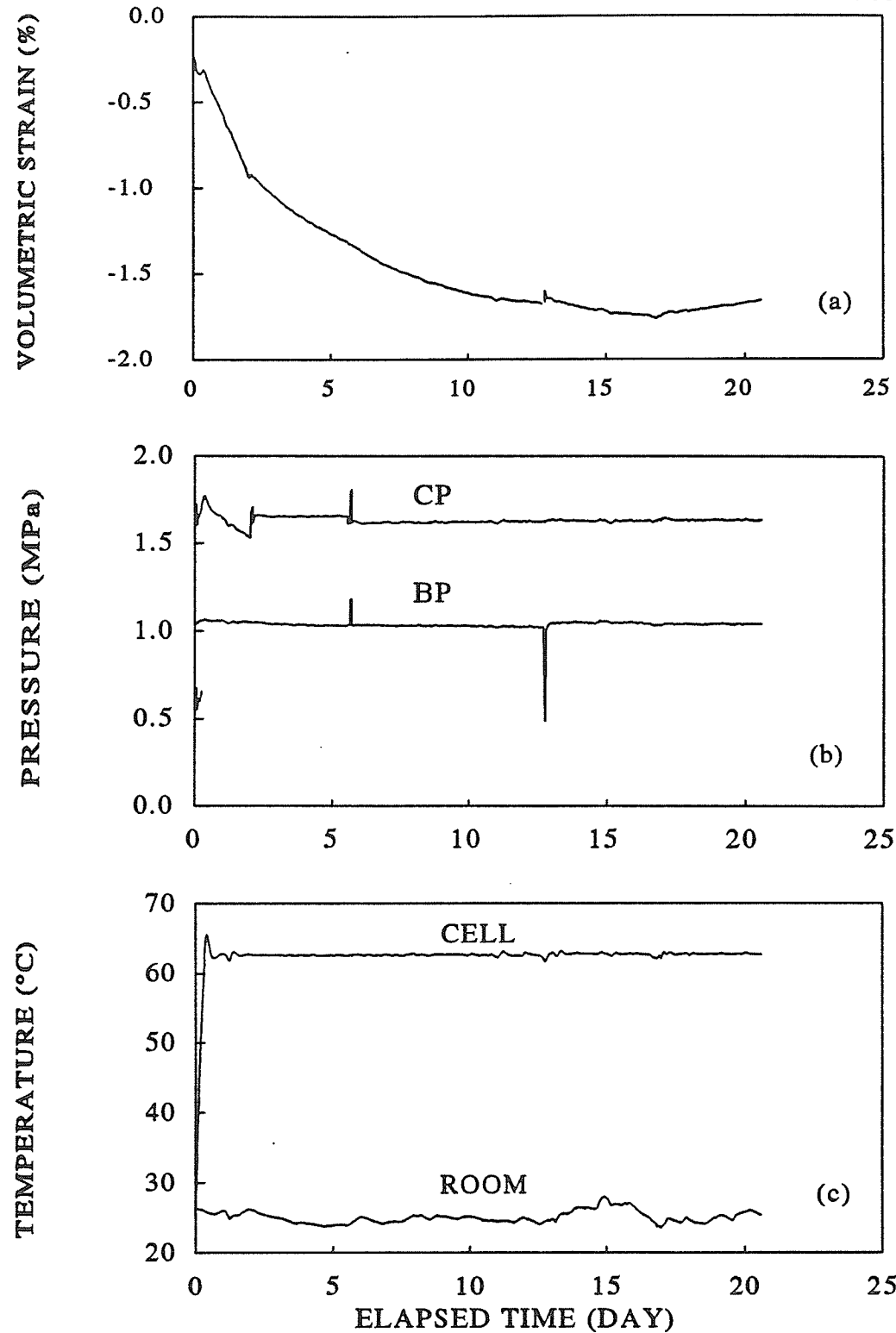


FIGURE 5.6 Consolidation results from CIU(TXC) test T1225: (a) volumetric strain versus elapsed time; (b) pressure versus elapsed time; and (c) temperature versus elapsed time

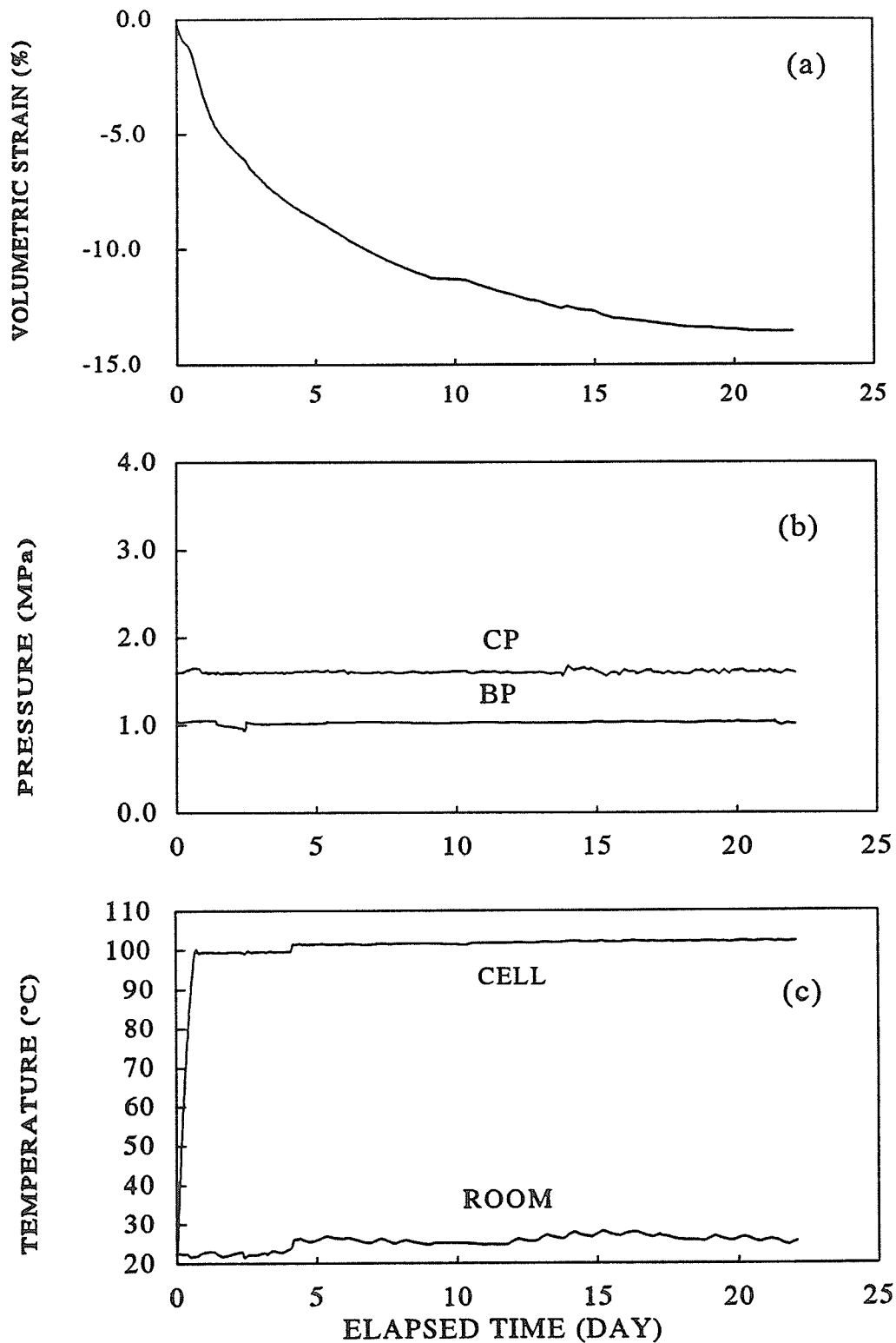


FIGURE 5.7 Consolidation results from CIU(TXC) test T1233: (a) volumetric strain versus elapsed time; (b) pressure versus elapsed time; and (c) temperature versus elapsed time

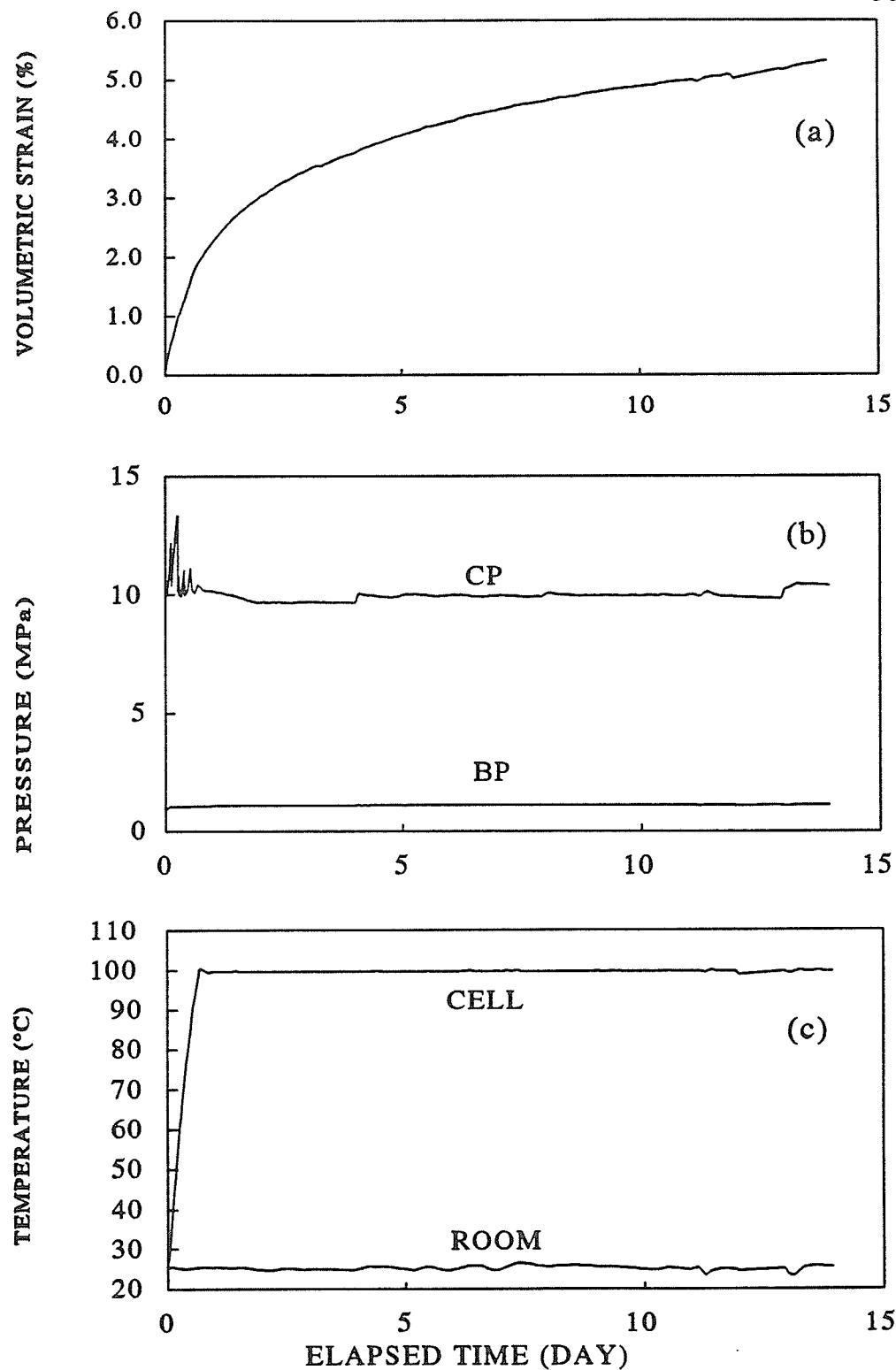


FIGURE 5.8 Consolidation results from CIU(TXC) test T1235: (a) volumetric strain versus elapsed time; (b) pressure versus elapsed time; and (c) temperature versus elapsed time

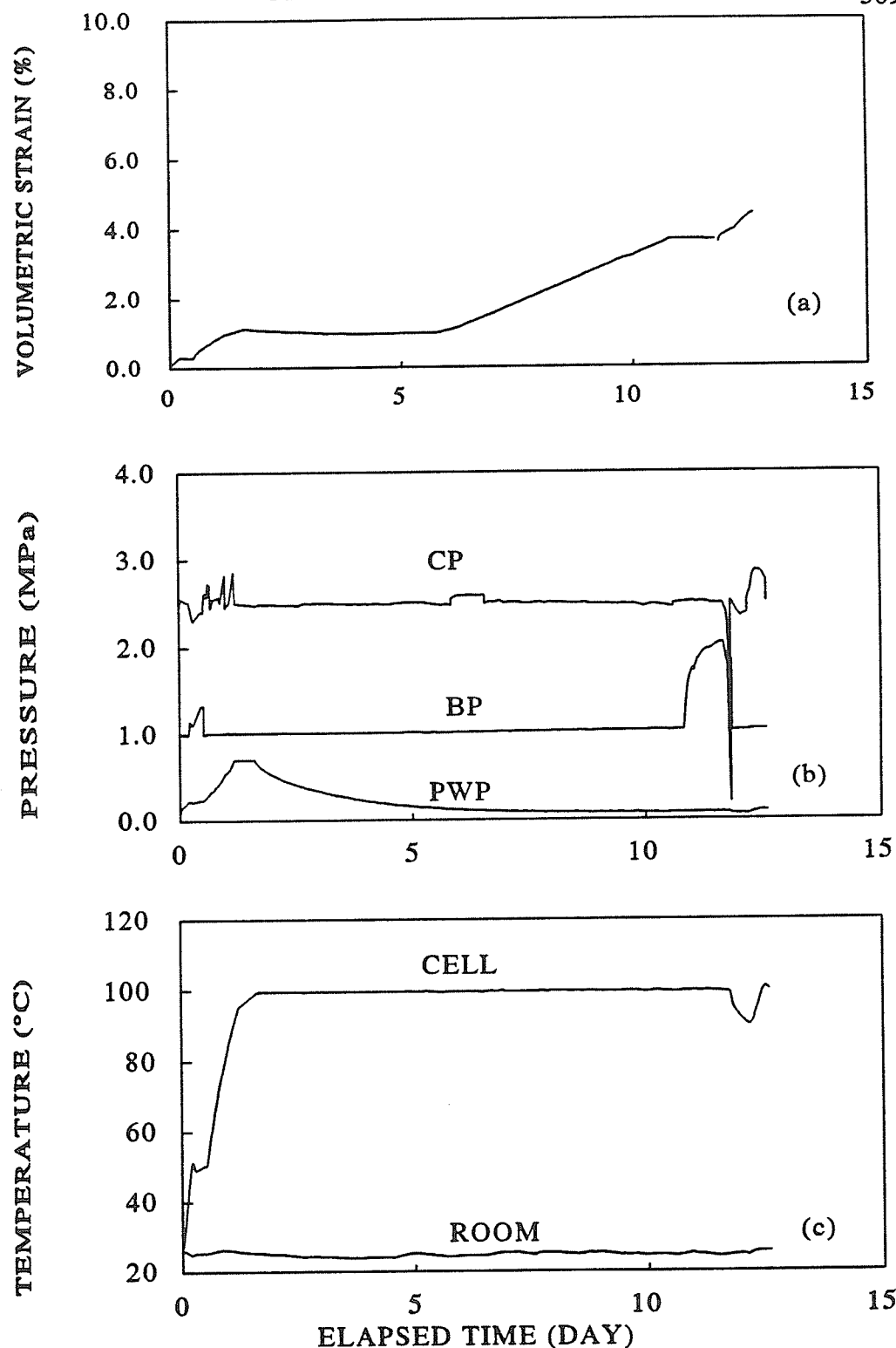


FIGURE 5.9 Consolidation results from CIU(TXC) test T1227: (a) volumetric strain versus elapsed time; (b) pressure versus elapsed time; and (c) temperature versus elapsed time

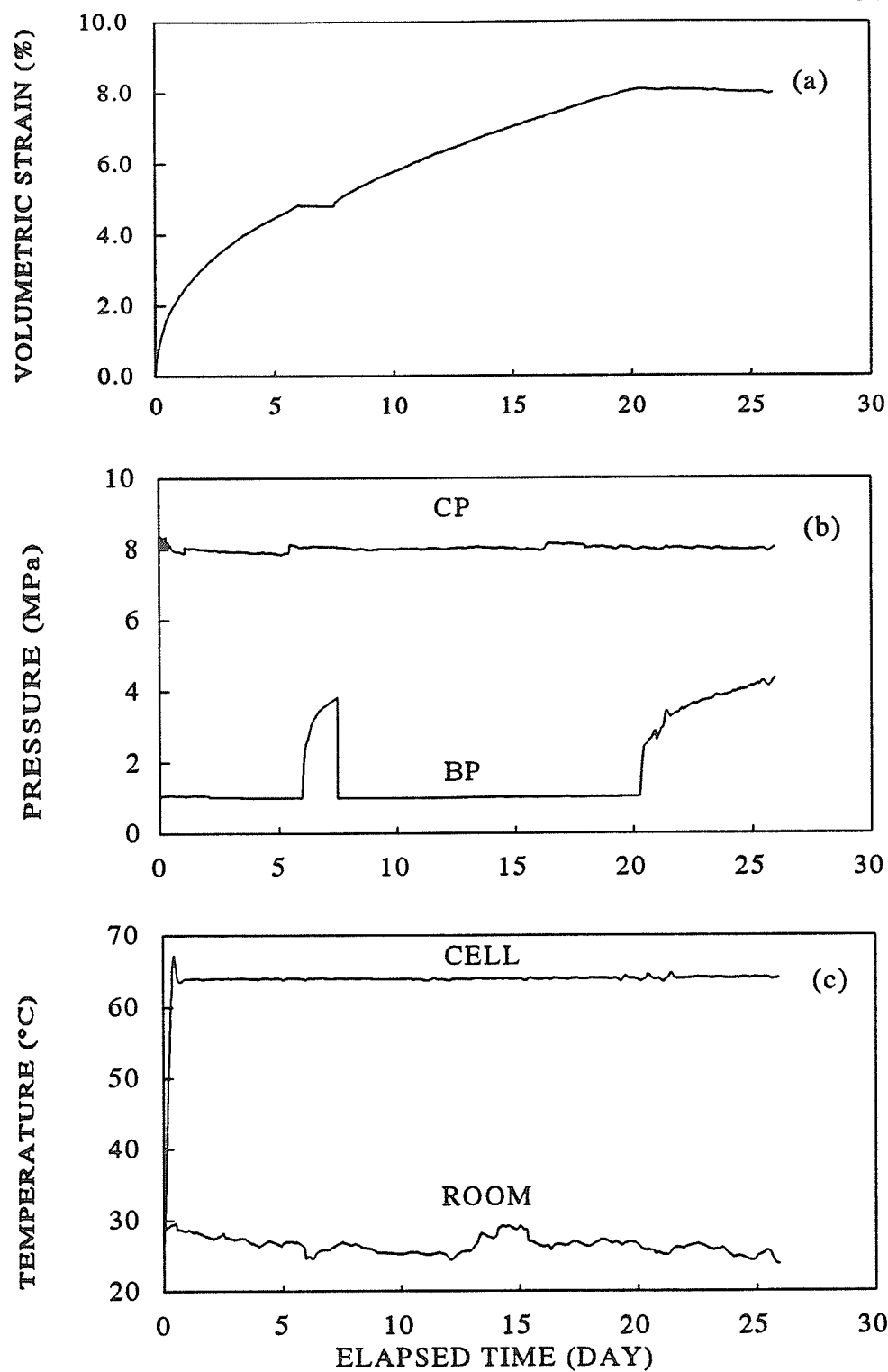


FIGURE 5.10 Consolidation results from CIU(TXC) test T1229: (a) volumetric strain versus elapsed time; (b) pressure versus elapsed time; and (c) temperature versus elapsed time

T1229: BUFFER THERMO-CONSOLIDATION

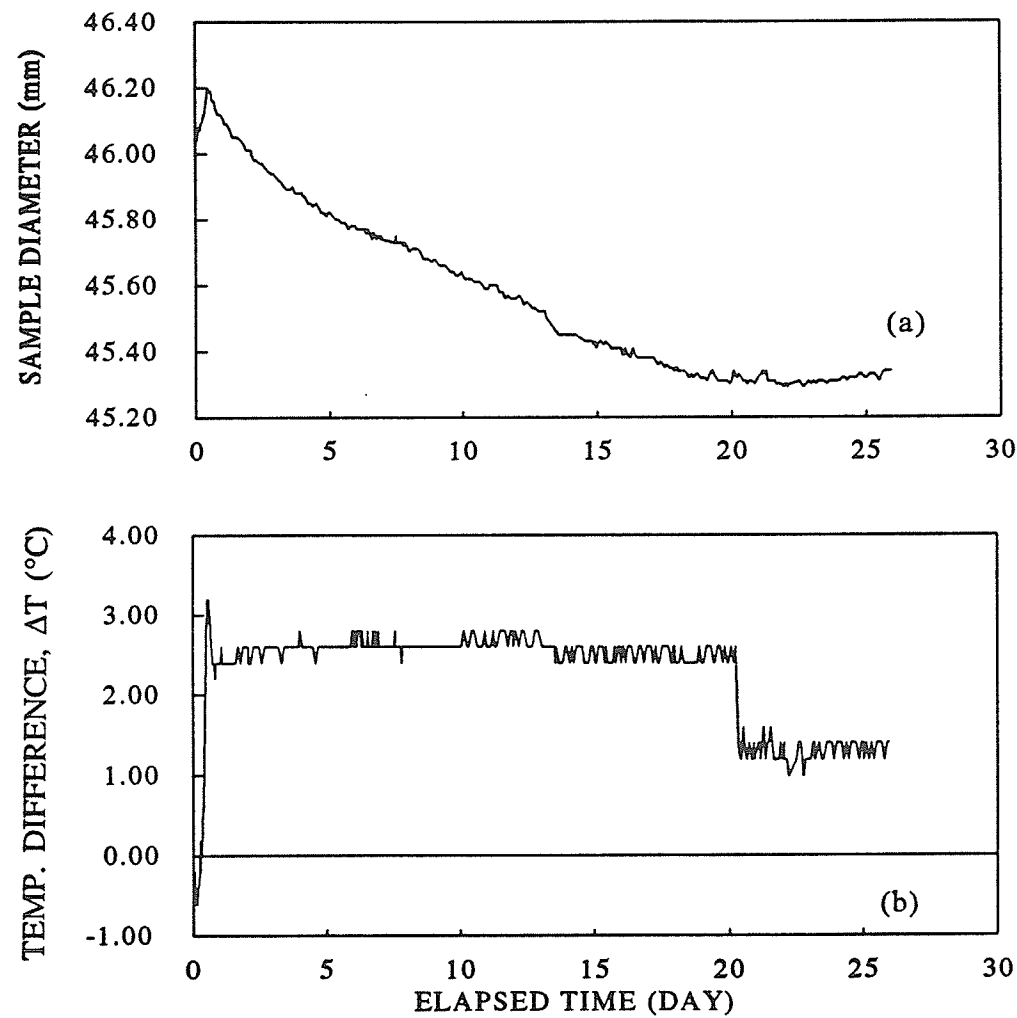


FIGURE 5.11 Consolidation results from CIU(TXC) test T1229: (a) lateral strain gauge readings versus elapsed time; and (b) temperature versus elapsed time

SUMMARY: TRIAXIAL CONSOLIDATION $T = 26^\circ C$, 65 C , 100 C ; HIGH DENSITY

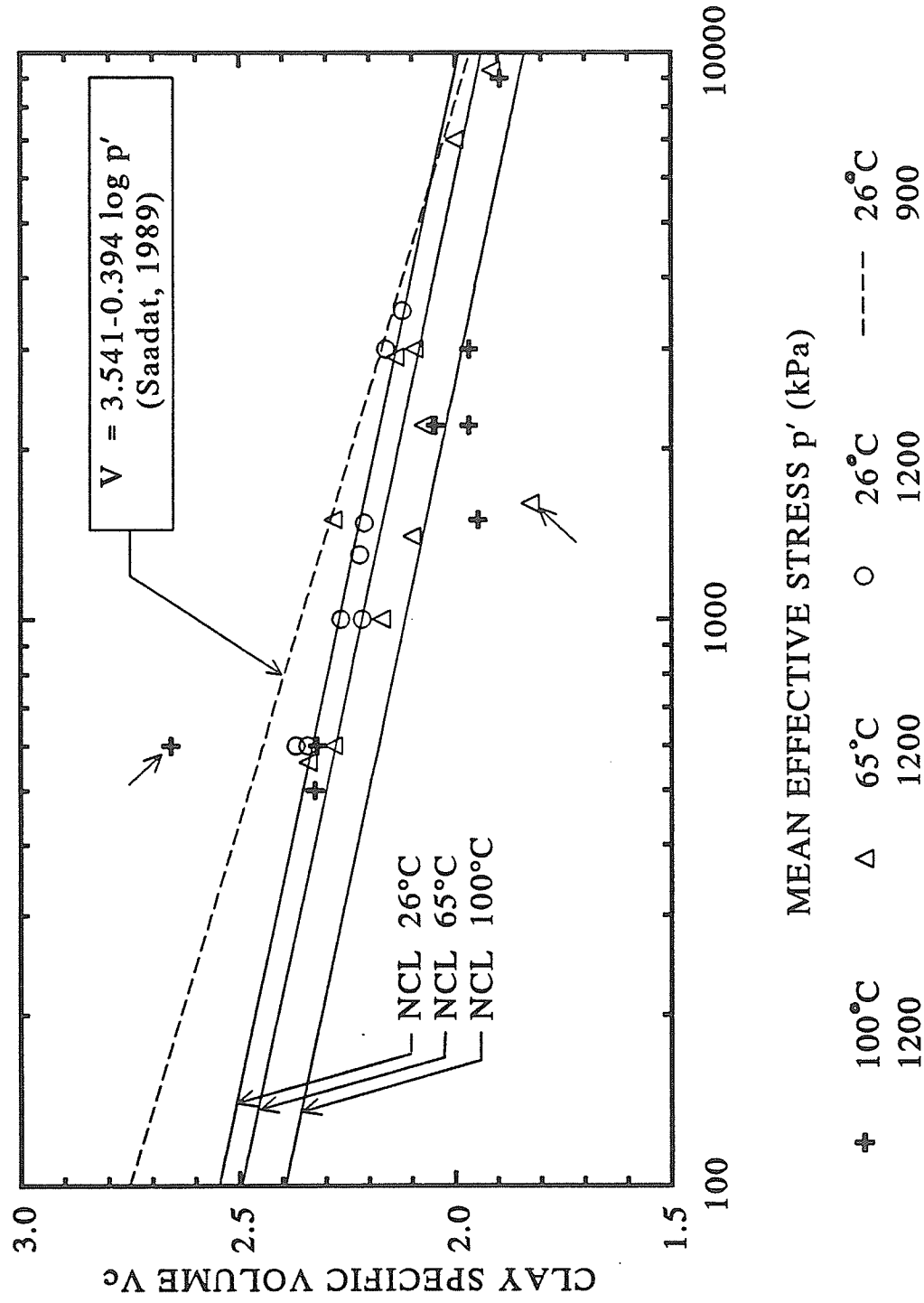


FIGURE 5.12 Summary of triaxial isotropic consolidation results

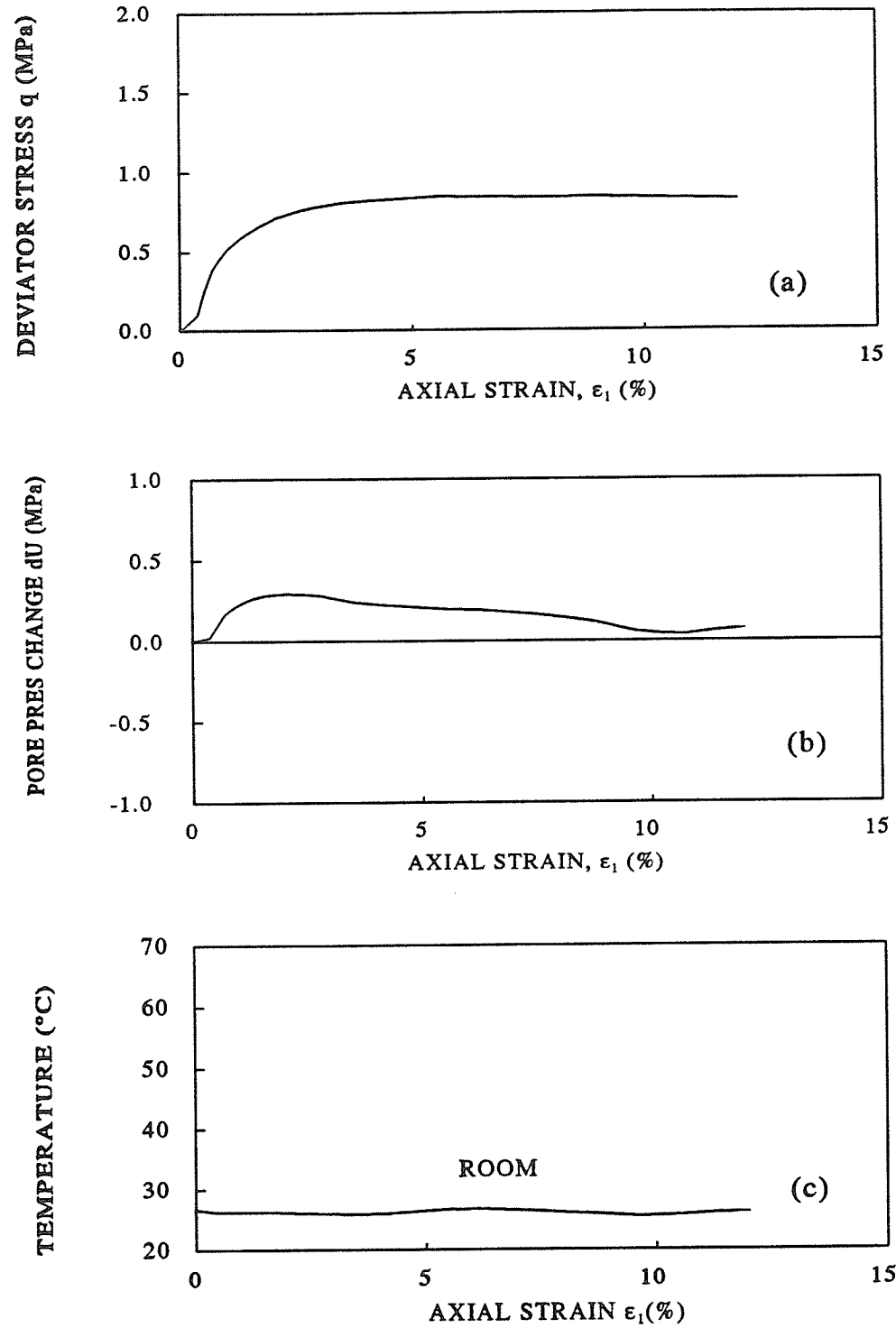


FIGURE 5.13 Undrained shear results from CIU(TXC) test T1221: (a) deviator stress versus axial strain; (b) pore pressure change versus axial strain; and (c) temperature versus axial strain

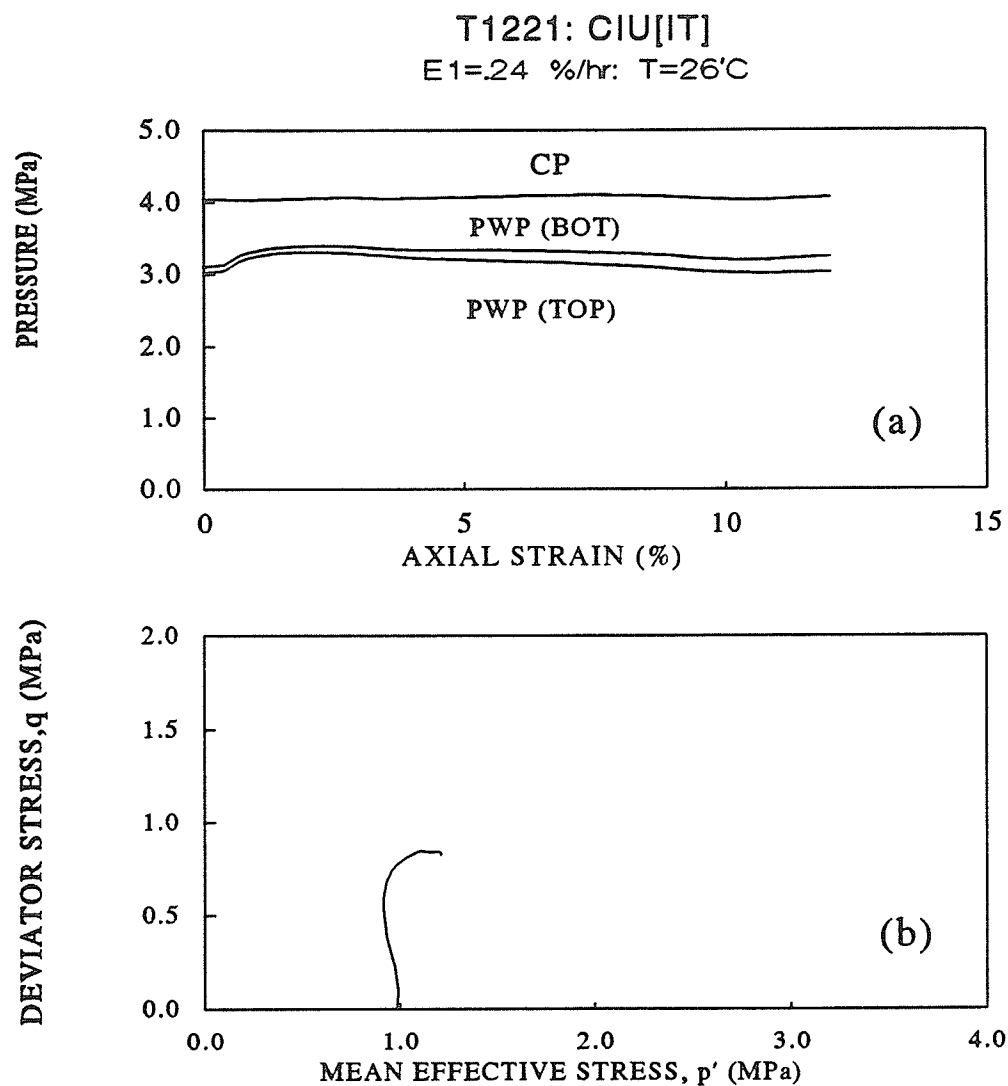


FIGURE 5.14 Undrained shear results from CIU(TXC) test T1221: (a) pressure versus axial strain and (b) deviator stress versus mean effective stress

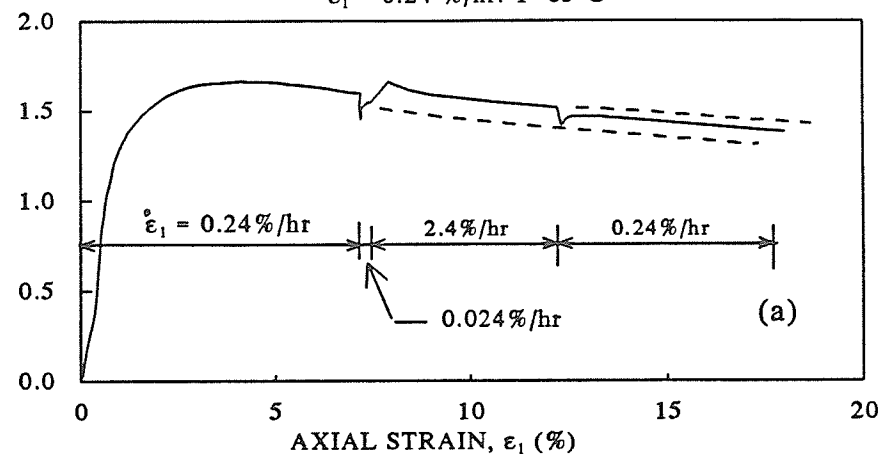
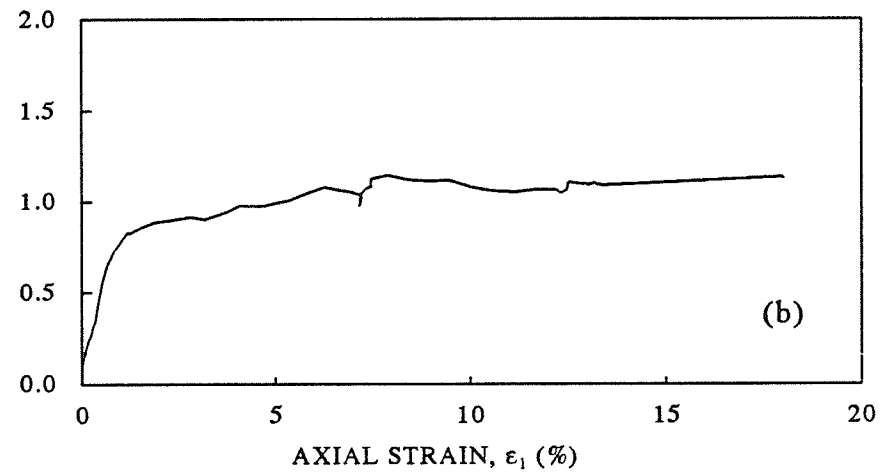
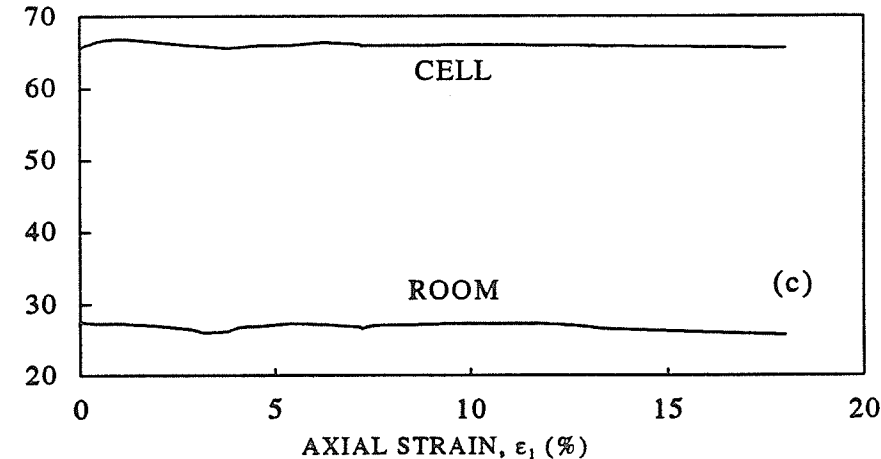
DEVIATOR STRESS q (MPa)PORE PRES CHANGE dU (MPa)TEMPERATURE ($^\circ\text{C}$)

FIGURE 5.15 Undrained shear results from CIU(TXC) test T1211: (a) deviator stress versus axial strain; (b) pore pressure change versus axial strain; and (c) temperature versus axial strain

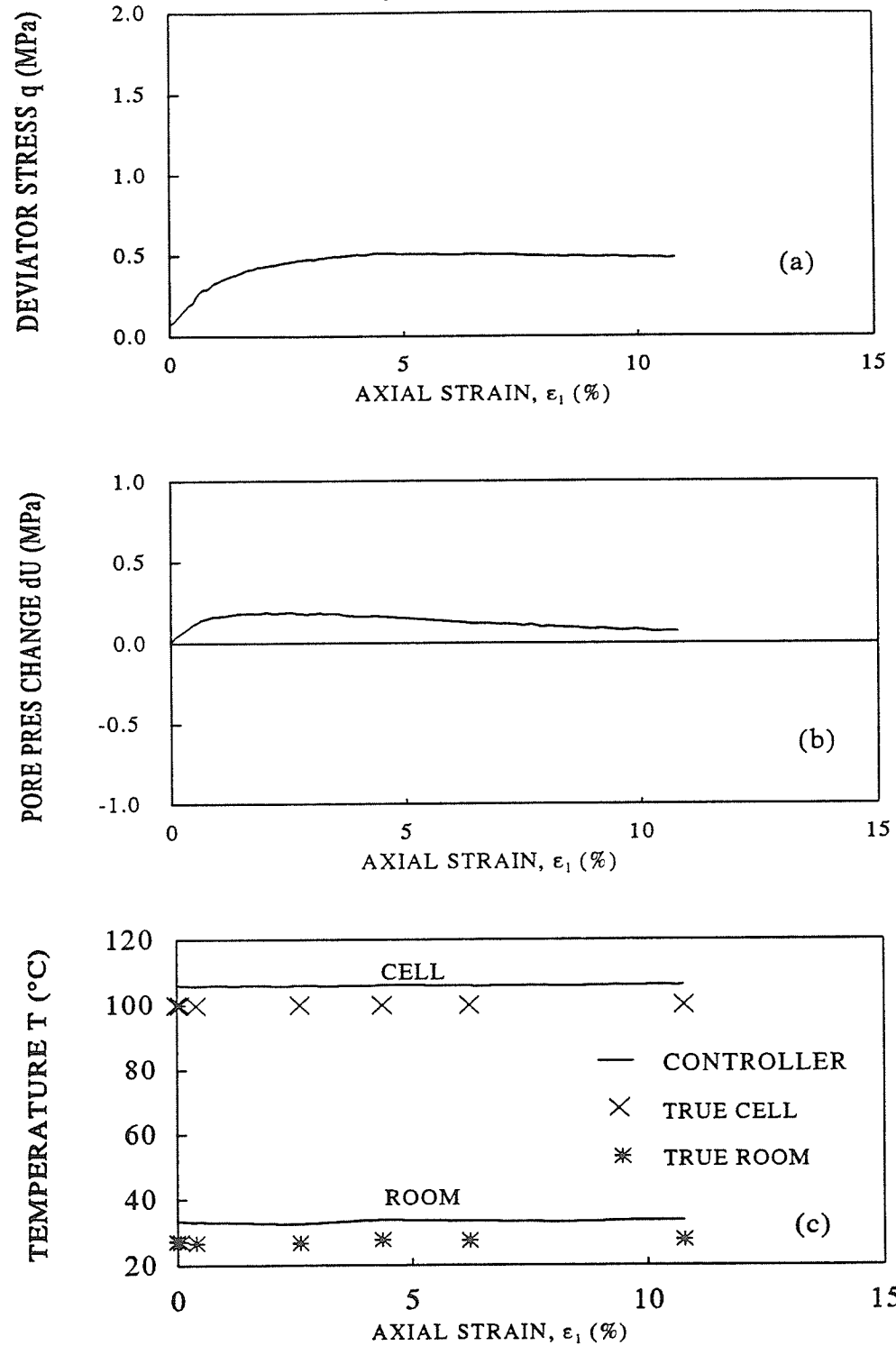


FIGURE 5.16 Undrained shear results from CIU(TXC) test T1233: (a) deviator stress versus axial strain; (b) pore pressure change versus axial strain; and (c) temperature versus axial strain

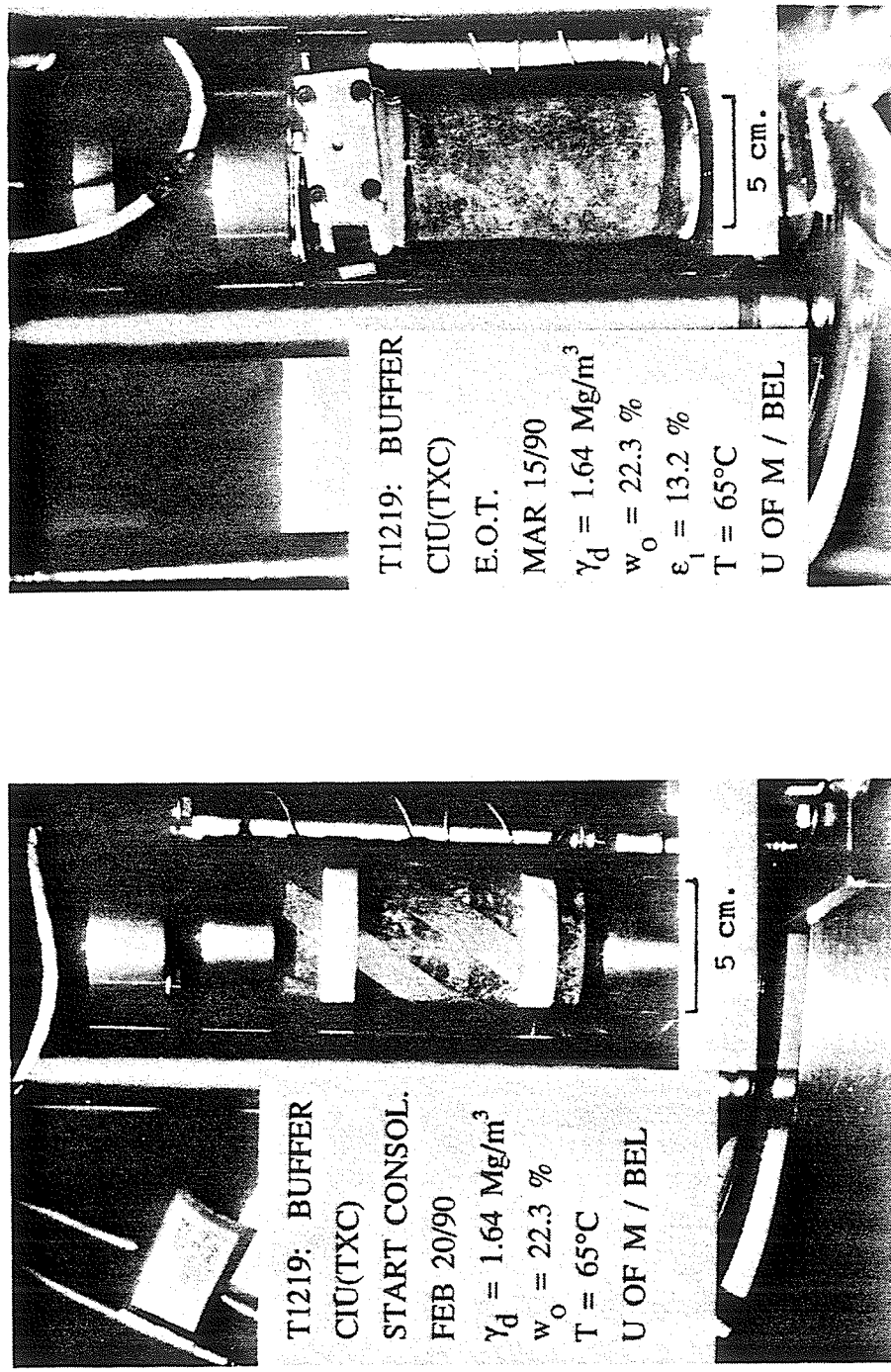


FIGURE 5.17 Photographs of specimen T1219: (a) before consolidation; and (b) after undrained triaxial shear, CIU(TXC).

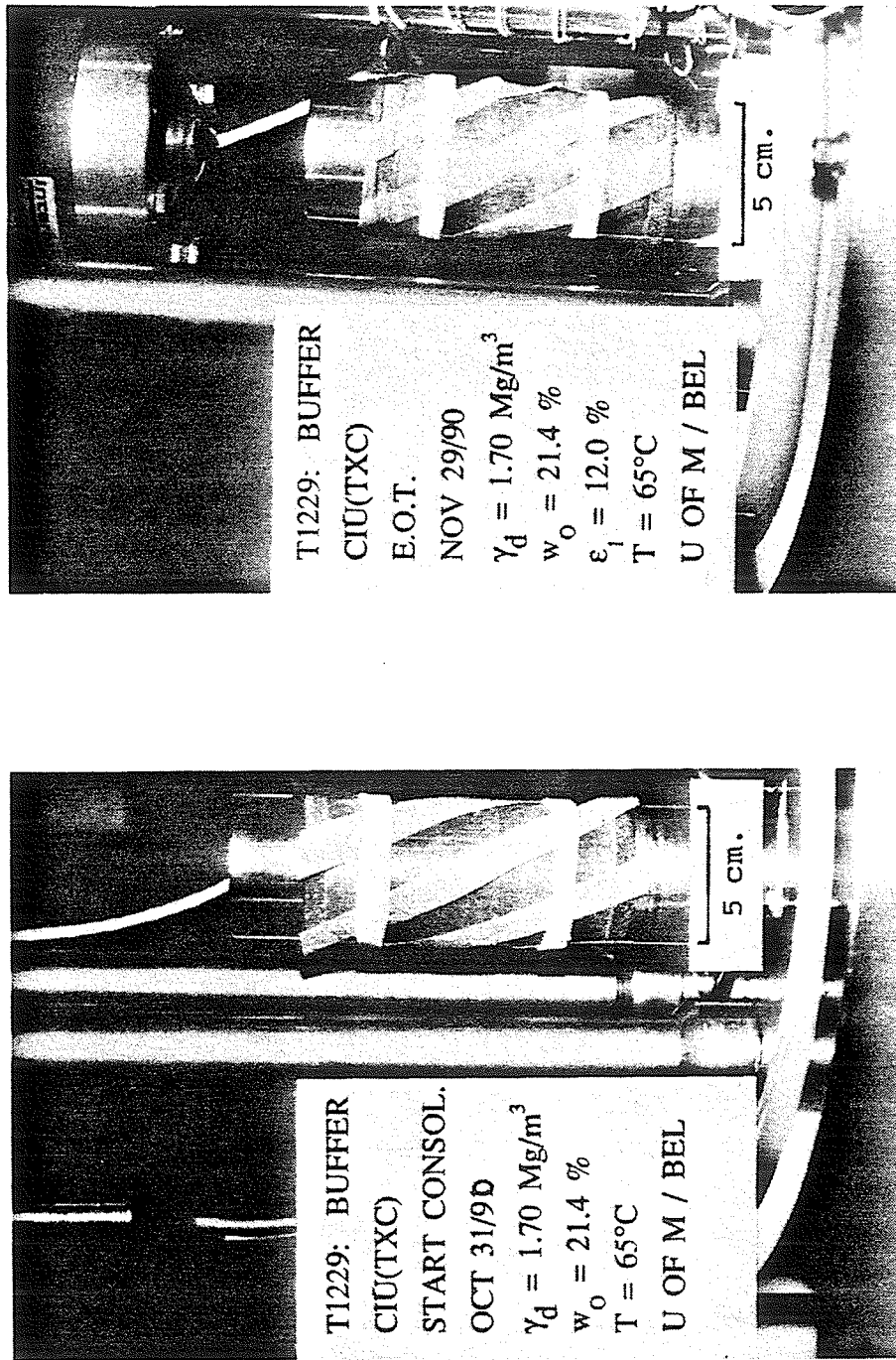


FIGURE 5.18 Photographs of specimen T1229: (a) before consolidation; and (b) after undrained triaxial shear, CIU(TXC).

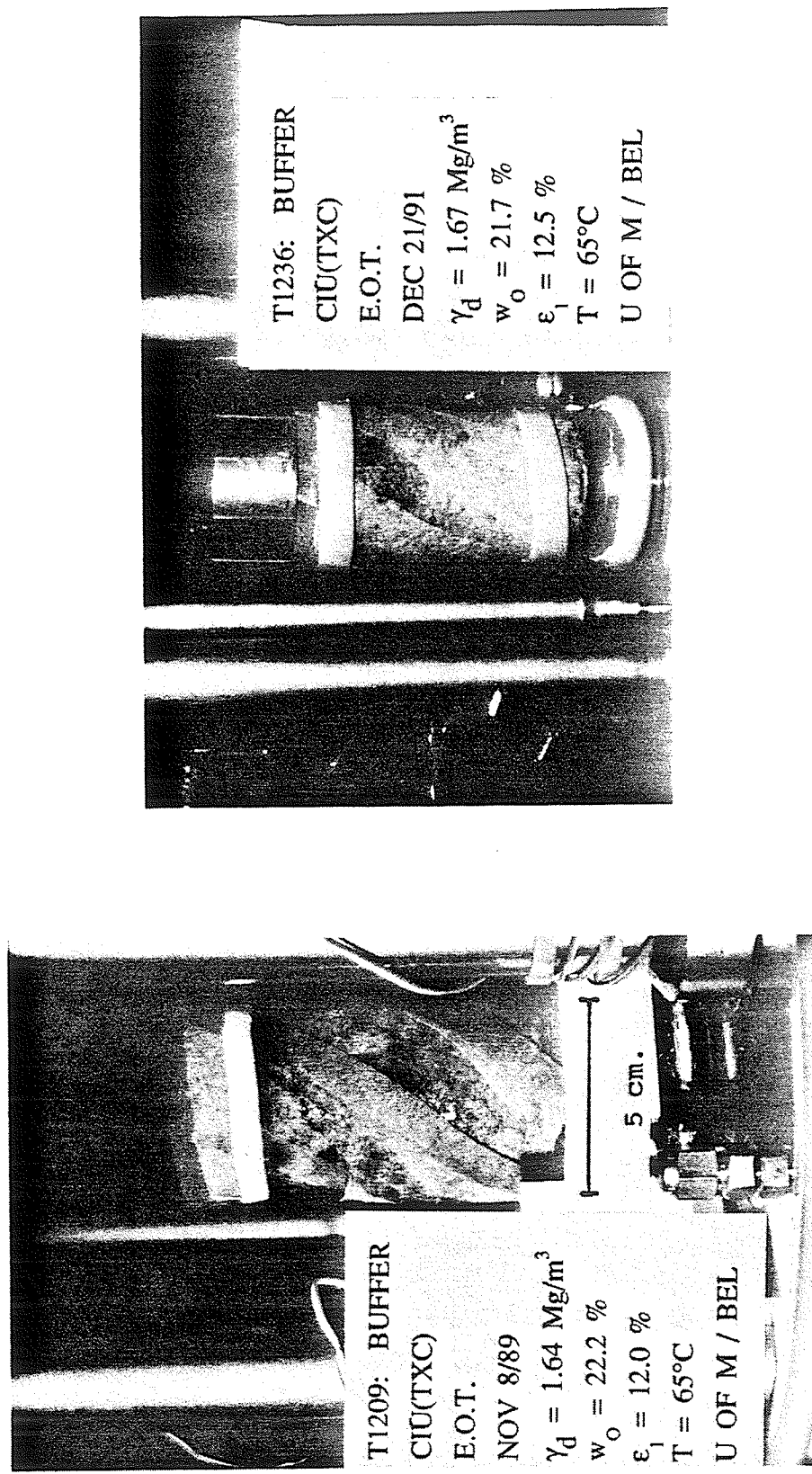


FIGURE 5.19 Photographs of specimens after undrained triaxial shear CIU(TXC):
(a) T1209; and (b) T1236

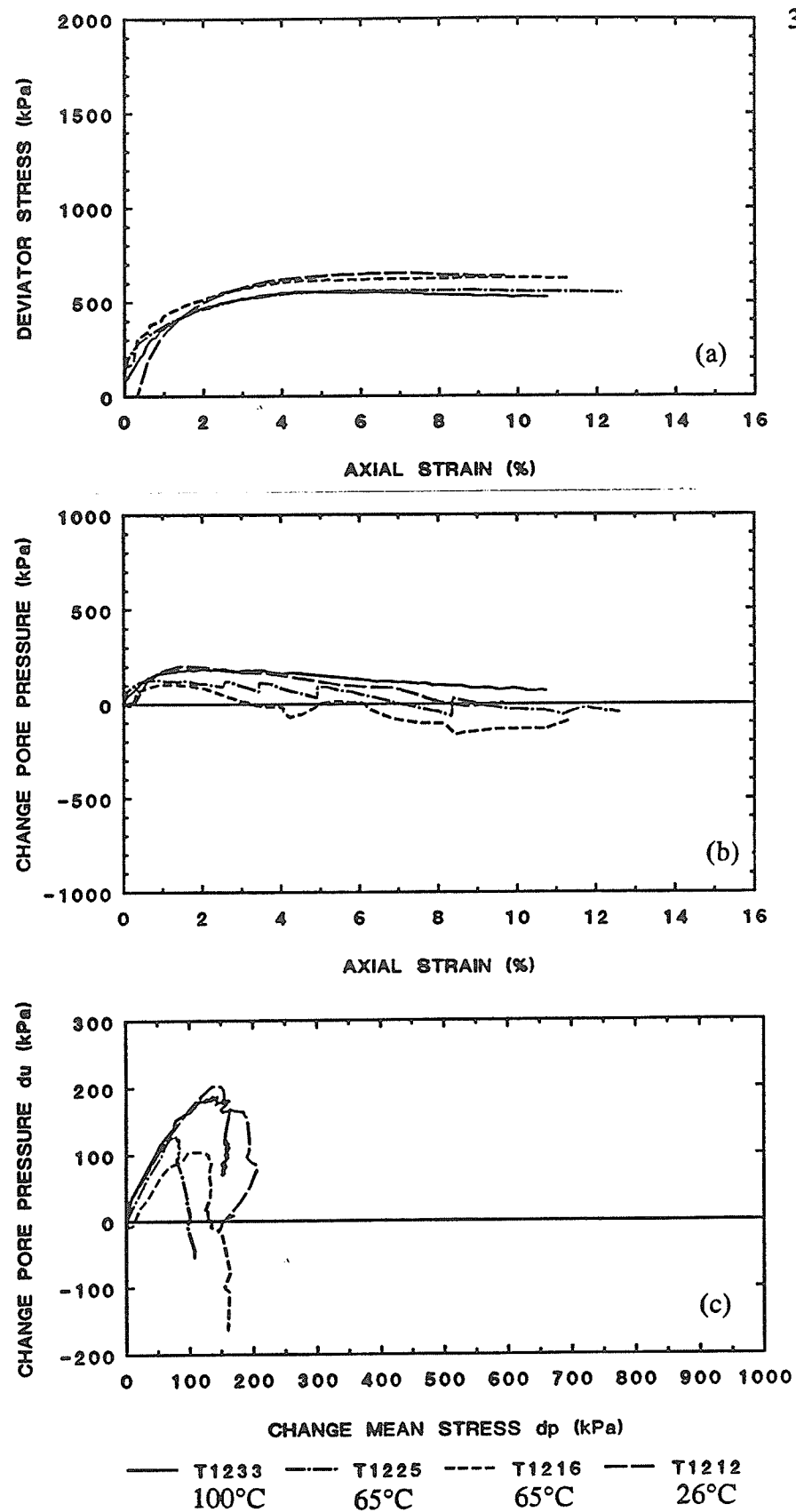


FIGURE 5.20 Comparison of results from CIU(TXC) tests, $\sigma'_{\text{cons}} = 0.6 \text{ MPa}$: (a) q versus ϵ_1 , (b) Δu versus ϵ_1 and (c) Δu versus Δp

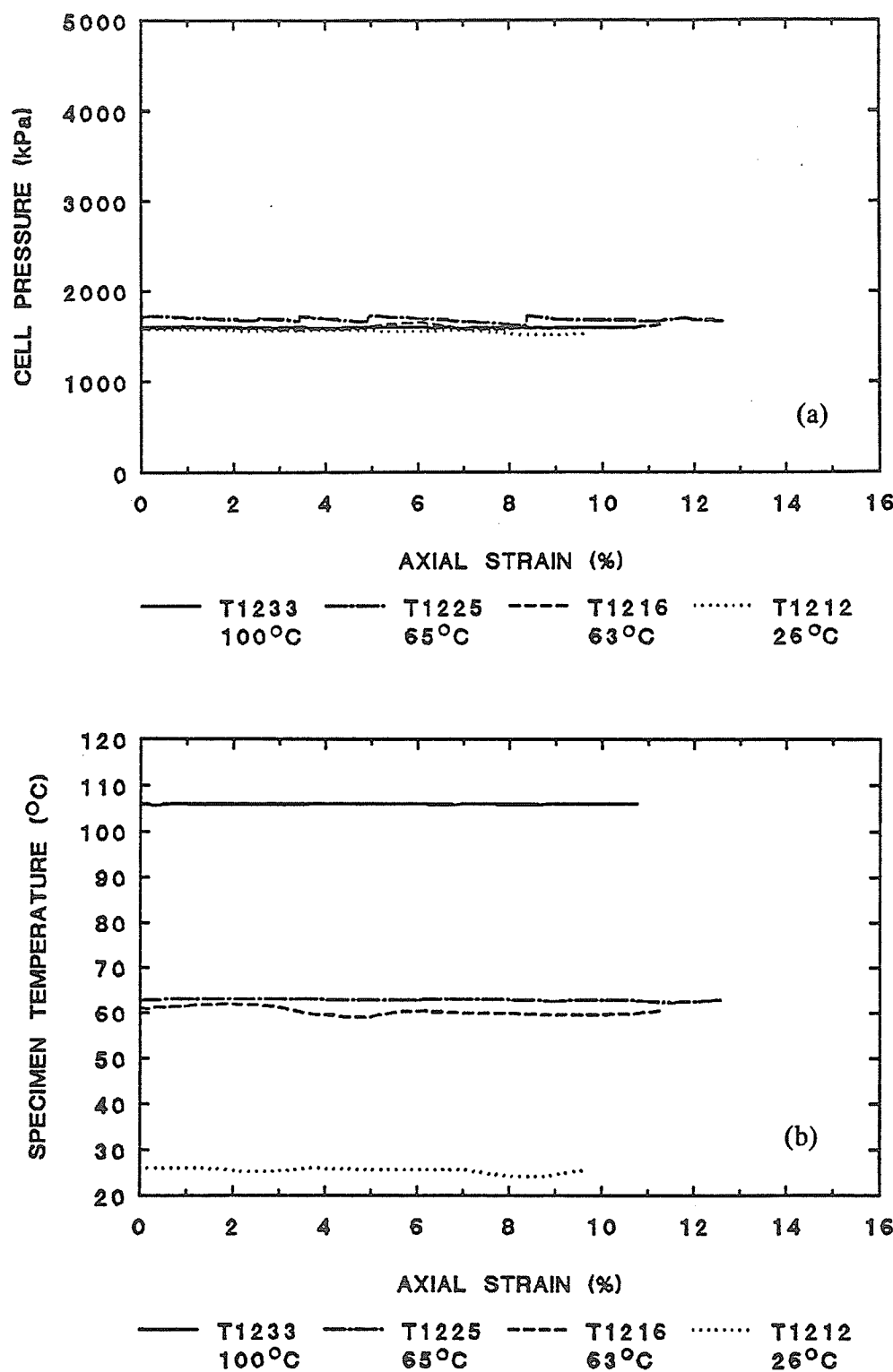


FIGURE 5.21 Comparison of results from CIU(TXC) tests, $\sigma'_{\text{cons}} = 0.6 \text{ MPa}$: (a) σ_3 versus ε_1 ; and (b) T versus ε_1

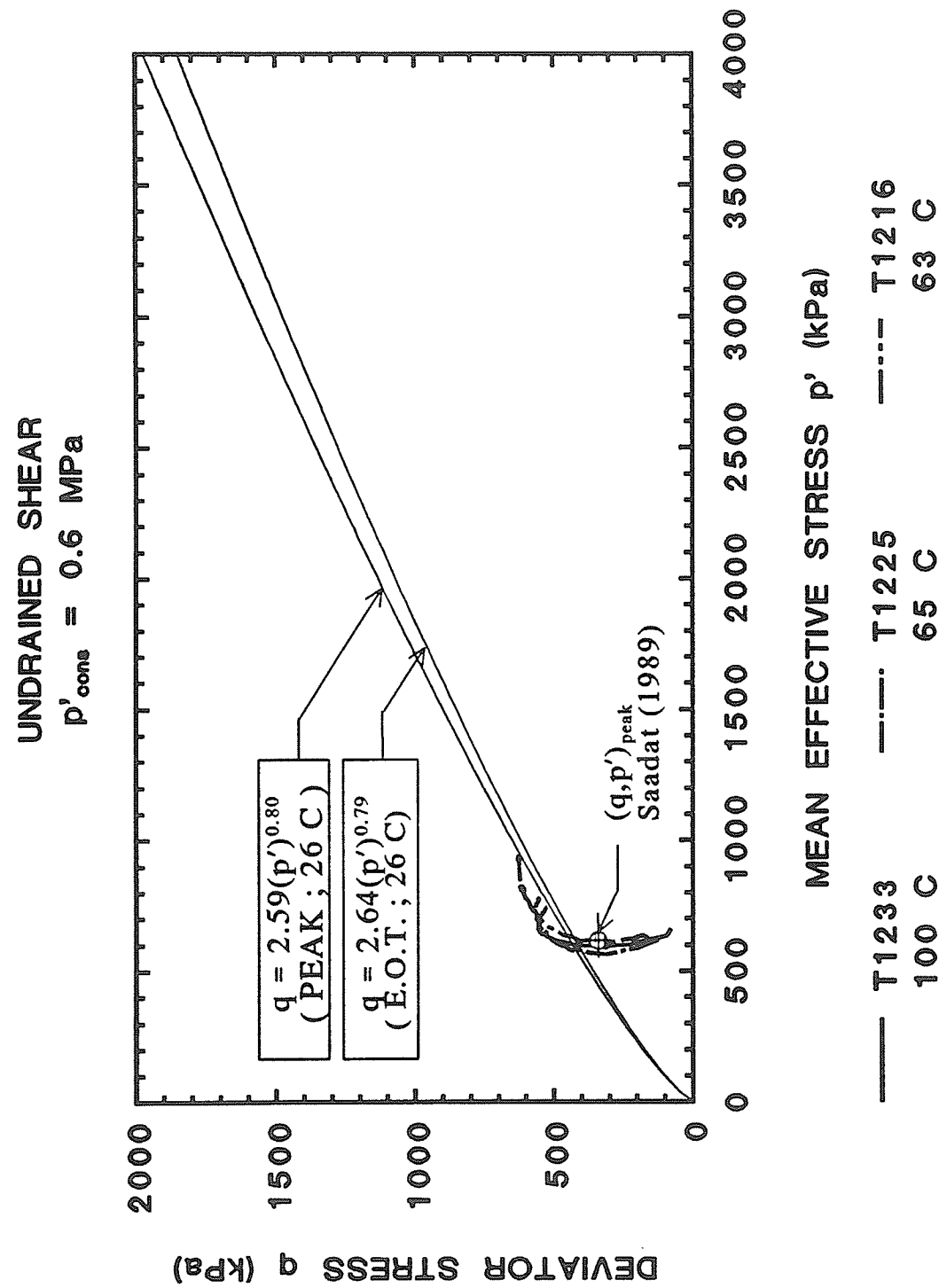


FIGURE 5.22 Comparison of results from CIU(TRXC) tests, $\sigma'_{\text{cons}} = 0.6 \text{ MPa}$:
 q versus p'

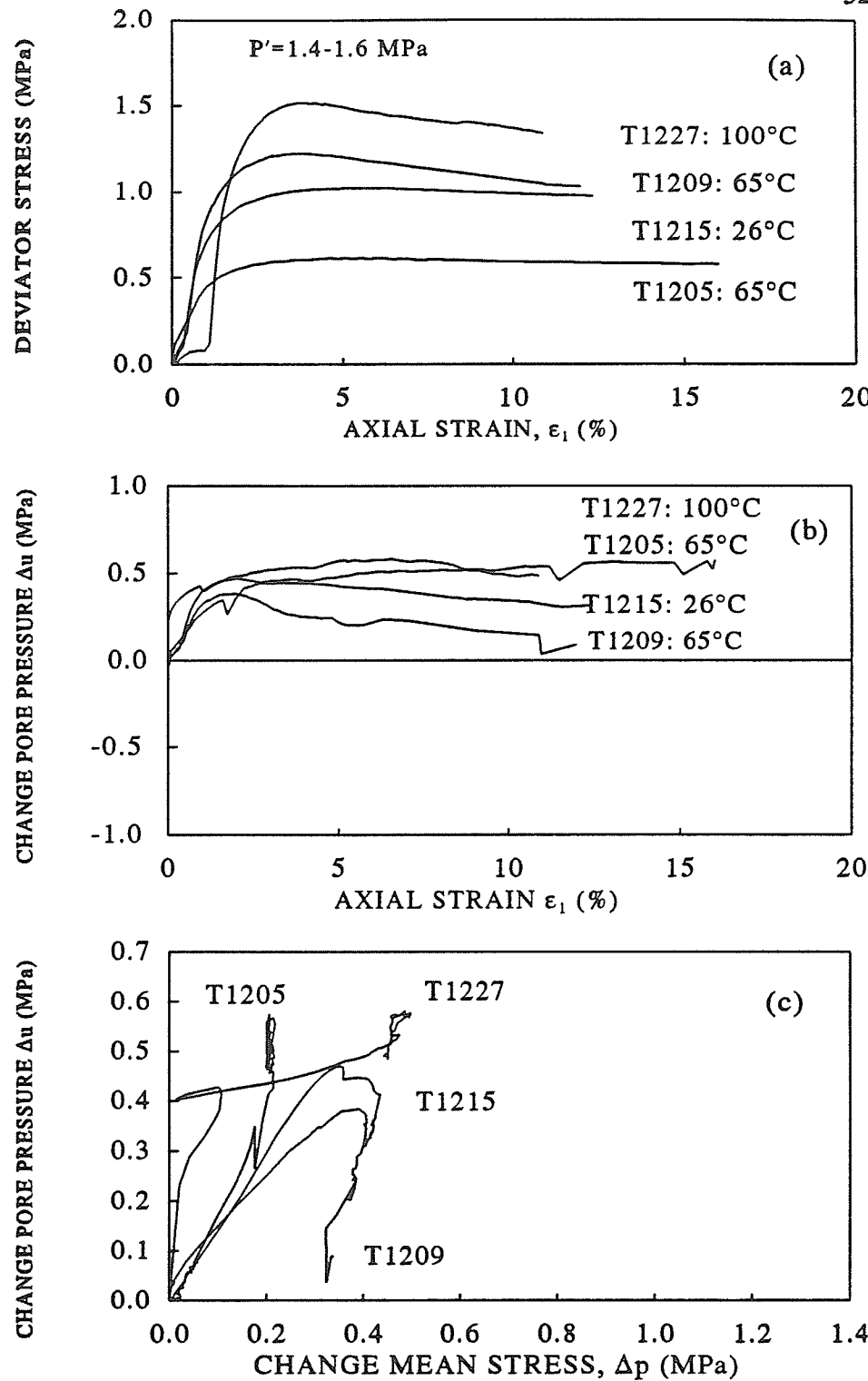


FIGURE 5.23 Comparison of results from CIU(TXC) tests, $\sigma'_\text{cons} = 1.6 \text{ MPa}$: (a) q versus ϵ_1 ; (b) Δu versus ϵ_1 ; and (c) Δu versus Δp

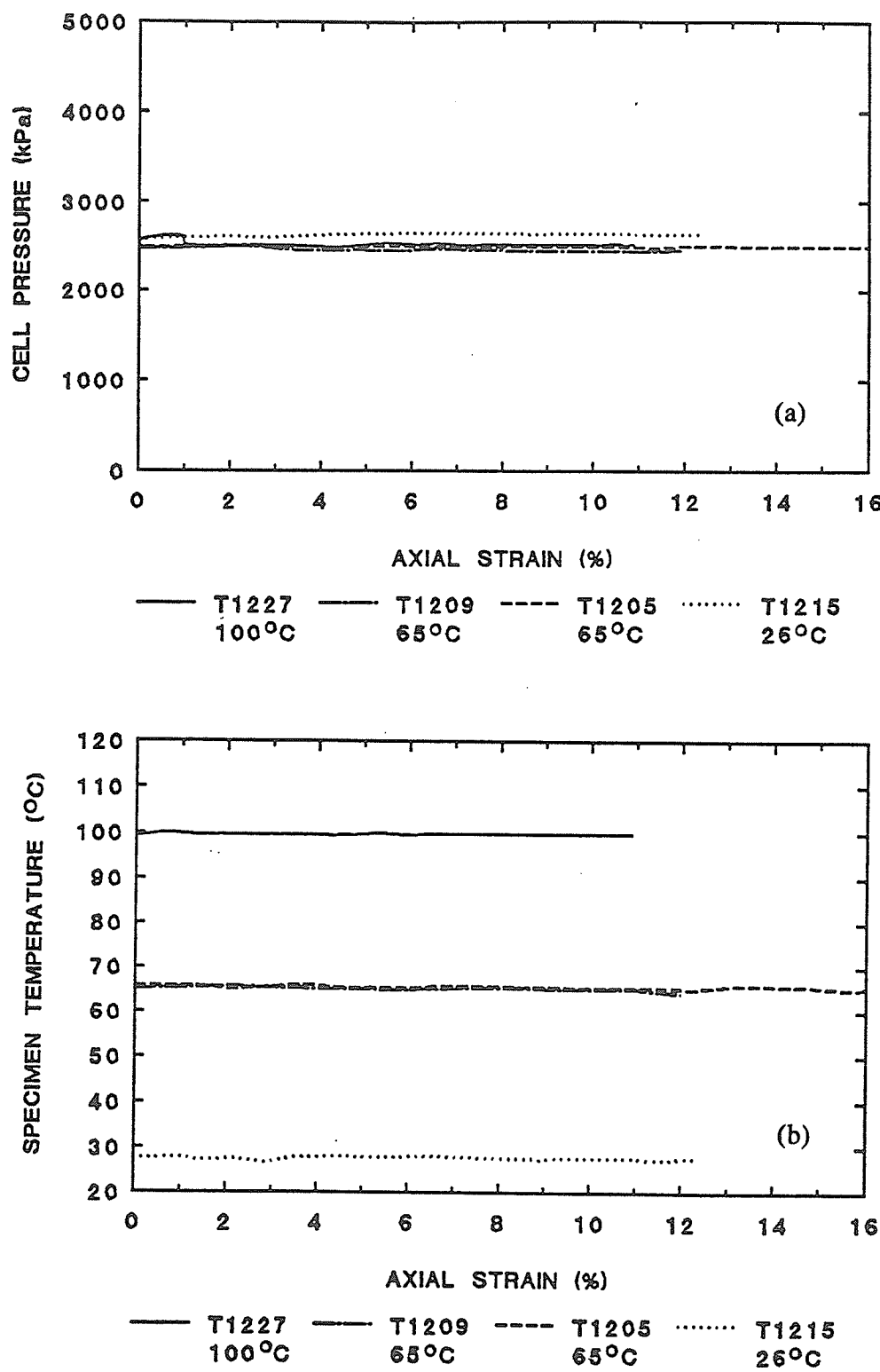


FIGURE 5.24 Comparison of results from CIU(TXC) tests, $\sigma'_{\text{cons}} = 1.6 \text{ MPa}$: (a) σ_3 versus ϵ_1 ; and (b) T versus ϵ_1

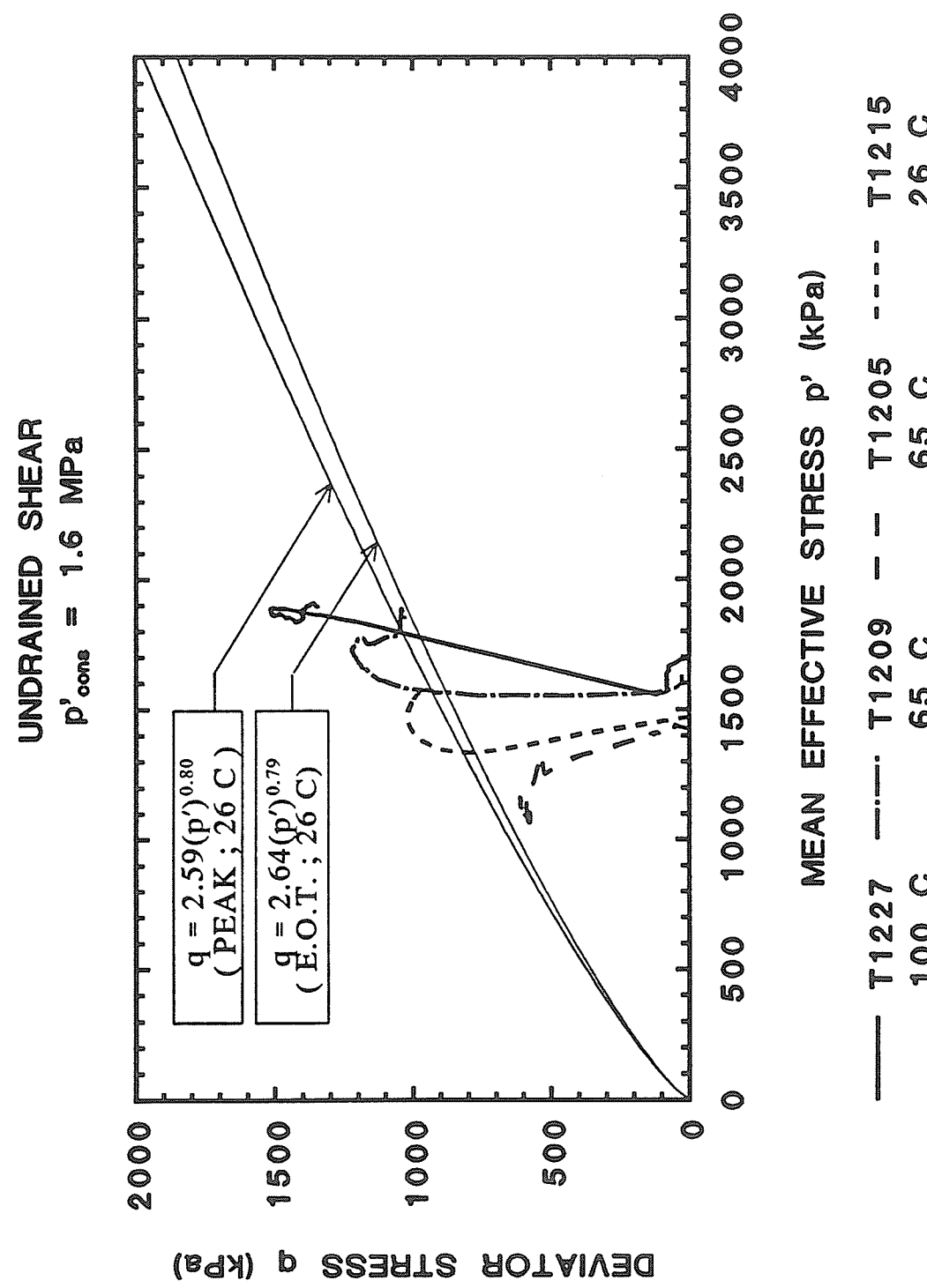


FIGURE 5.25 Comparison of results from CIU(TXC) tests, $\sigma'_{\text{cons}} = 1.6 \text{ MPa}$:
 q versus p'

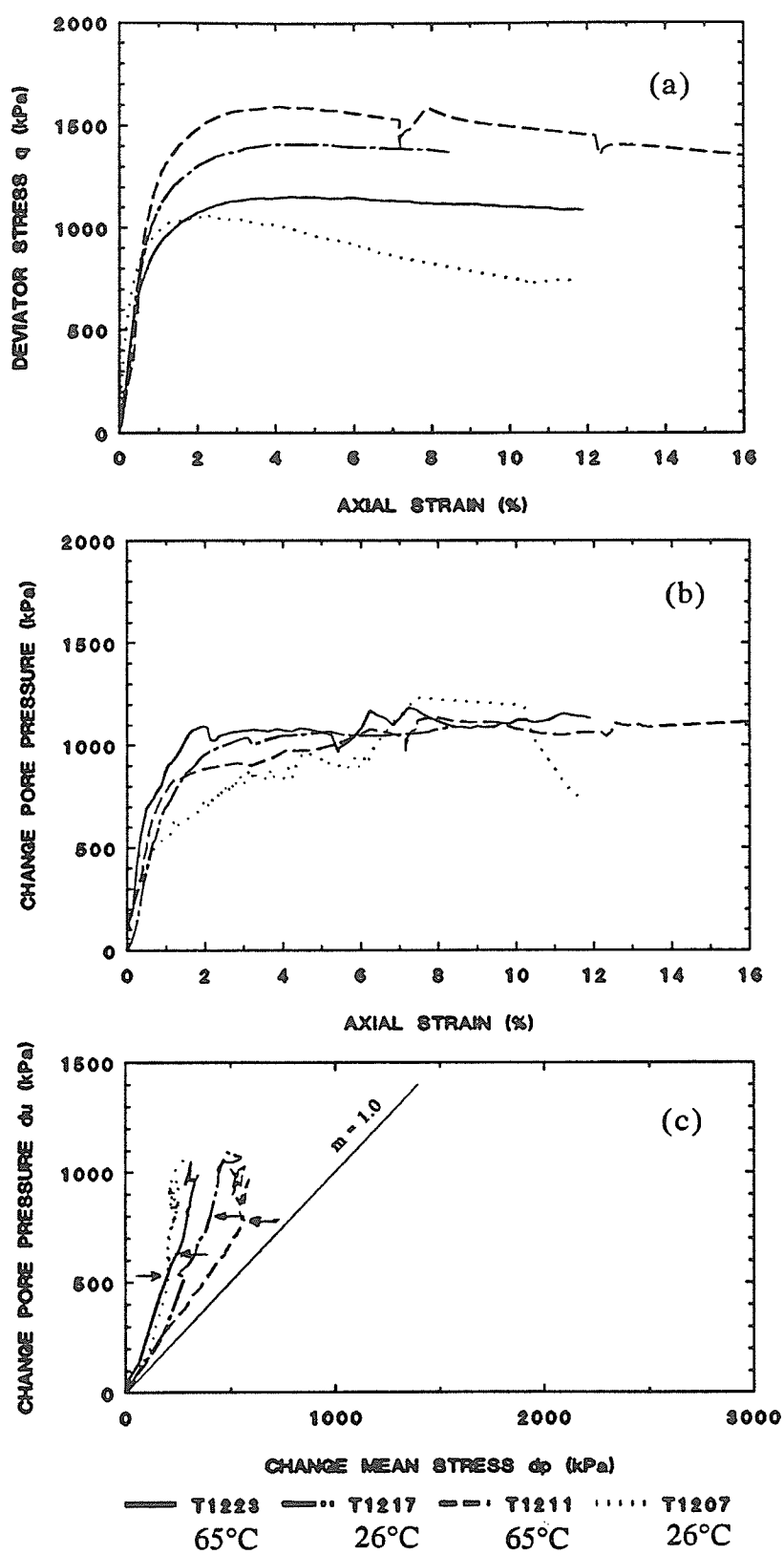


FIGURE 5.26 Comparison of results from CIU(TXC) tests, $\sigma'_{\text{cons}} = 3.0 \text{ MPa}$: (a) q versus ε_1 ; (b) Δu versus ε_1 ; and (c) Δu versus Δp

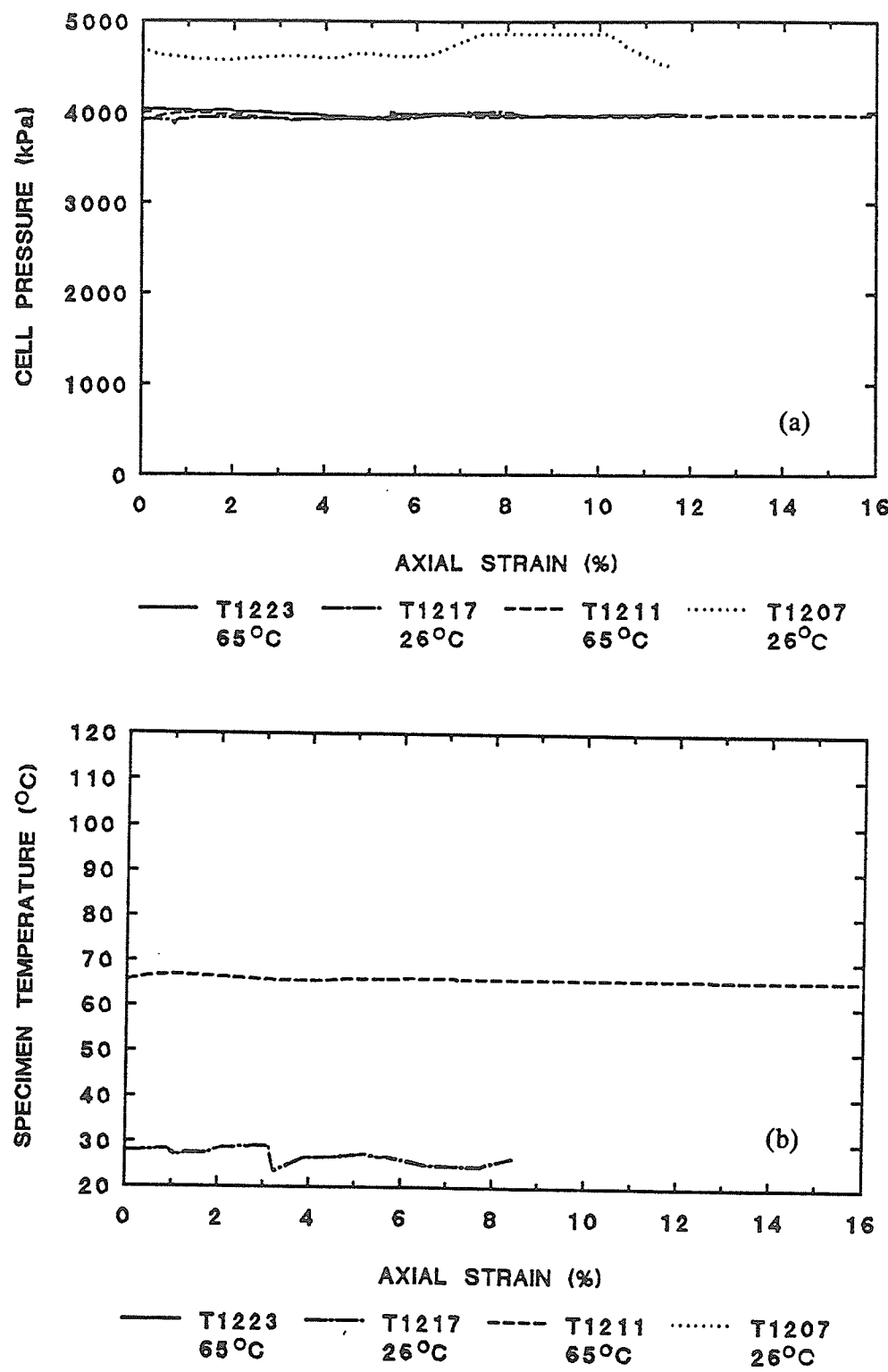


FIGURE 5.27 Comparison of results from CIU(TXC) tests, $\sigma'_{\text{cons}} = 3.0 \text{ MPa}$: (a) σ_3 versus ϵ_1 ; and (b) T versus ϵ_1

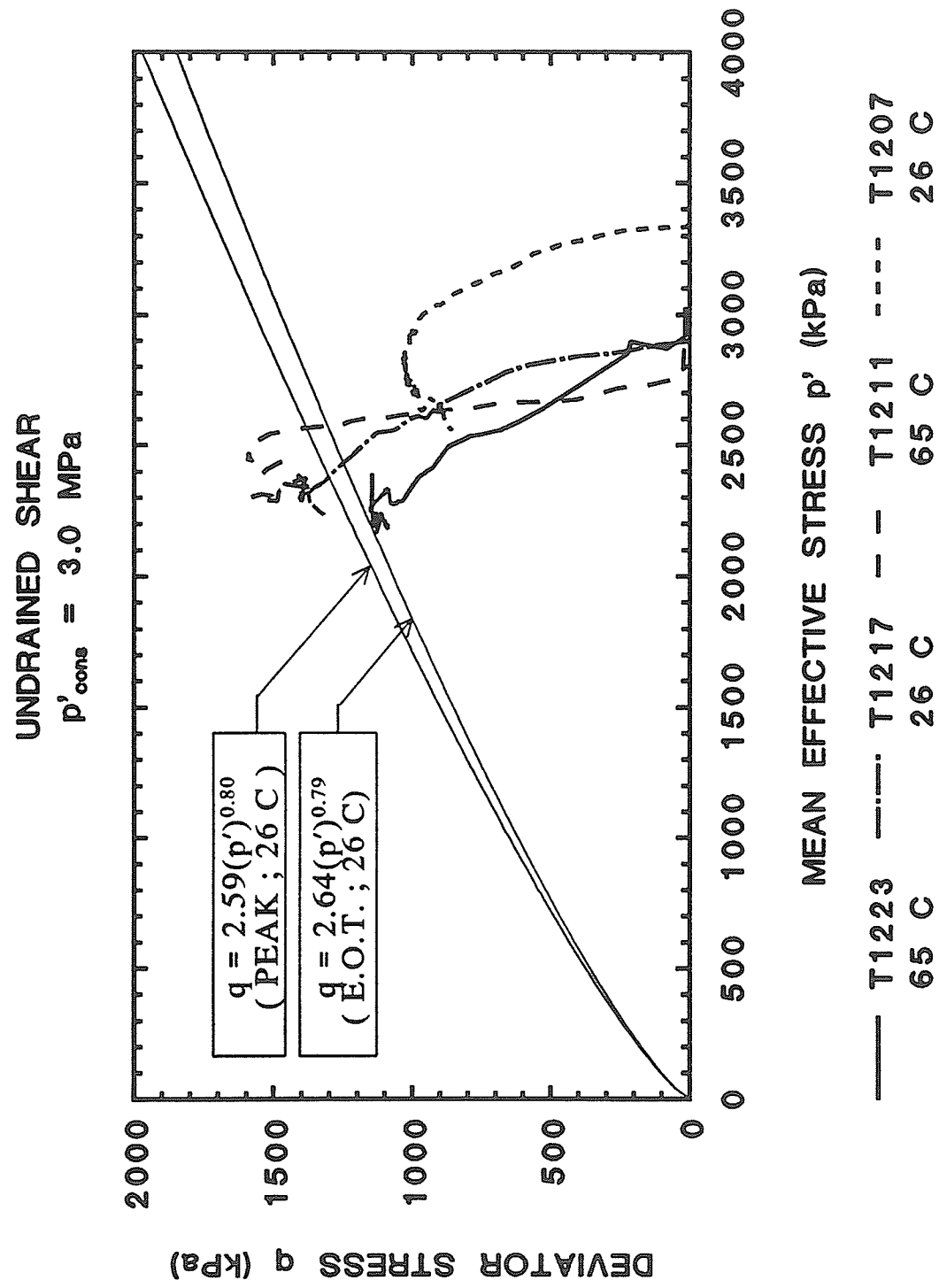


FIGURE 5.28 Comparison of results from CIU(TXC) tests, $\sigma'_{\text{cons}} = 3.0 \text{ MPa}$:
 q versus p'

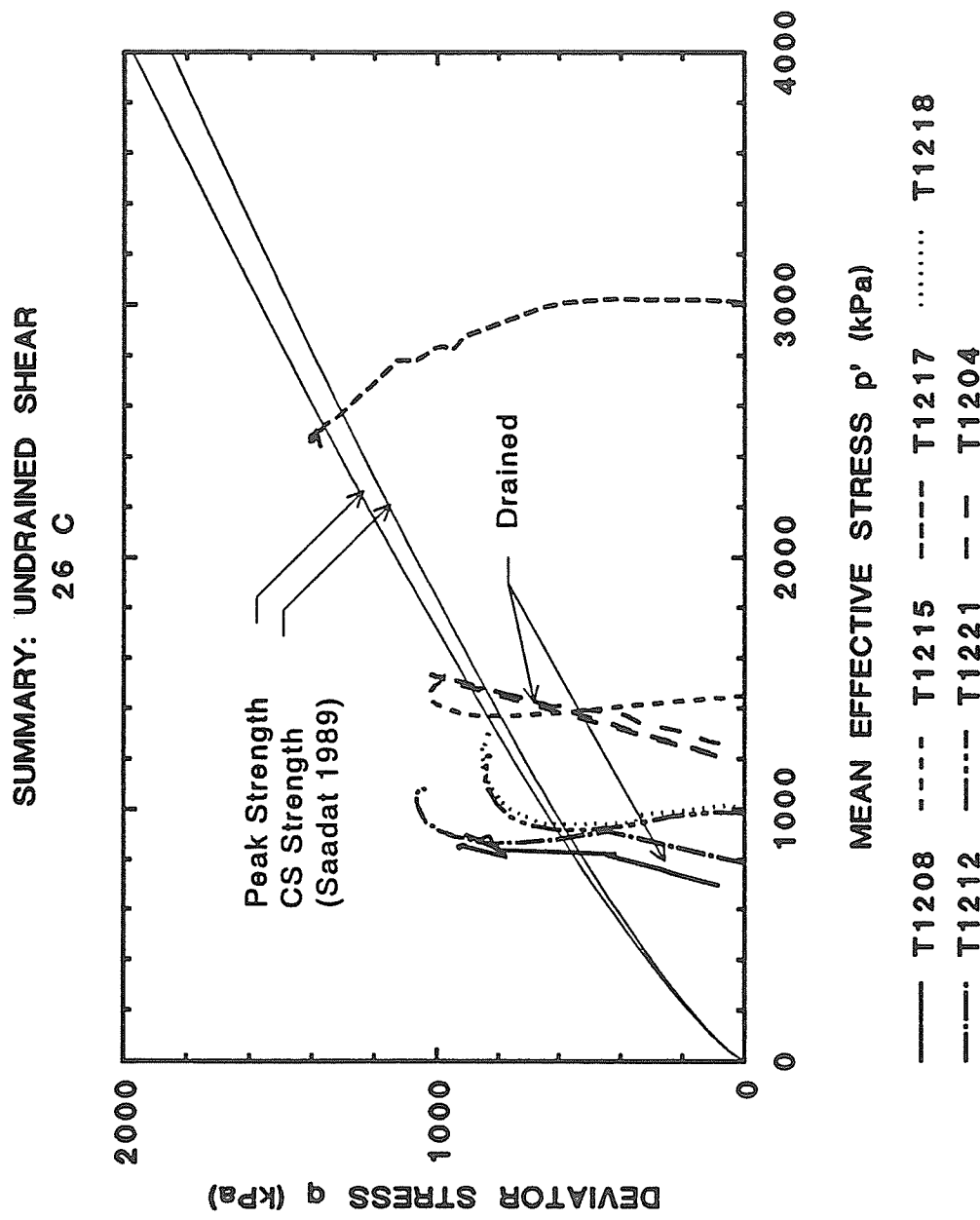


FIGURE 5.29 Summary of stress paths from tests at 26°C

SUMMARY: UNDRAINED SHEAR
65 °C (CONTINUED)

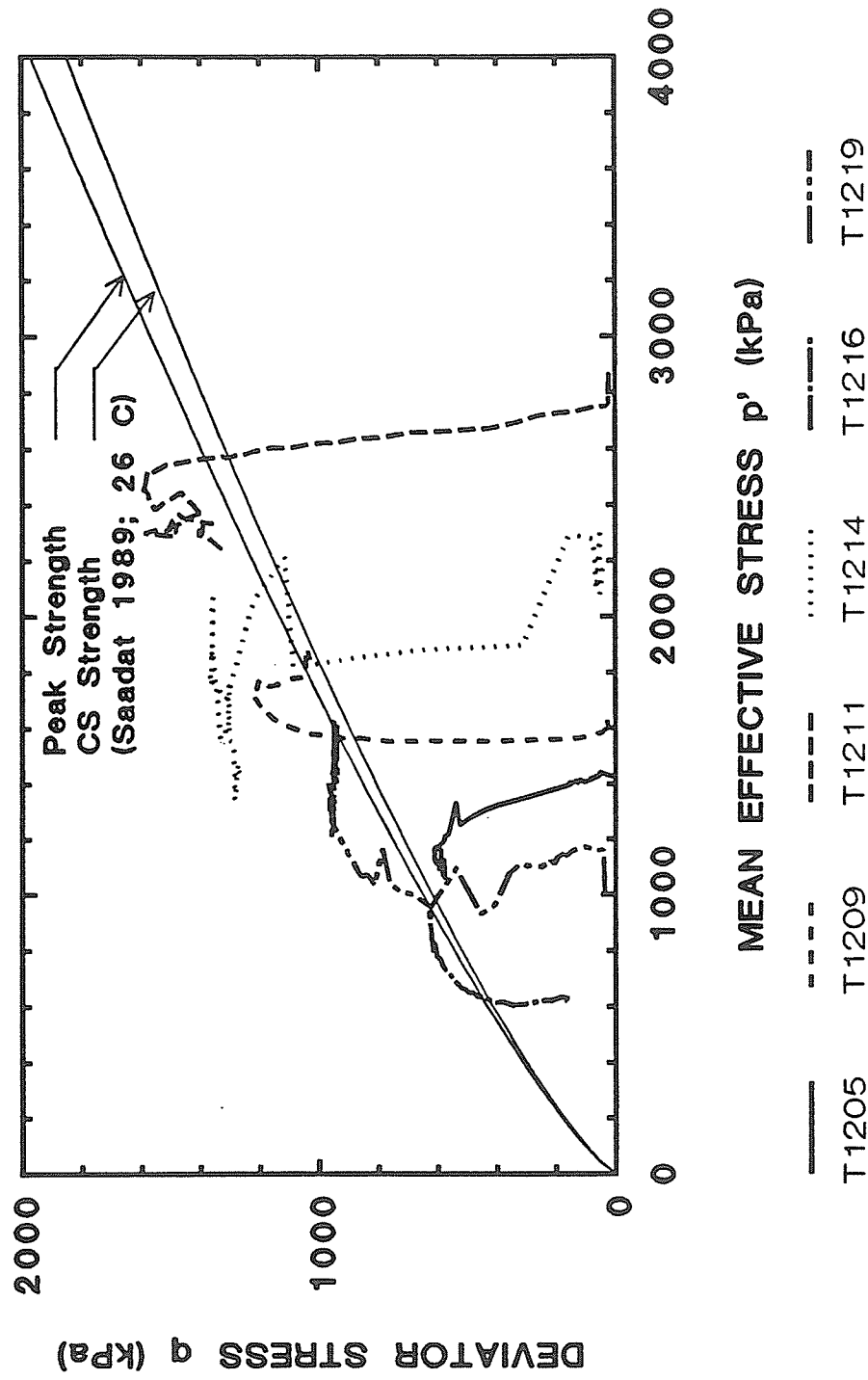


FIGURE 5.30 Summary of stress paths from tests at 65°C

**SUMMARY: UNDRAINED SHEAR
65 °C (CONTINUED)**

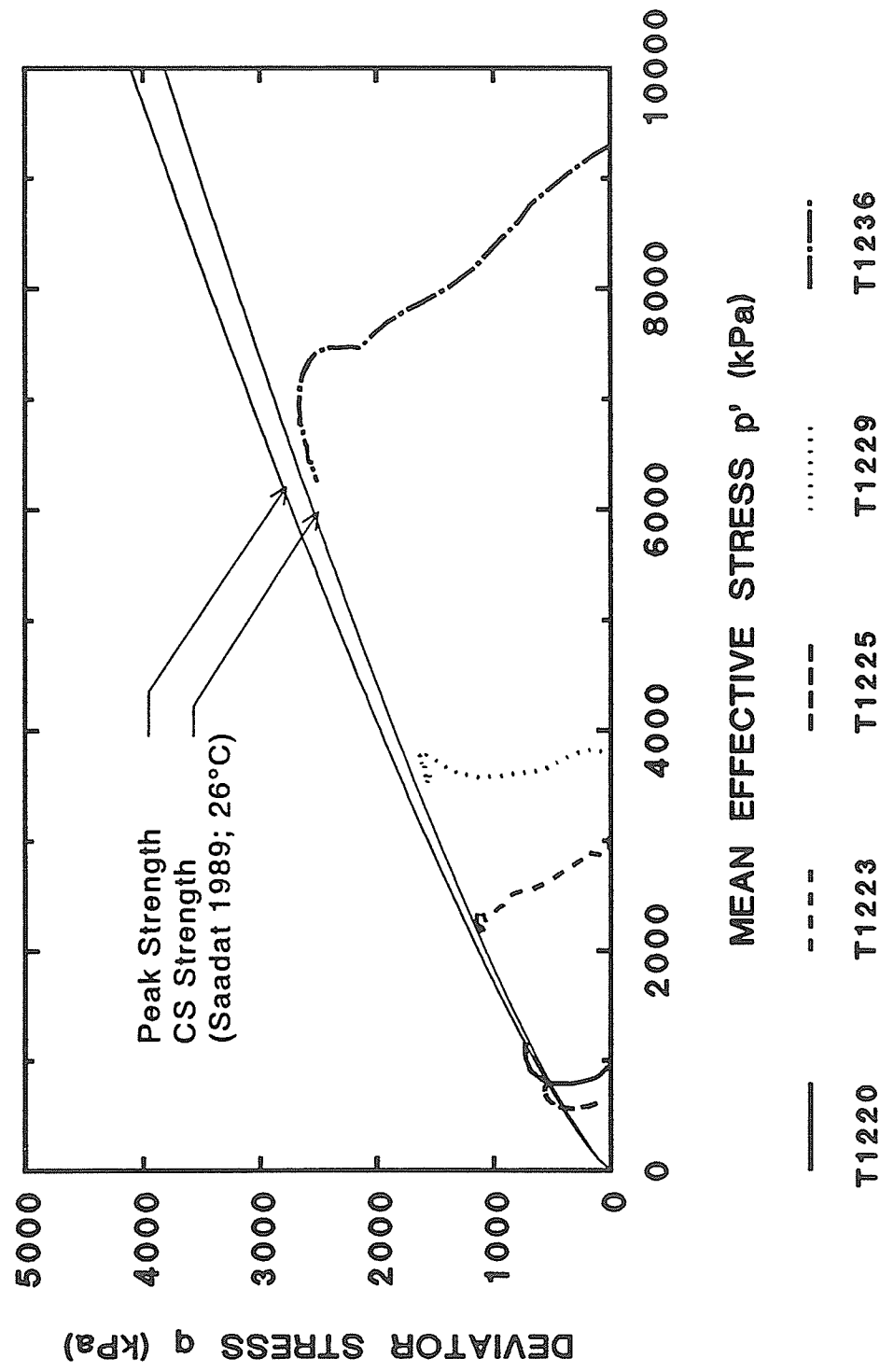


FIGURE 5.31 Summary of stress paths from tests at 65°C

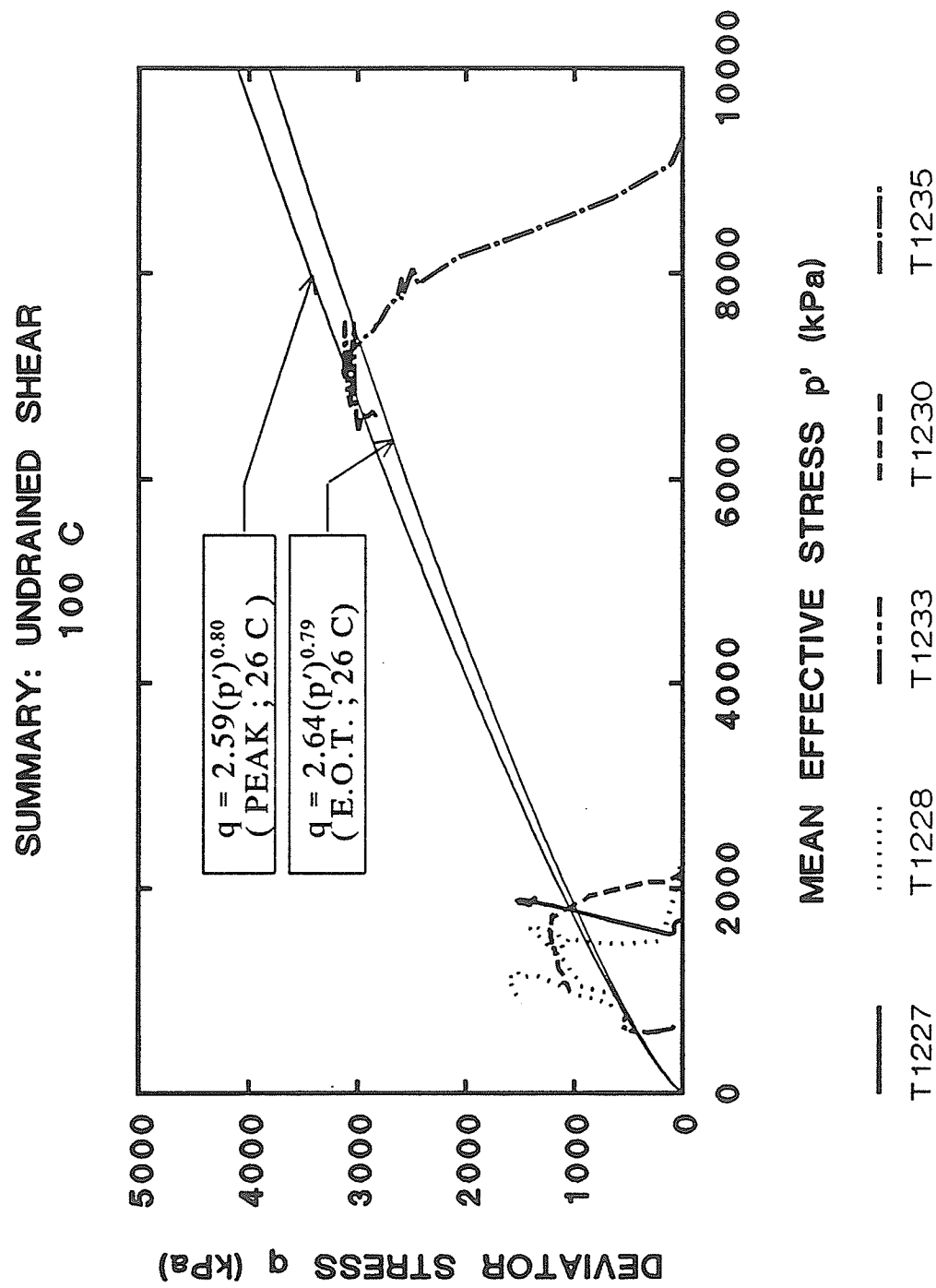


FIGURE 5.32 Summary of stress paths from tests at 100°C

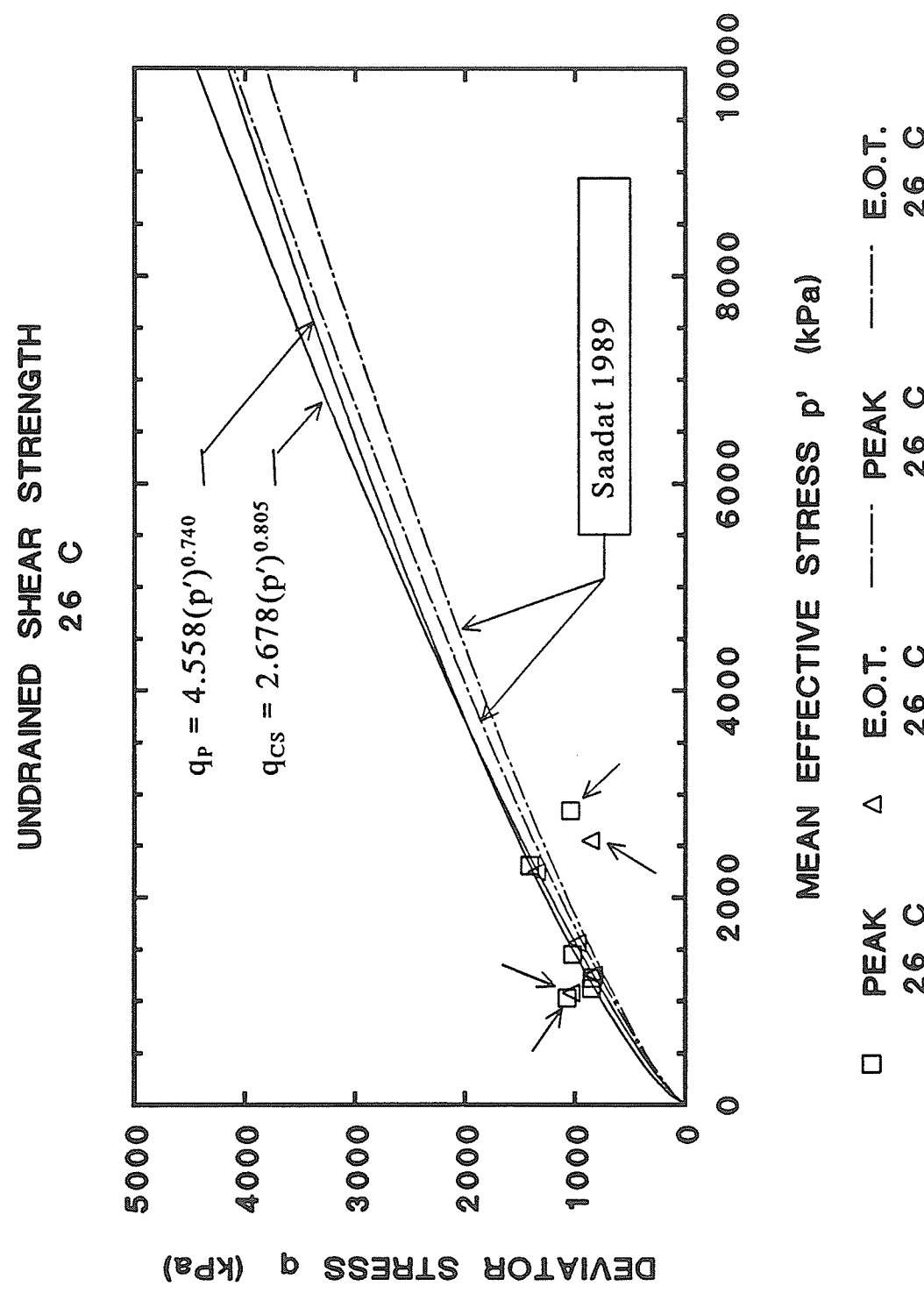


FIGURE 5.33 Summary of peak and end-of-test strength results at 26°C

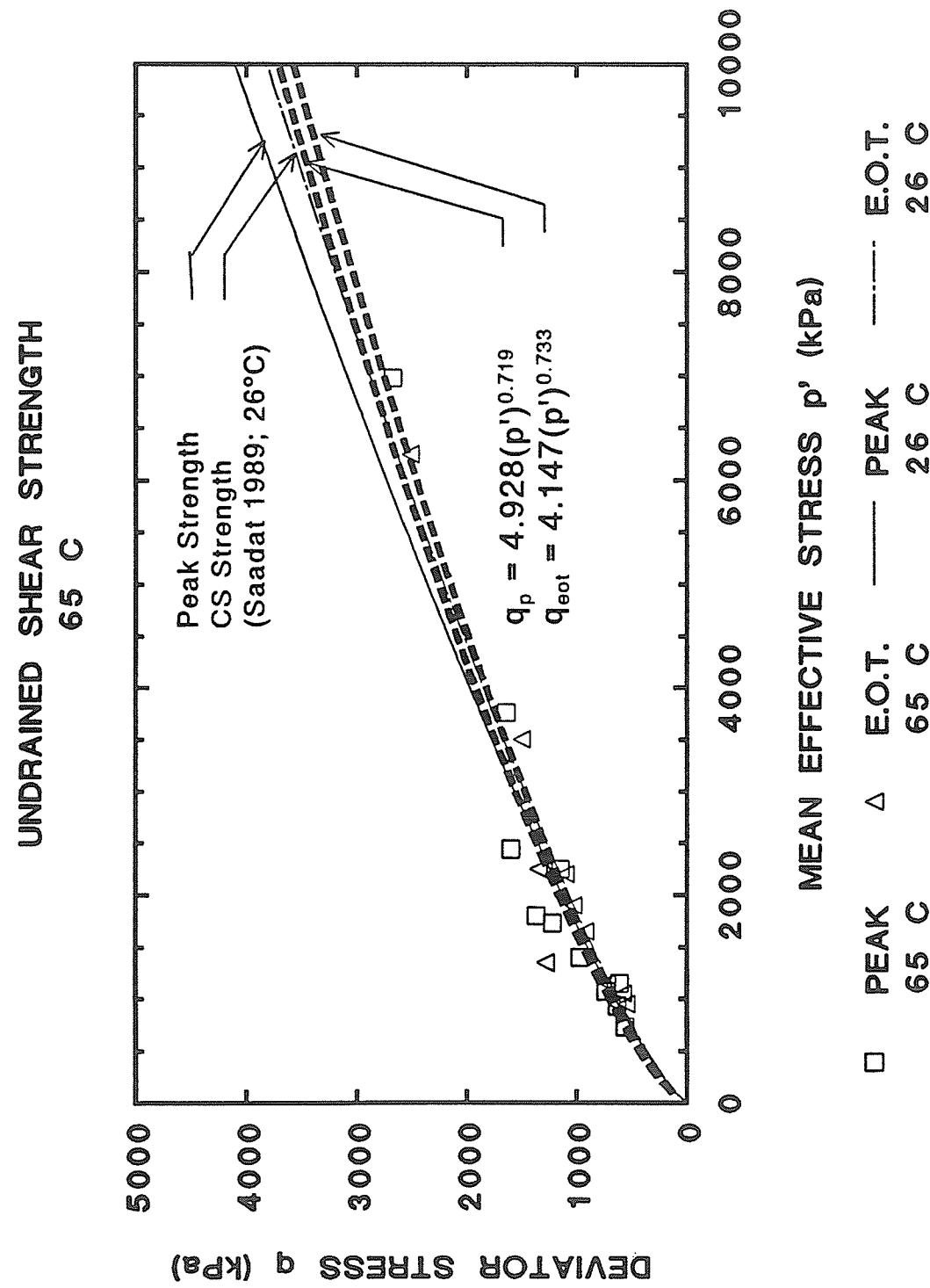


FIGURE 5.34 Summary of peak and end-of-test strength results at 65°C

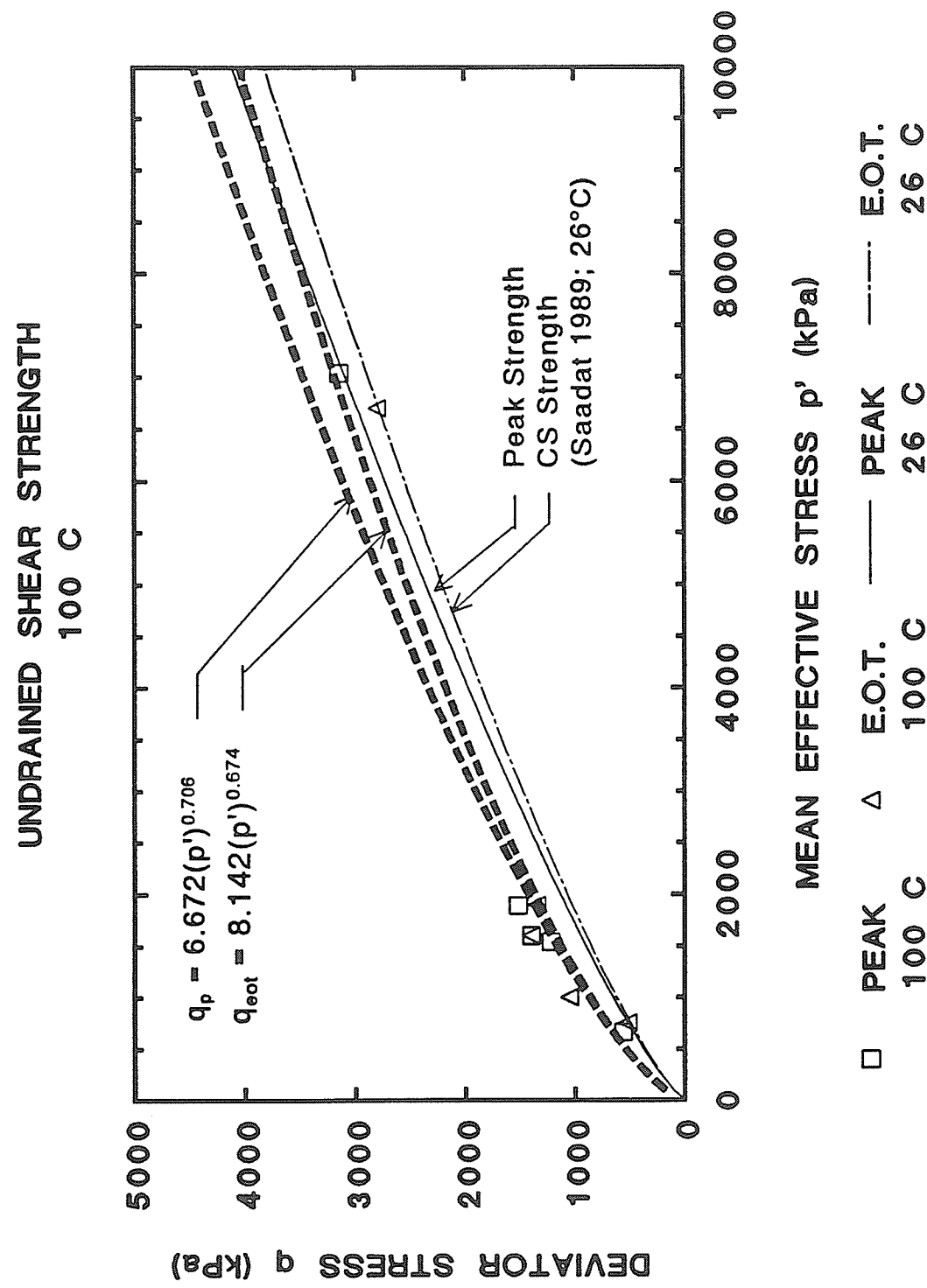


FIGURE 5.35 Summary of peak and end-of-test strength results at 100°C

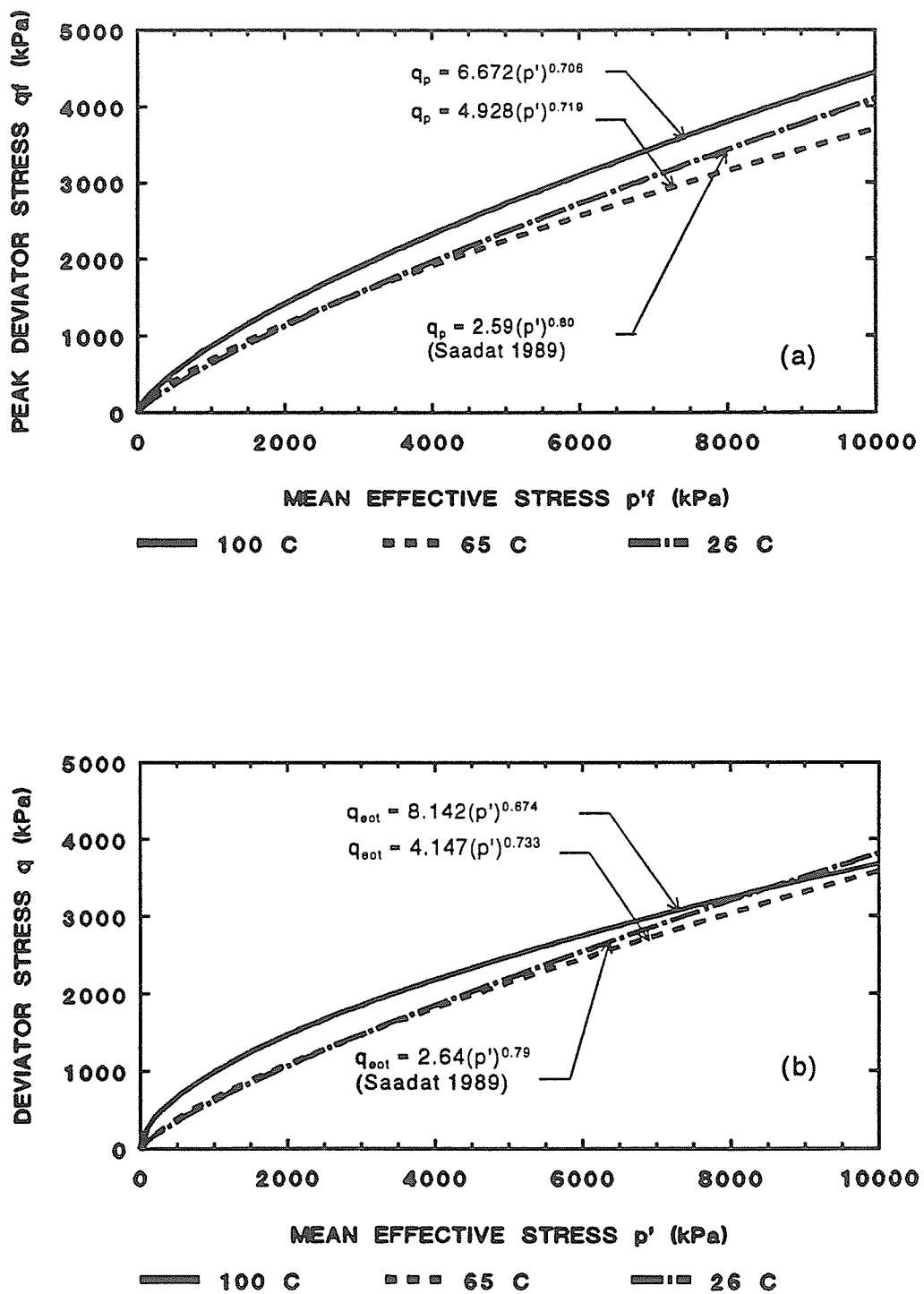


FIGURE 5.36 Comparison of strength envelopes at 26°C, 65°C, and 100°C: (a) peak; (b) end-of-test

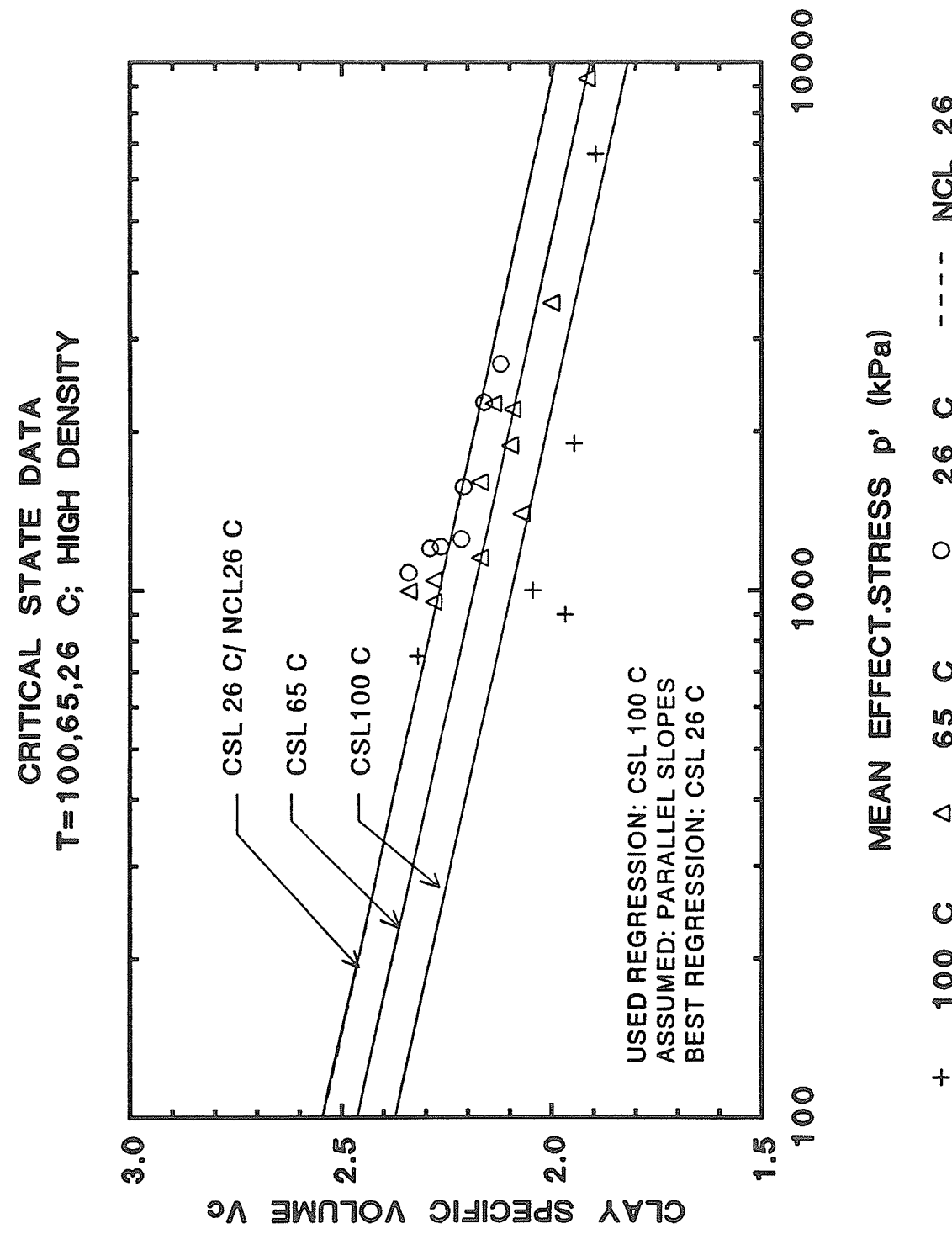


FIGURE 5.37 Summary of critical state lines in V_c versus $\log(p')$ space

HARDENING LAWS AND CRITICAL STATE LINES
 $T = 100, 65, 26^\circ C$; HIGH DENSITY

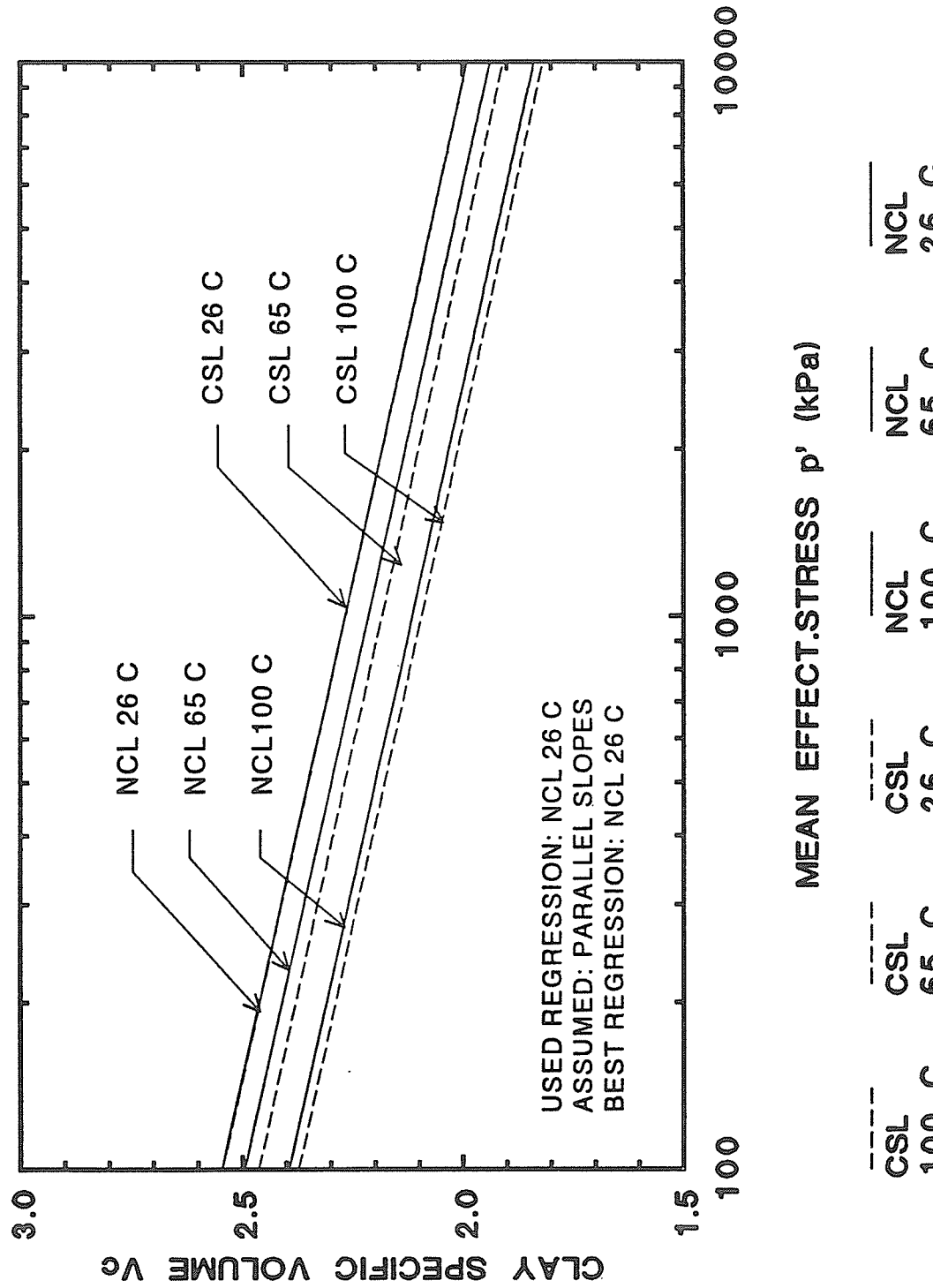


FIGURE 5.38 Summary of critical state lines and normal consolidation lines in V_c versus $\log(p')$ space

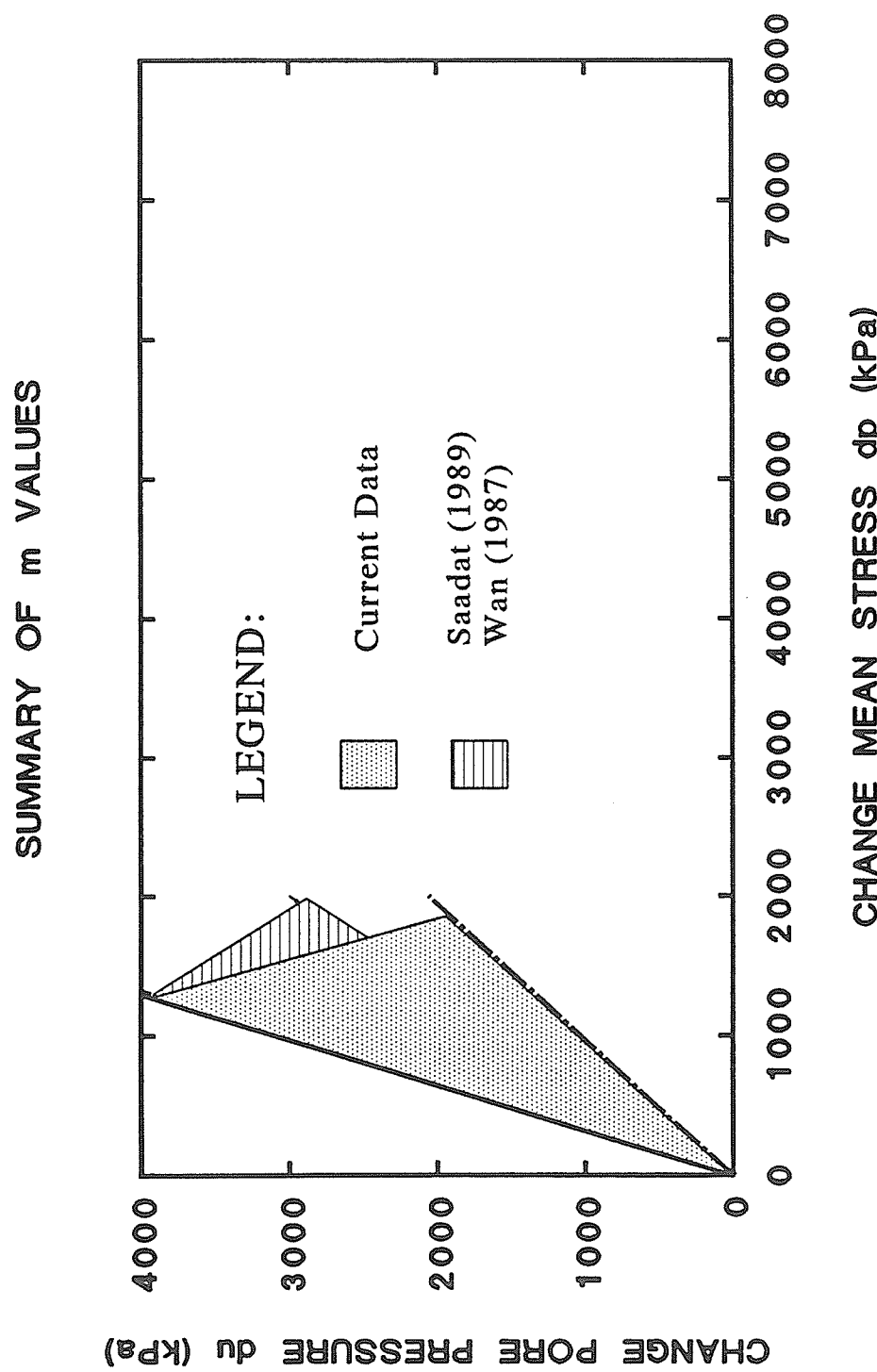


FIGURE 5.39 Summary of values of $m = \Delta u / \Delta p$

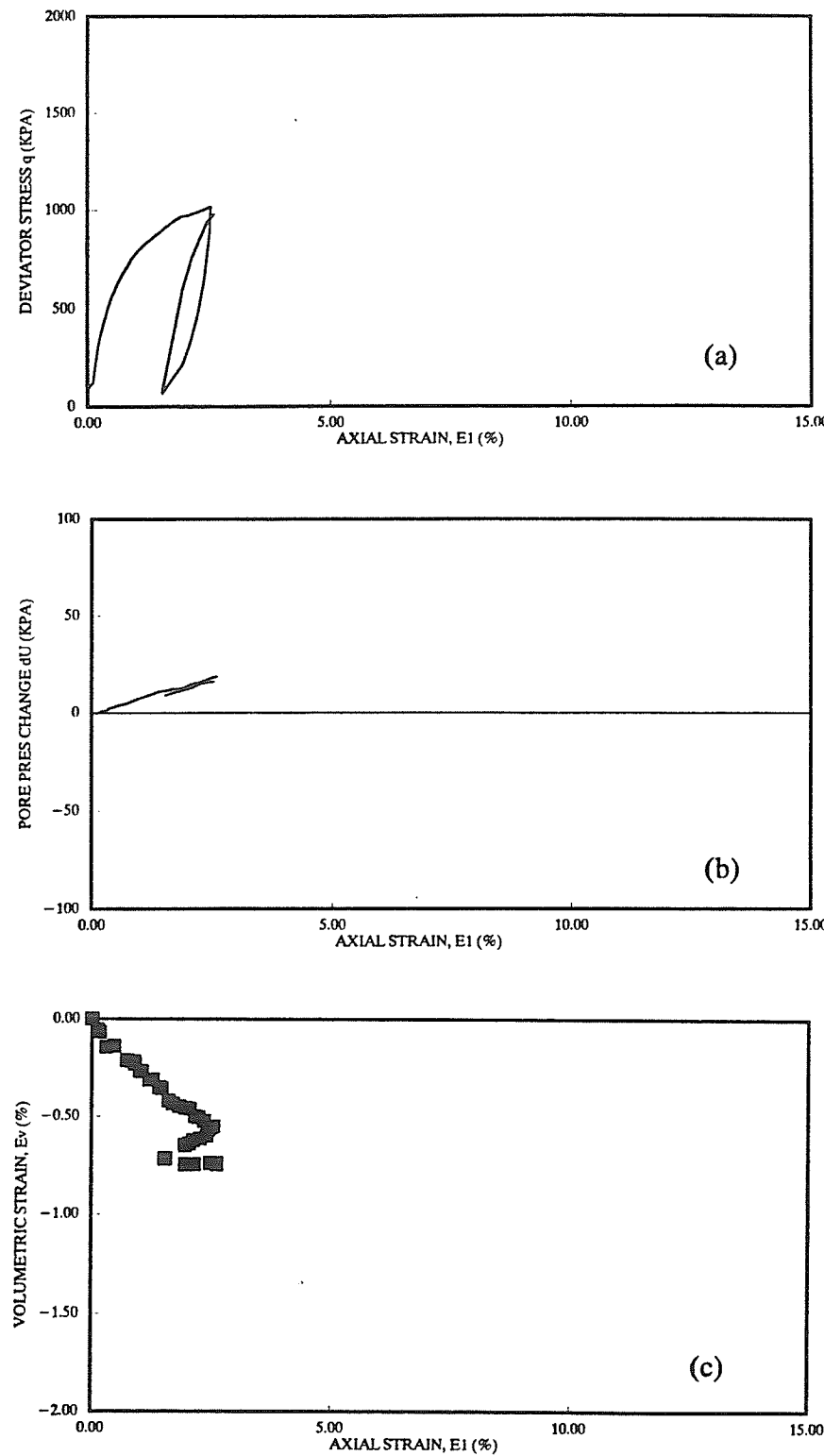


FIGURE 5.40 Drained shear results from CID(TXC) test T1204: (a) deviator stress versus axial strain; (b) pore pressure change versus axial strain; and (c) volumetric strain versus axial strain

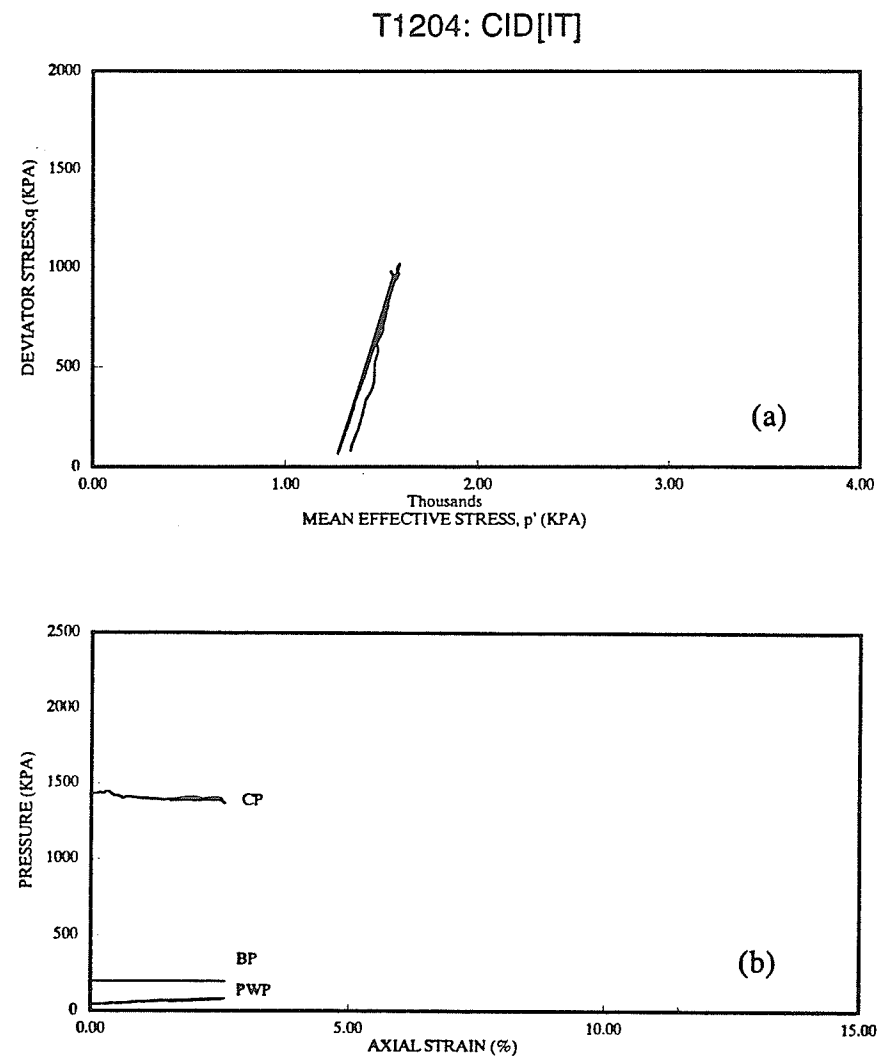


FIGURE 5.41 Drained shear results from CID(TXC) test T1204: (a) deviator stress versus mean effective stress; and (b) pressure versus axial strain

BUFFER MASS LOSS
COMPACTED SPECIMEN: OVEN DRIED 110°C

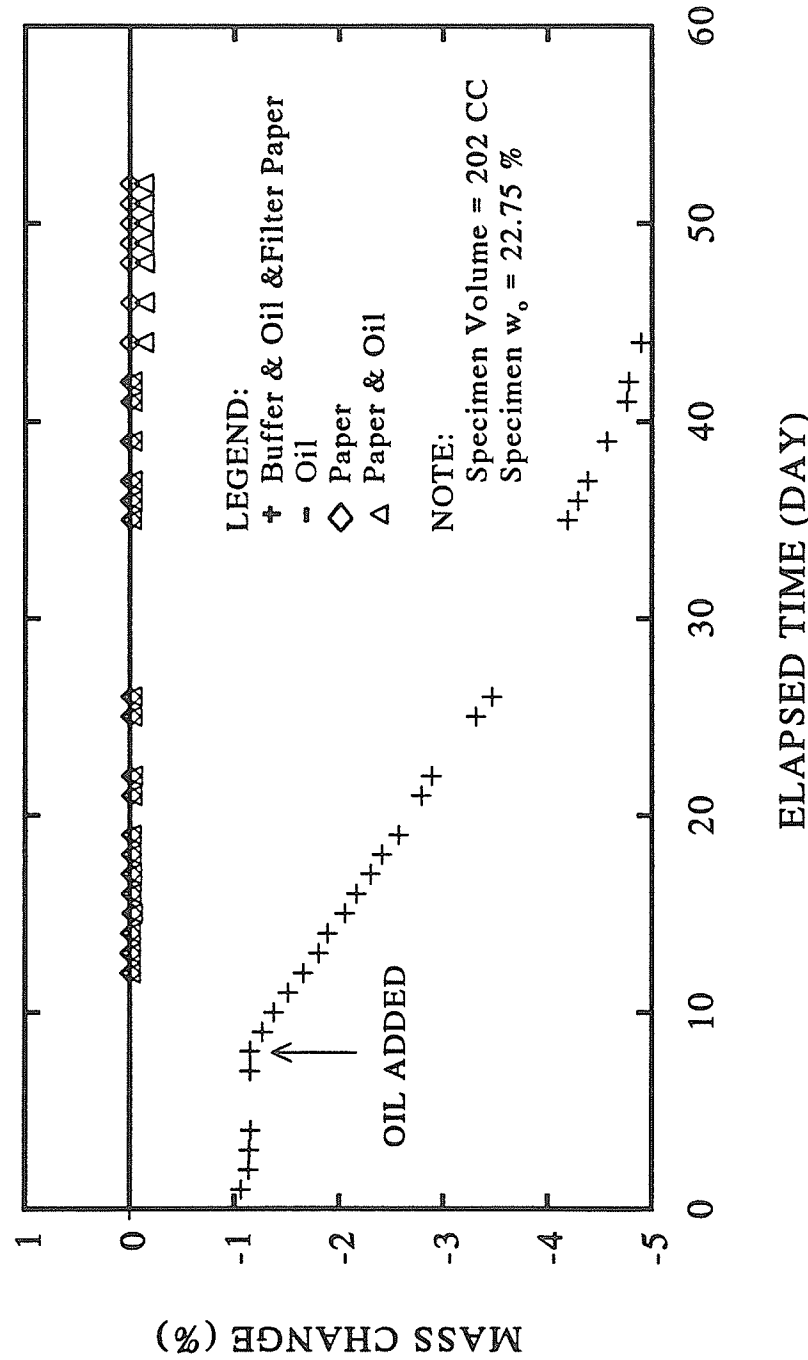


FIGURE 5.42 Effect of silicone oil contamination on the measurement of dry mass of compacted buffer at 110°C

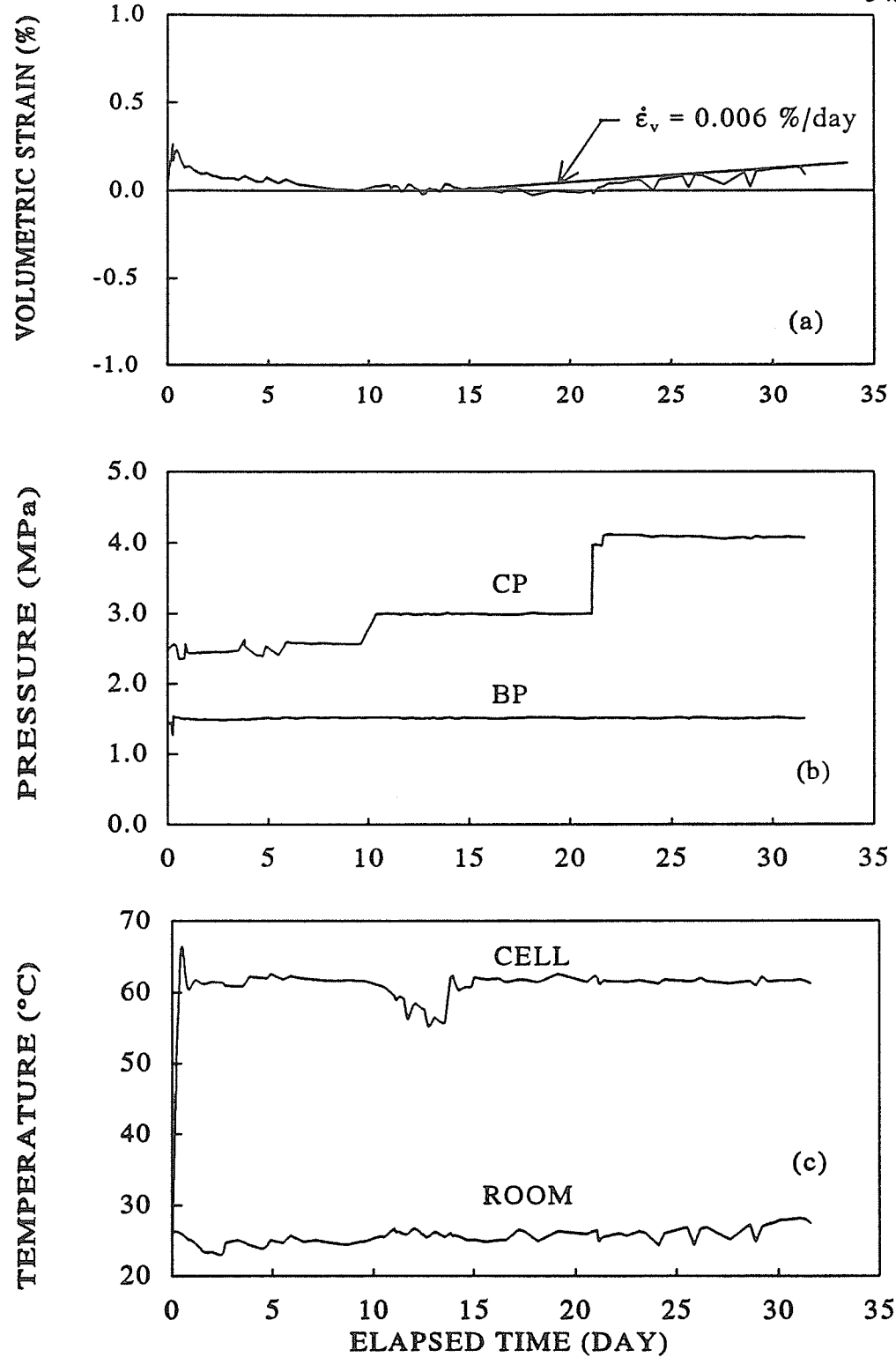


FIGURE 5.43 Leakage rate in test Leak#1

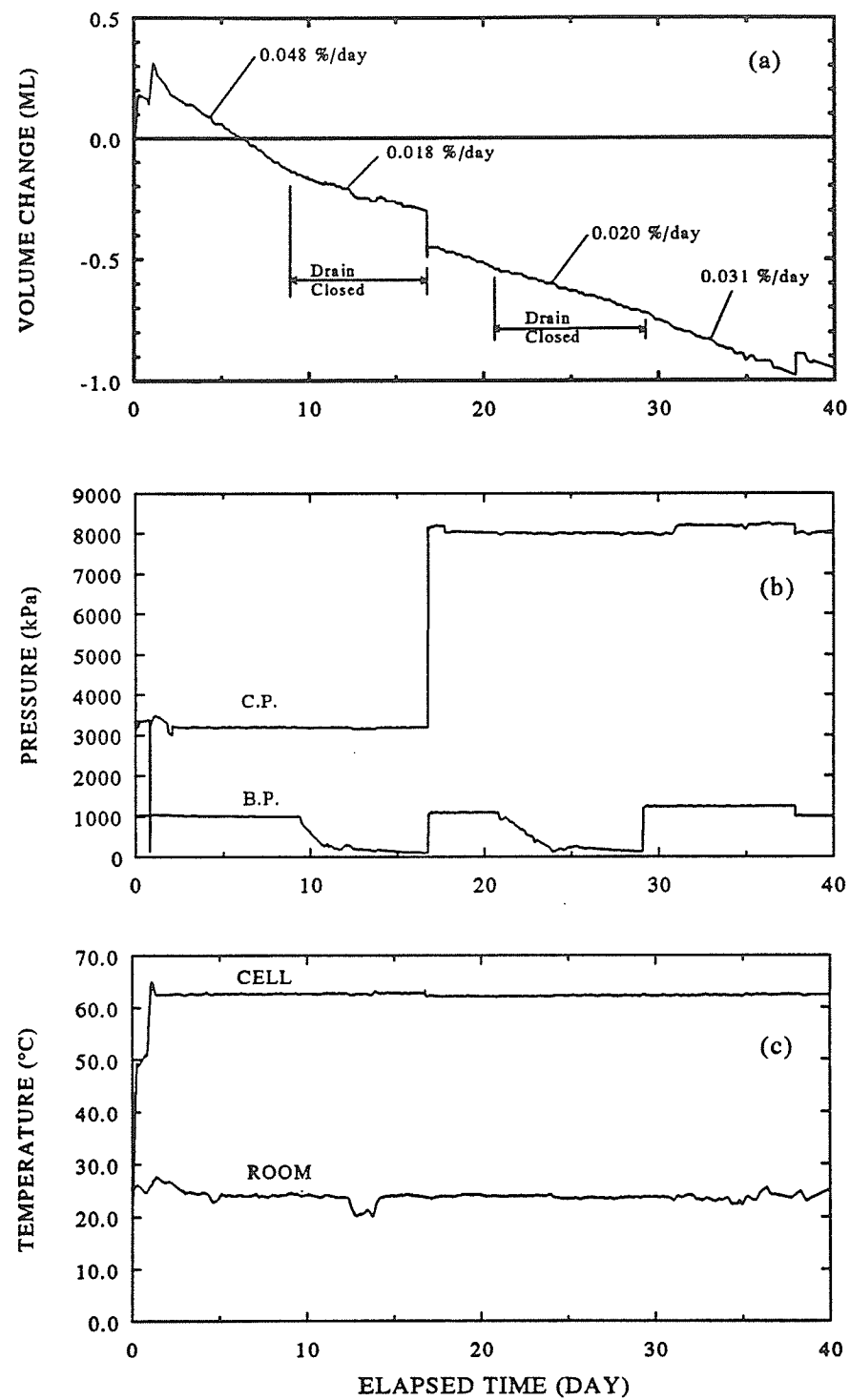


FIGURE 5.44 Leakage rate in test Leak#1

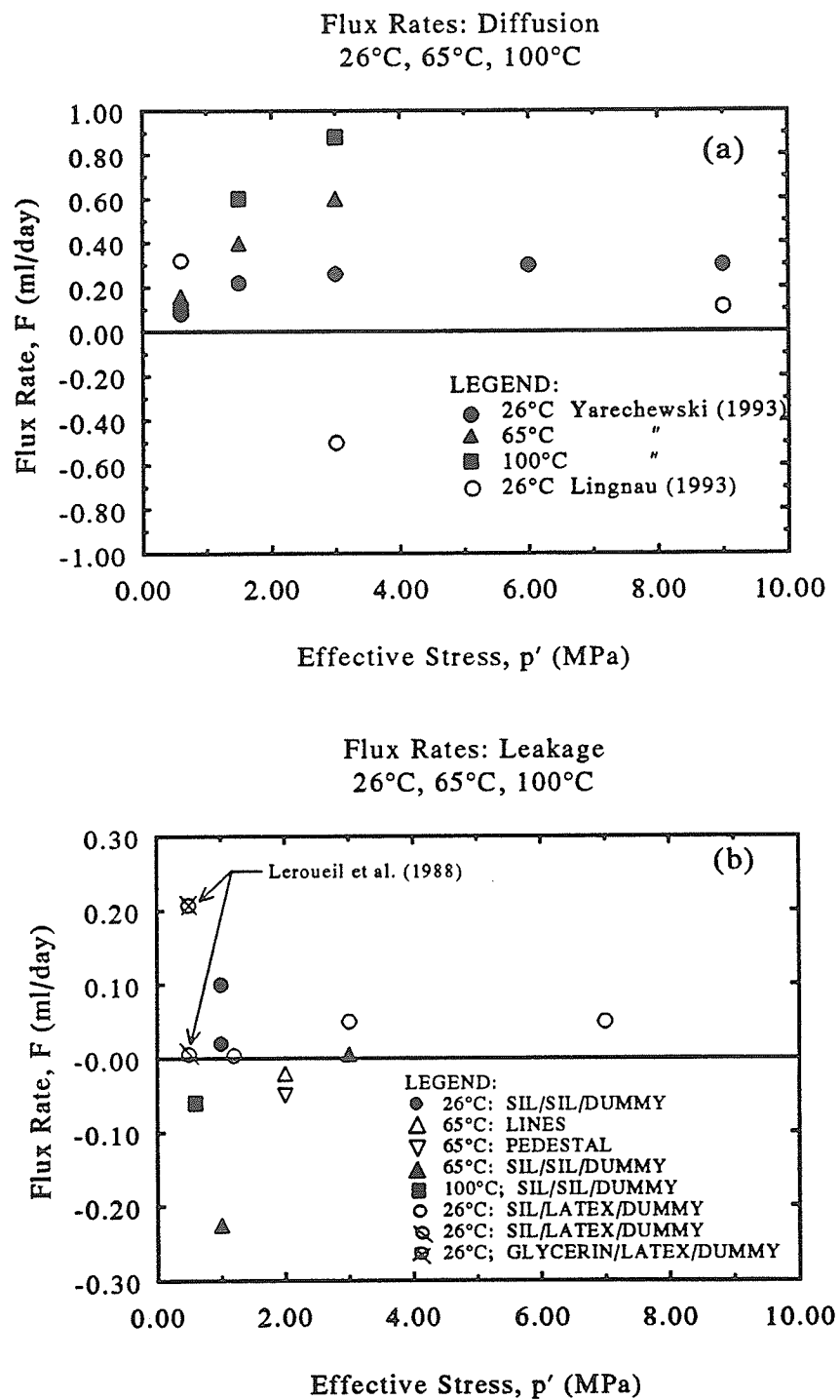
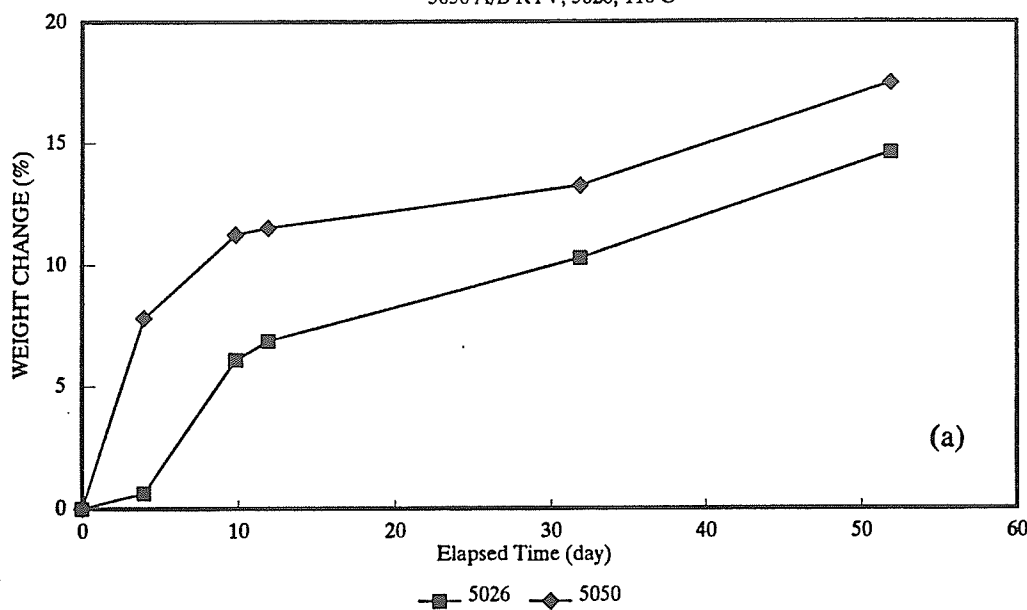


FIGURE 5.45 Diffusion and leakage tests on silicone and latex membranes using different cell fluids. (a) results of diffusion tests on silicone membranes at 26°C, 65°C and 100°C using the diffusion apparatus; and (b) leakage test results for membranes in triaxial cells

Silicone Rubber Swell Test

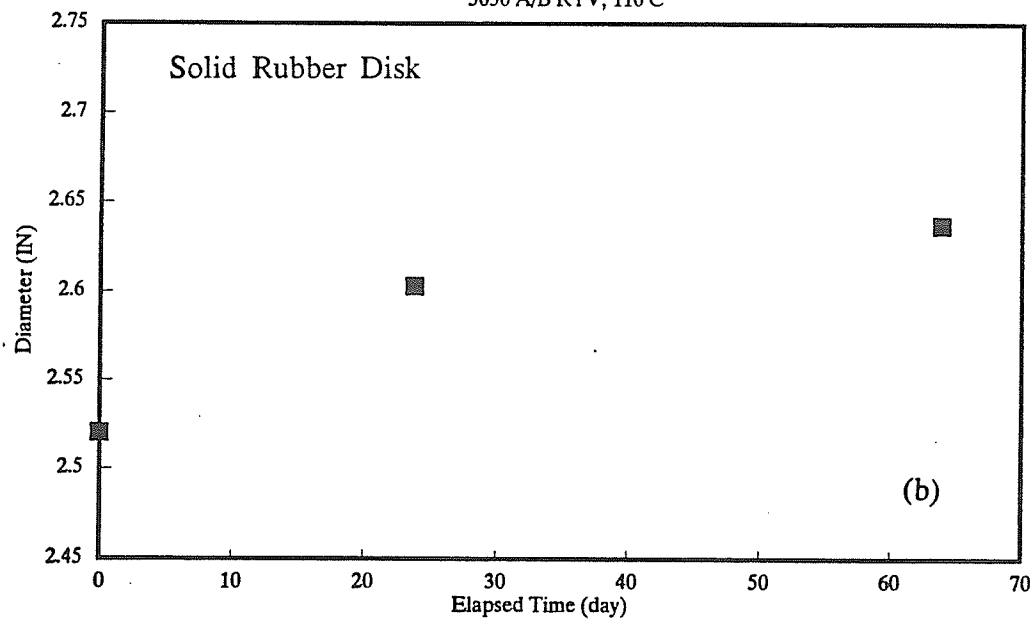
5050 A/B RTV; 5026; 110 C



(a)

Silicone Rubber Swell Test

5050 A/B RTV; 110 C



(b)

FIGURE 5.46 Swelling of silicone rubber immersed in silicone oil at 110°C: (a) change in weight of test sample (b) diameter of solid rubber disk

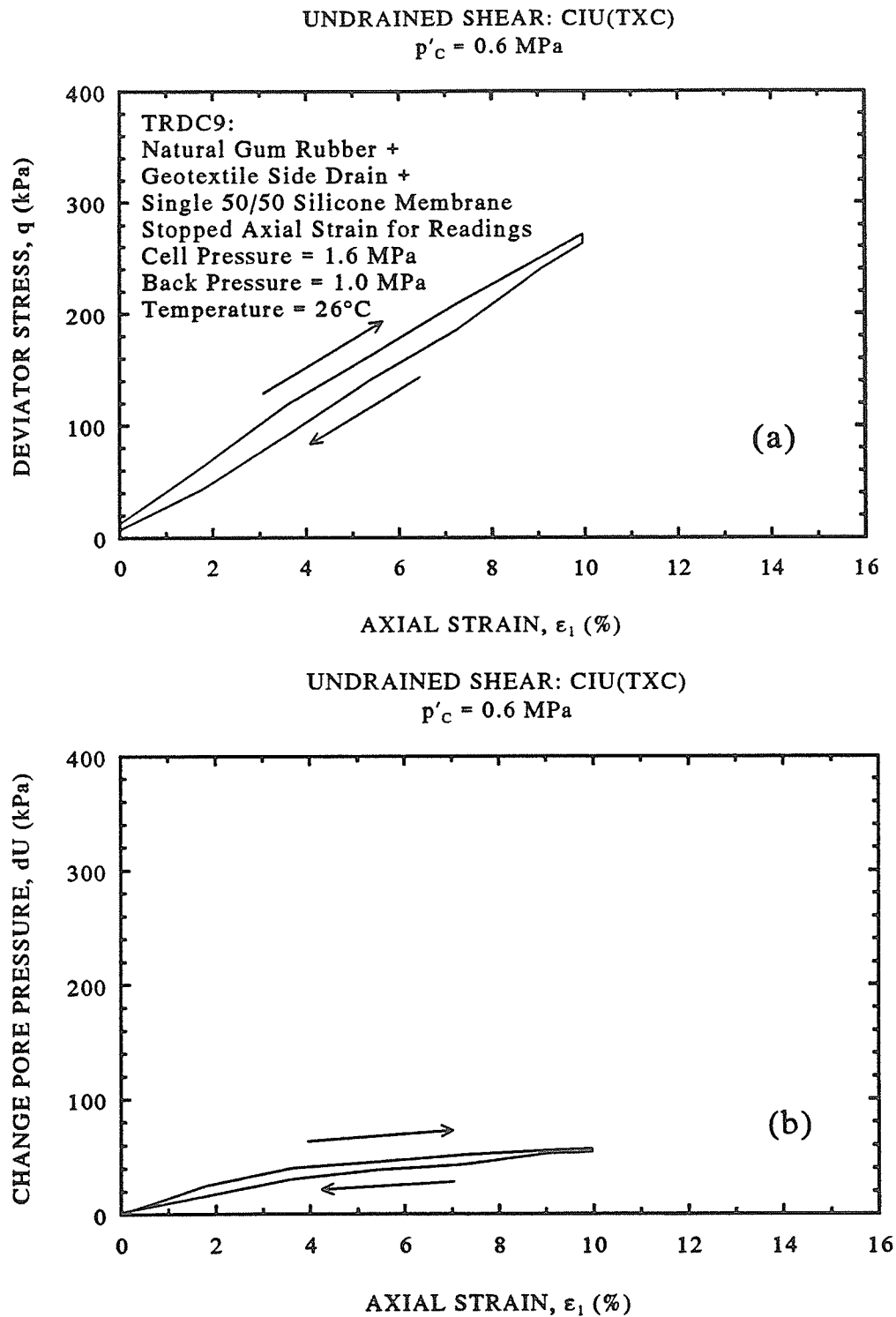


FIGURE 5.47 Undrained shear results from CIU(TXC) test TRDC9 (triaxial rubber dummy compression test 9): (a) deviator stress versus axial strain; and (b) pore pressure change versus axial strain

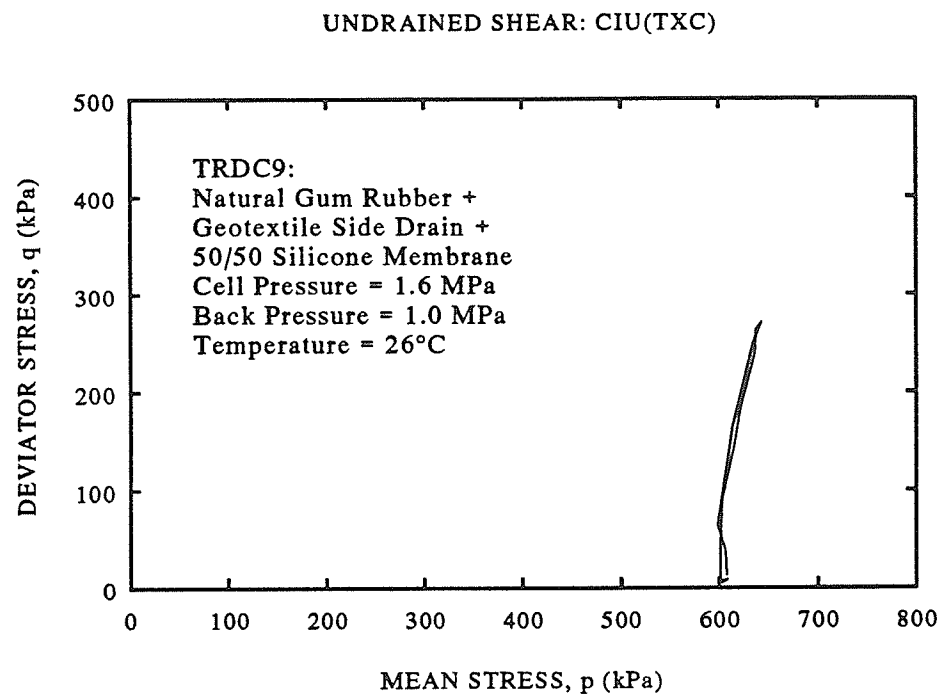


FIGURE 5.48 Undrained shear results from CIU(TXC) test TRDC9 (triaxial rubber dummy compression test 9): Deviator stress versus mean effective stress

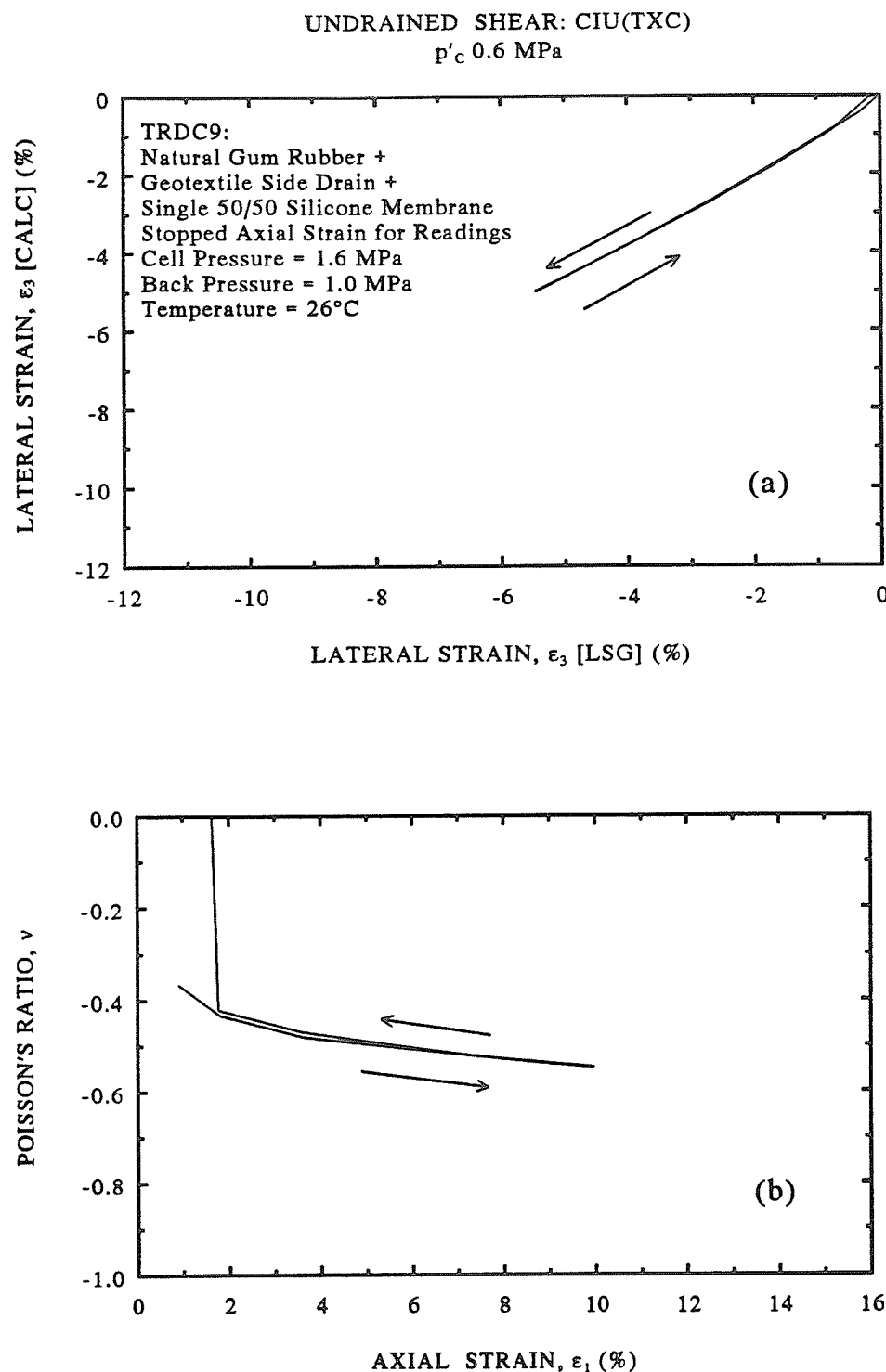


FIGURE 5.49 Undrained shear results from CIU(TXC) test TRDC9 (triaxial rubber dummy compression test 9): (a) calculated lateral strain versus measured lateral strain; and (b) Poisson's ratio versus axial strain

UNCONFINED UNIAXIAL SHEAR

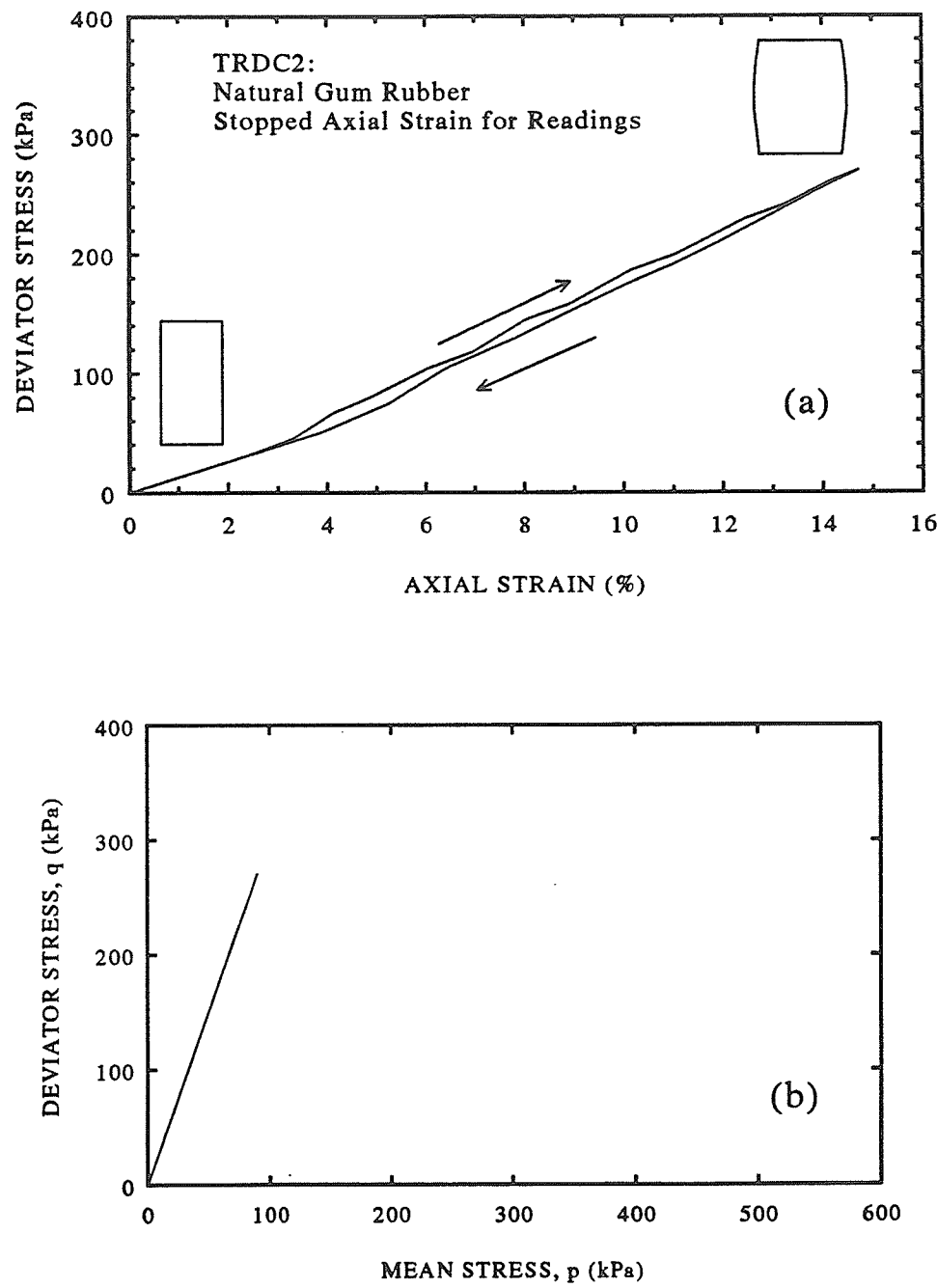


FIGURE 5.50 Undrained shear results from CIU(TXC) test TRDC2 (triaxial rubber dummy compression test 2): (a) deviator stress versus axial strain; and (b) deviator stress versus mean effective stress

UNCONFINED UNIAXIAL SHEAR

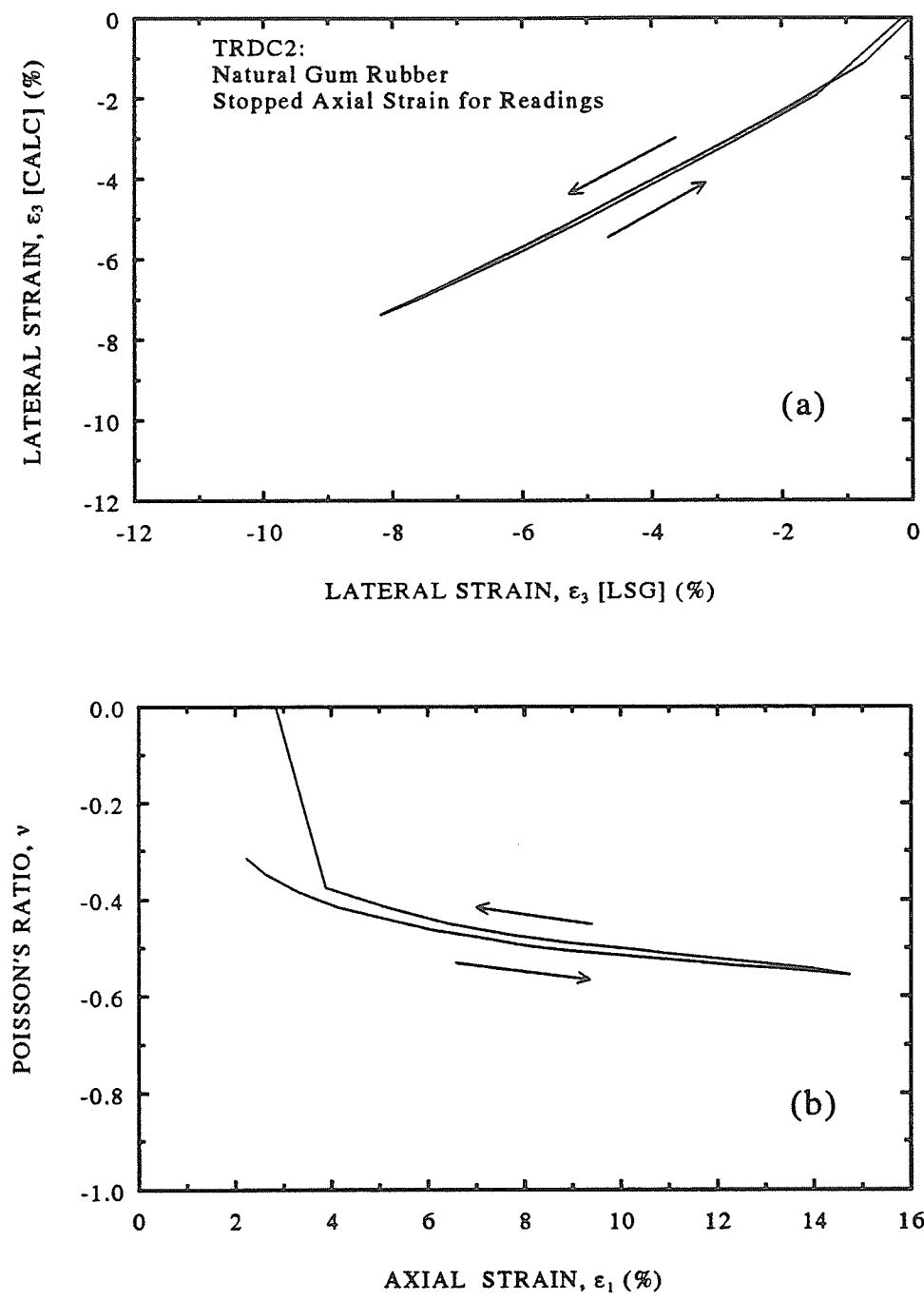


FIGURE 5.51 Undrained shear results from CIU(TXC) test TRDC2 (triaxial rubber dummy compression test 2): (a) calculated lateral strain versus measured lateral strain; and (b) Poisson's ratio versus axial strain

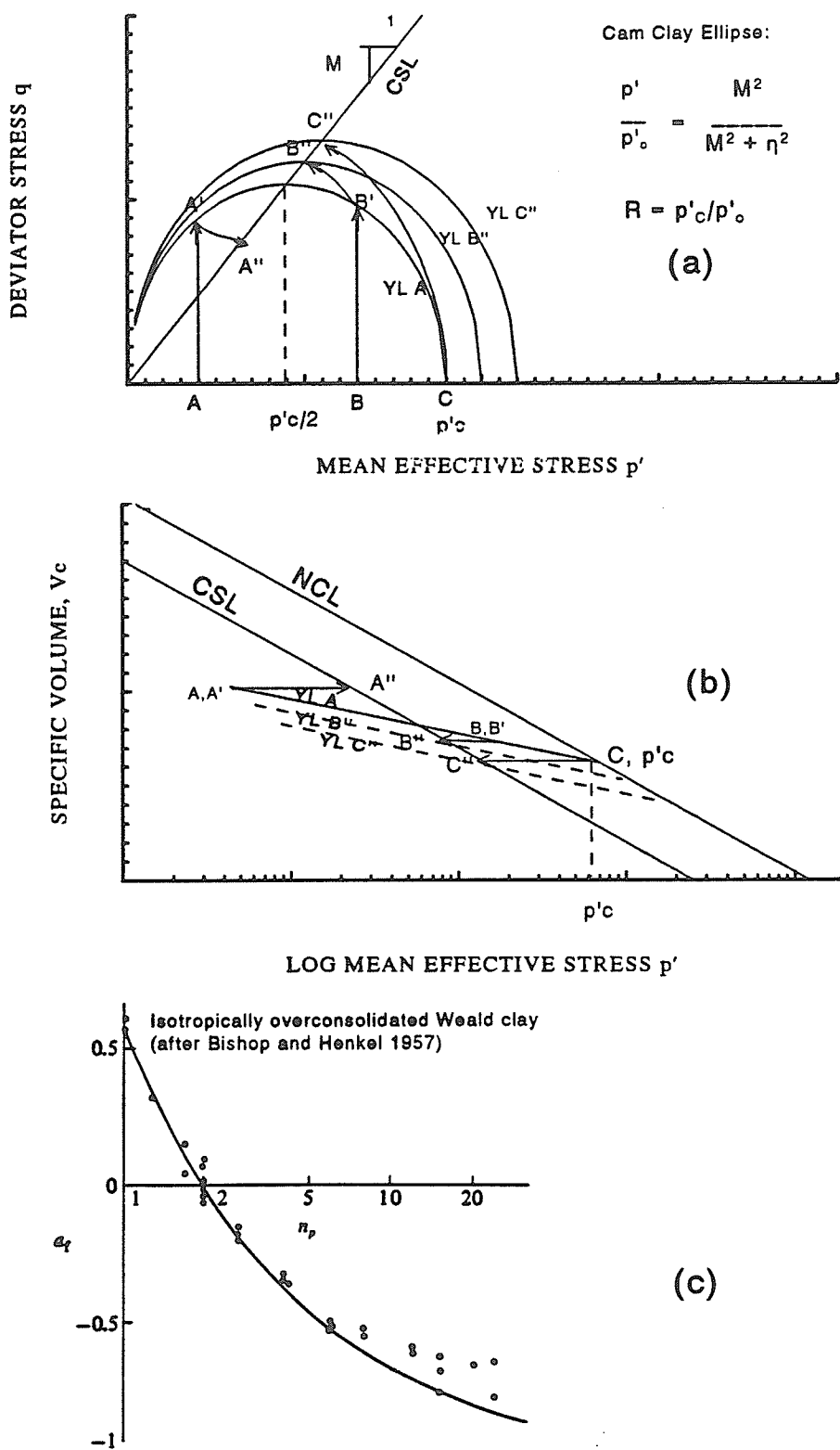


FIGURE 5.52 Definition of isotropic overconsolidation ratio, R using modified Cam clay: (a) deviator stress versus mean effective stress; (b) clay specific volume versus mean effective stress (log scale); and (c) pore pressure parameter, a_f versus n_p ($=R$) (Wood 1990)

UNDRAINED SHEAR
 $Pc' = 1.6 \text{ MPa}$

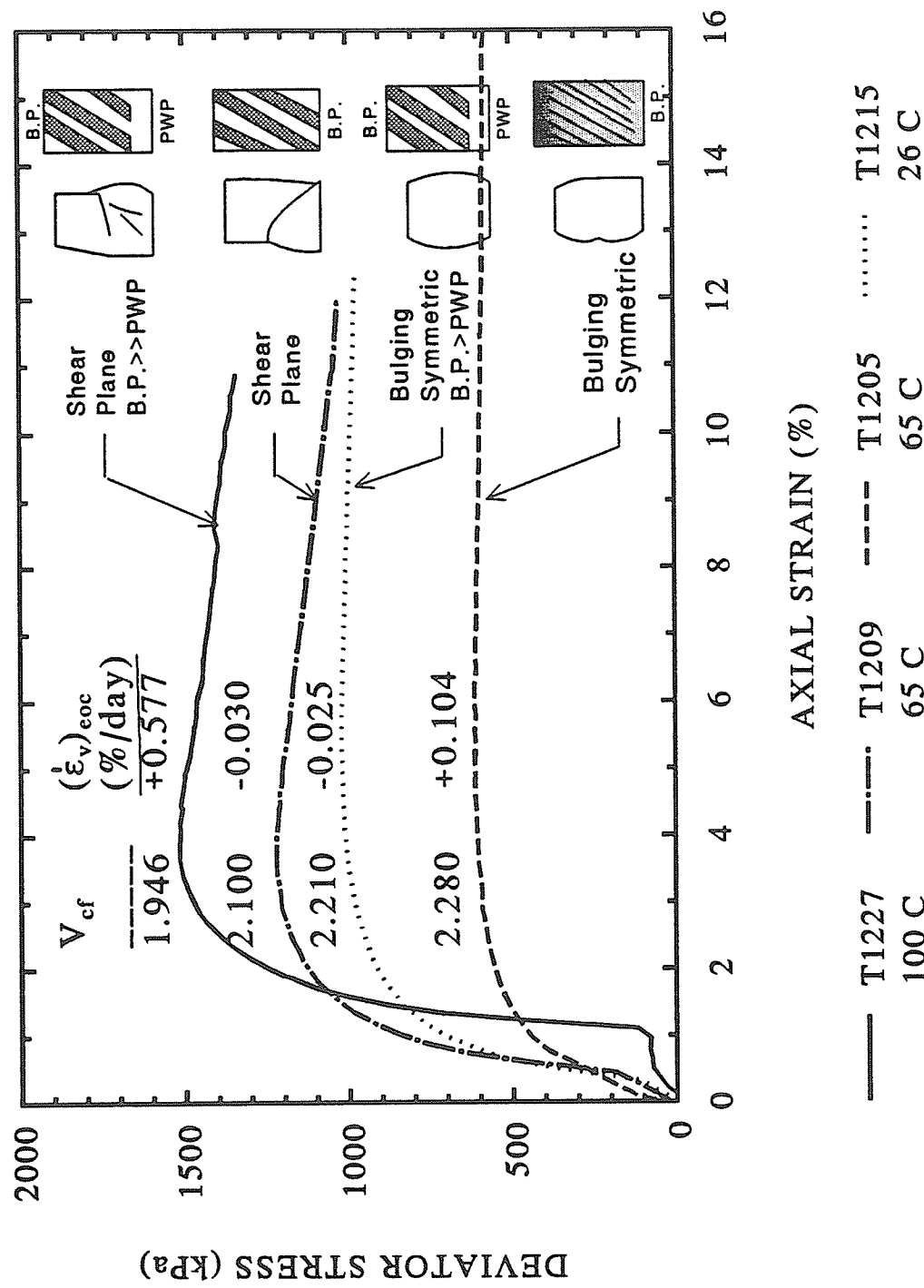


FIGURE 5.53 Failure modes in selected test specimens

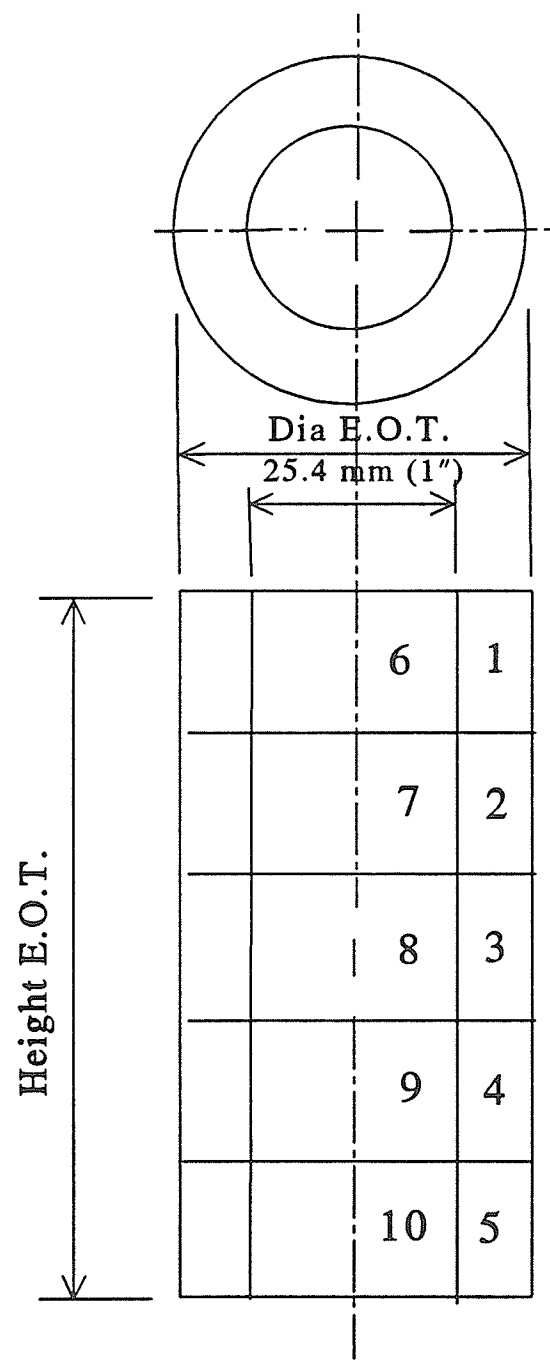


FIGURE 6.1 Division of buffer specimens for final moisture content determination

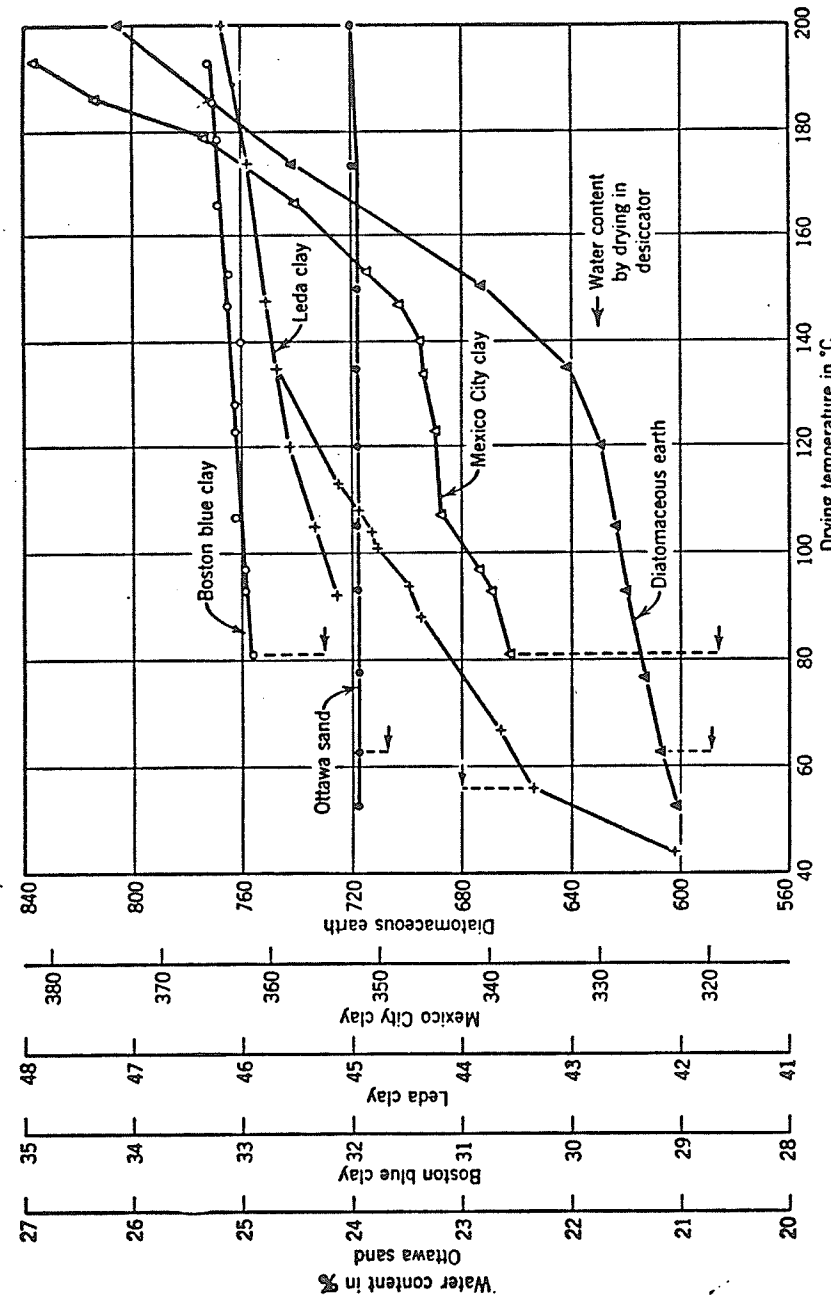


FIGURE 6.2 Drying curves for natural soils (After Lambe, 1951)

FINAL SPECIFIC VOLUME
(All 10 Slices of Specimen)

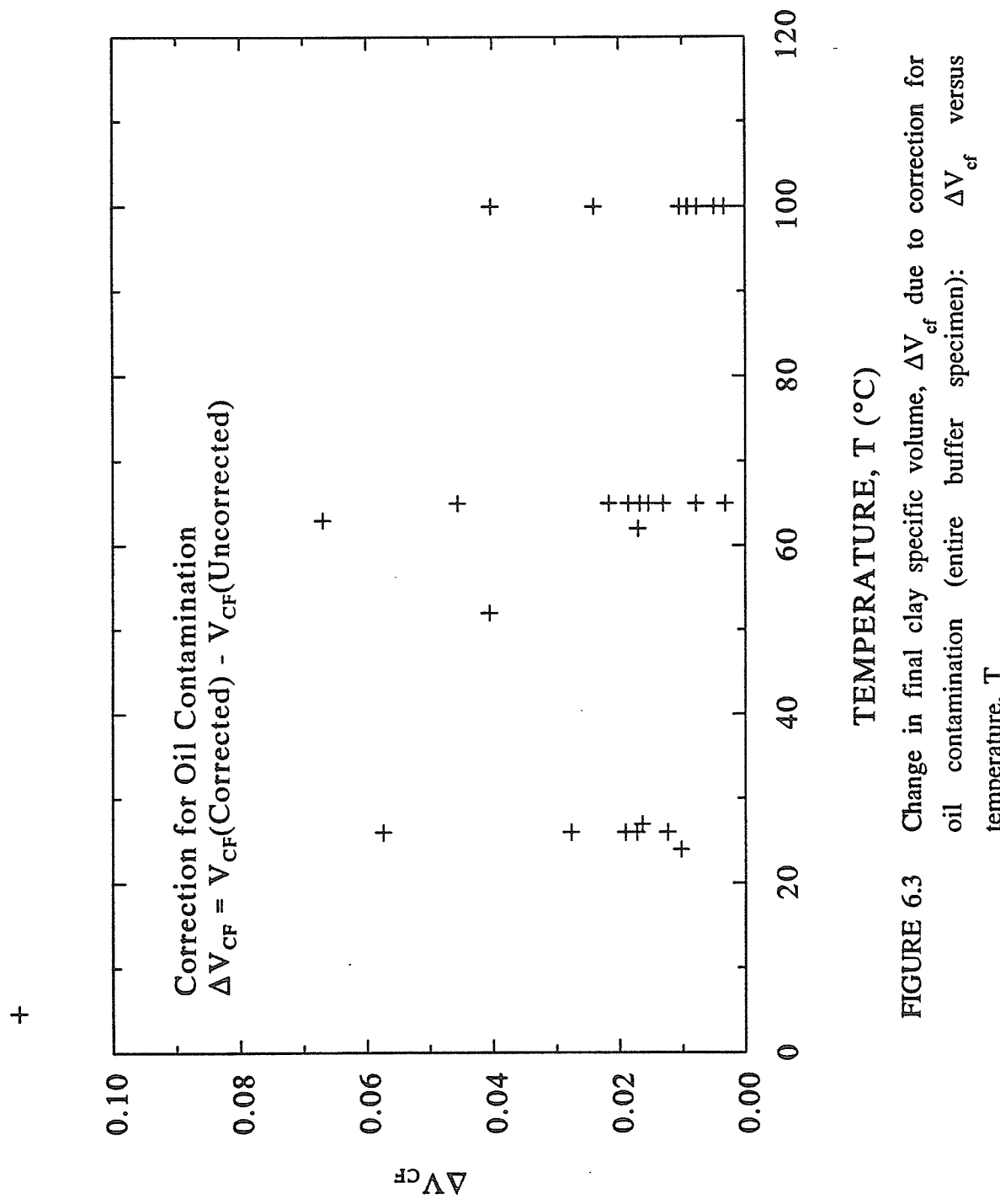


FIGURE 6.3 Change in final clay specific volume, ΔV_{cf} due to correction for oil contamination (entire buffer specimen): ΔV_{cf} versus temperature, T

SUMMARY: TRIAXIAL CONSOLIDATION

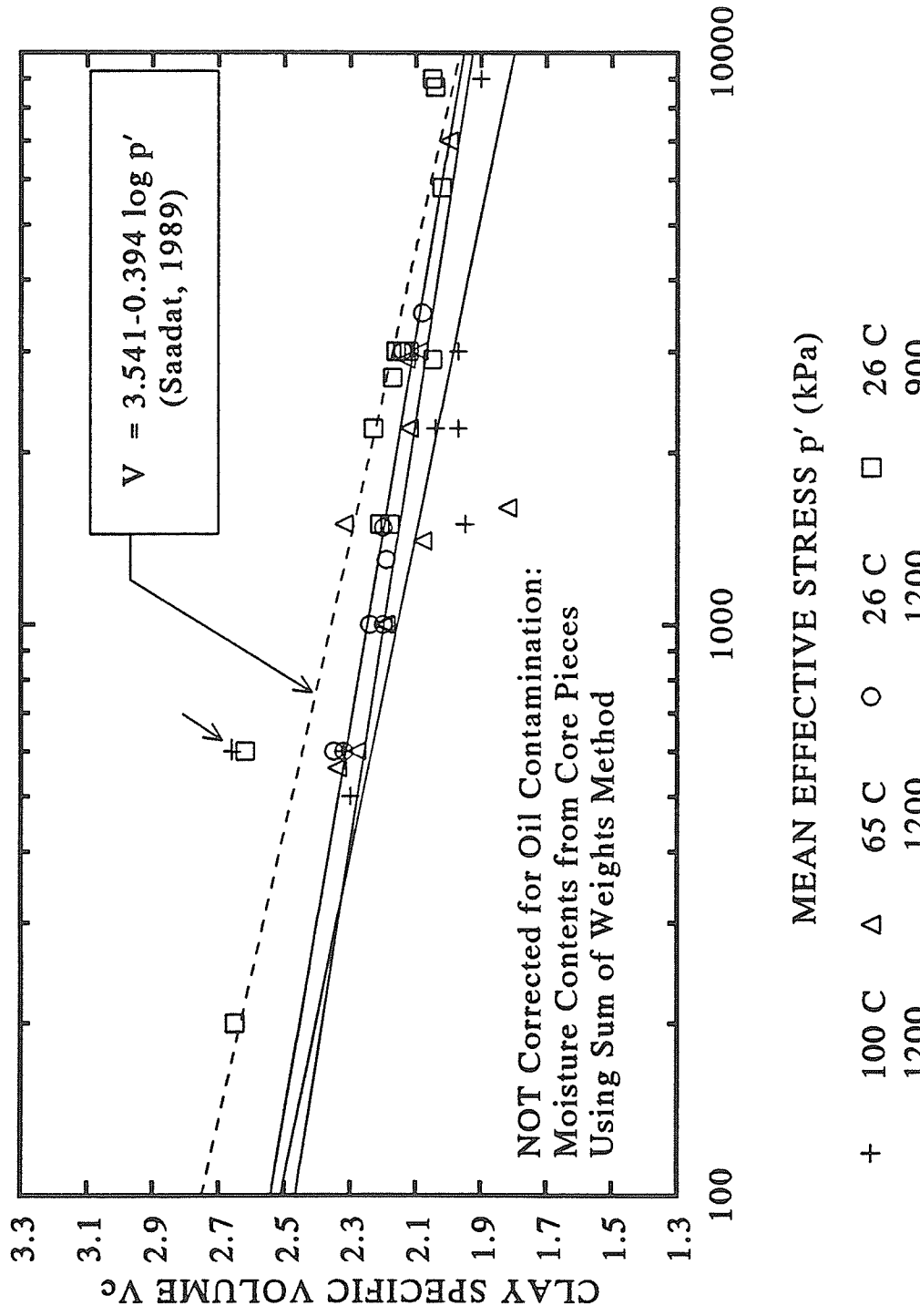


FIGURE 6.4 Clay specific volume, V_c versus mean effective stress, p' for uncorrected data

SUMMARY: TRIAXIAL CONSOLIDATION

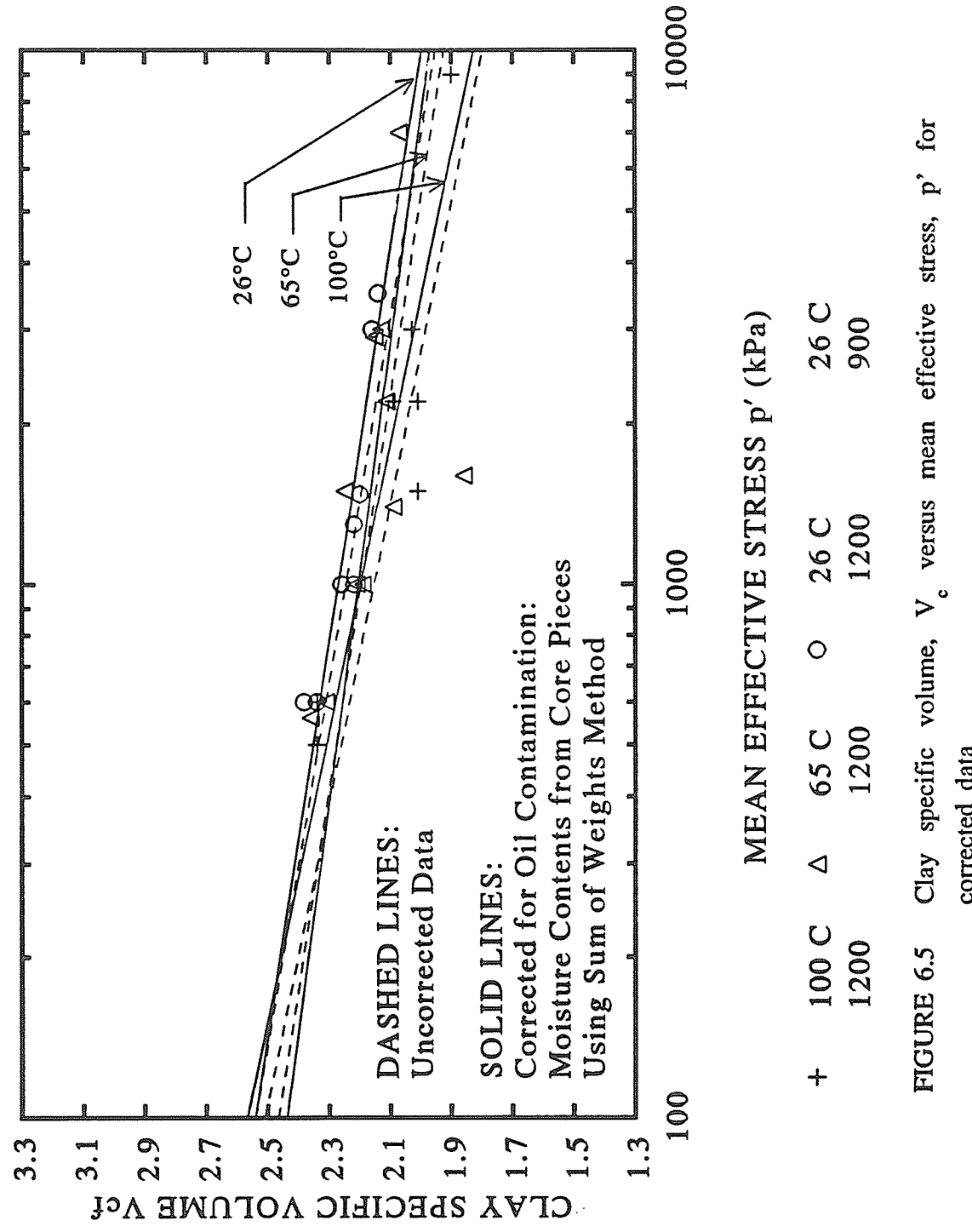


FIGURE 6.5 Clay specific volume, V_c' versus mean effective stress, p' for corrected data

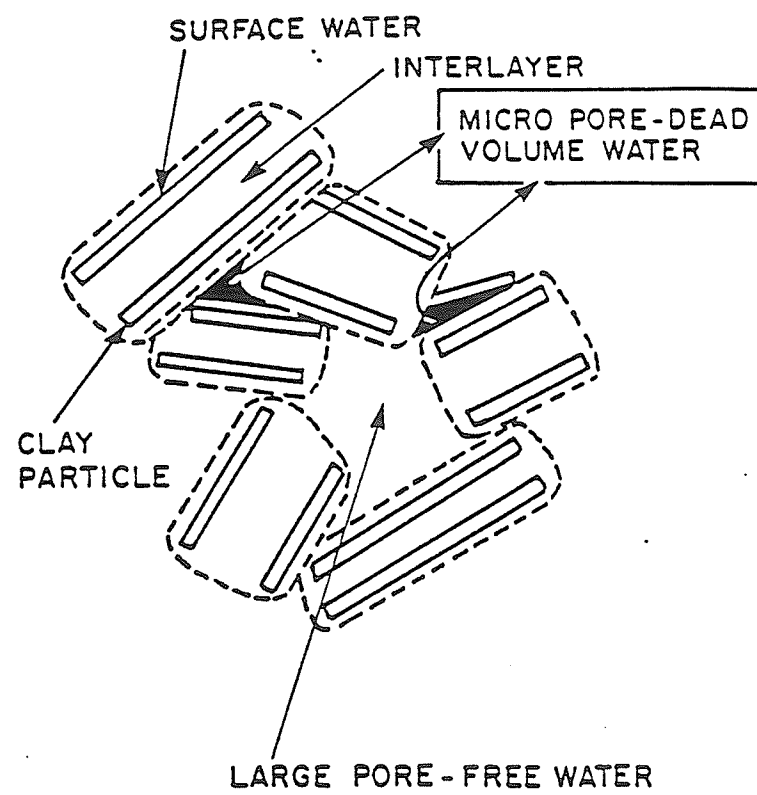


FIGURE 6.6 Schematic illustrating different types of water in clay
(after Baldi *et al.* 1991)

SUMMARY: TRIAXIAL CONSOLIDATION
CORRECT THERMAL EXPANSION; HIGH DENSITY

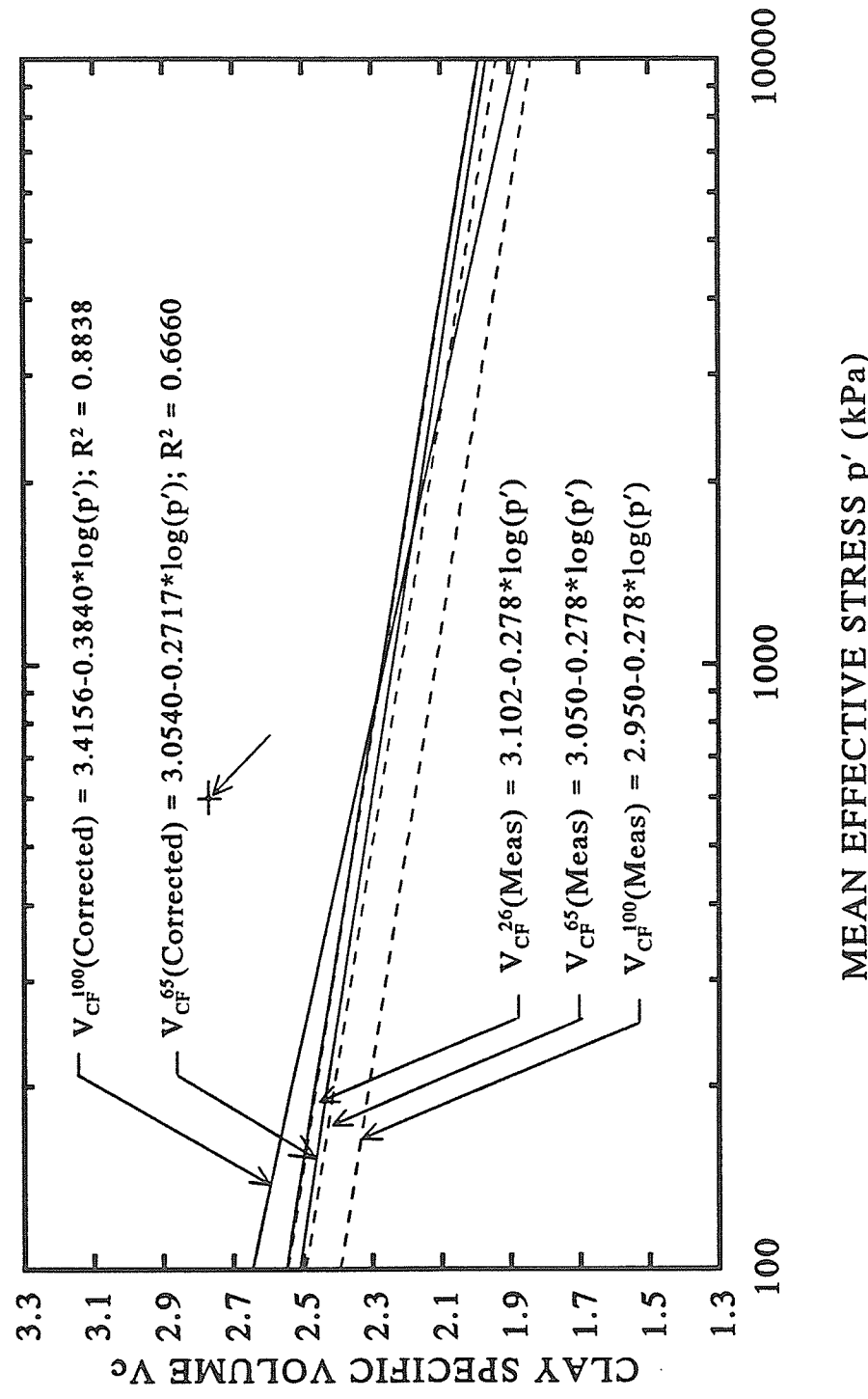


FIGURE 6.7 Back calculation of final specific volume at 26°C, V_{CF}^{26} , using measured final specific volumes at elevated temperatures, $V_{CF}^{65}[\text{meas}]$, and $V_{CF}^{100}[\text{meas}]$

SUMMARY: TRIAXIAL CONSOLIDATION
CORRECT THERMAL EXPANSION; HIGH DENSITY

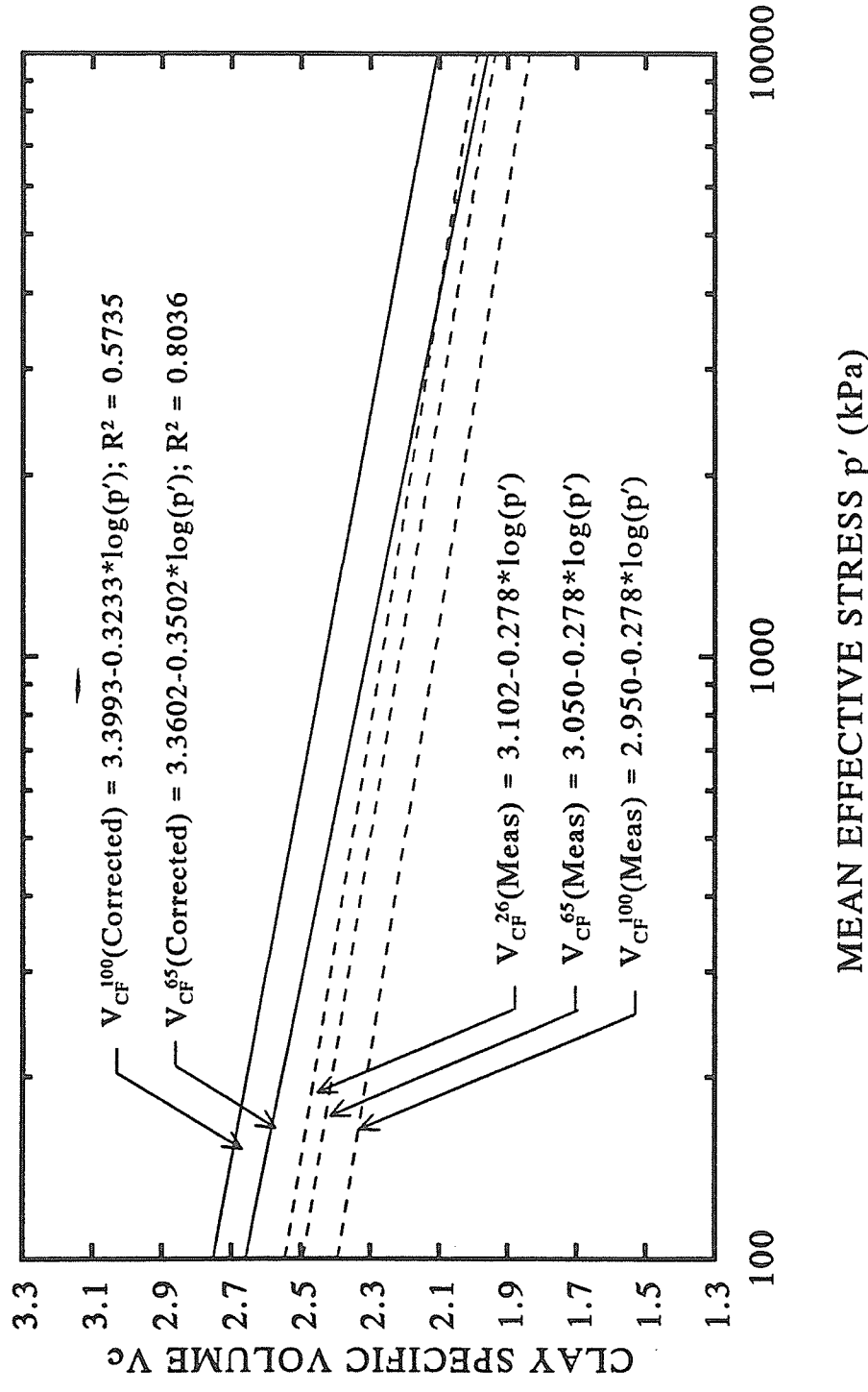


FIGURE 6.8 Forward calculation of final specific volume at 26°C, V_{cF}^{26} , using measured initial specific volume of buffer specimens, measured volume changes at elevated temperatures, and thermal expansion coefficients for bulk water.

Consolidation Summary

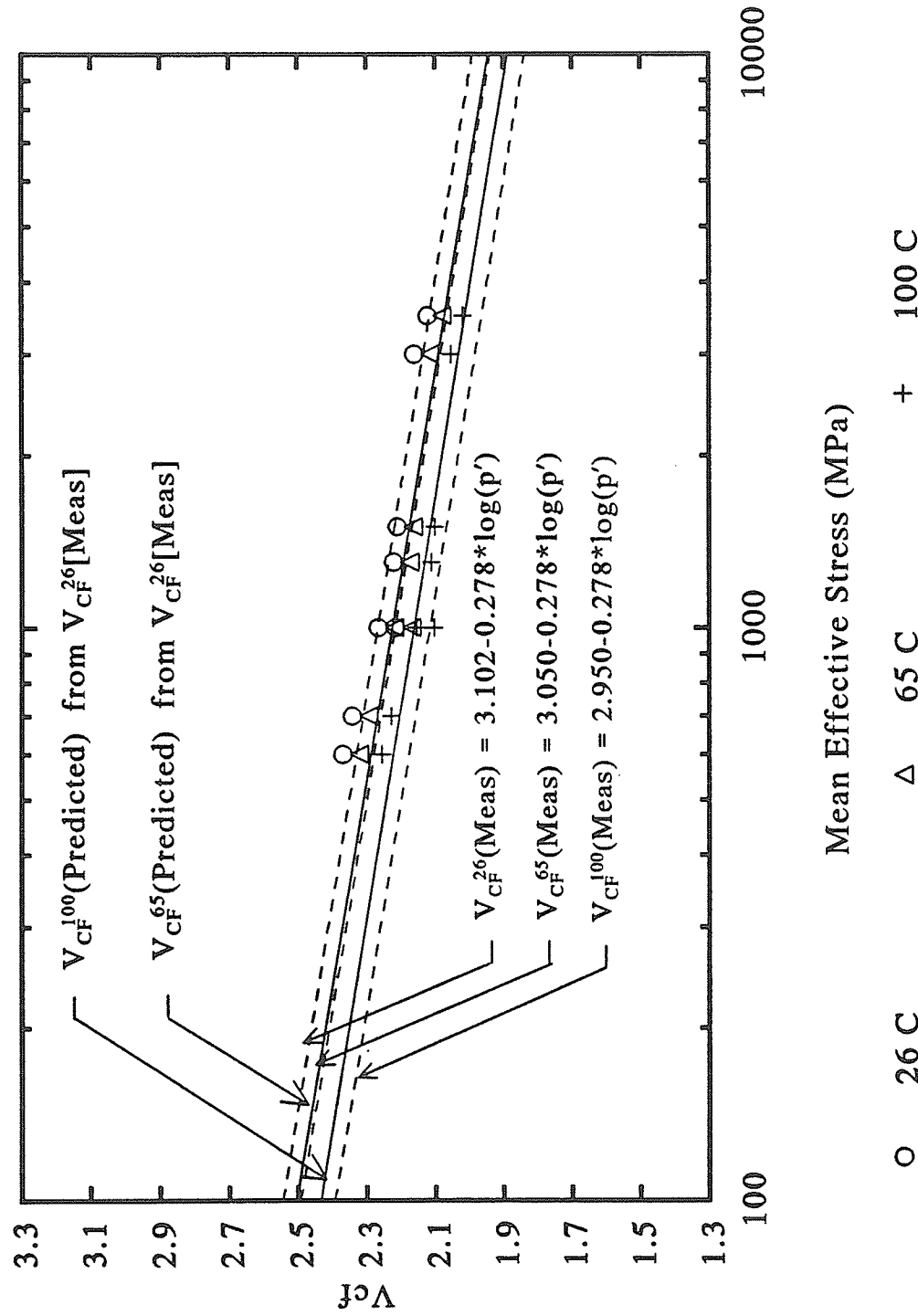


FIGURE 6.9 Prediction of final specific volume at elevated temperatures, $V_{CF}^{65}[\text{Predicted}]$ and $V_{CF}^{65}[\text{Measured}]$ using final specific volume measured at room temperature, $V_{CF}^{26}[\text{Meas}]$, and thermal expansion calculations for pore water and soil voids.

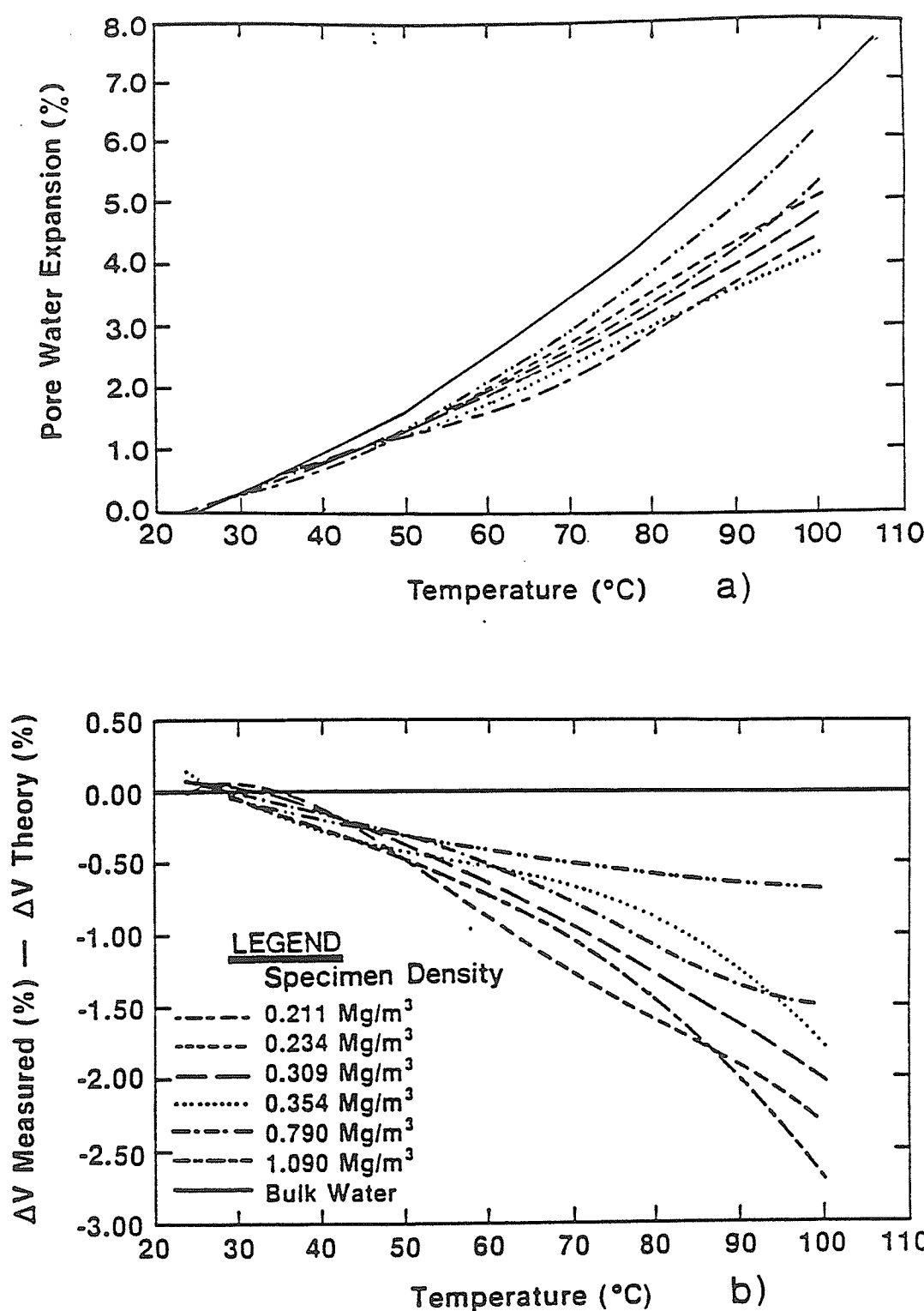


FIGURE 6.10 Data from thermal expansion tests on Na-bentonite showing: (a) percent expansion, and (b) difference between % expansion of porewater and % expansion of bulk water with temperature (after Baldi *et al* 1991)

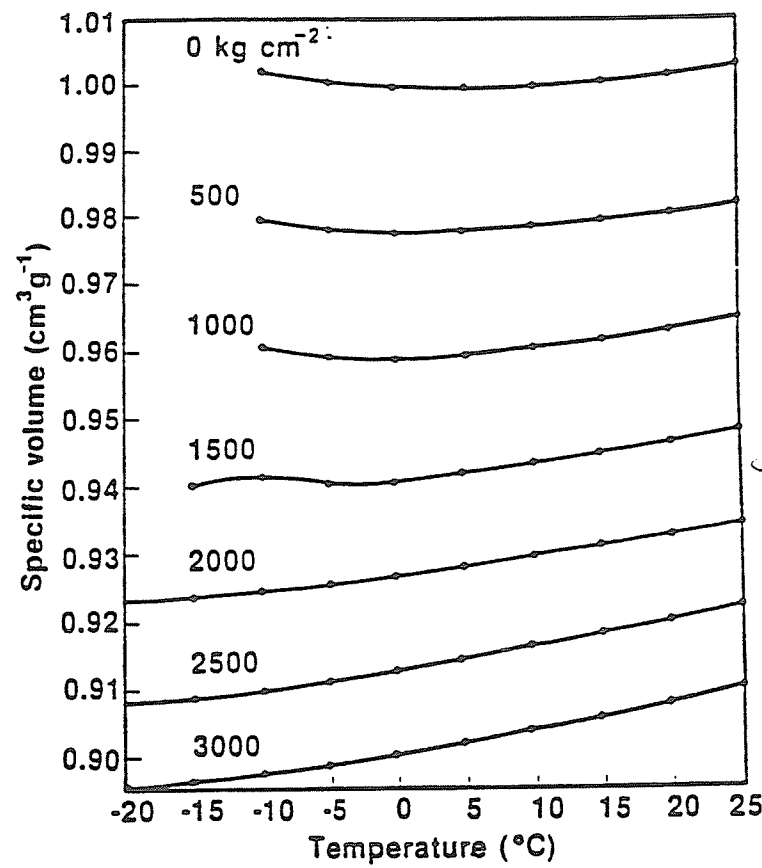


FIGURE 6.11 Effects of pressure on the specific volume of bulk water (after Eisenberg and Kauzmann 1969). Note: Specific volume of bulk water is defined as the reciprocal of density.

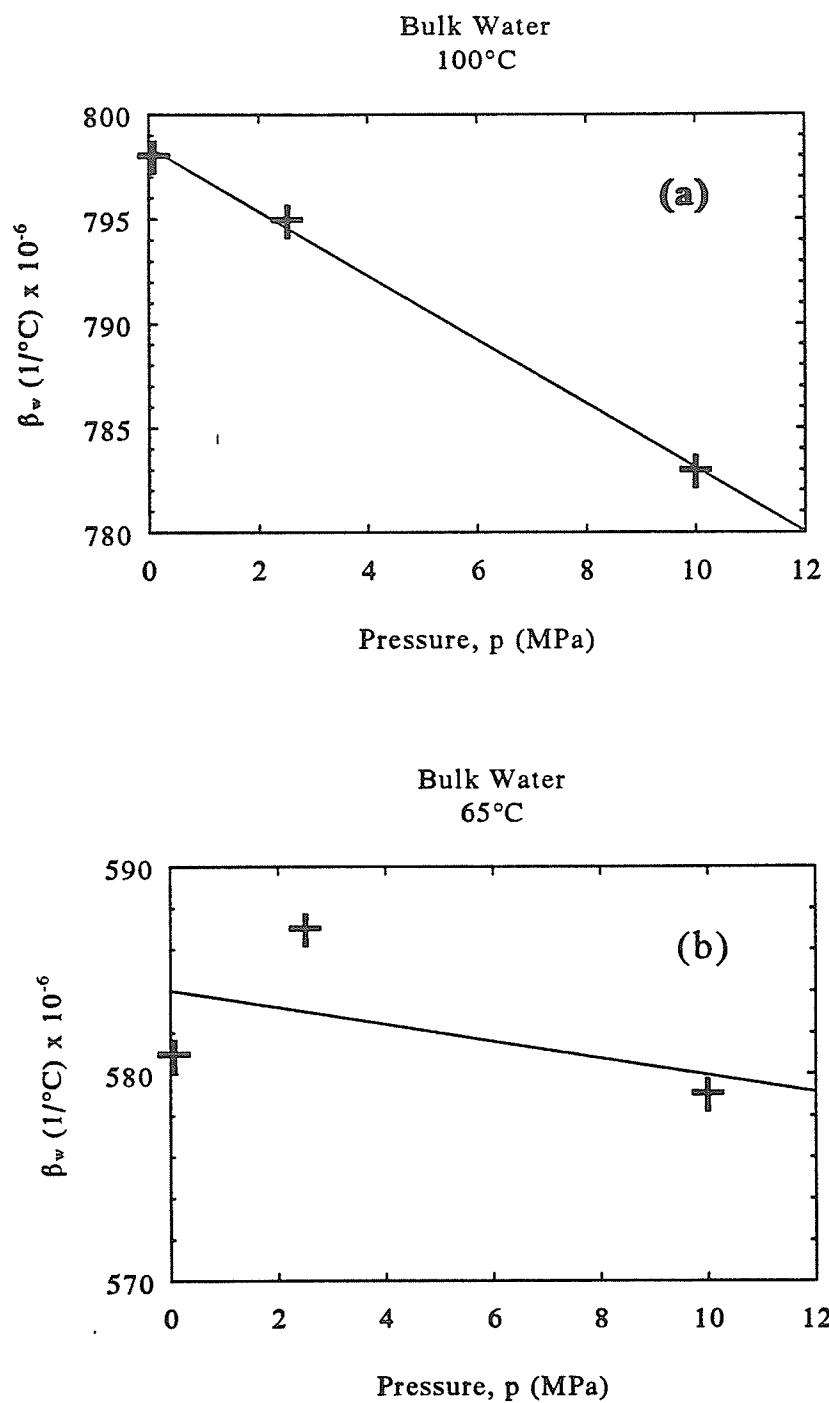


FIGURE 6.12 Pressure dependency of β_w at (a) 100°C; and (b) 65°C

Buffer Consolidation Volumetric Expansion Coefficient

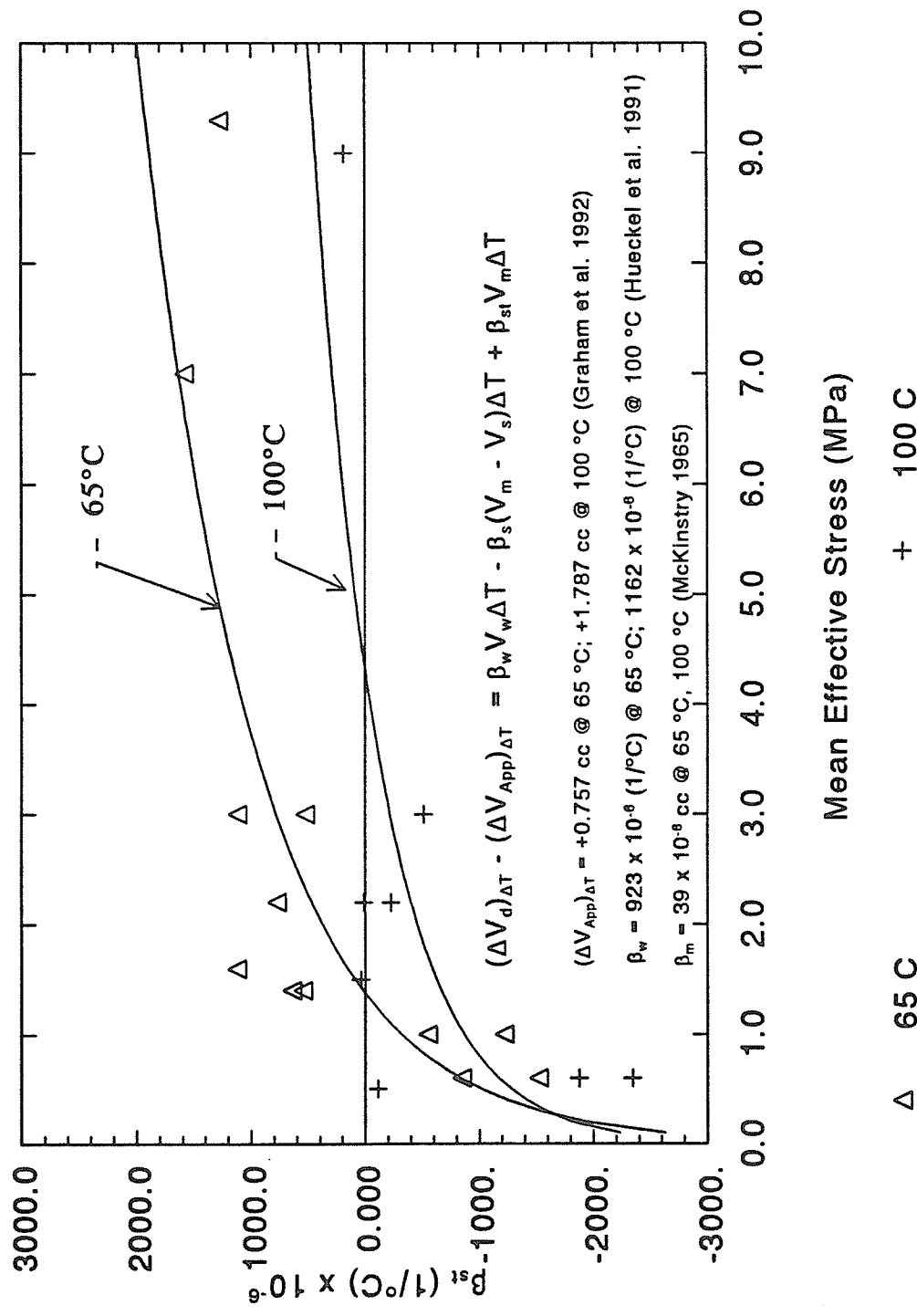


FIGURE 6.13 Coefficient of volume change for thermo-mechanically induced particle rearrangement (skeletal changes)

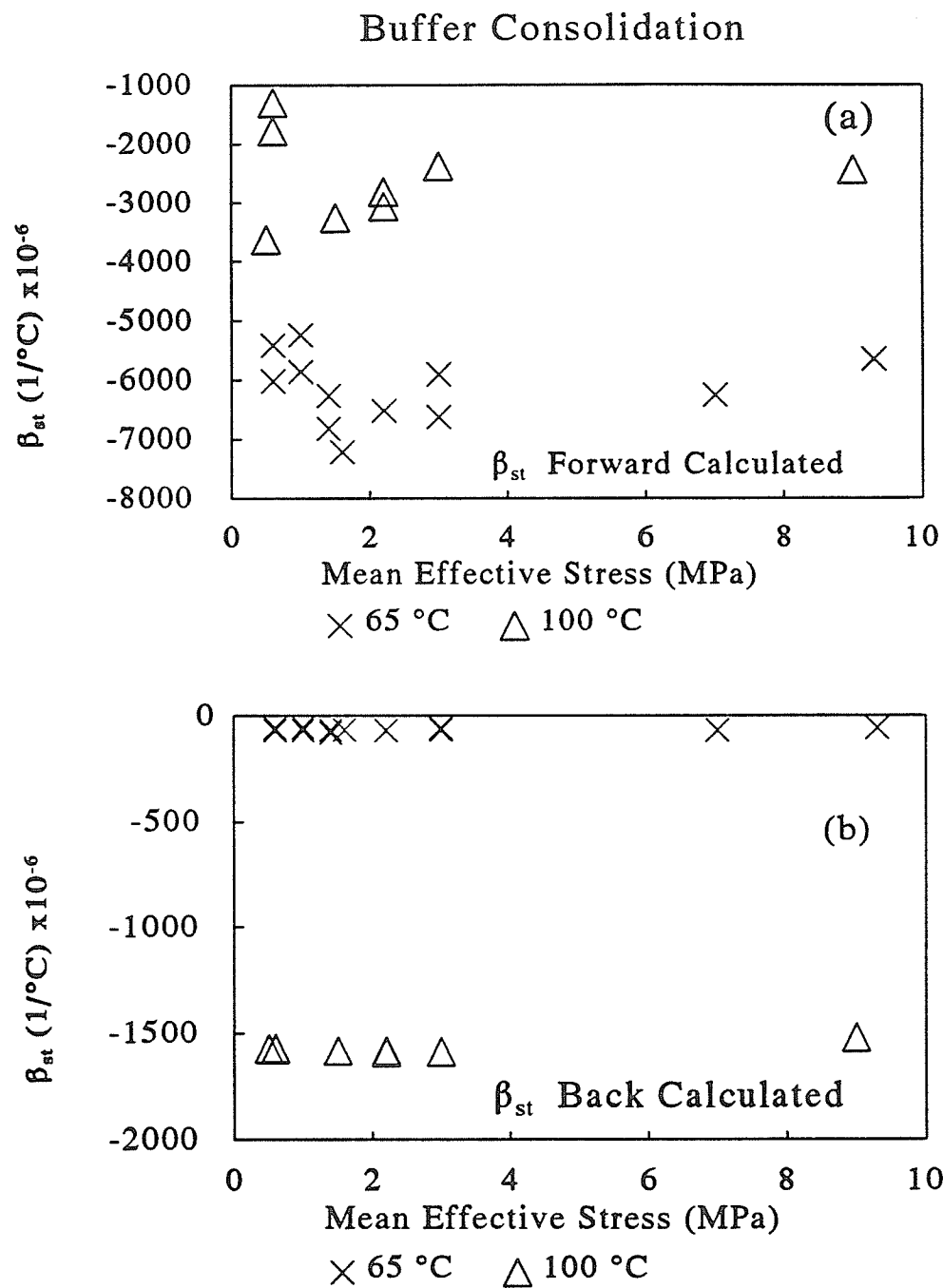
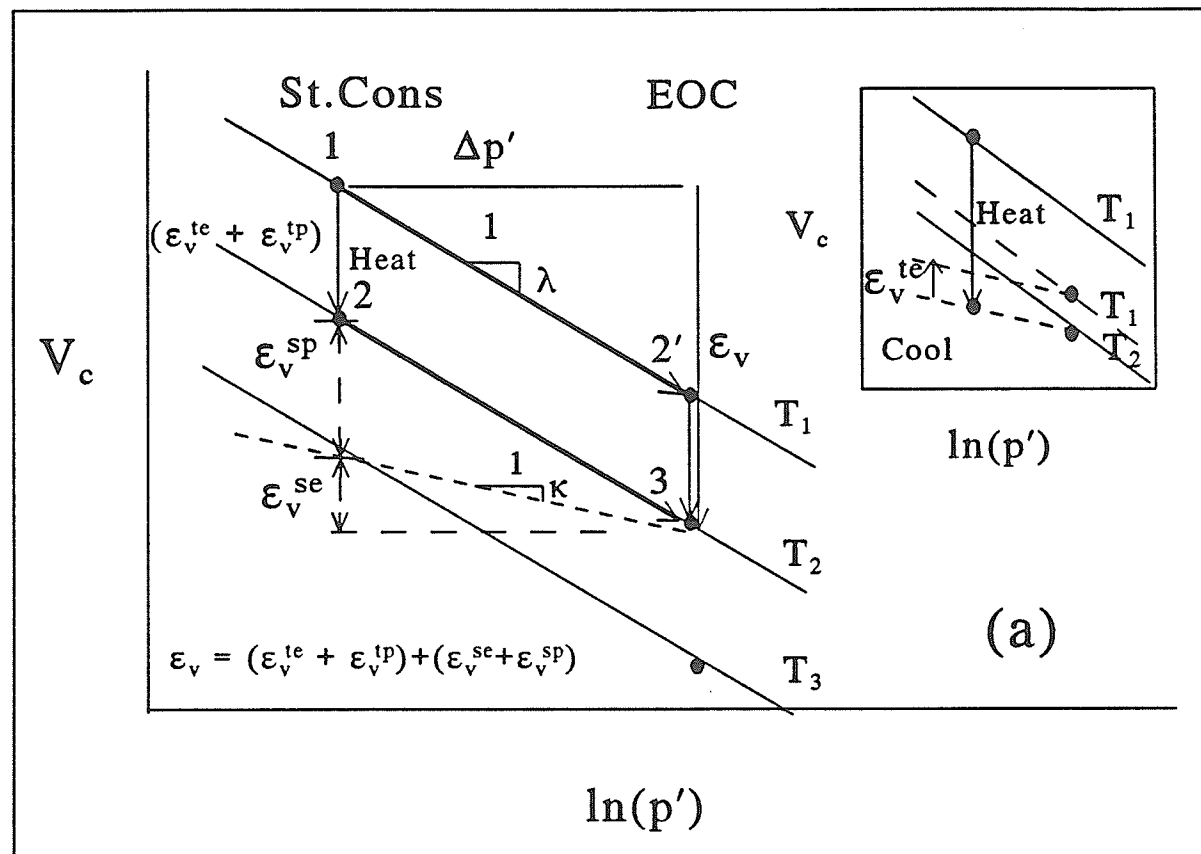


FIGURE 6.14 Calculation of β_{st} (a) using V_{co} , ε_v , β_w and β_s (Forward); (b) using V_{cf} , β_w and β_s (Backward)



(a)

FIGURE 6.15 Thermo-mechanical strains for buffer consolidation (path 1-2-3), Inset: Definition of thermo-elastic strain (from Heat-Cool cycle)

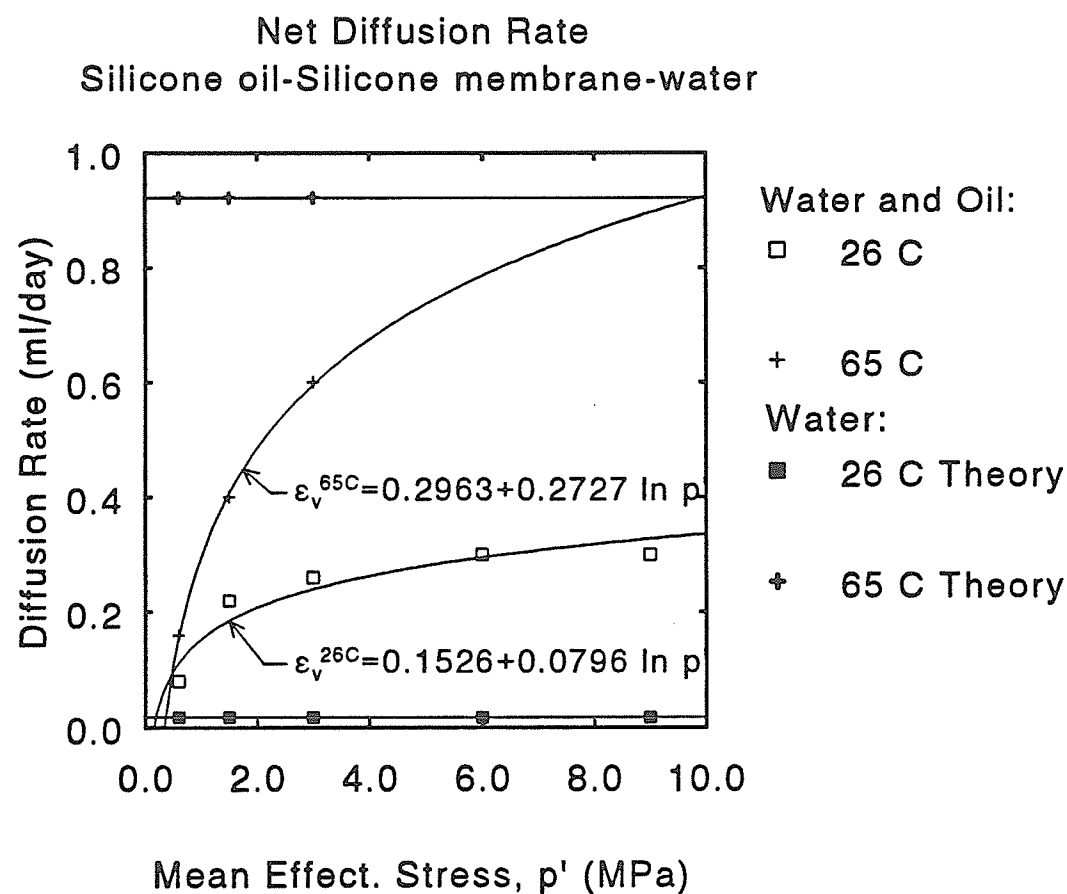


FIGURE 6.16 Comparison of measured and predicted diffusion rates across a silicone membrane.

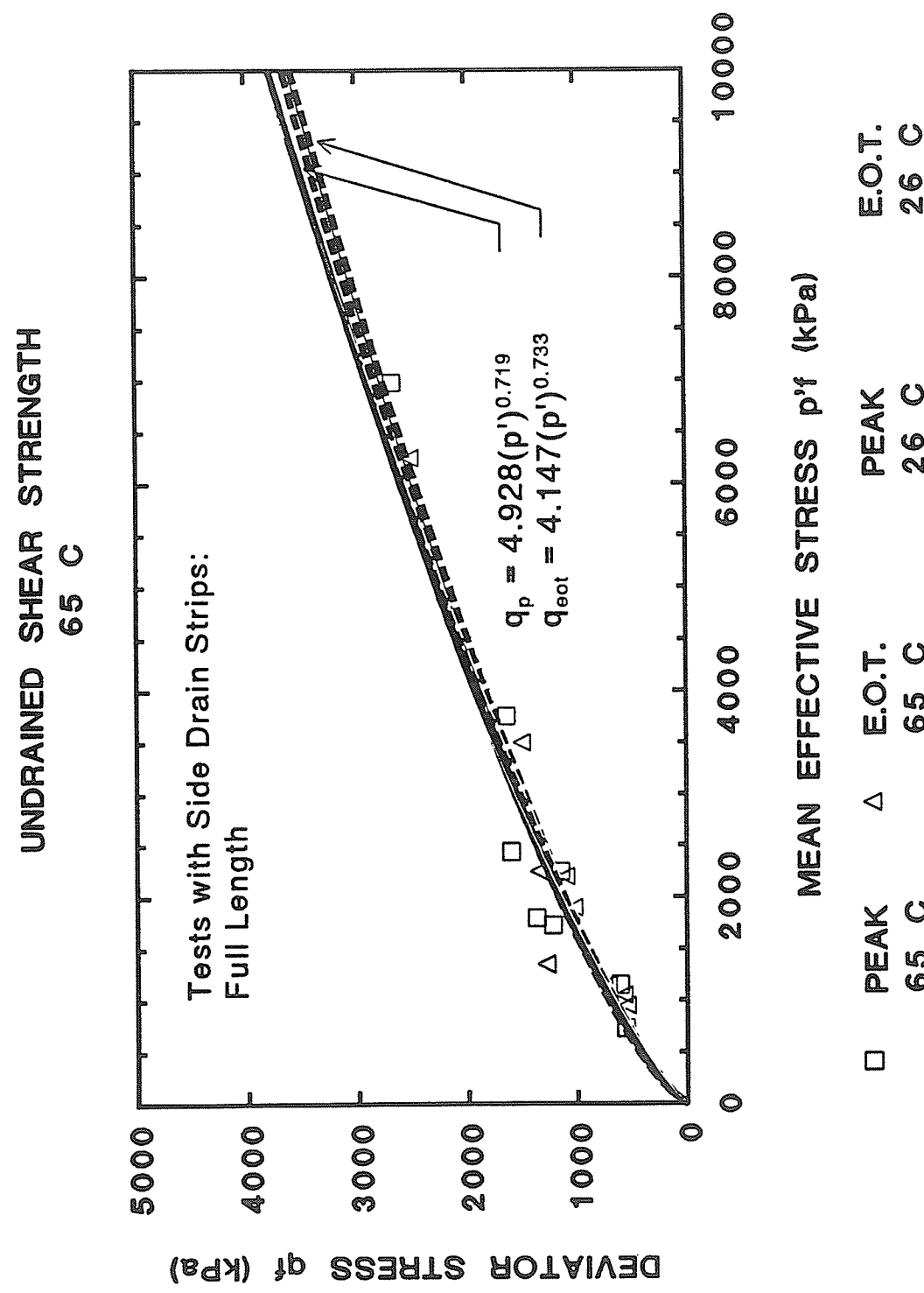


FIGURE 6.17 Regression of peak and end-of-test data where full length side drainage strips were used.

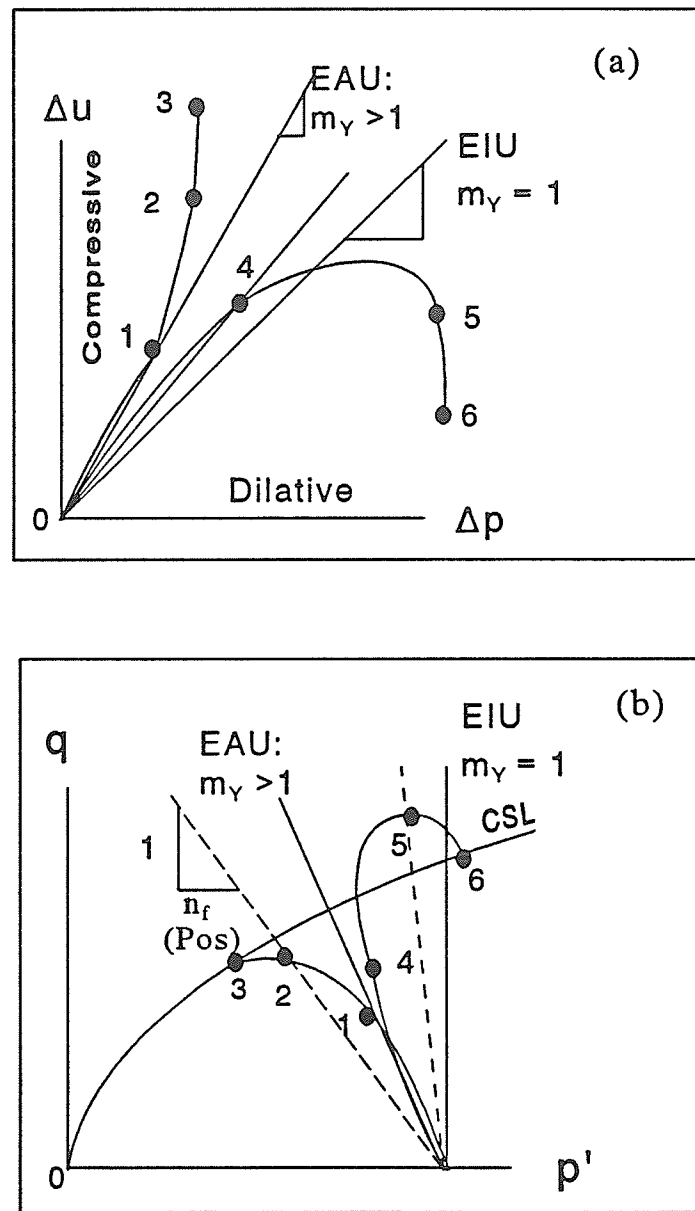


FIGURE 7.1 Definition of pore pressure parameters:

$$(a) m_Y = \Delta u / \Delta p$$

$$(b) n_f = -\Delta p' / \Delta q$$

m versus p'_{cons} High Density Specimens

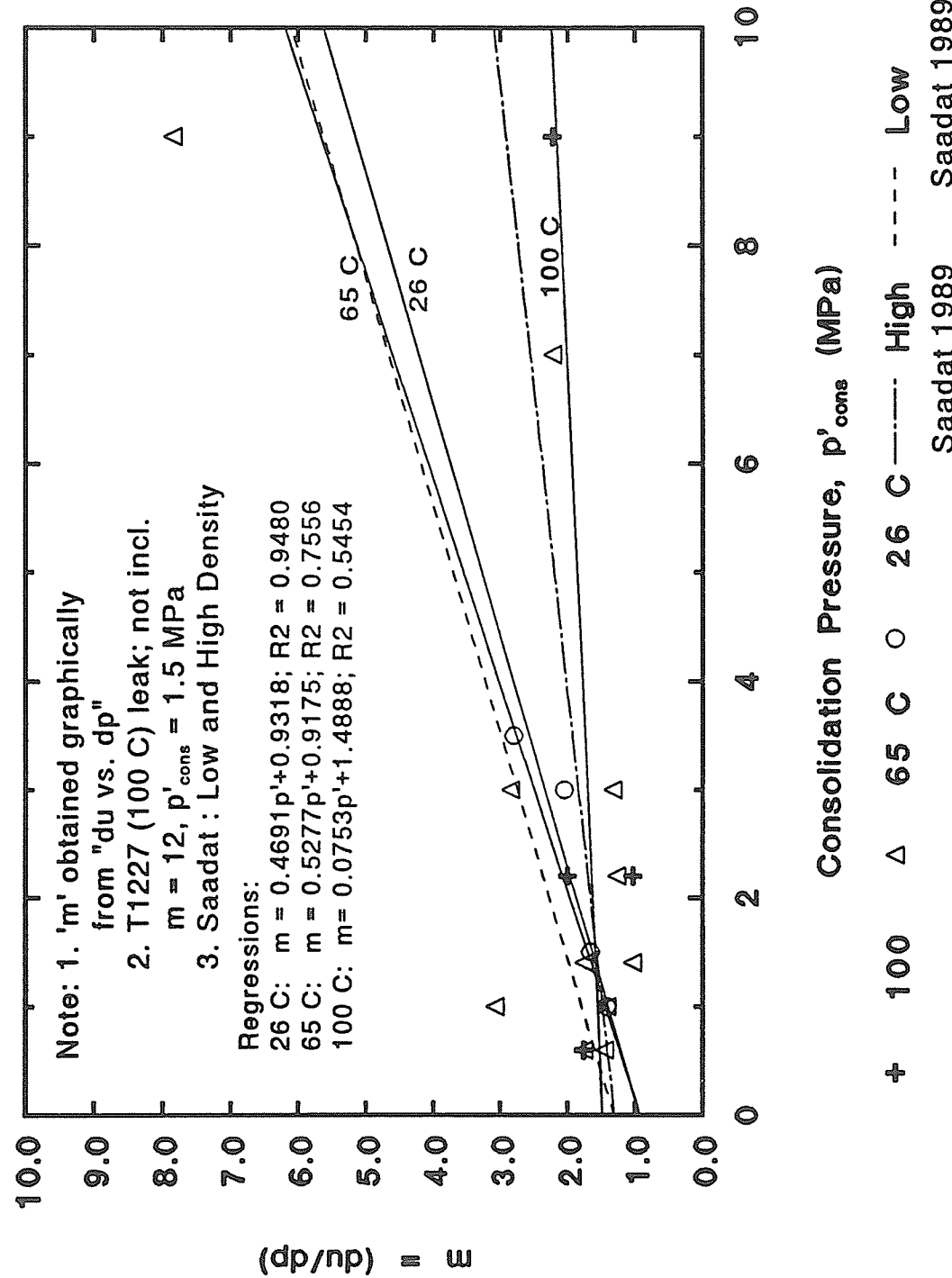


FIGURE 7.2 Pore pressure parameter m versus consolidation pressure p'_{cons} for Buffer at 26°C, 65°C, and 100°C.

m versus ε_v

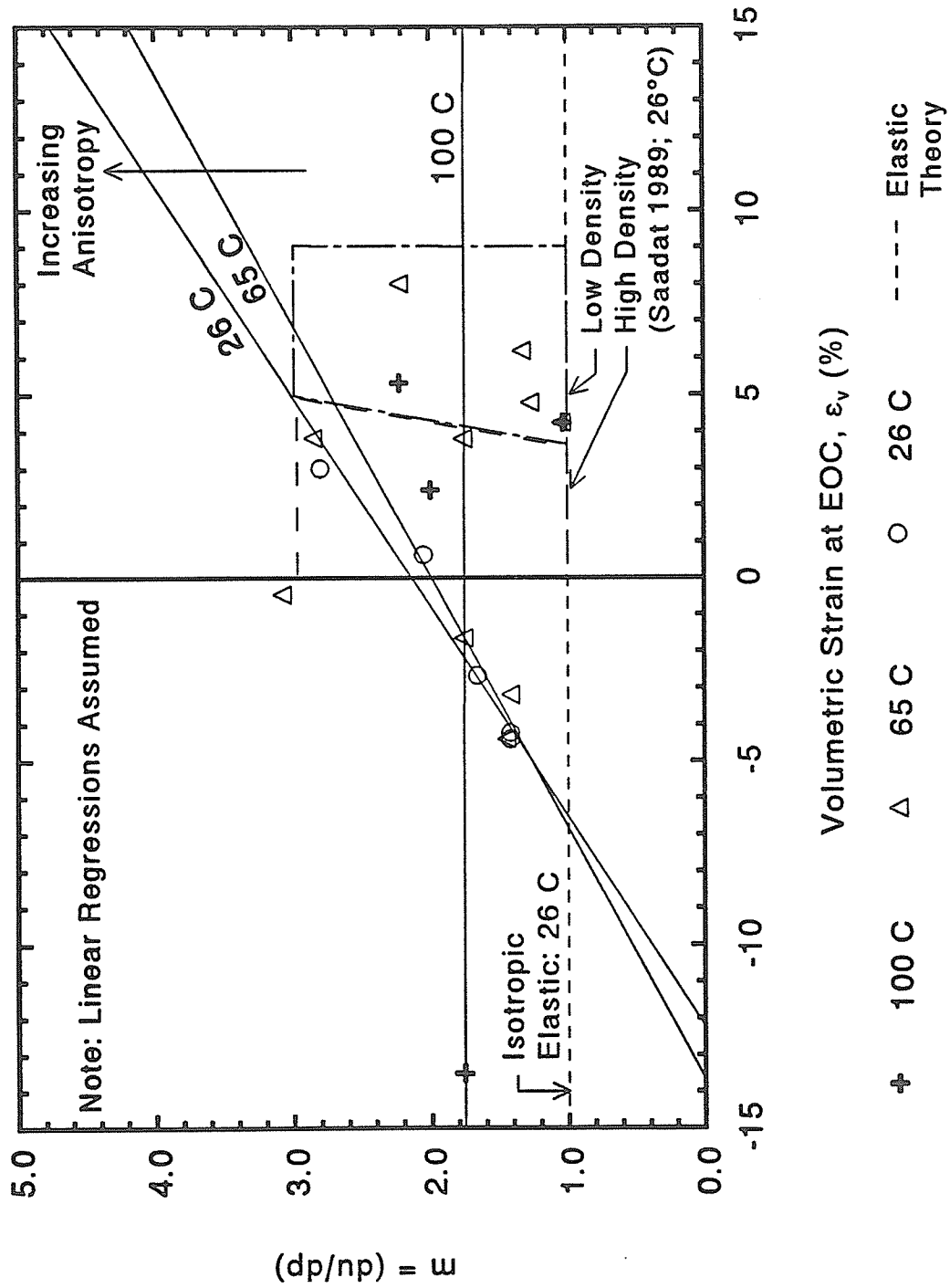


FIGURE 7.3 Pore pressure parameter m versus volumetric strain, ε_v , for Buffer at 26°C, 65°C, and 100°C.

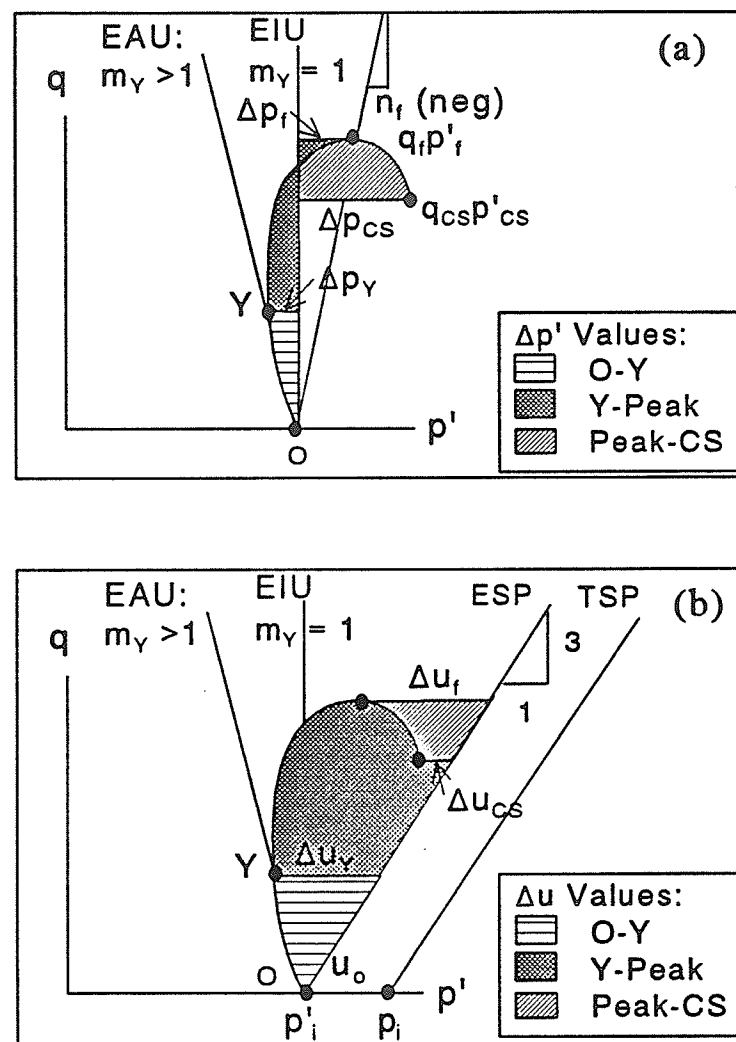


FIGURE 7.4 Stress changes in a heavily overconsolidated (H-OC) specimen:
 (a) $\Delta p'$ values
 (b) Δu values

n_y versus p'_{cons}
High Density Specimens

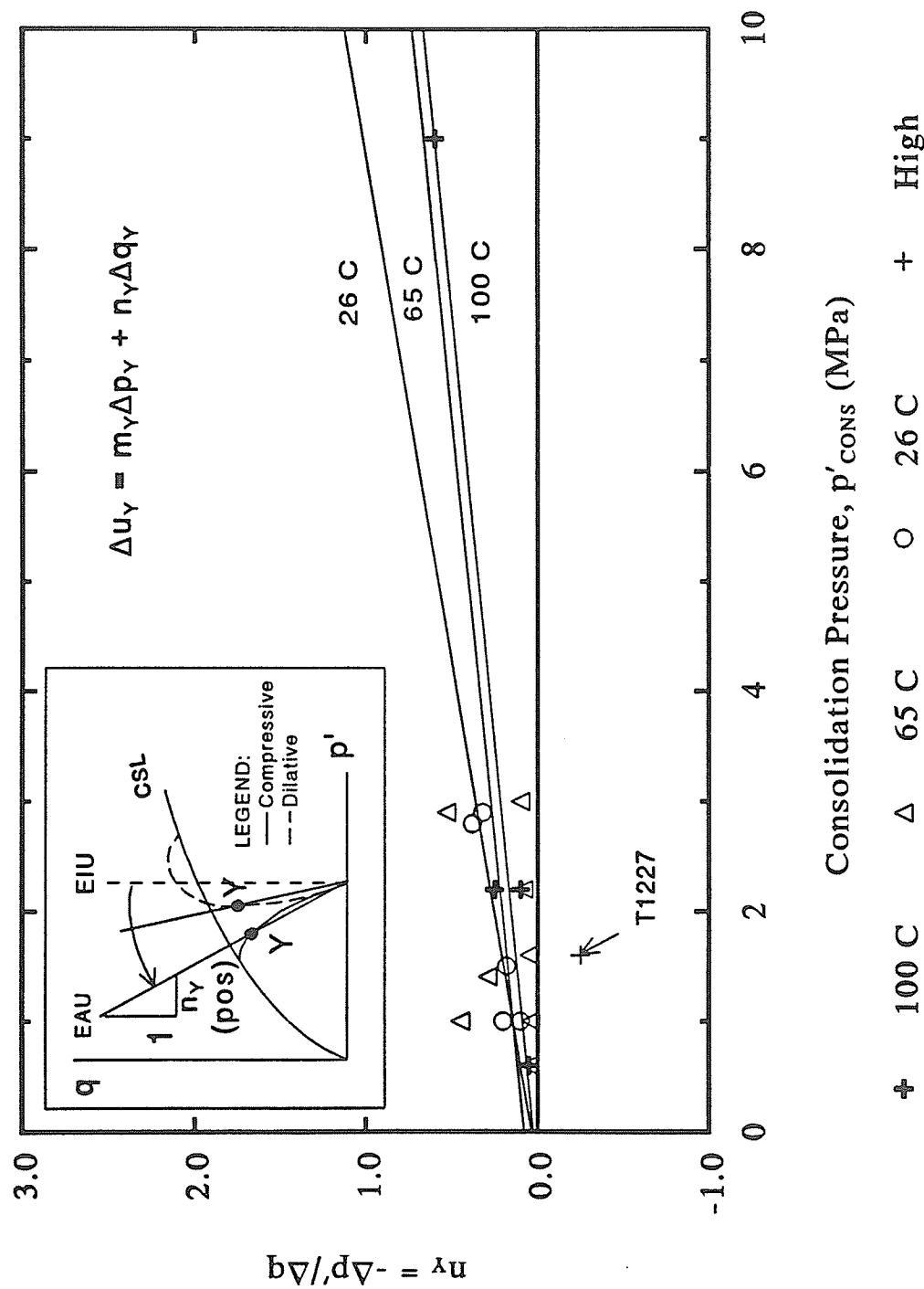


FIGURE 7.5 Pore pressure parameter ' n_y ' versus consolidation pressure p'_{cons} for
Buffer at 26°C, 65°C, and 100°C.

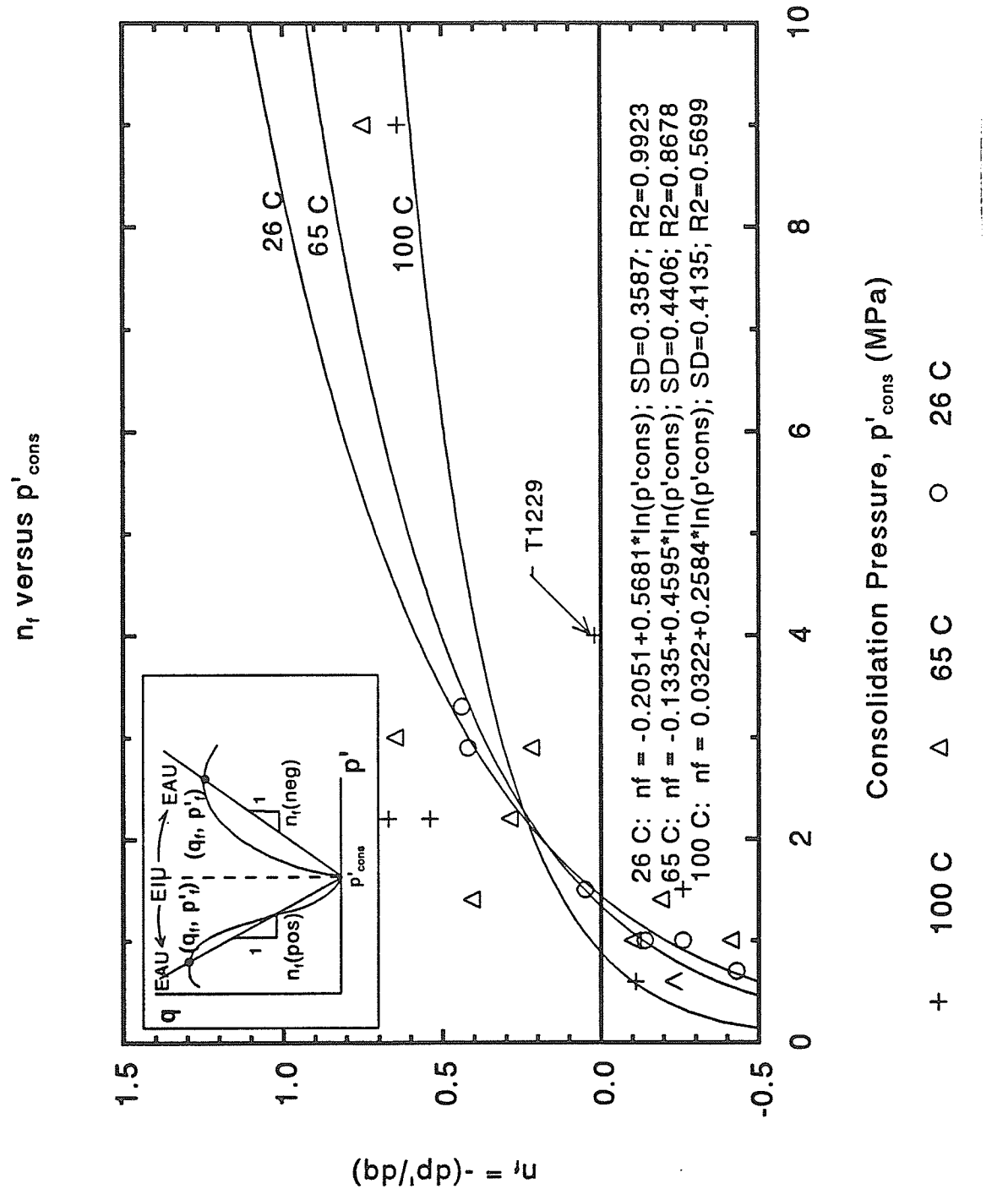


FIGURE 7.6 Pore pressure parameter ' n_f ' versus consolidation pressure p'_{cons} for Buffer at 26°C, 65°C, and 100°C.

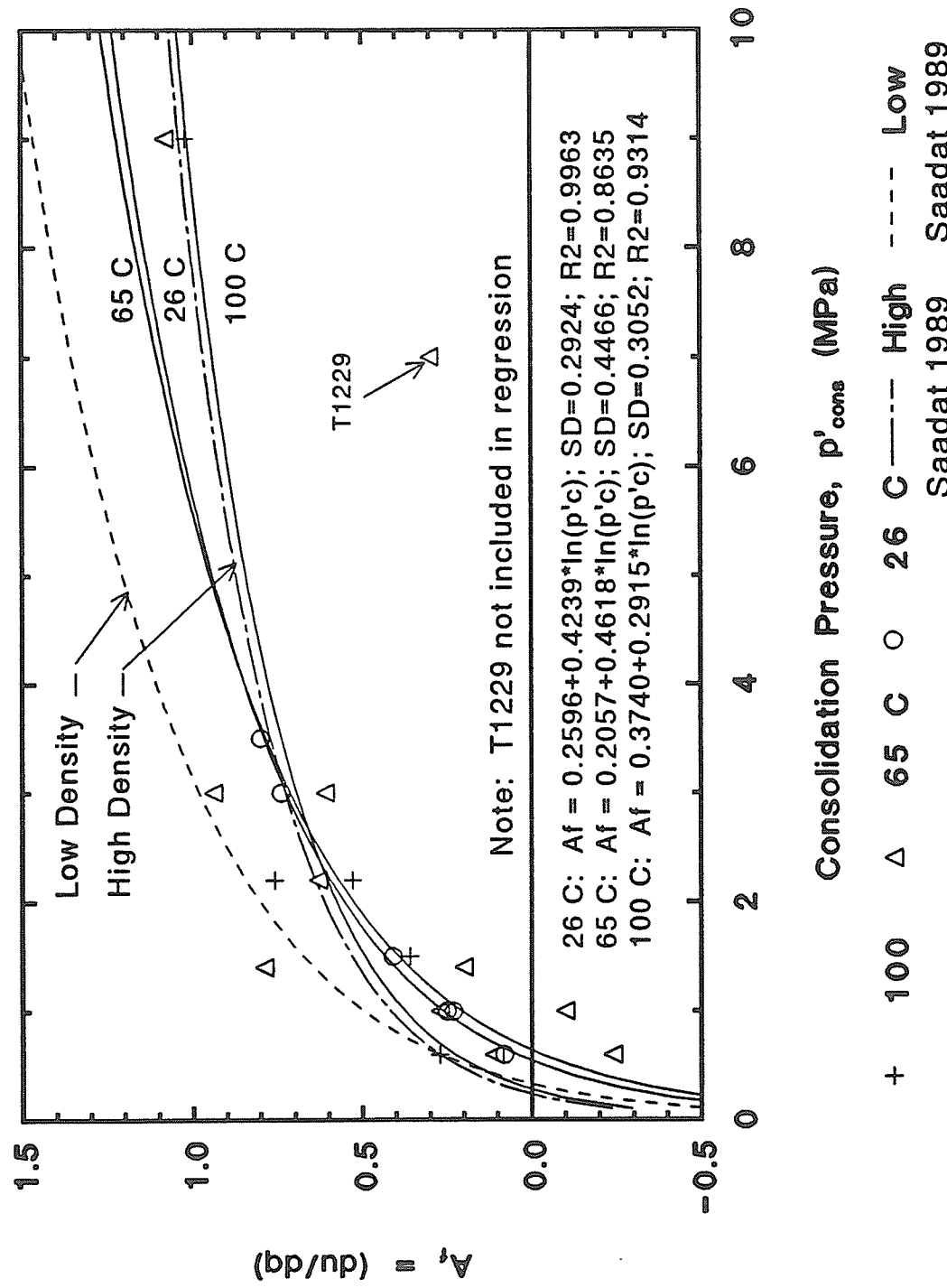
A_f versus p'_cons 

FIGURE 7.7 Pore pressure parameter ' A_f ' versus consolidation pressure p'_Cons for Buffer at 26°C, 65°C, and 100°C.

A_f versus ϵ_v

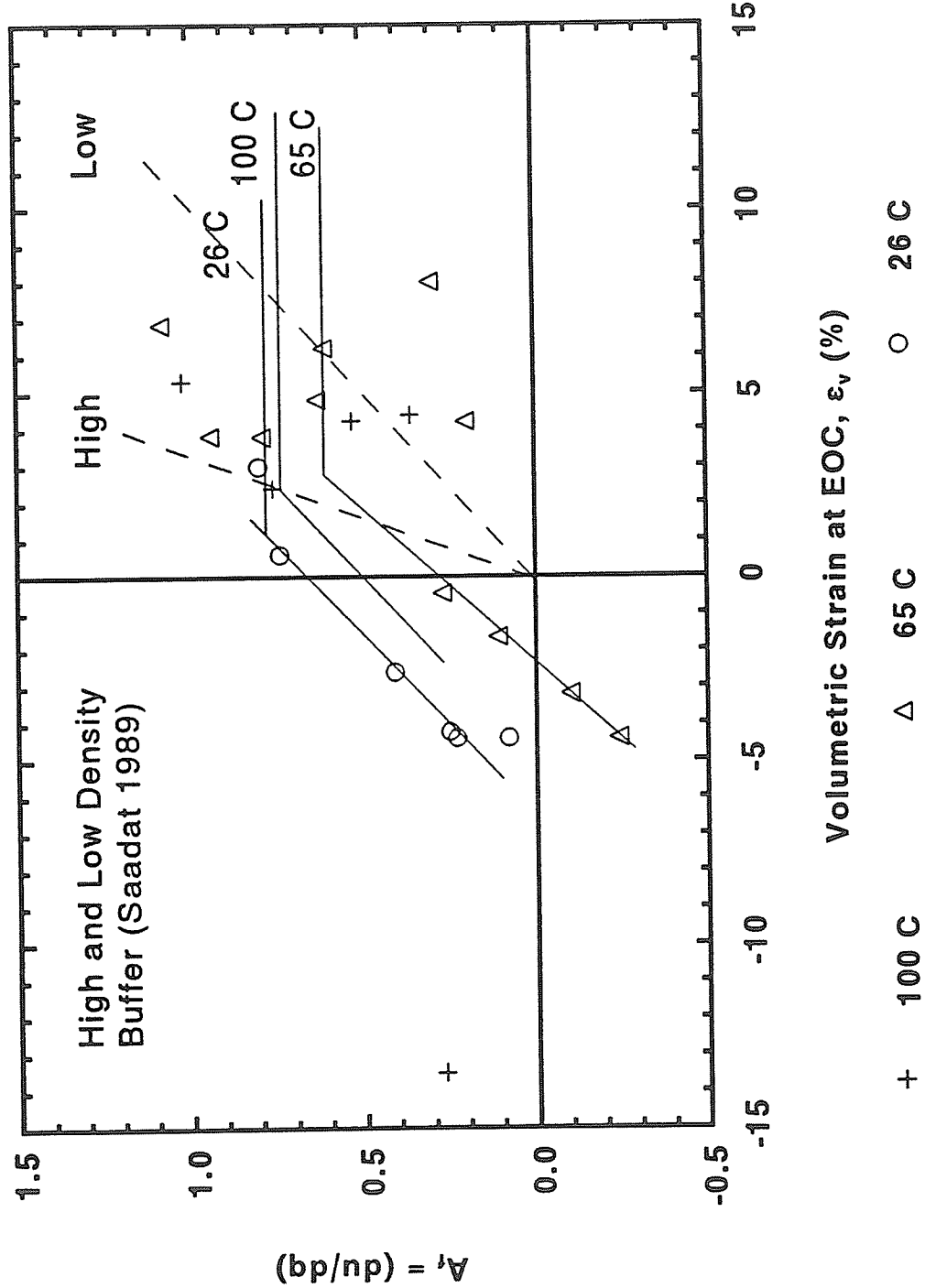


FIGURE 7.8 Pore pressure parameter ' A_f ' versus volumetric strain, ϵ_v , for Buffer at 26°C, 65°C, and 100°C.

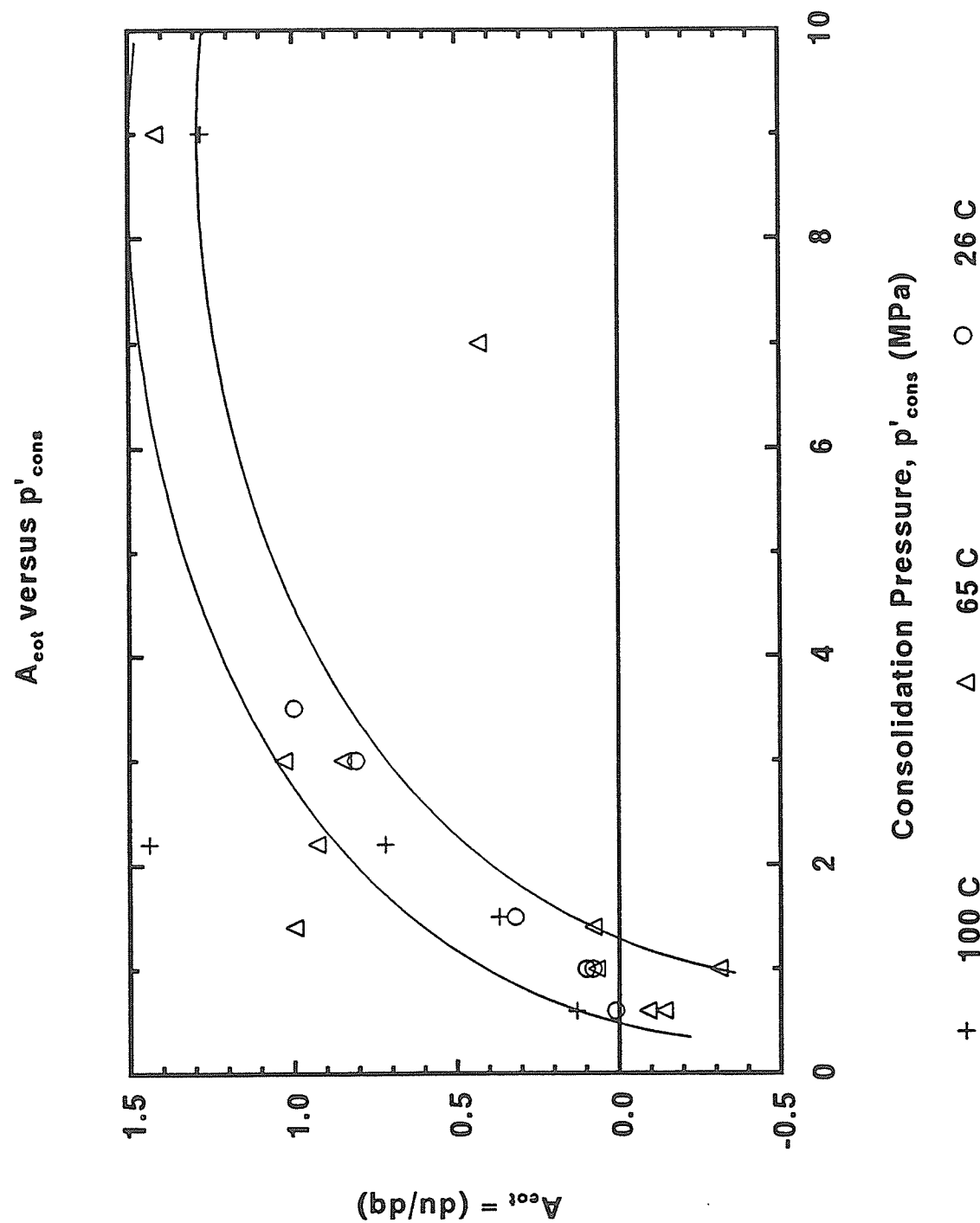


FIGURE 7.9 Pore pressure parameter ' A_{EOT} ' versus consolidation pressure p'_{cons} for Buffer at 26°C, 65°C, and 100°C.

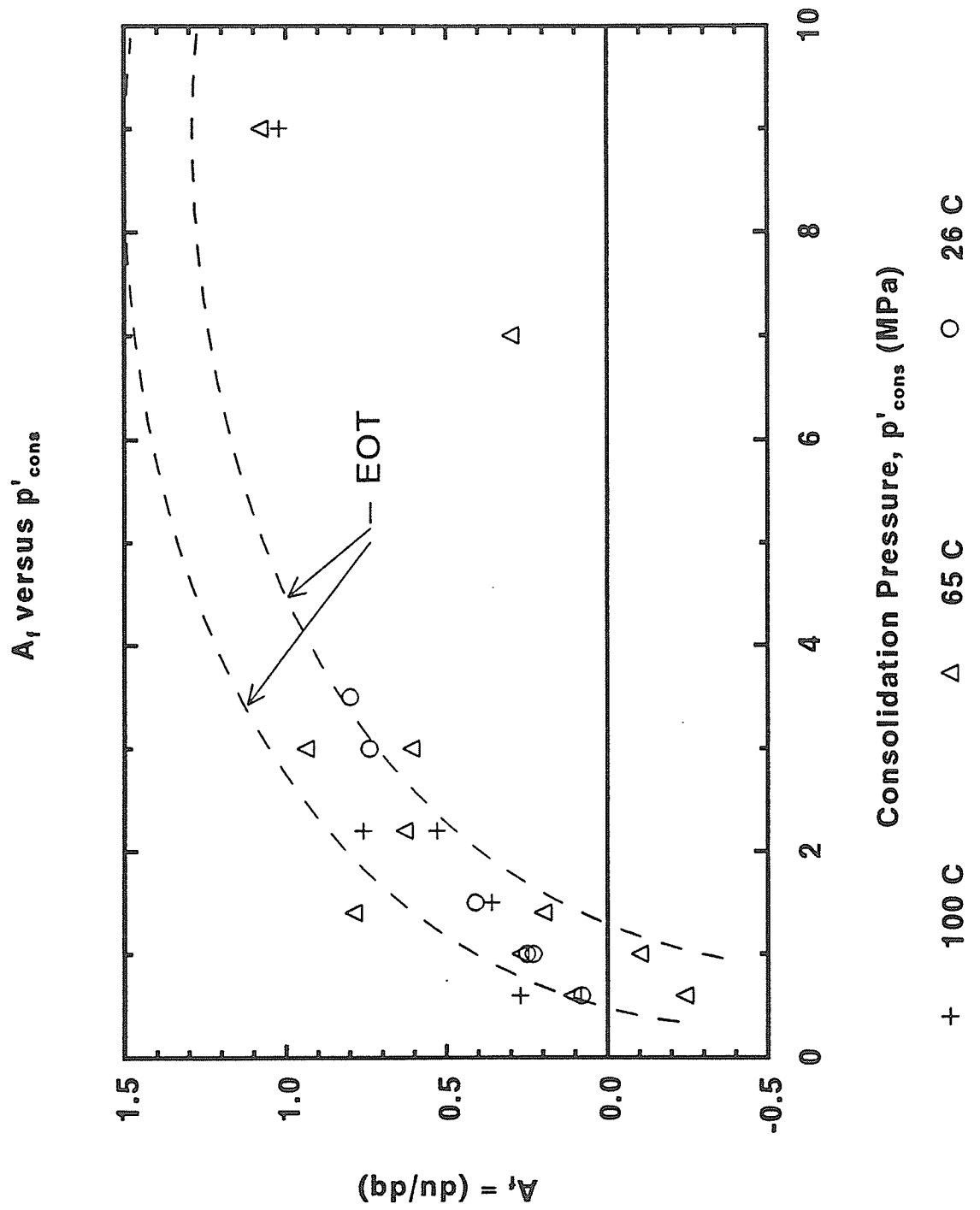


FIGURE 7.10 Comparison of pore pressure parameters A_f and A_{EOT}

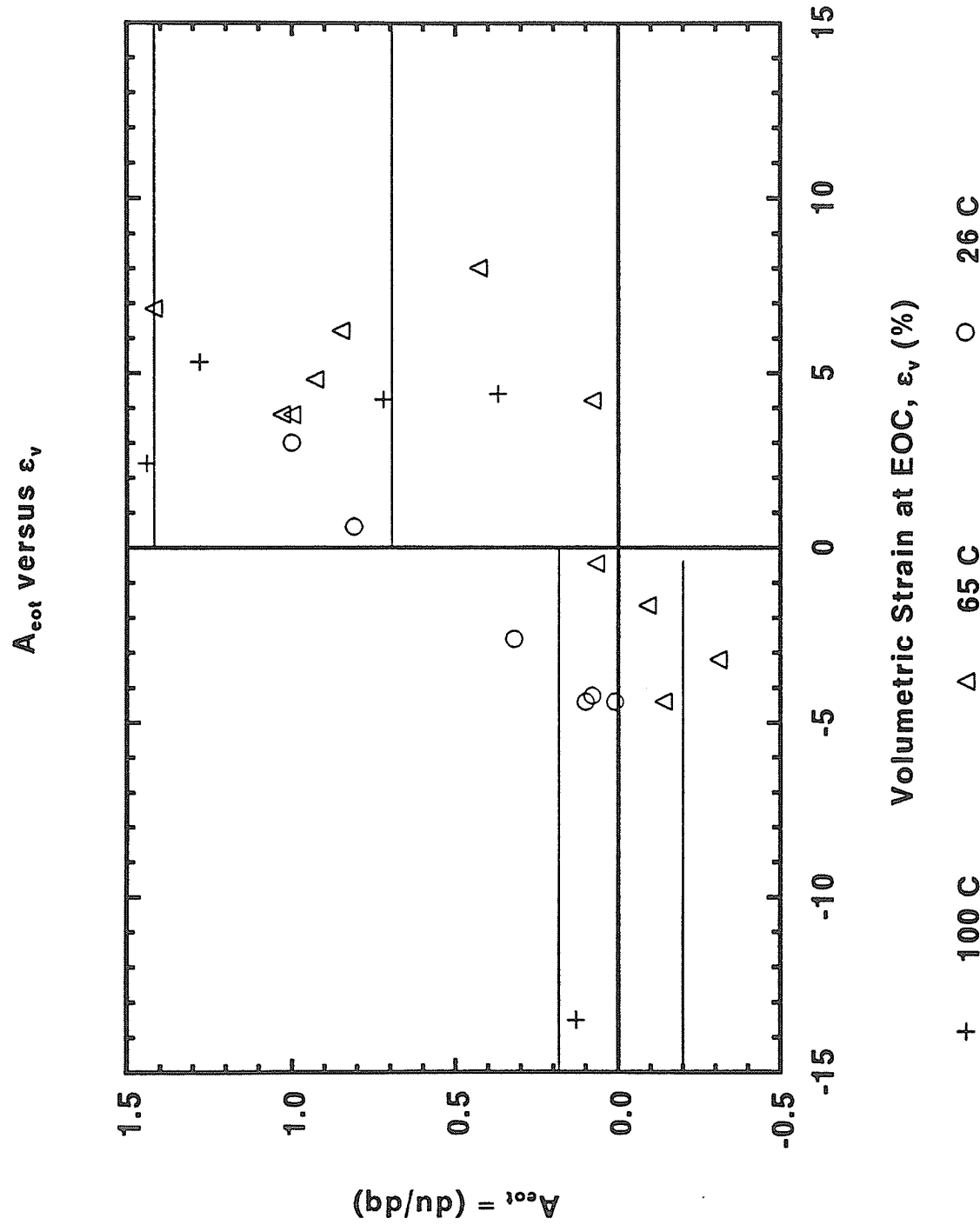


FIGURE 7.11 Pore pressure parameter ' A_{eot} ' versus volumetric strain, ϵ_v , for Buffer at 26°C, 65°C, and 100°C.

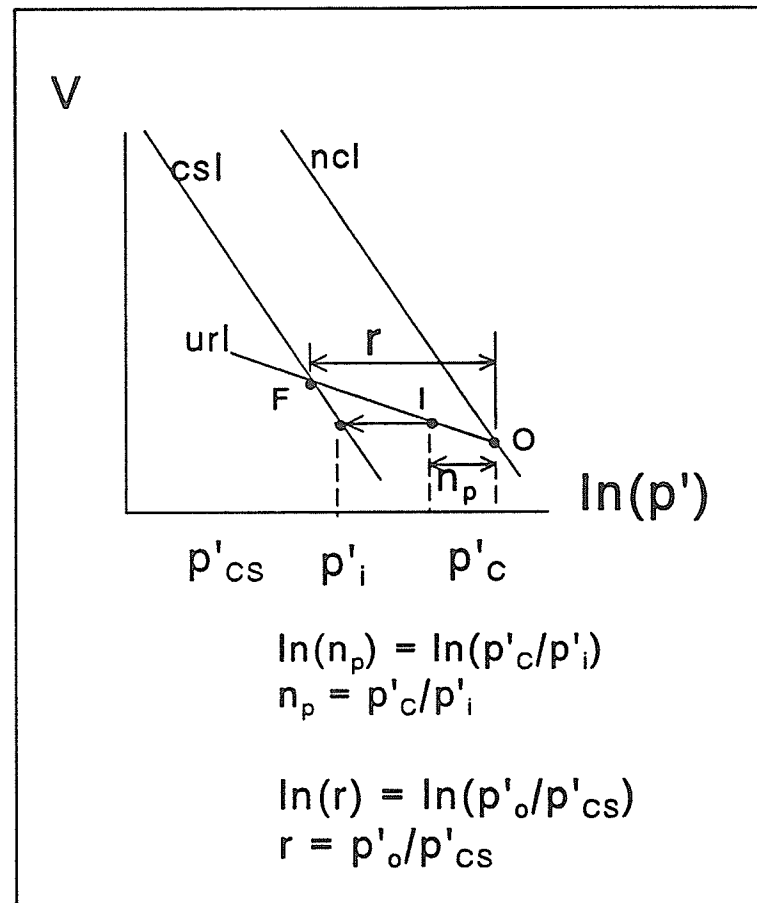


FIGURE 7.12 Definition of isotropic overconsolidation ratio ' n_p ' and parameter ' r '

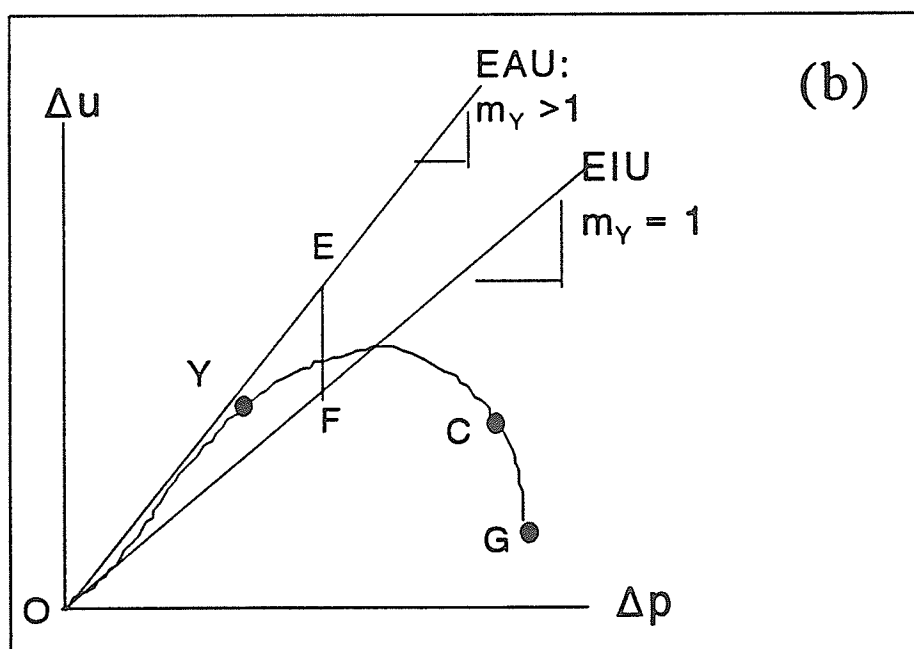
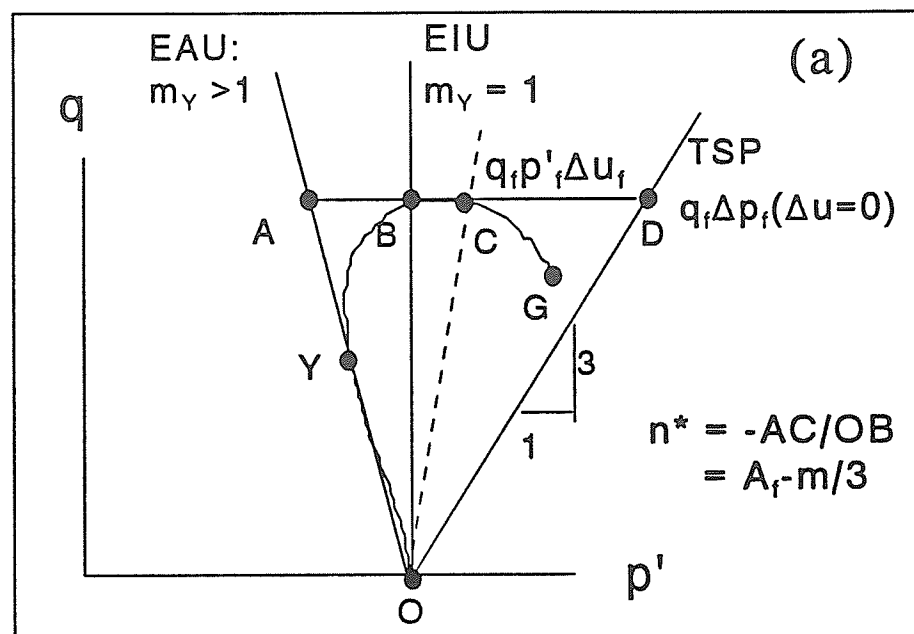


FIGURE 7.13: Definition of pore pressure parameter $n^* = A_f \cdot m/3$:
 (a) referenced to line AO in $q-p'$ space; and
 (b) referenced to line $m=1$ in $\Delta u-\Delta p$ space

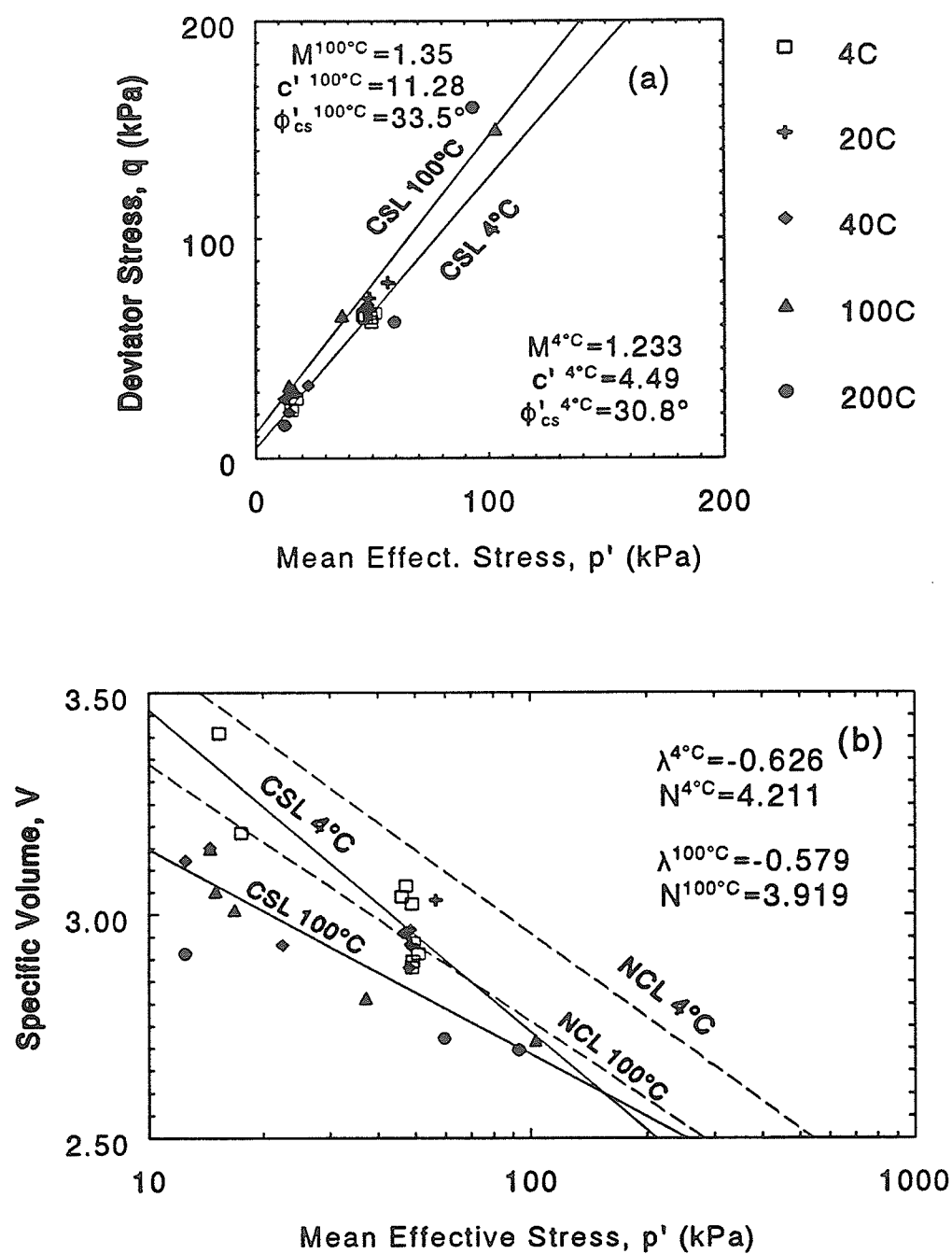


FIGURE 7.14 Critical state behavior of pacific illite at elevated temperature:

(a) in the q - p' effective stress plane;
(b) in the V -log(p') compression plane
(After Green 1984)

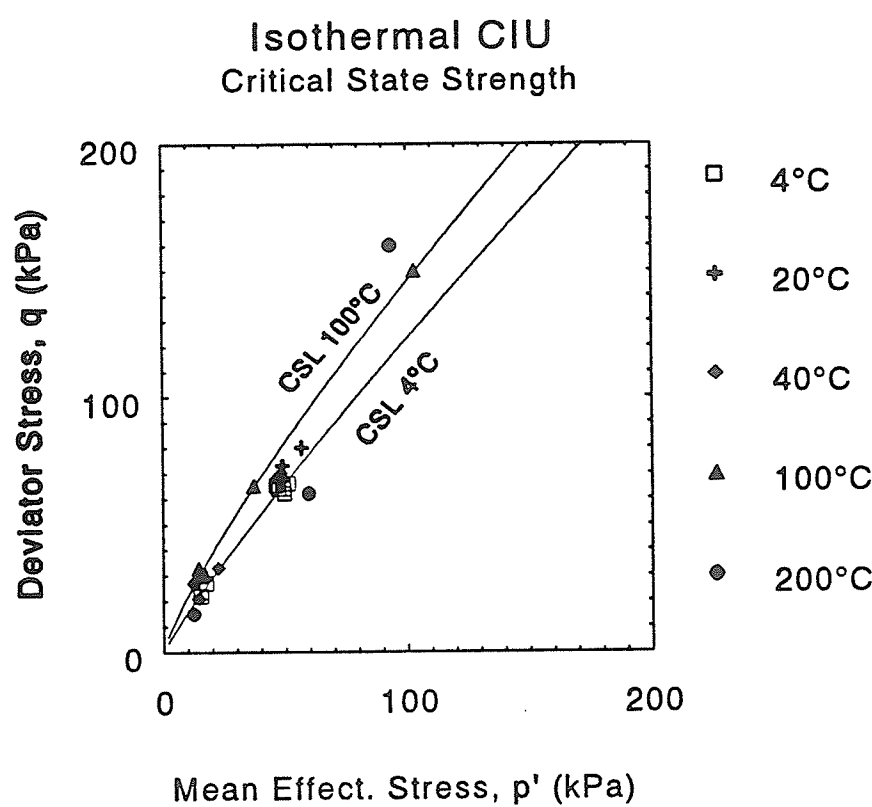
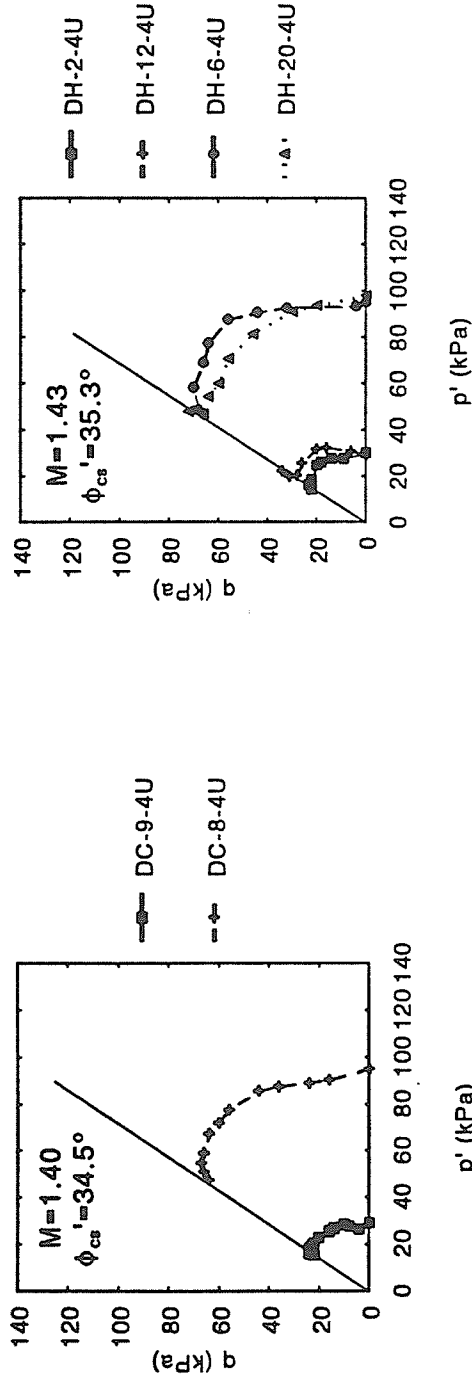


FIGURE 7.15 Power law fit to critical state data for pacific illite
(After Green 1984)

T = 4°C



T = 100°C

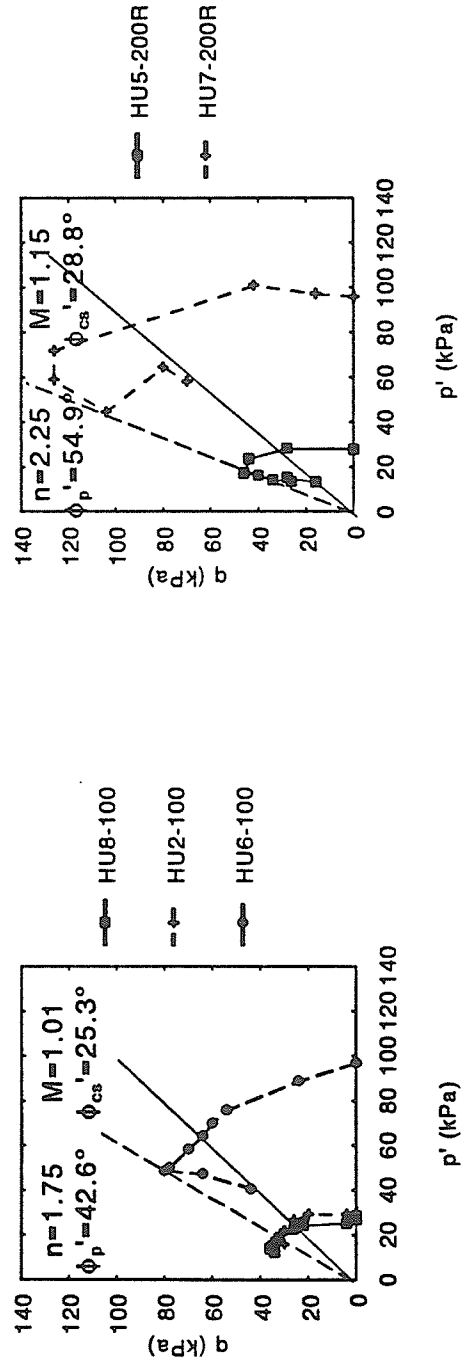


FIGURE 7.16 Stress paths of CIU(TXC) tests on pacific illite at 4°C , 40°C , 100°C , and 200°C (After Green 1984)

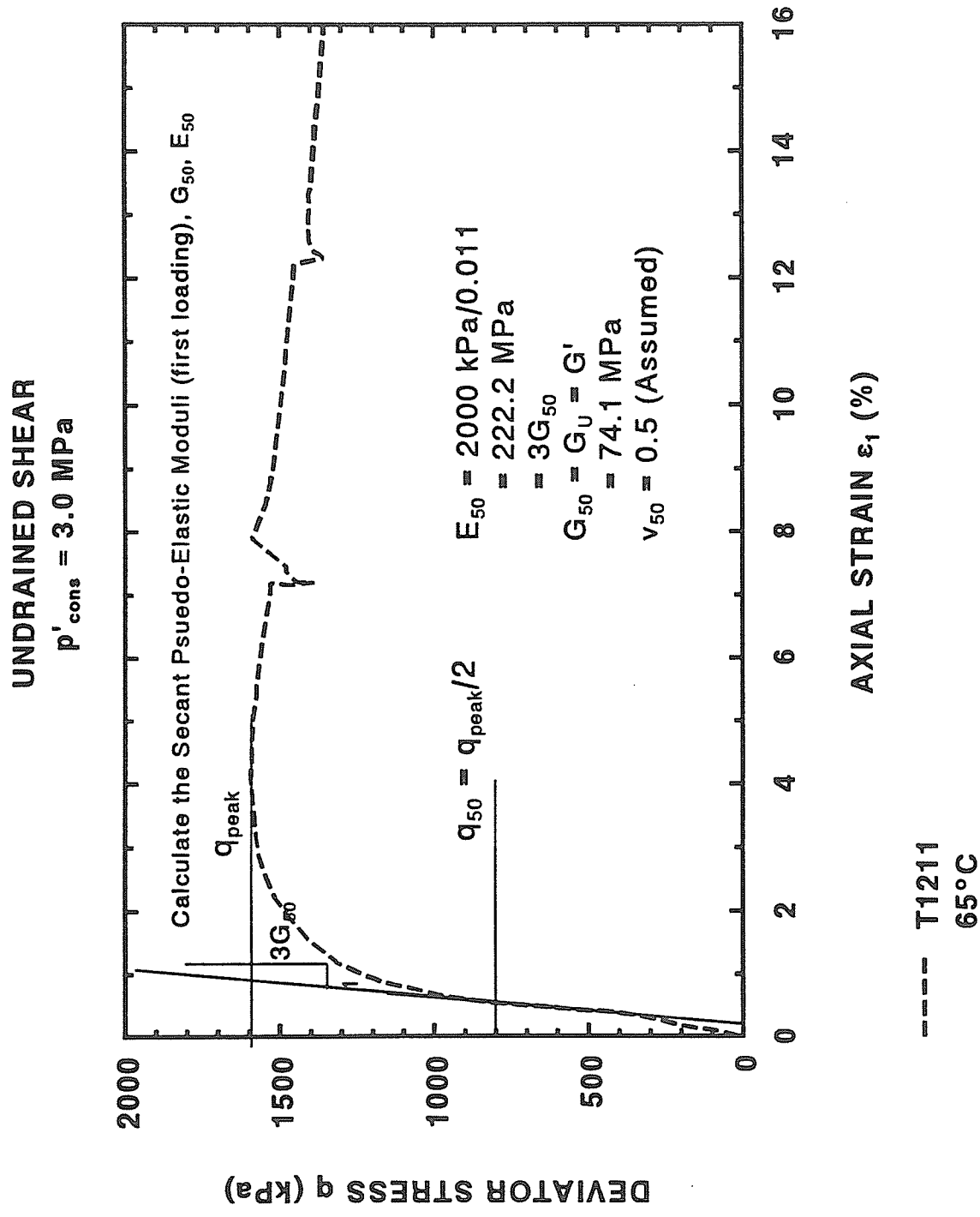


FIGURE 8.1 Graphical method for obtaining the secant shear modulus, G_{50} , from CIU(TXC) tests

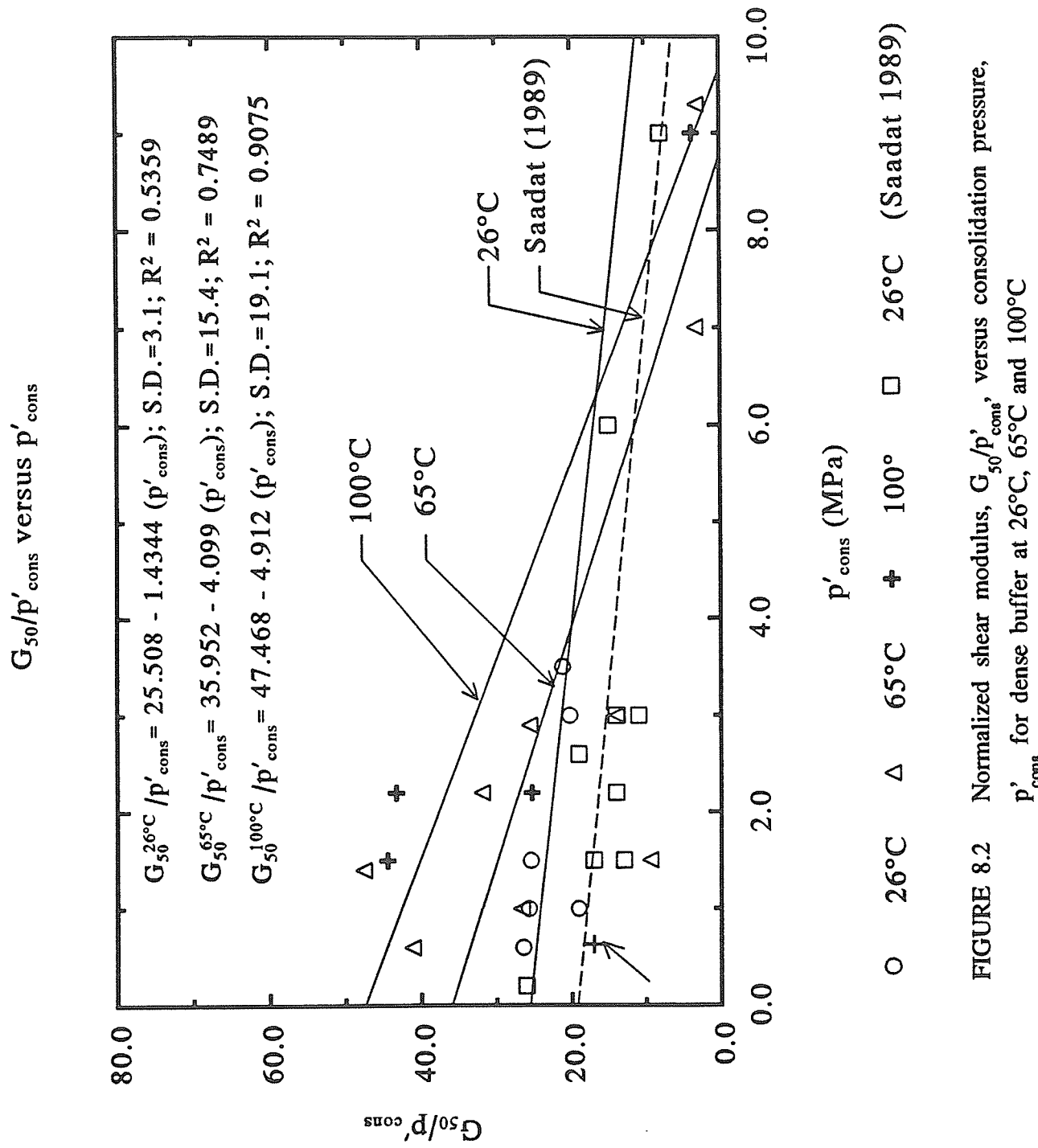


FIGURE 8.2 Normalized shear modulus, G_{50}/p'_{cons} , versus consolidation pressure, p'_{cons} for dense buffer at 26°C, 65°C and 100°C

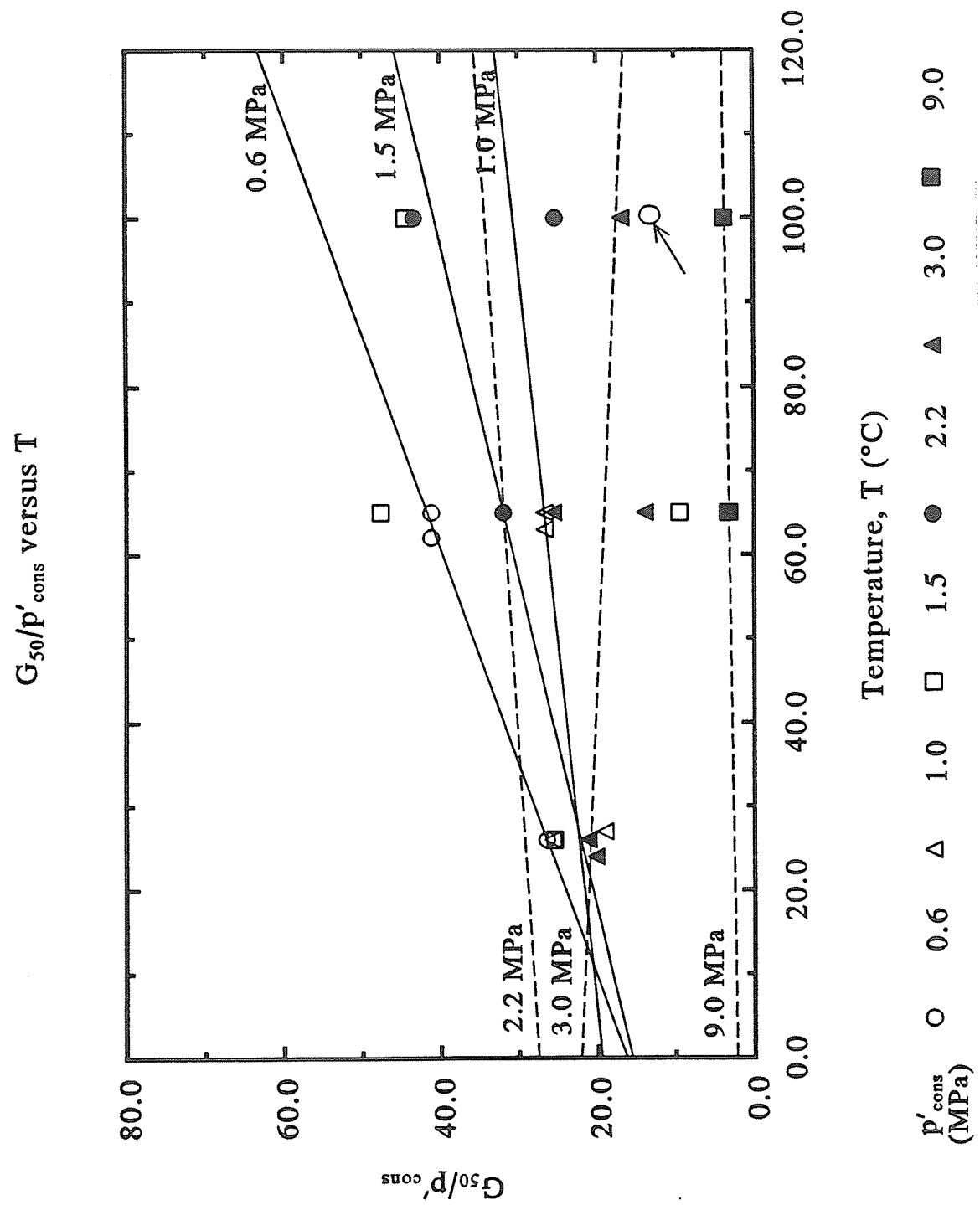


FIGURE 8.3 Normalized shear modulus, G_{50}/p'_{cons} , versus temperature, T , for dense buffer at different consolidation pressures.

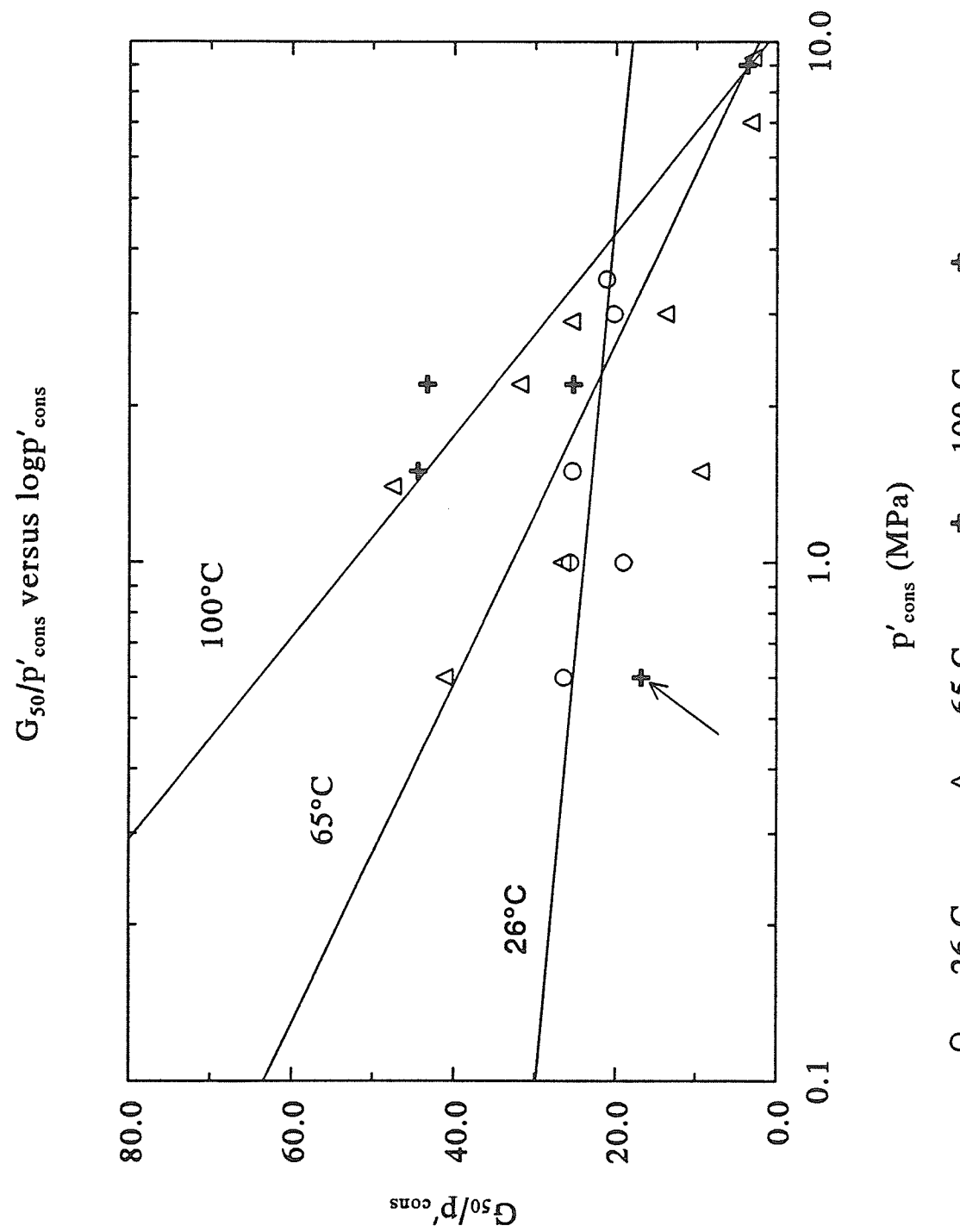


FIGURE 8.4 Normalized shear modulus, G_{50}/p'_{cons} , versus log of consolidation pressure, p'_{cons} for dense buffer at 26°C, 65°C and 100°C

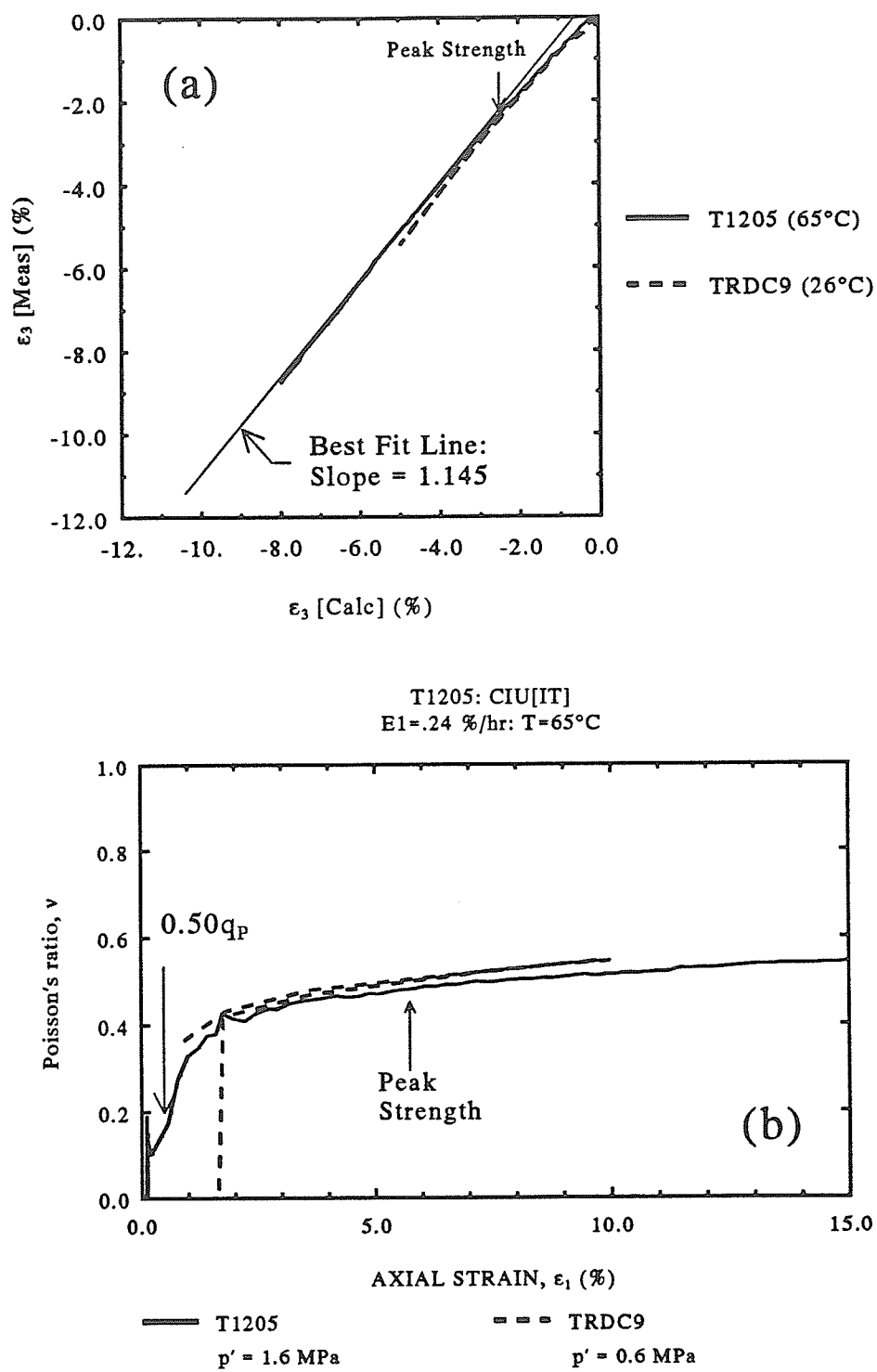


FIGURE 8.5 Comparison of Poisson's ratio for T1205 and Specimen (TRDC9):
 (a) ϵ_3 [Meas] versus ϵ_3 [Calc];
 (b) Poisson's ratio versus Axial Strain ϵ_1

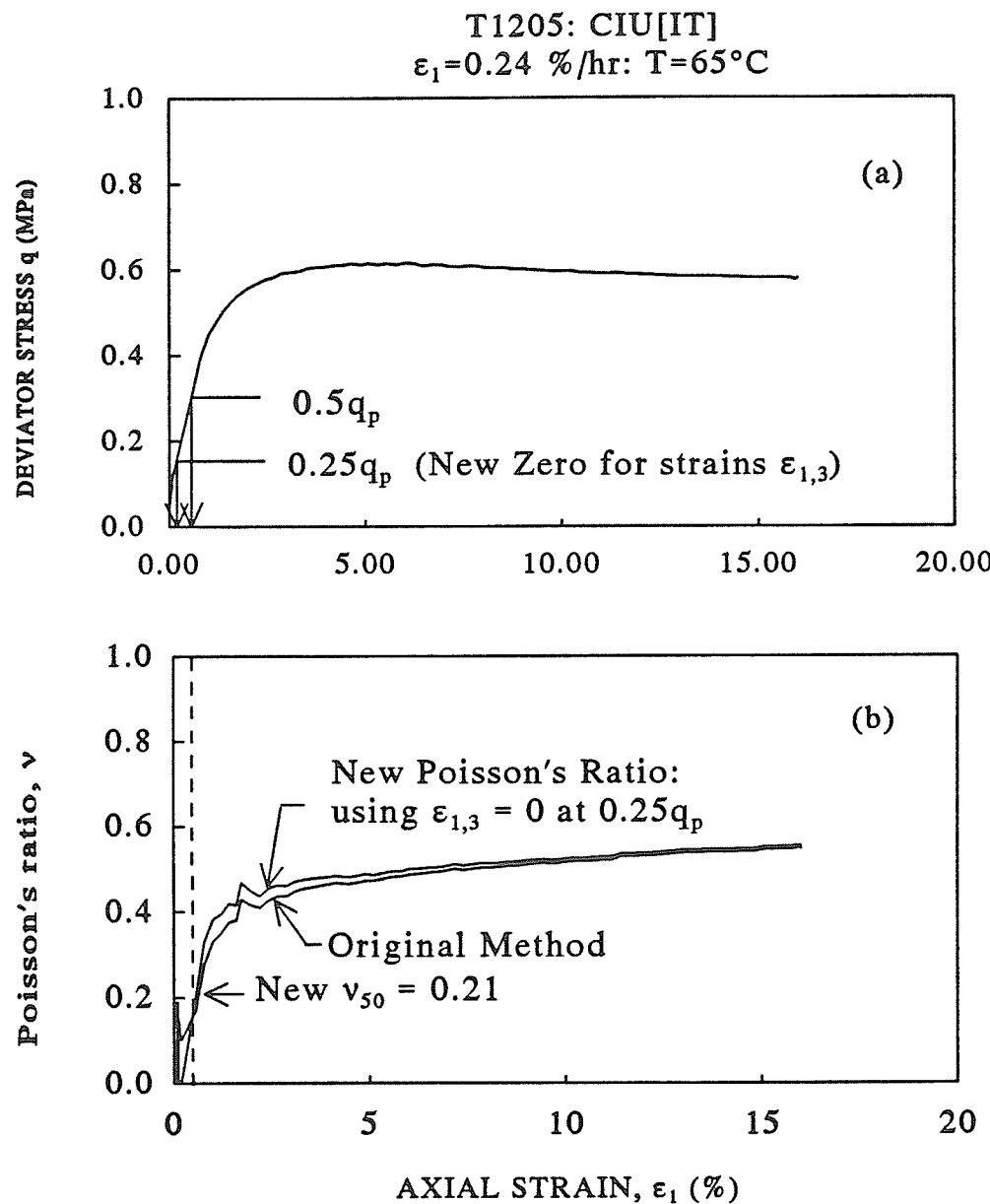


FIGURE 8.6 Modified method for calculating poisson's ratio, ν , for Buffer specimens at low axial strains, ε_1

UNDRAINED SHEAR

$p'_{\text{cons}} = 2.2 \text{ MPa}$

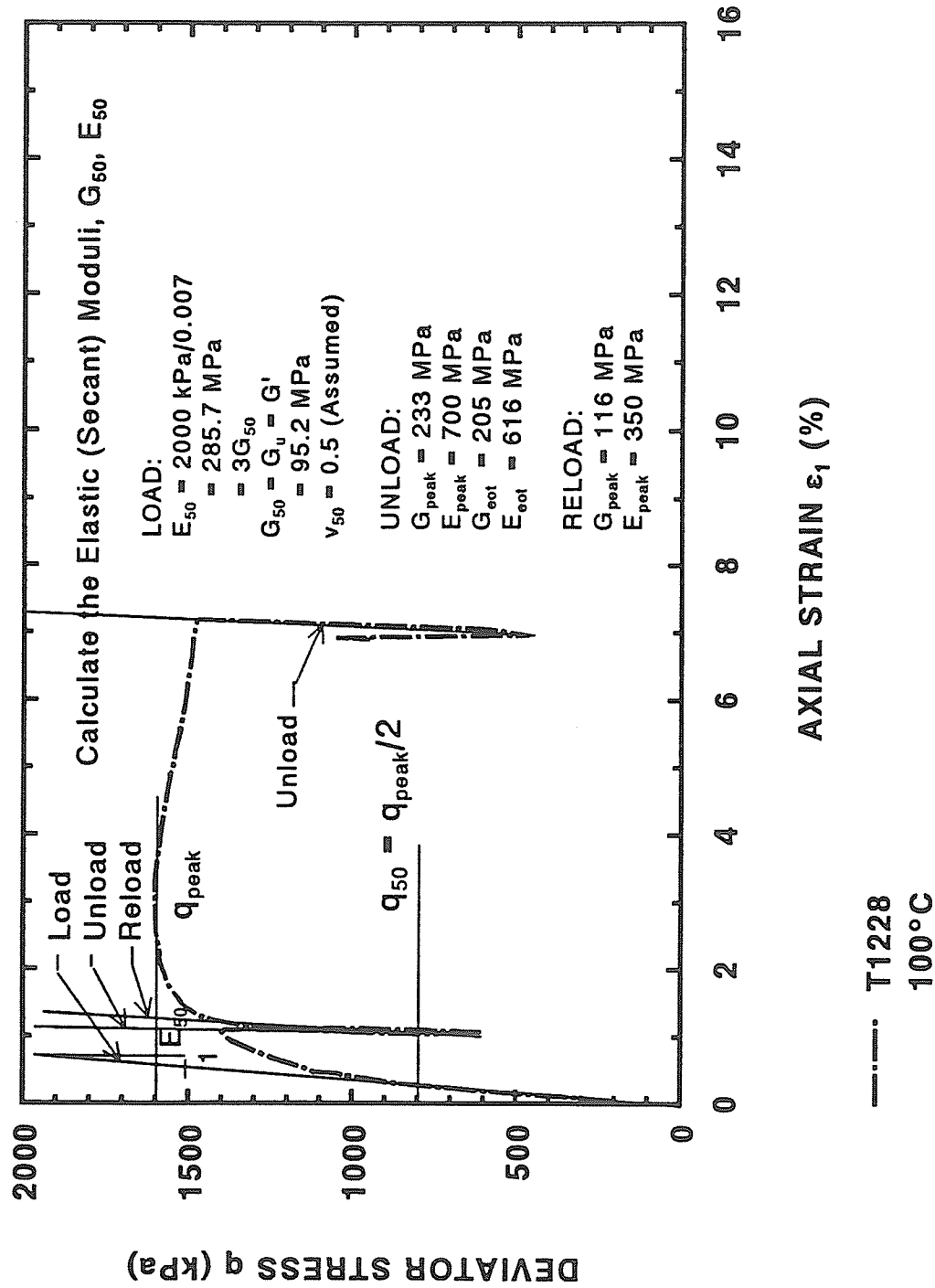


FIGURE 8.7 Method of calculating elastic secant modulus, G^e , from buffer specimen T1228 for unloading and reloading

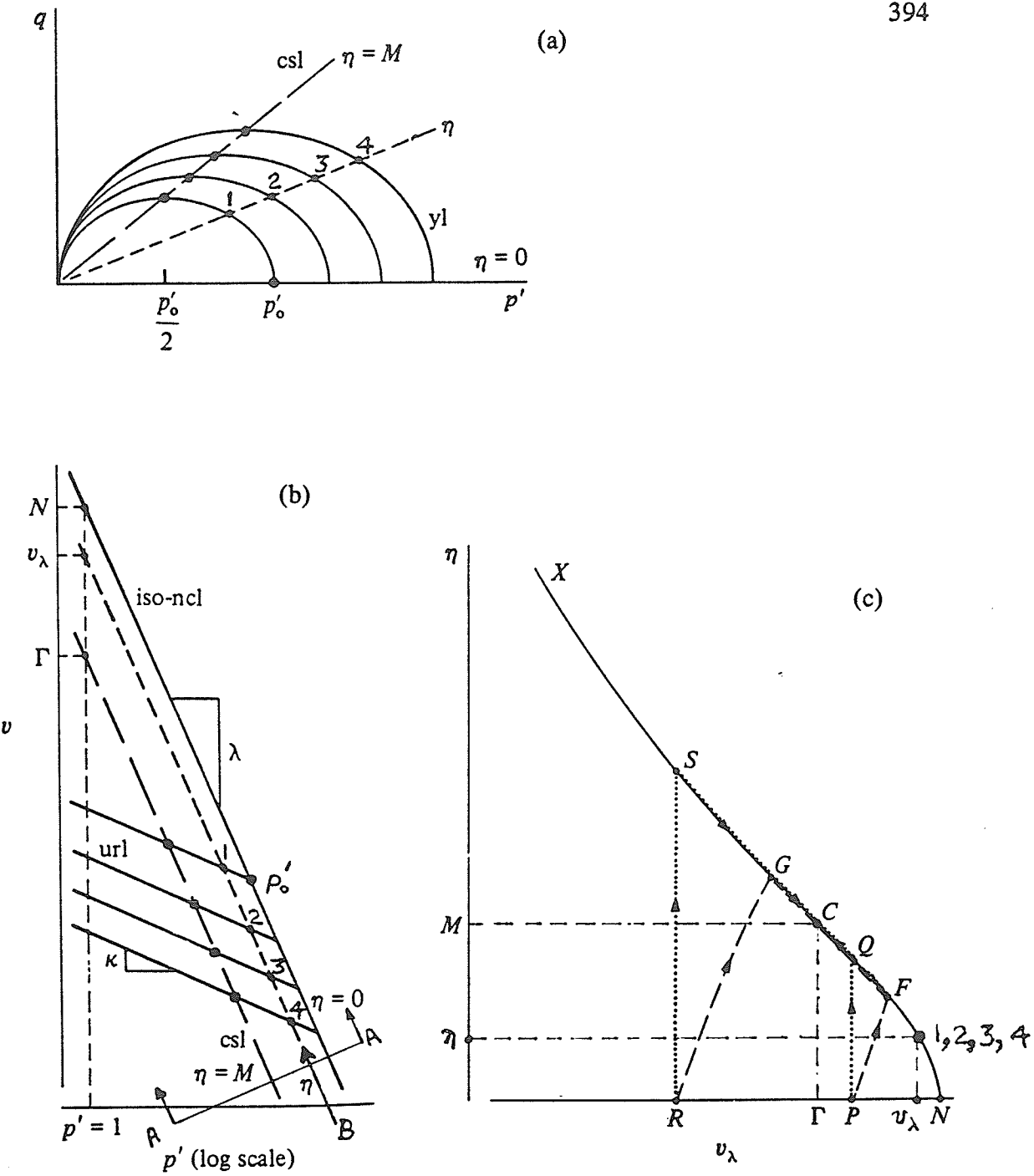


FIGURE 8.8 State Boundary Surface (SBS) viewed in V_λ space:

- (a) CSL and Yield Loci in $q-p'$ stress space;
- (b) Definition of V_λ ; SBS is viewed as a section A-A in the direction of the arrow;
- (c) appearance of SBS and paths of conventional drained and undrained triaxial compression tests in V_λ space
(after Wood 1990)

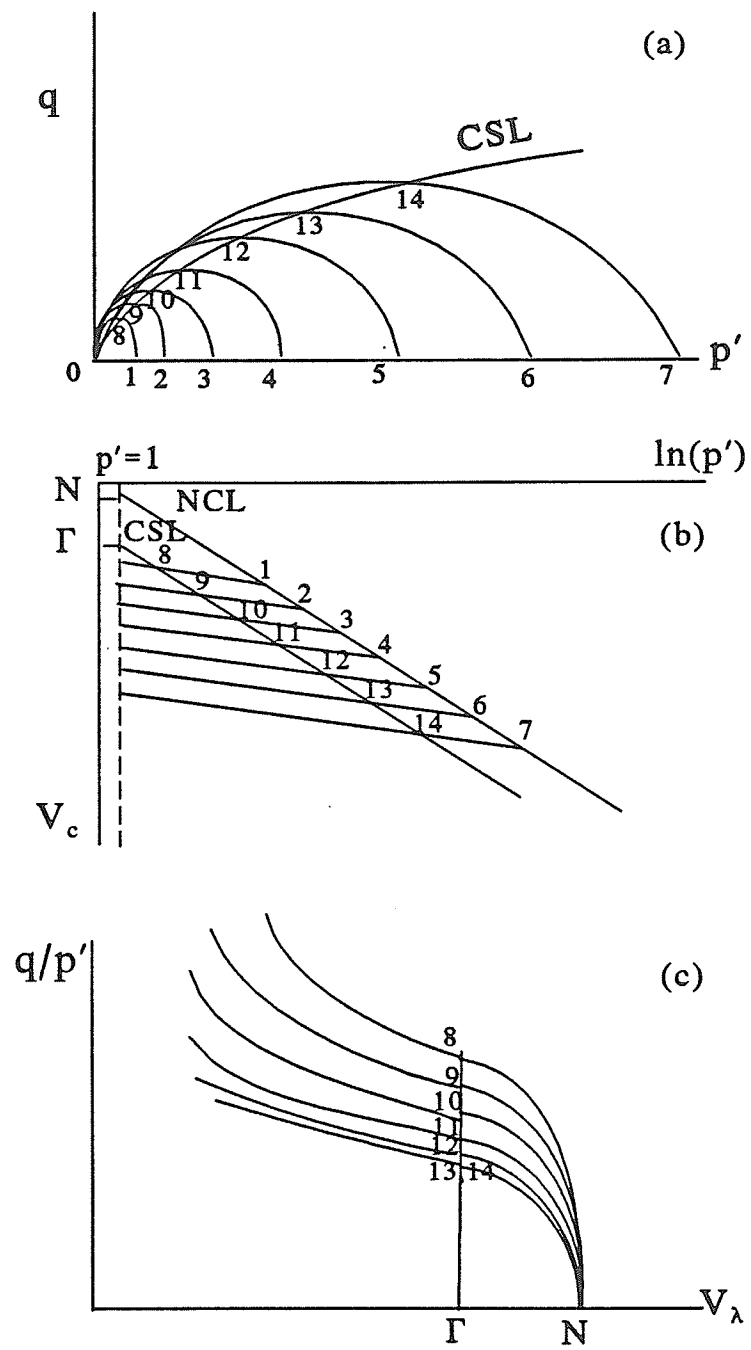


FIGURE 8.9 Description of SBS:

- (a) with curved CSL in q - p' stress space;
- (b) linear CSL in V_c - $\ln(p')$ compression space;
- (c) CSL in q/p' - V_λ space.

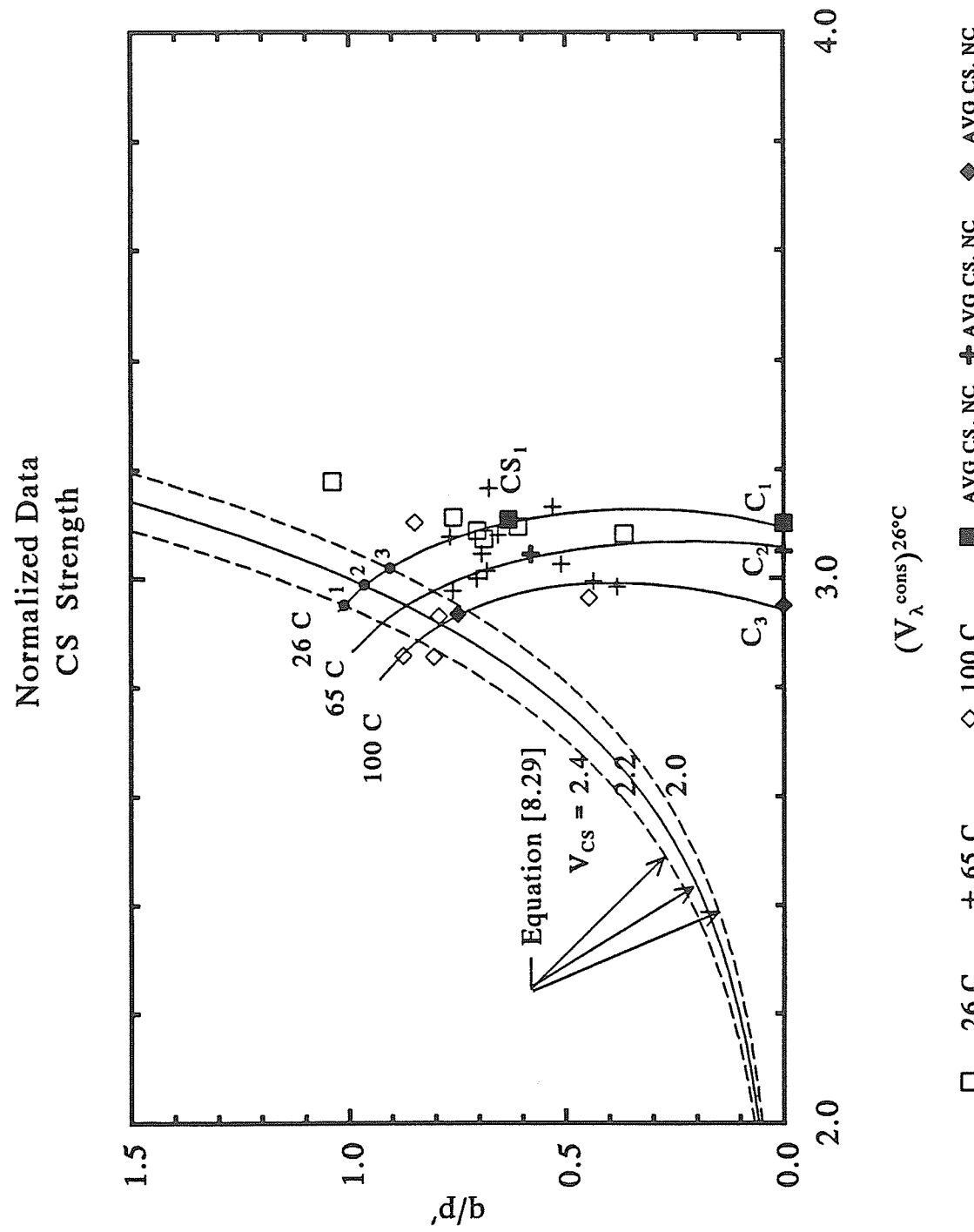


FIGURE 8.10 Comparison of CSL predicted from Equation 8.24 and average critical state data point CS₁ in normalized q/p'-V_λ space.

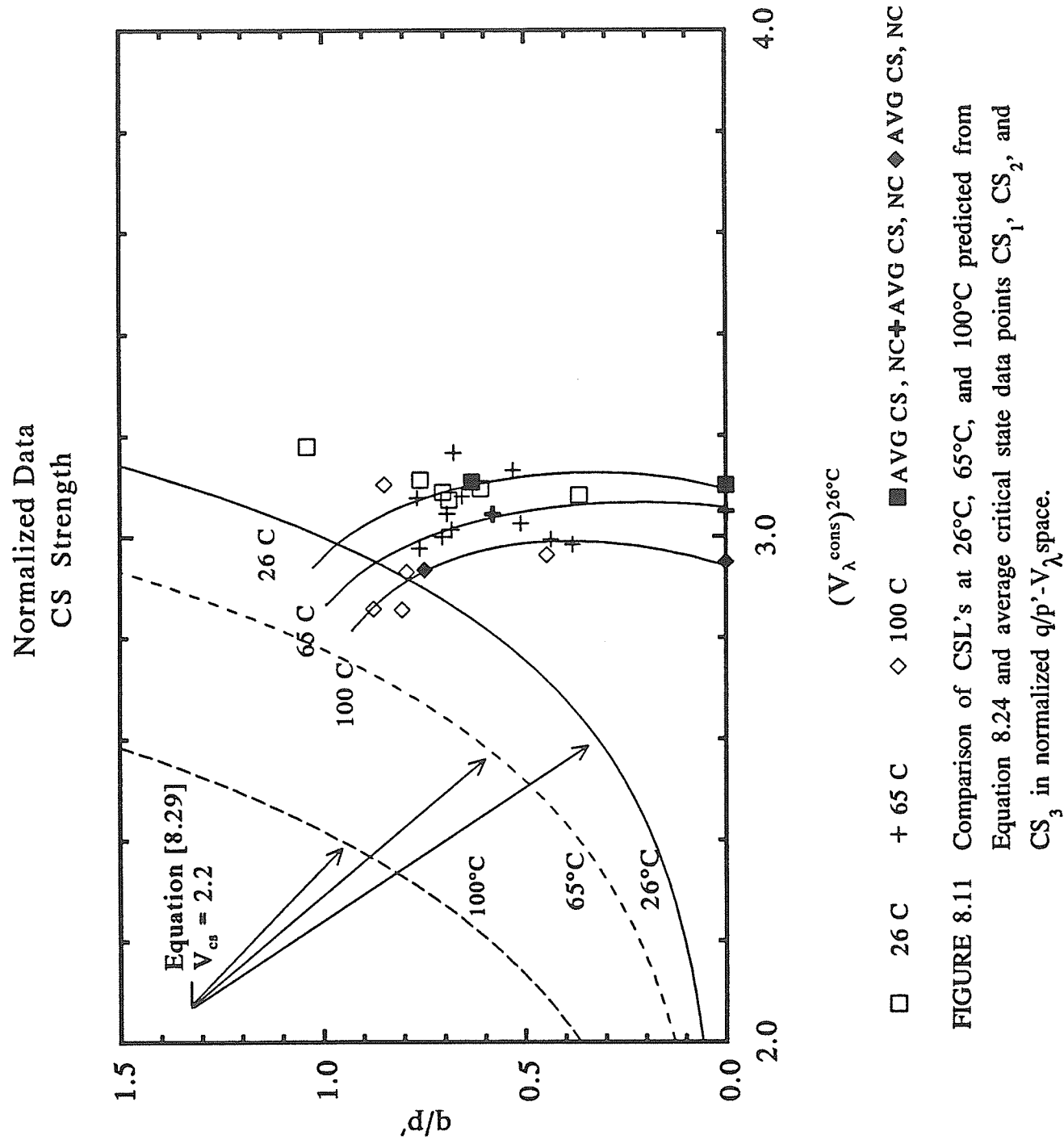


FIGURE 8.11 Comparison of CSL's at 26°C, 65°C, and 100°C predicted from Equation 8.24 and average critical state data points CS_1 , CS_2 , and CS_3 in normalized q/p - V_λ space.

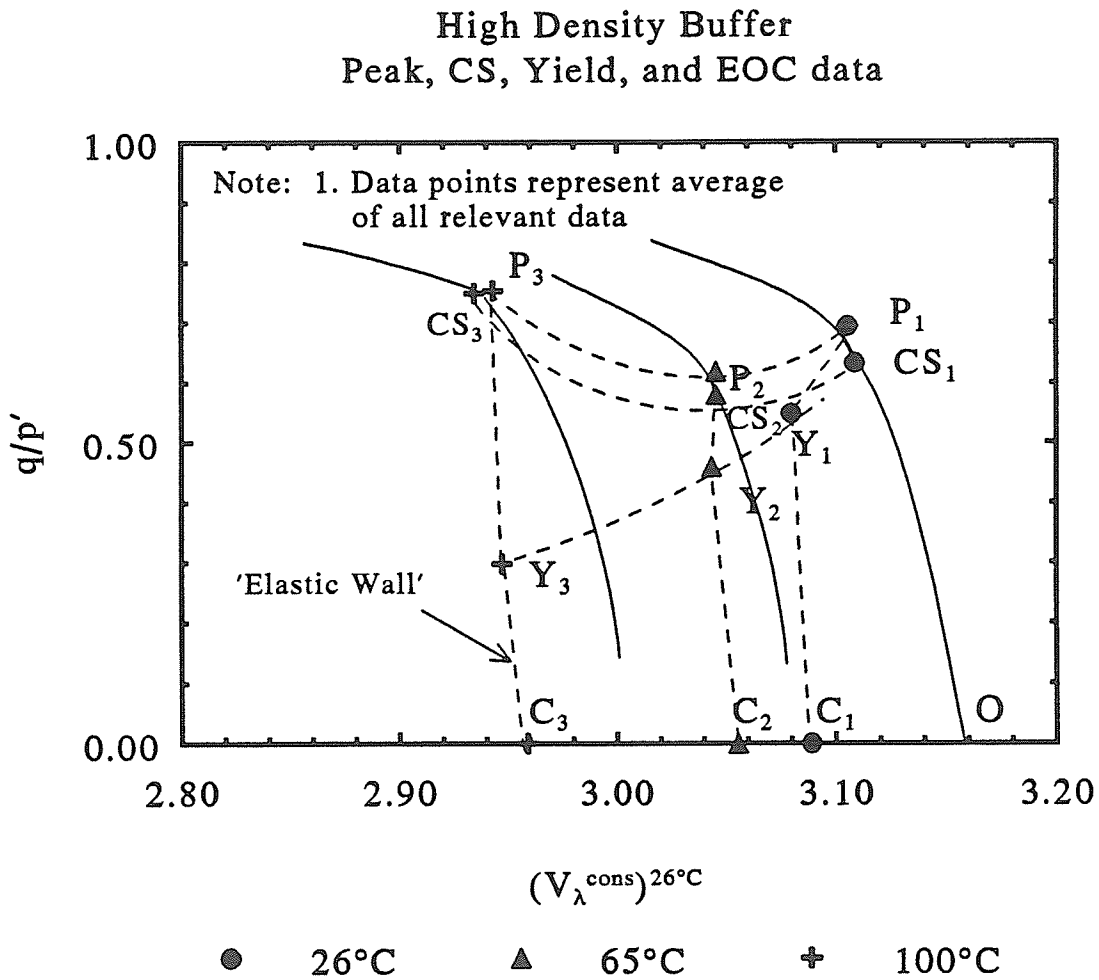


FIGURE 8.12 Average stress paths for 26°C , 65°C and 100°C buffer data in q/p' - V_λ space. Average data points are shown for End-Of-Consolidation (EOC), Yield (Y), Peak (P), and Critical State (CS)

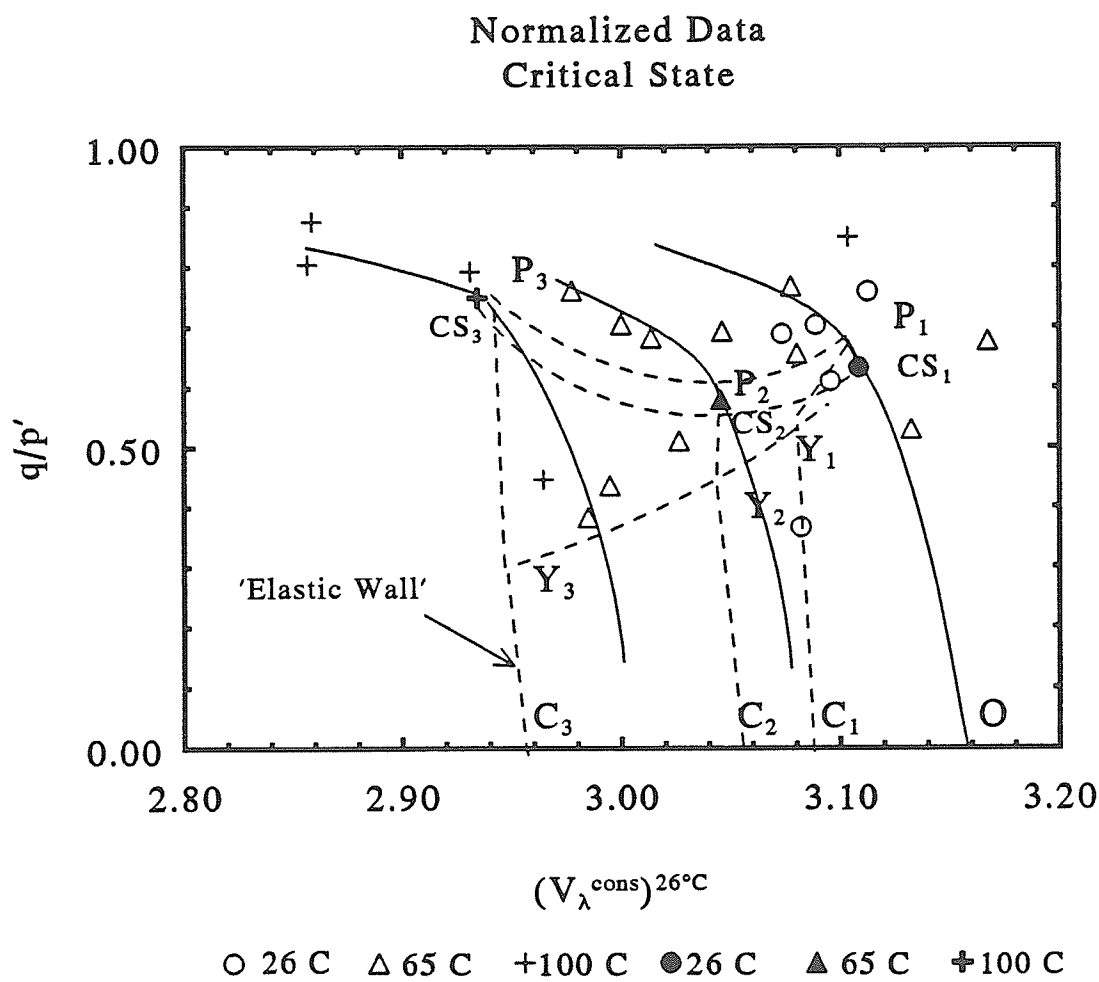


FIGURE 8.13 Critical state data at 26°C, 65°C and 100°C shown in q/p' - V_λ space.

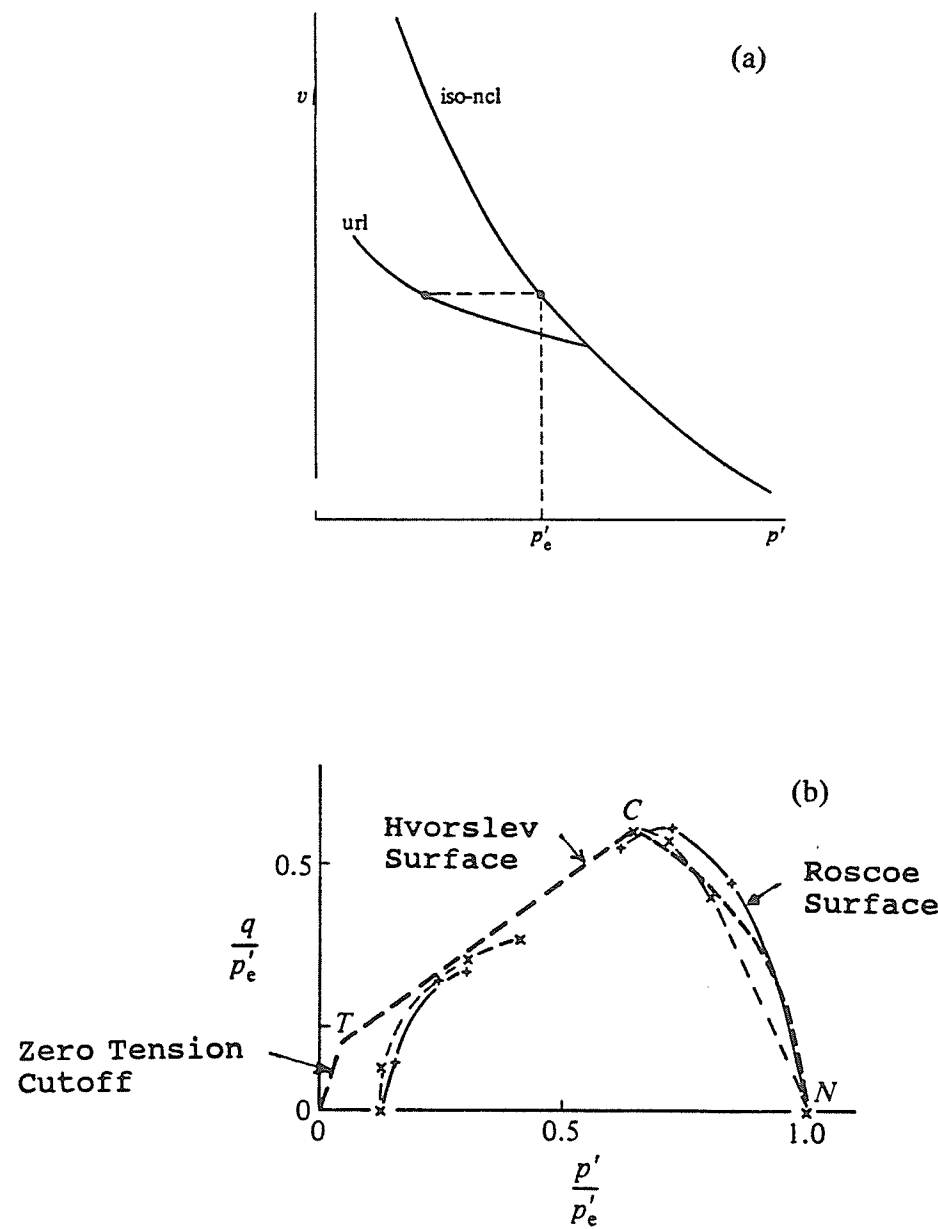


FIGURE 8.14 Description of SBS using normalization to equivalent pressure:
 (a) Definition of equivalent pressure, p'_e ;
 (b) SBS in q/p'_e - p'/p'_e stress space

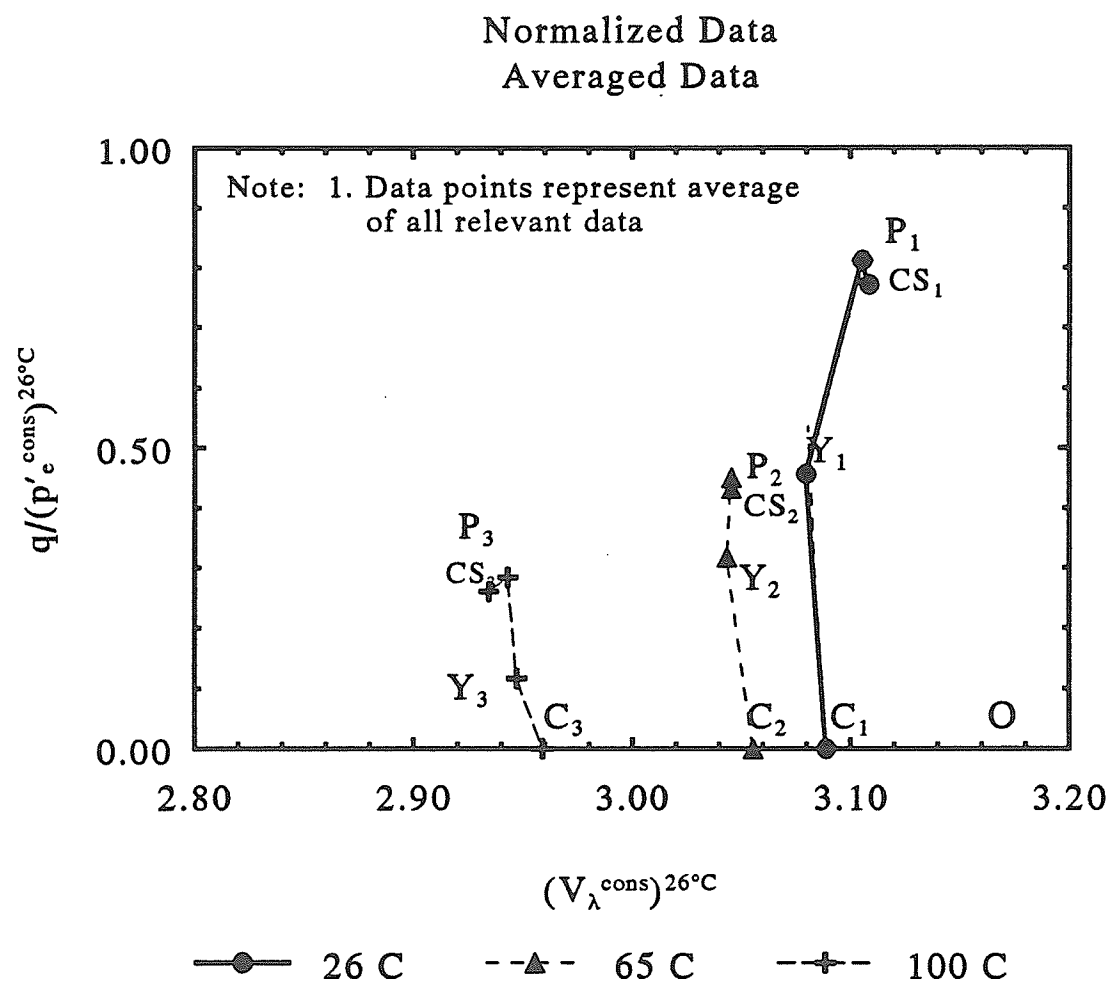


FIGURE 8.15 Average data points for EOC, Yield, Peak and Critical State in V_λ space normalized to the 26°C NCL from the current program

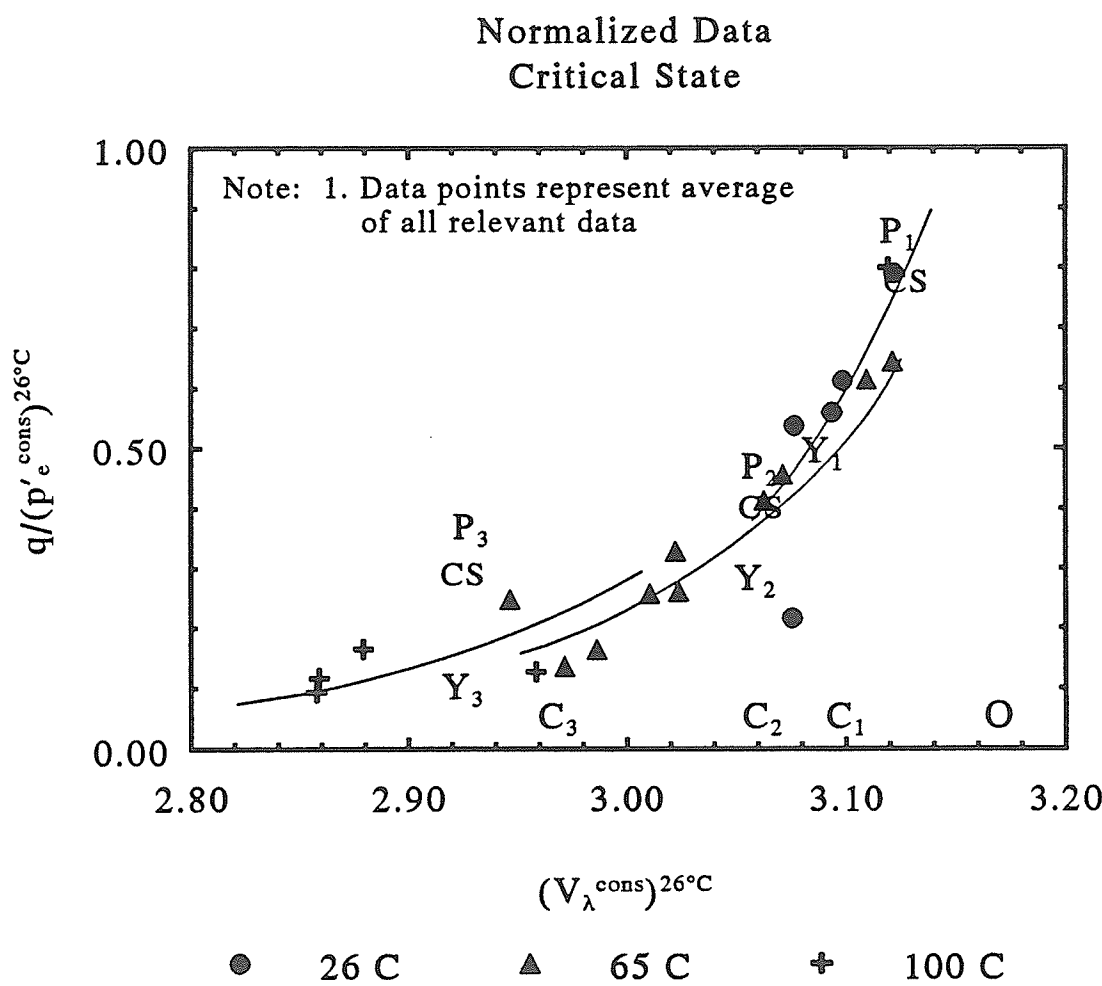


FIGURE 8.16 Critical state data for 26°C, 65°C and 100°C in V_λ space normalized to the 26°C NCL from the current program

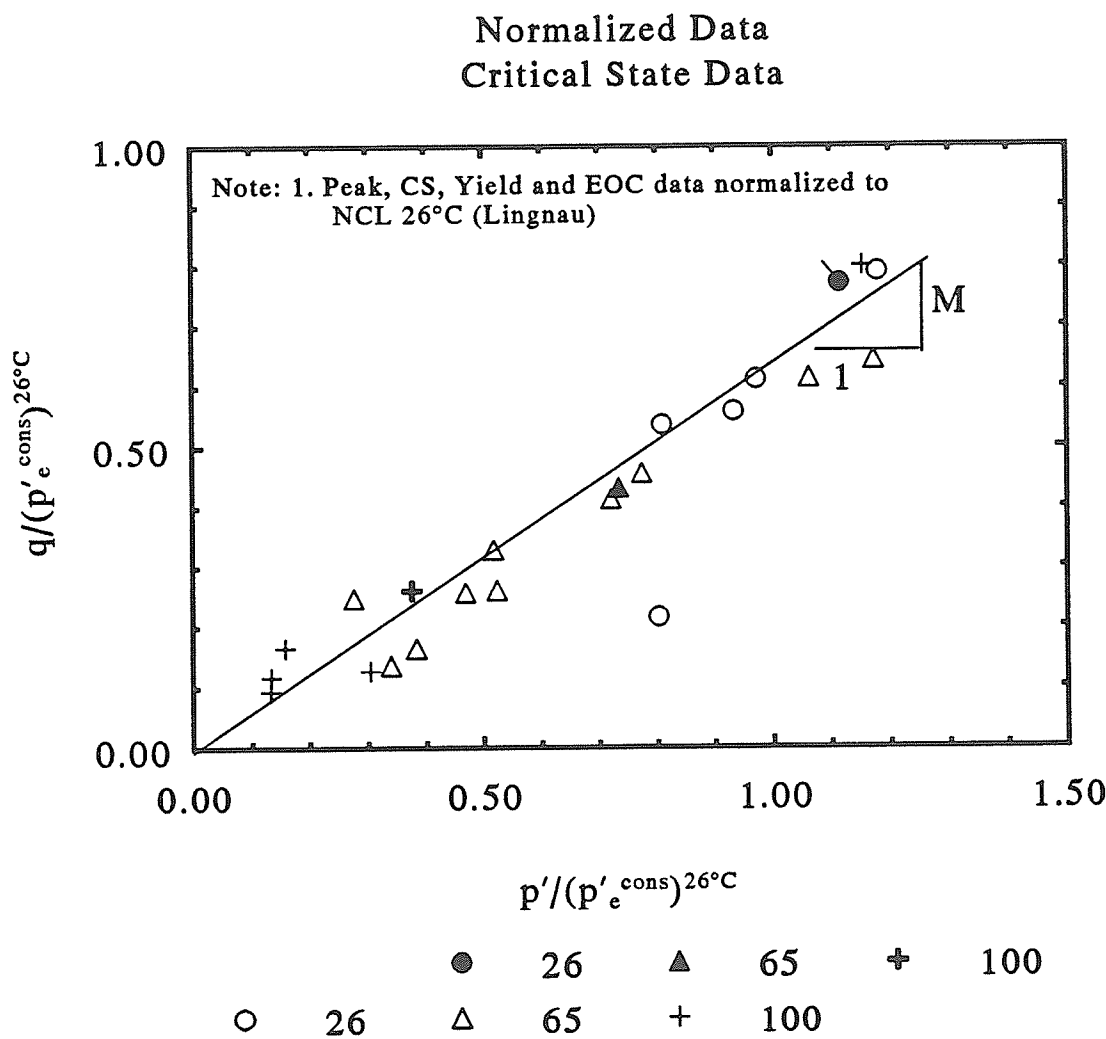


FIGURE 8.17 Critical state data for 26°C, 65°C and 100°C in q - p' stress space normalized to the 26°C NCL from the current program

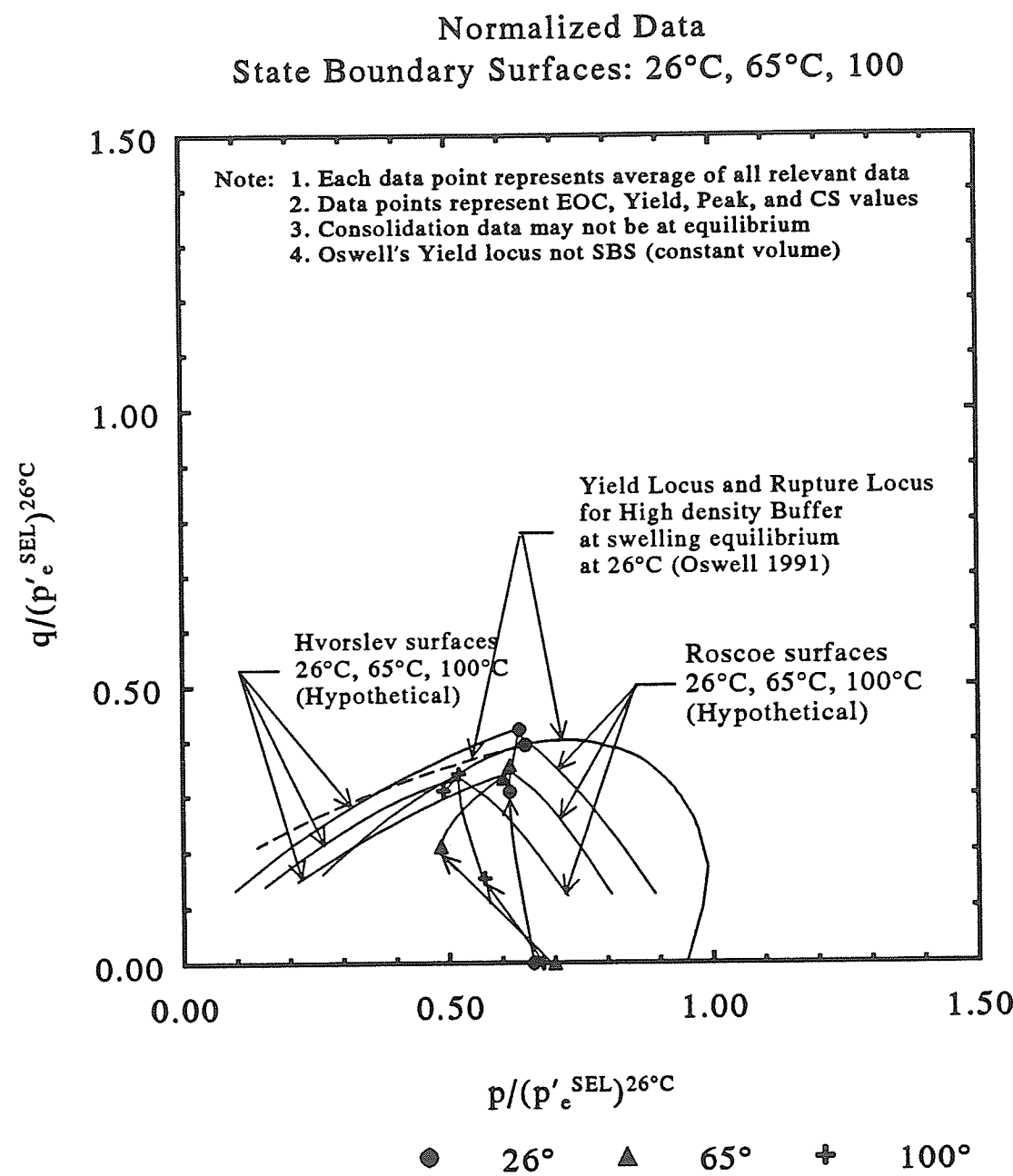


FIGURE 8.18 State boundary surfaces for 26°C, 65°C, and 100°C interpreted from $q-p'$ stress space normalized to 26°C Swelling Equilibrium Line (SEL).

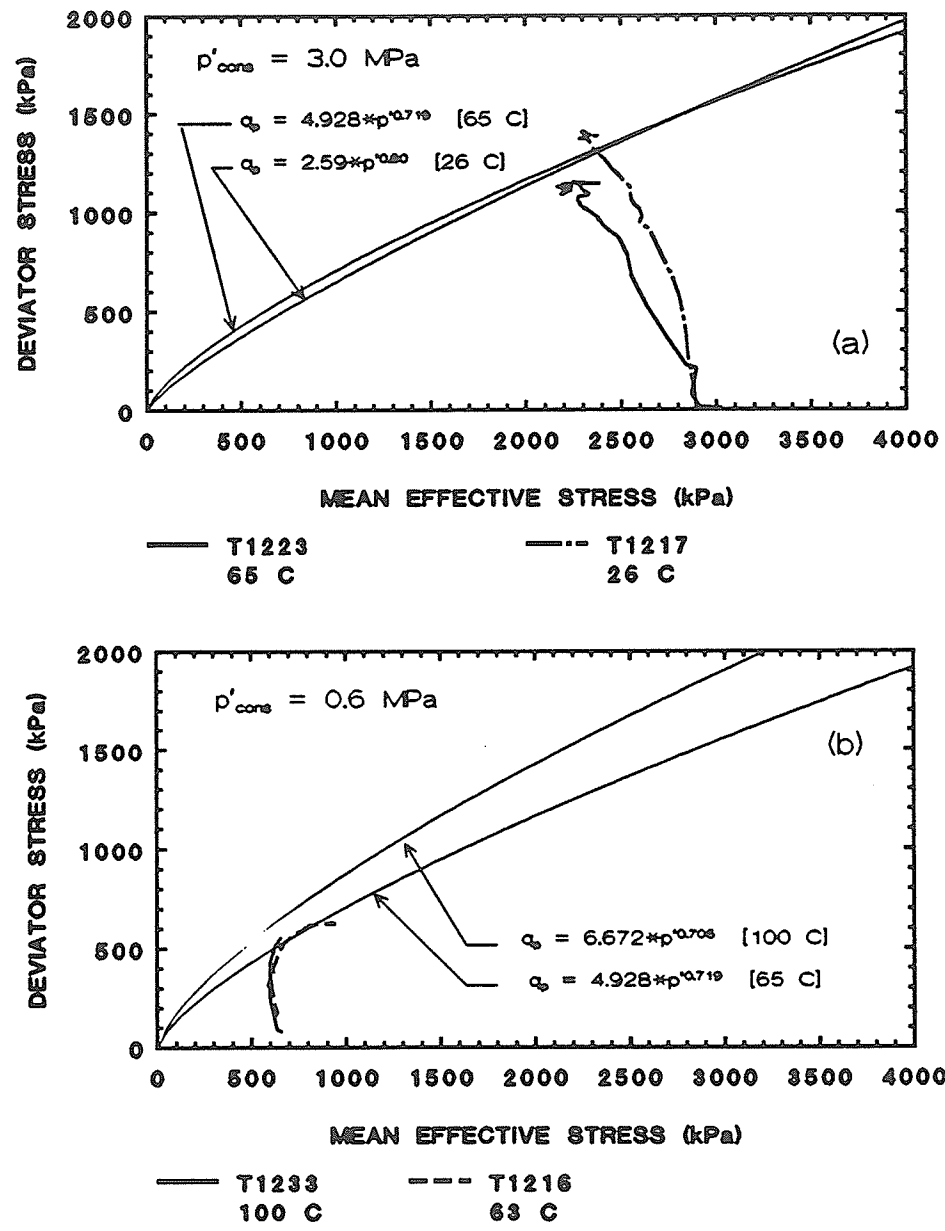


FIGURE 8.19 Examples of peak strength behavior for specimens at the same effective stress:
 (a) at $p' = 3.0 \text{ MPa}$;
 (b) at $p' = 0.6 \text{ MPa}$

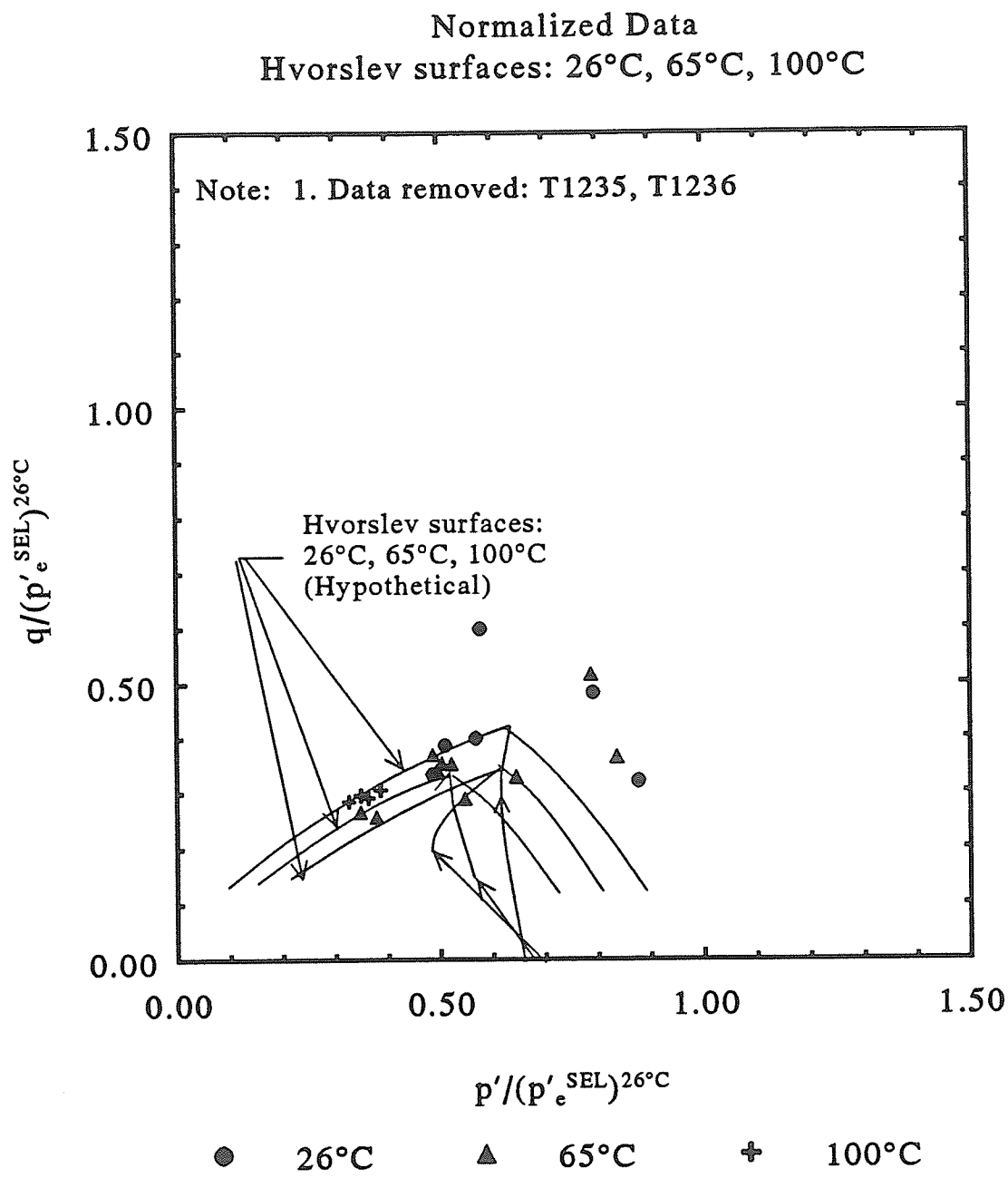


FIGURE 8.20 Hvorslev surfaces interpreted from 26°C, 65°C and 100°C data plotted in q-p' stress space normalized to the 26°C SEL

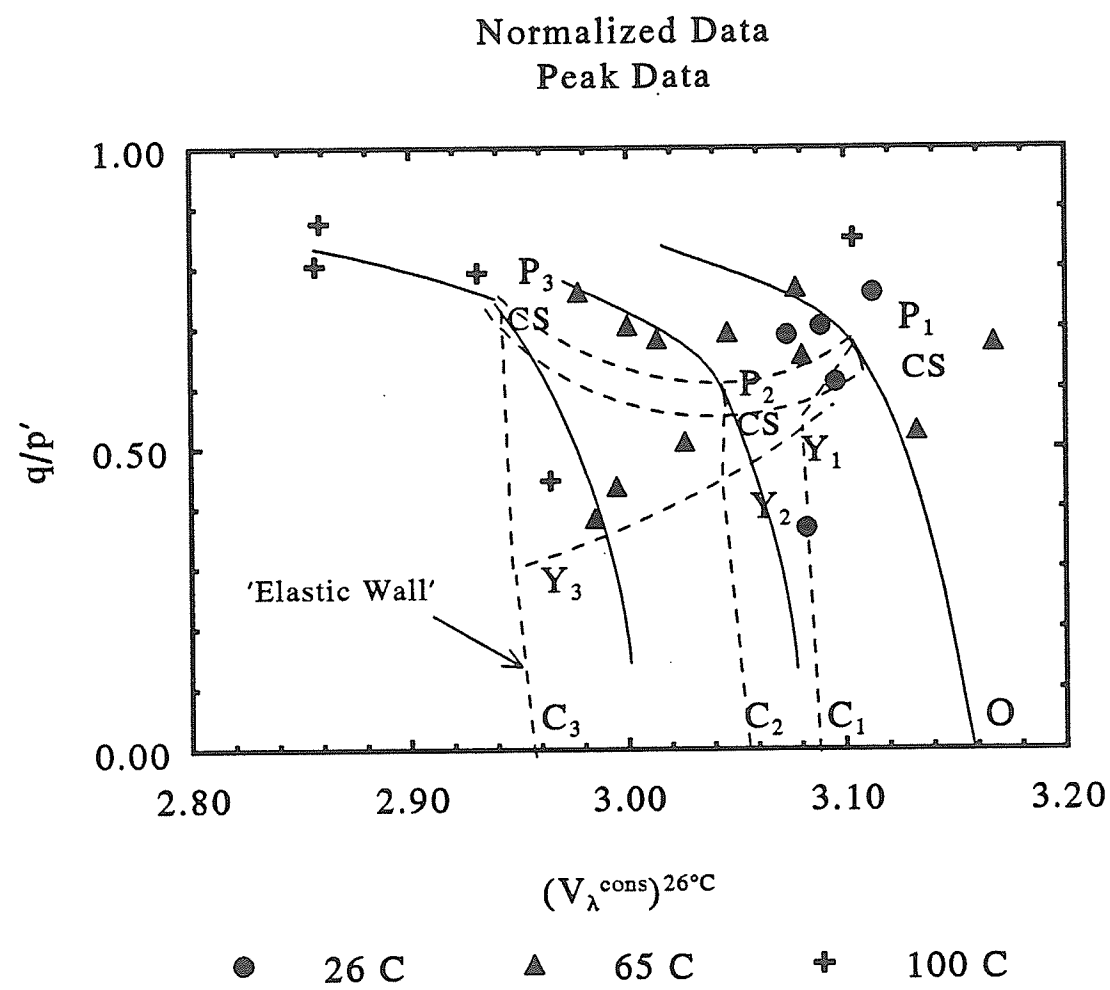


FIGURE 8.21 Peak strength data at 26°C, 65°C and 100°C plotted in V_λ space and normalized to the 26°C NCL. The Hvorslev surfaces are also shown.

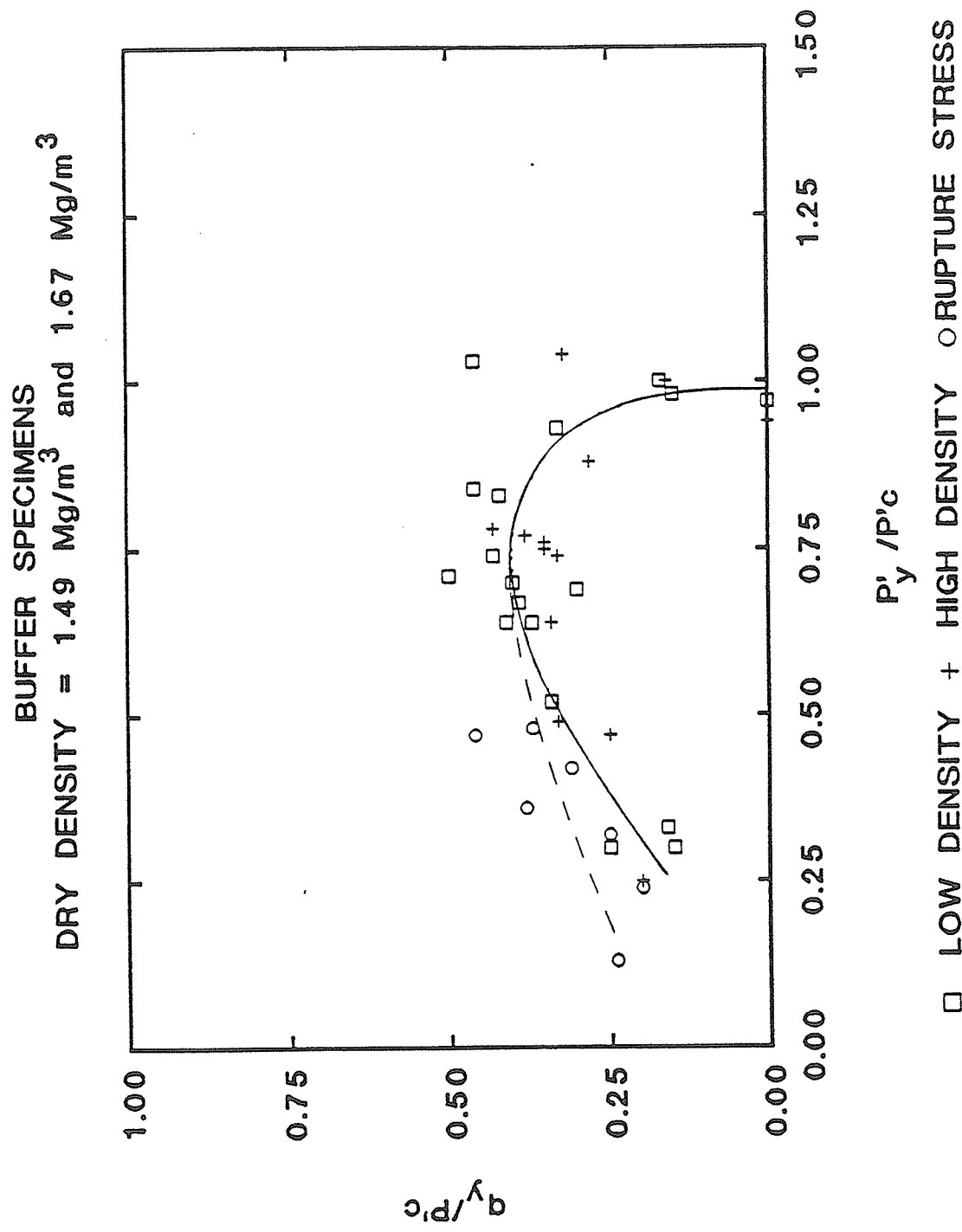


FIGURE 8.22 Yield data (early) and rupture data in q,p' -space. The solid yield locus is the original "first" early locus. The dashed yield locus is the "second" rupture locus (Oswell (1991))

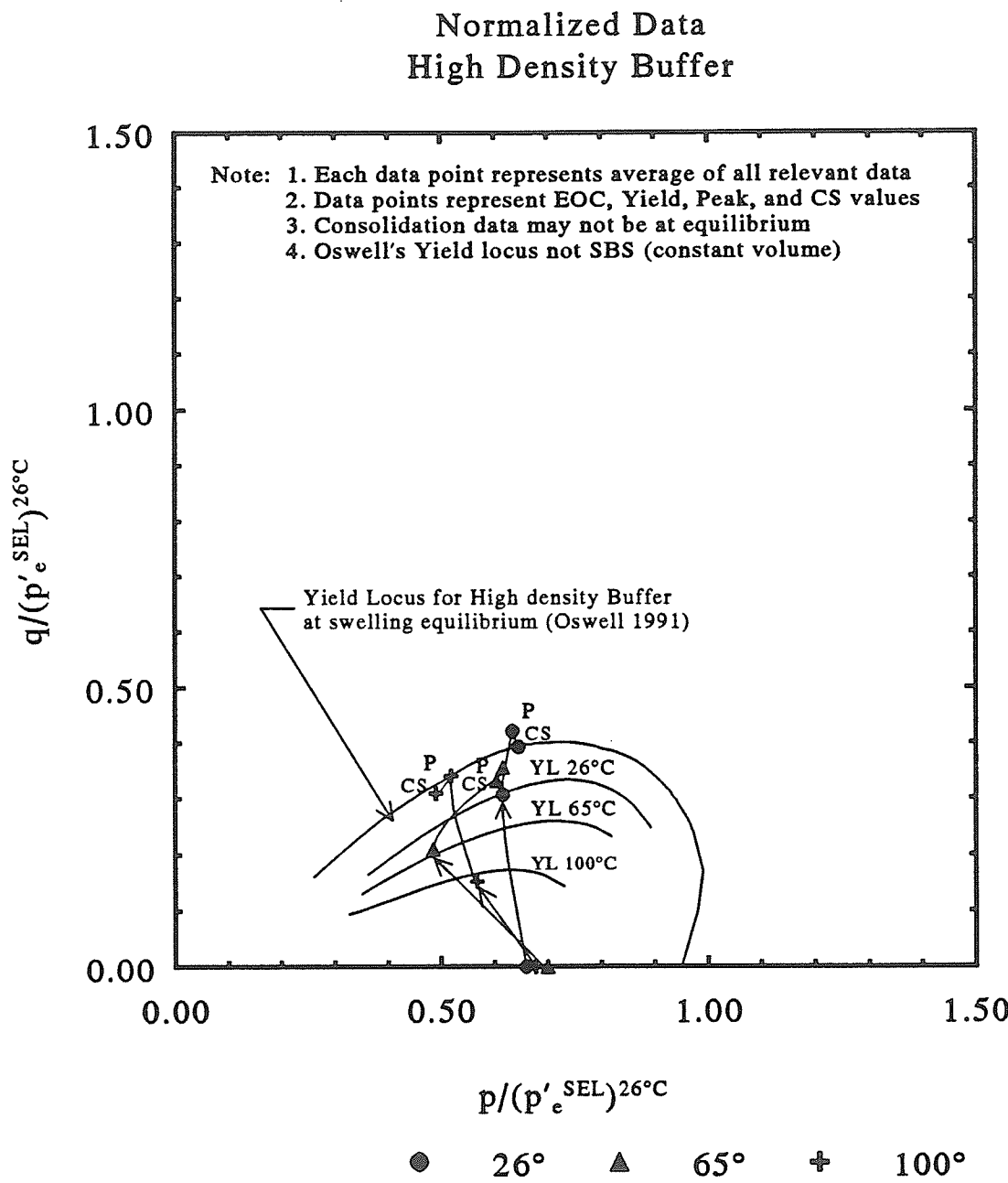


FIGURE 8.23 Average yield data at 26°C, 65°C, and 100°C plotted in $q-p'$ stress space normalized to equivalent pressure from the 26°C SEL. Early yield loci are interpreted for each temperature.

High Density Buffer: Yield Loci and Stress Paths for Averaged Data

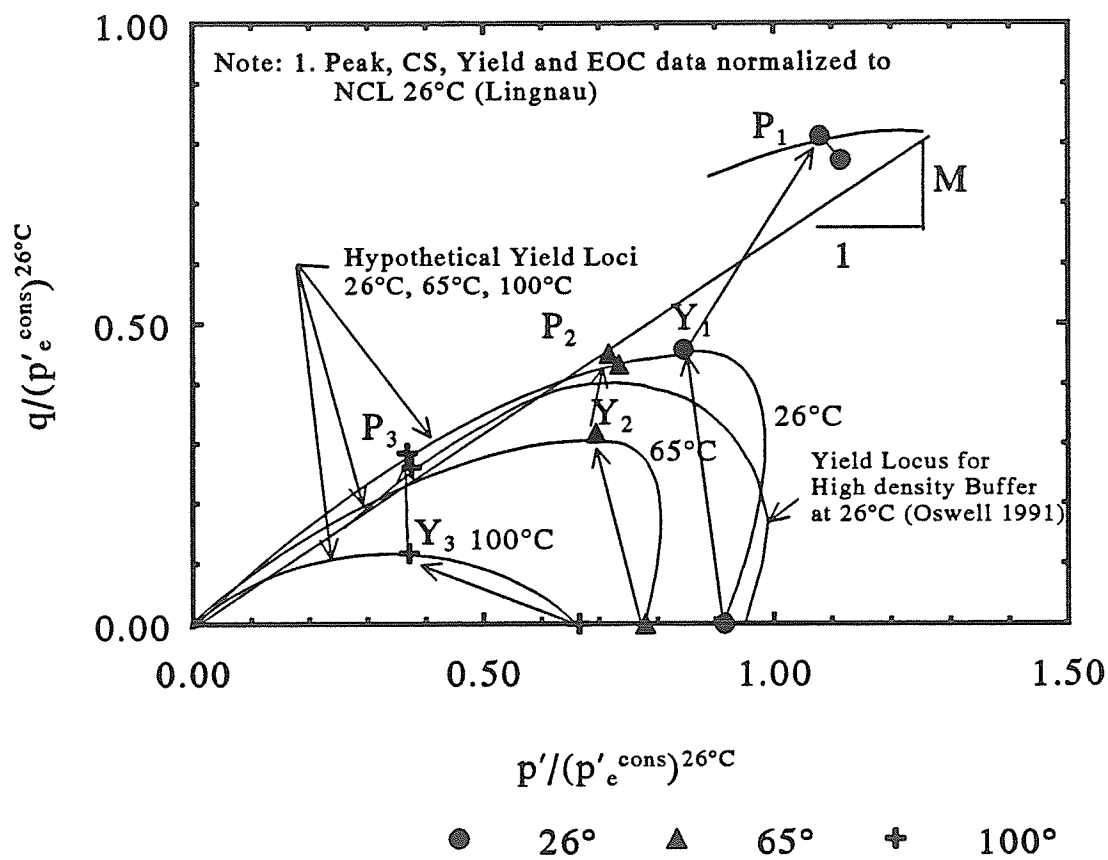


FIGURE 8.24 Yield loci and stress paths for averaged data at 26°C, 65°C, and 100°C in q - p' stress space normalized to equivalent pressure from the 26°C NCL.

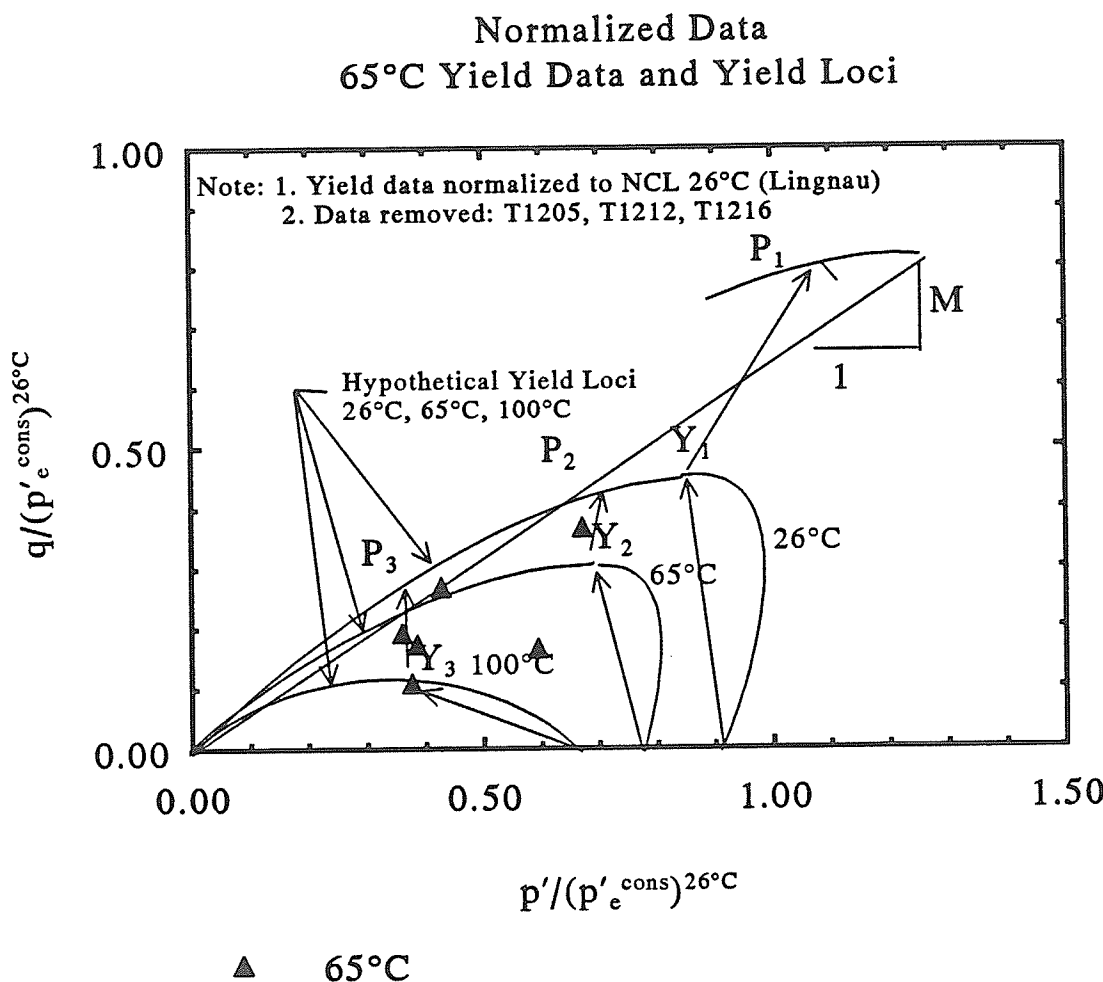


FIGURE 8.25 Yield data from 65°C specimens plotted in $q\text{-}p'$ stress space normalized to equivalent pressure from the 26°C NCL.

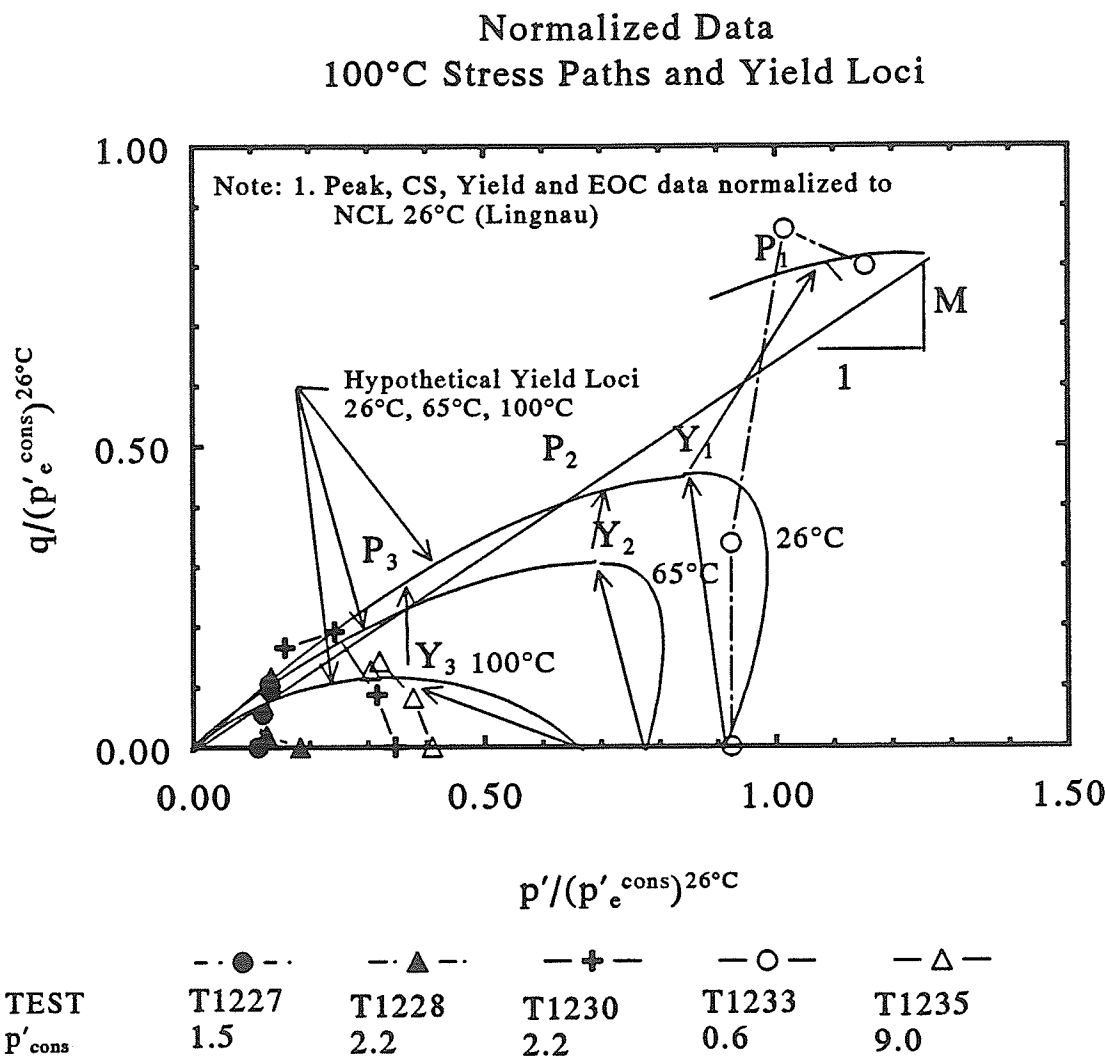


FIGURE 8.26 Stress paths for 100°C specimens plotted in q - p' stress space normalized to equivalent pressure from the 26°C NCL.

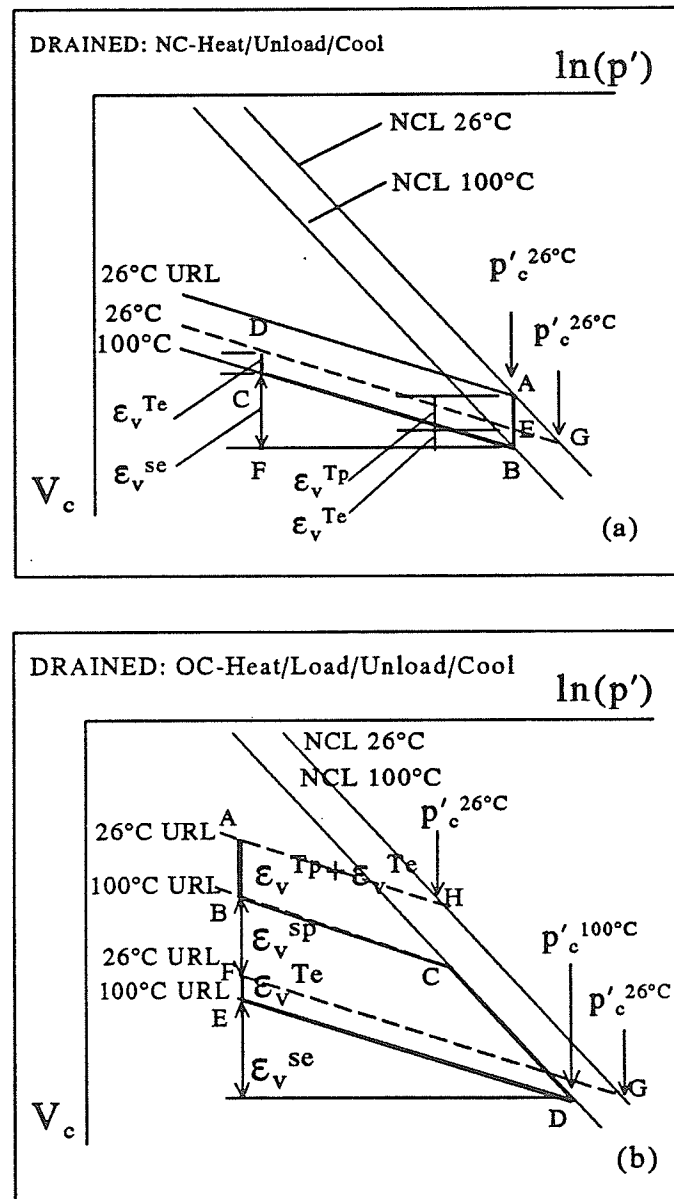


FIGURE 8.27 Examples of mean effective stress-volumetric strain behavior due to drained heating and loading:

- For a normally consolidated specimen (NC)
- overconsolidated specimen (OC).

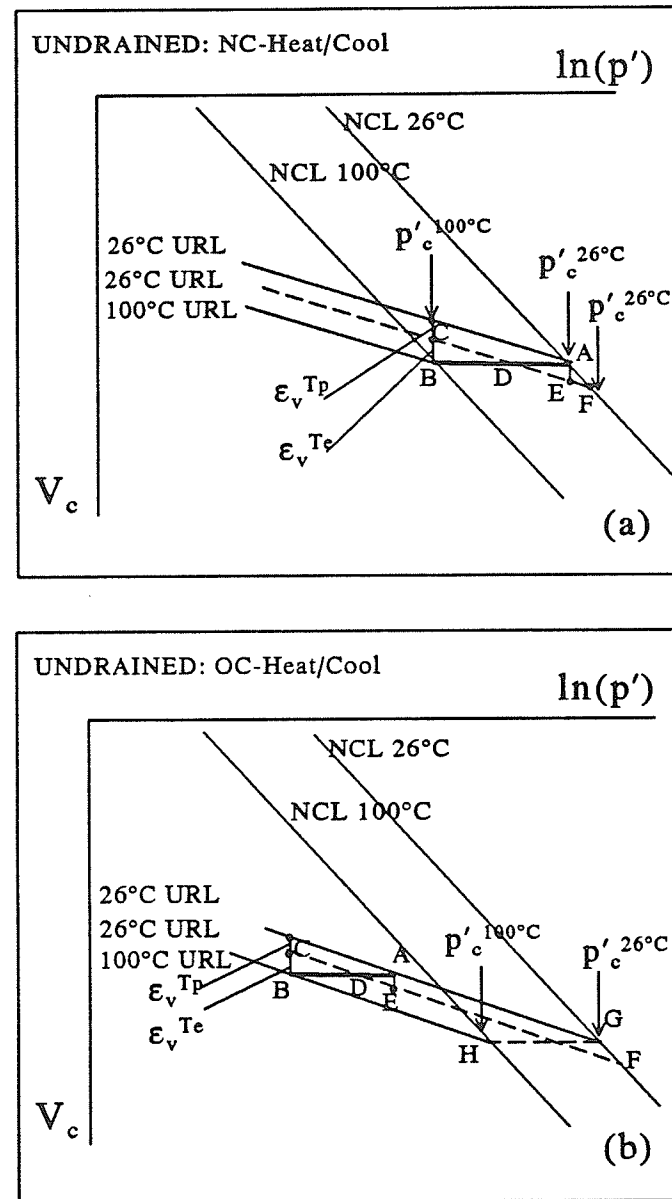


FIGURE 8.28 Examples of mean effective stress-volumetric strain behavior due to undrained heating:
 (a) for a NC specimen
 (b) for an OC specimen

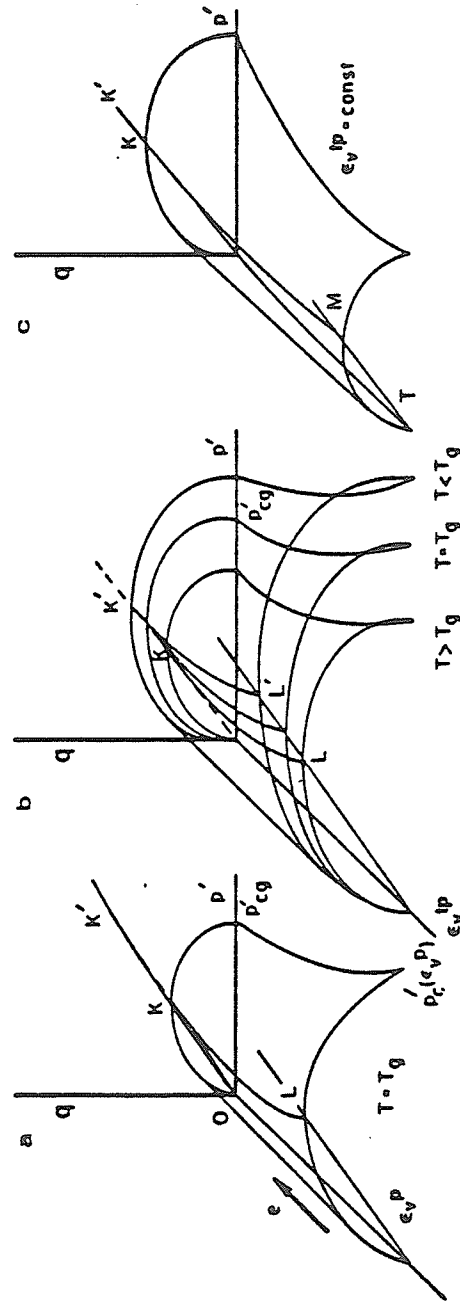


FIGURE 8.29 Cam-clay type representation of Yield surface:

- (a) Room temperature;
 - (b) at Variable ϵ_v^Tp and ΔT ;
 - (c) at constant ϵ_v^Tp and variable ΔT
- (after Hueckel and Baldi 1990)

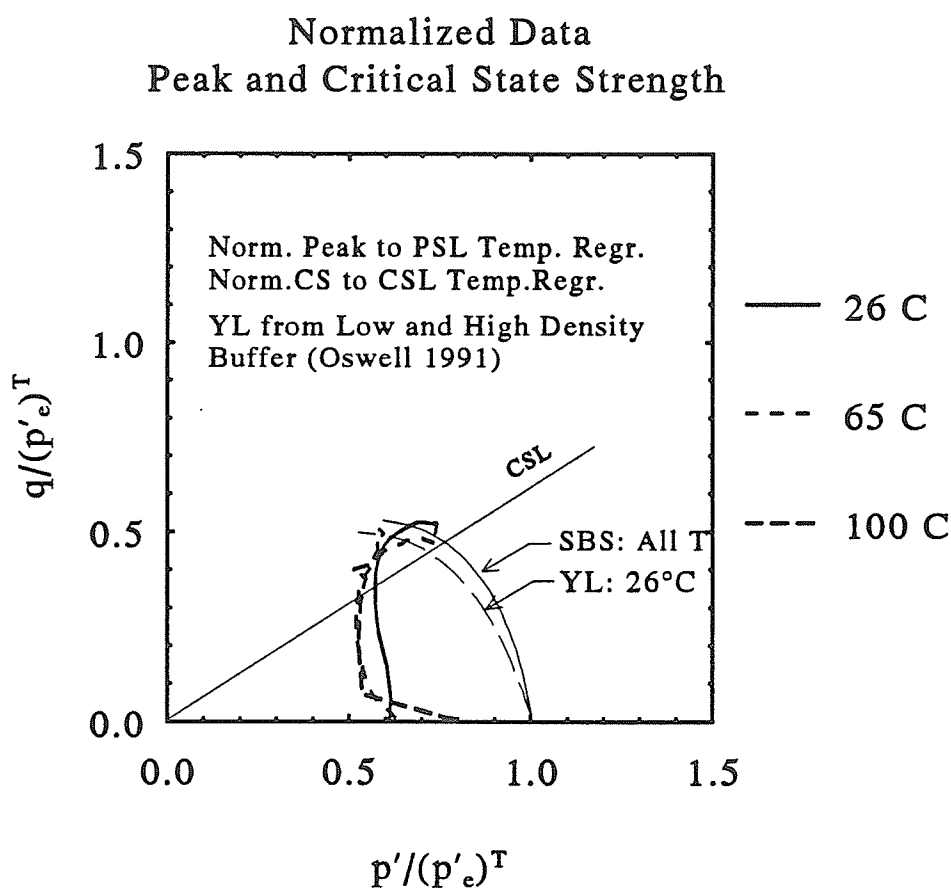


FIGURE 8.30 Stress paths for randomly selected tests plotted in $q-p'$ stress space normalized to equivalent pressures for each temperature. A single surface is produced for the SBS.

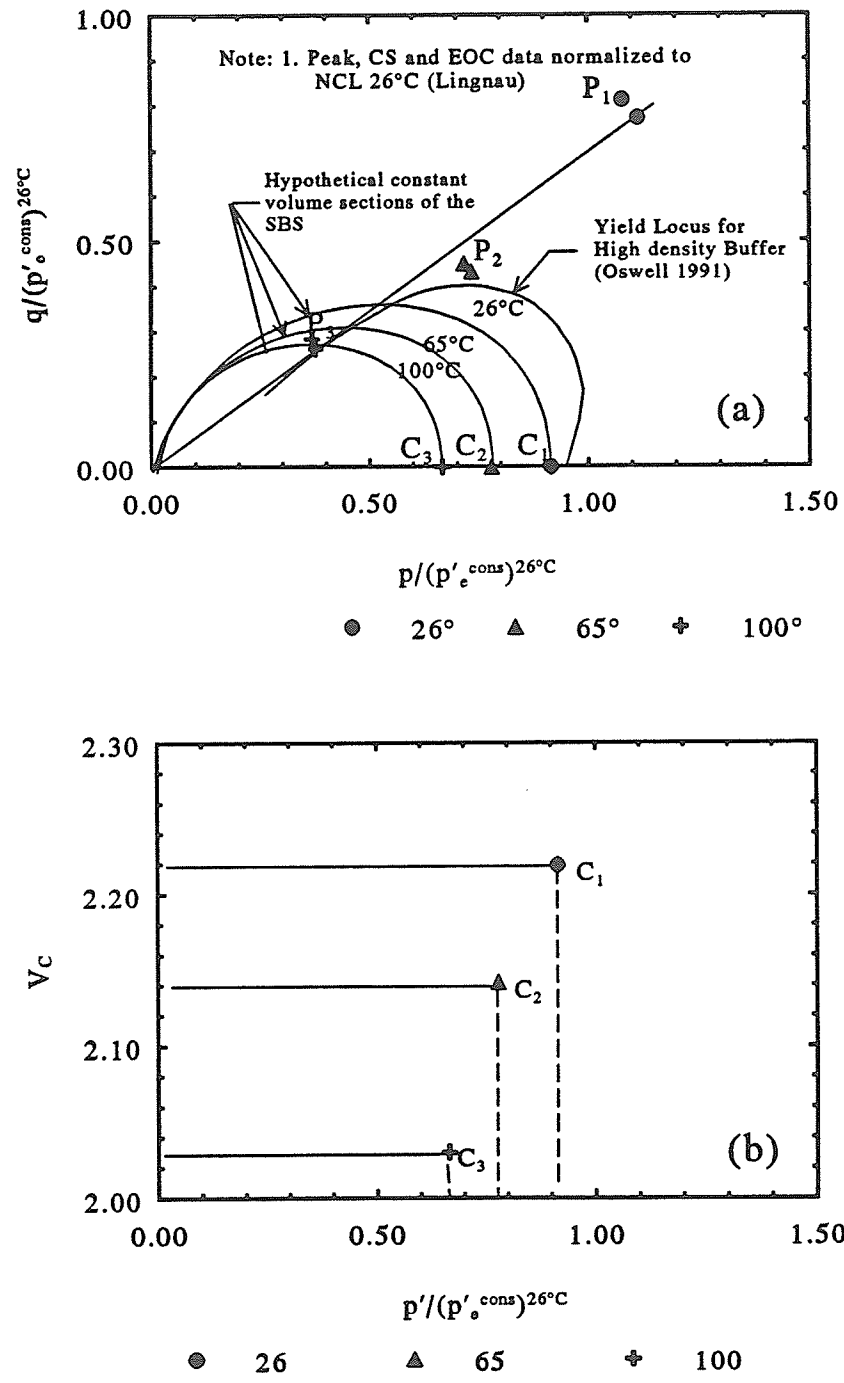


FIGURE 8.31 Representation of SBS:

- (a) constant volume sections in $q-p'$ stress space normalized to equivalent pressures from the 26°C NCL;
- (b) constant volume sections in normalized compression space

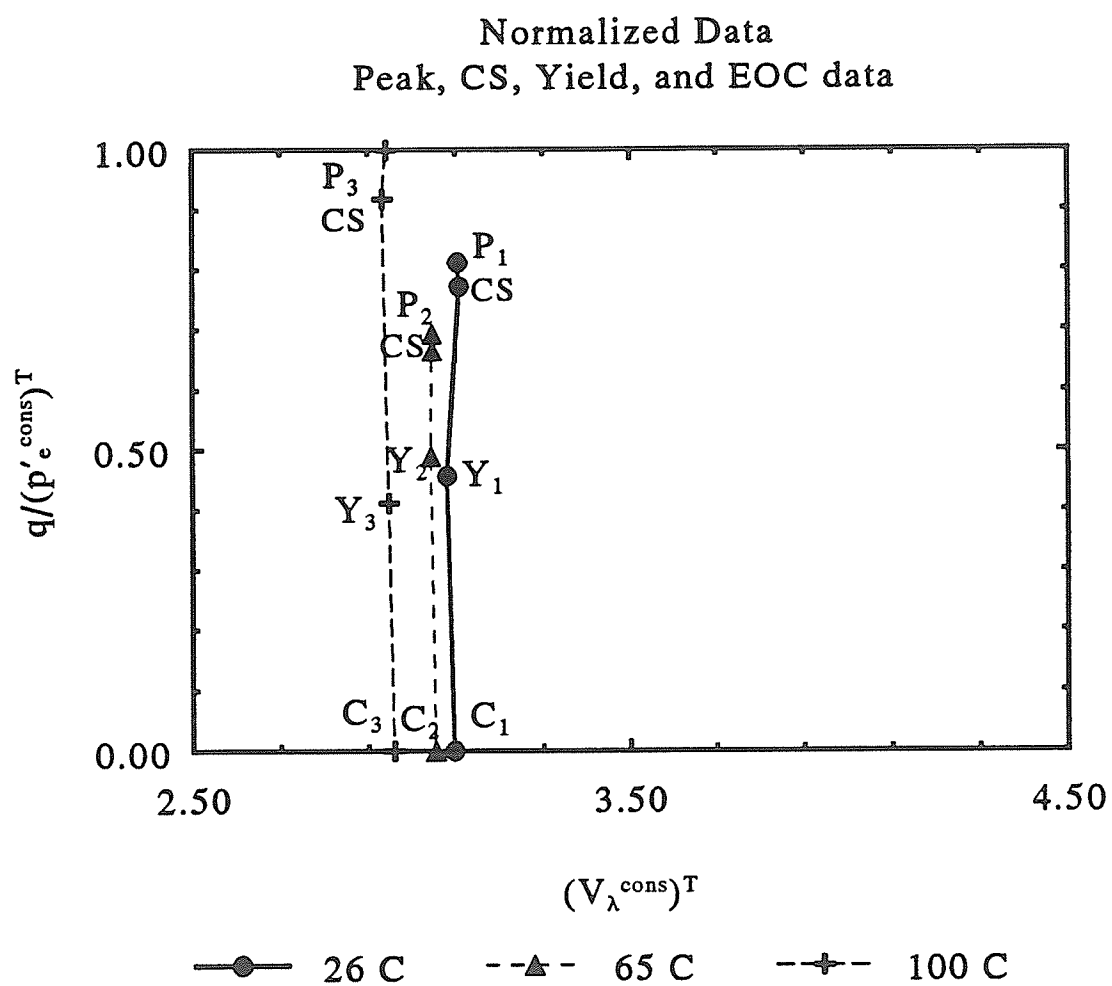


FIGURE 8.32 Average data points for EOC, Yield, Peak and CS in q/p' - V_λ space normalized to NCL's for each temperature.

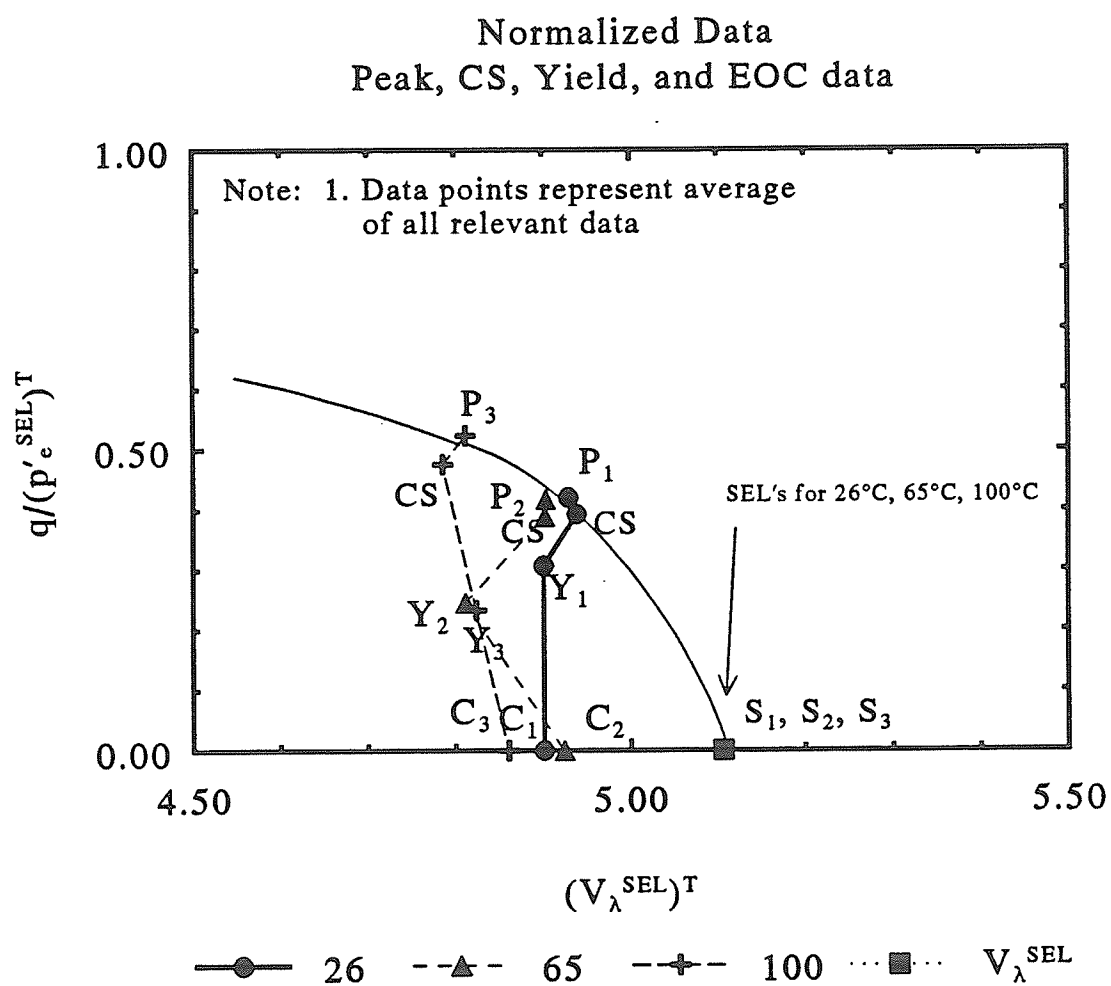


FIGURE 8.33 Average data points for EOC, Yield, Peak and CS in q/p' - V_λ space normalized to SEL's for each temperature

SUMMARY: TRIAXIAL CONSOLIDATION
 $T = 26^\circ C, 65^\circ C, 100^\circ C$; HIGH DENSITY

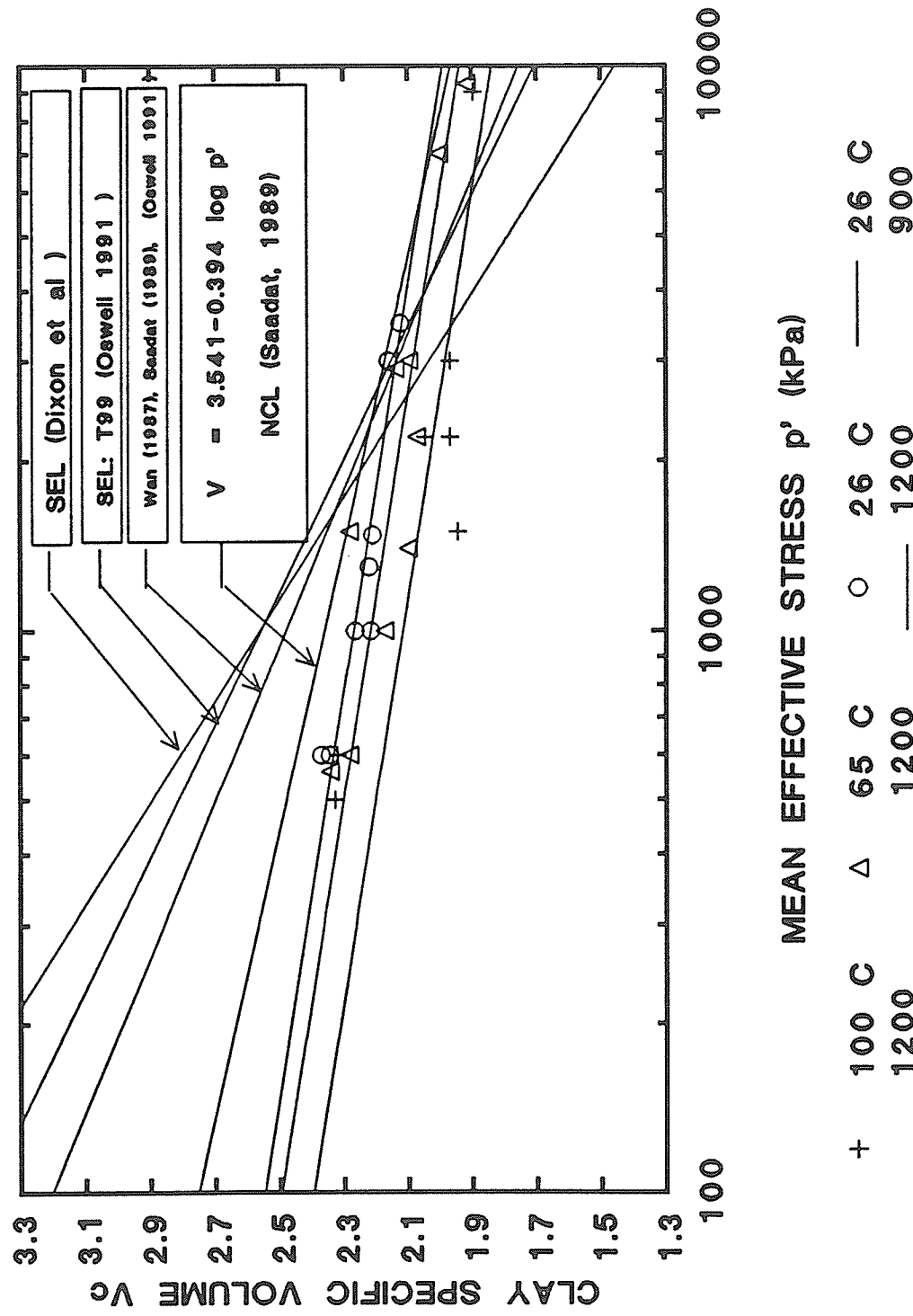


FIGURE 8.34 Hardening laws and SEL's lines in compression space

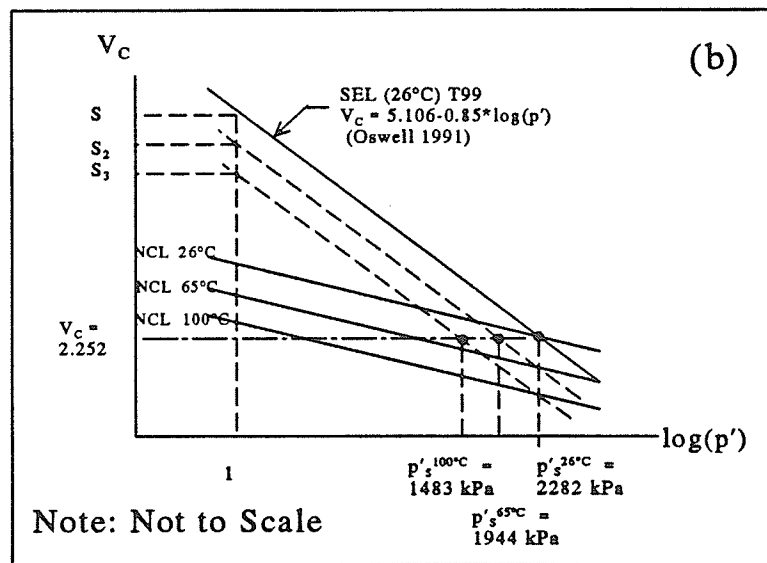
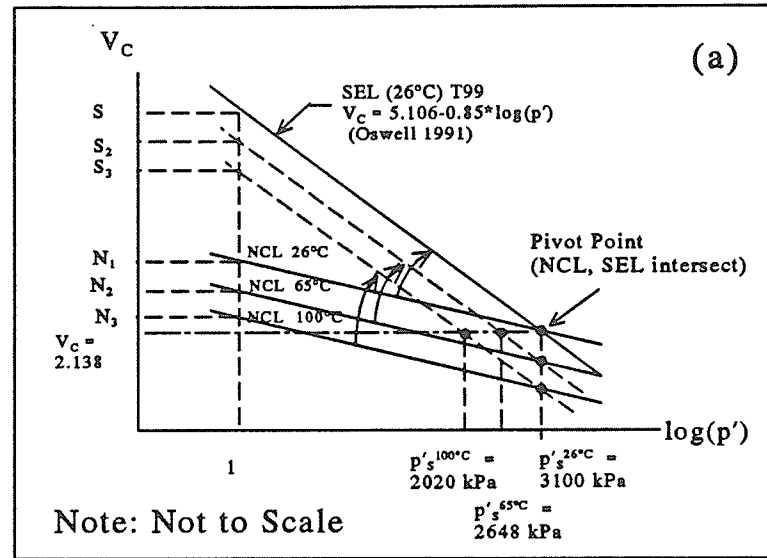


FIGURE 8.35 Interpretation of swelling equilibrium pressures (SEP's) at elevated temperature:
(a) from hardening laws at elevated temperature and 26°C SEL; and
(b) at compaction specific volume

APPENDIX A: Membrane Corrections

This appendix shows the methods used to calculate the membrane corrections discussed in Chapters 3 and 6. The corrections used here are for temperatures of 26°C only. However, it is possible conduct the ASTM tests at elevated temperature to obtain corrections for membranes in air at elevated temperature. This would not account for the effect of cell fluid interaction with the membranes.

The membrane correction depends mostly on extension modulus, E_m , and the amount of strain in the membrane. The stress-strain behavior of a thin membrane interacting with a soil specimen is complex. A simplified approach is used by the Larochelle *et al.* (1988). They suggest analyzing two modes of membrane deformation: (1) column deformation; and (2) buckling. The first mode implies strength added to the specimen through (a) resistance to vertical load and (b) horizontal confinement. The first mode is used to calculate membrane corrections for specimens at peak strength in Part I(A). This is justified for stiff buffer specimens. The effects of two membranes (yellow and blue) are summed in Part I(A)(3). ASTM D4767-88 gives an additional criterion for membrane corrections which is checked for Peak Strength in Part I(B).

The second mode implies large non-uniform lateral deformations. Hoop stresses adds more strength to the specimen as it strains, but at the same time the modulus of the membrane decreases due to decreased thickness. The second mode is used for calculating membrane corrections at End-of-test in Part II(A).

The method used in ASTM D4767-88 for calculating the extension modulus of membranes is also disussed briefly in Part III. This method is based on early work of Henkel and Gilbert (1965). The reader is referred to more recent work by Larochelle *et al.* (1988)

EXAMPLE CALCULATION OF MEMBRANE CORRECTION: SPECIMEN T1228I. PEAK DEVIATOR STRESS, q_{peak} :A. Method: Larochelle *et al.* (1988)

Assume that the membrane does not buckle at q_{peak} (small strain)

The following are known from T1228:

$$q_{peak} = 1600 \text{ kPa}; \sigma'_c = 2200 \text{ kPa}$$

$$(\varepsilon_1)_{peak} = 2.58\%; \varepsilon_v = 0$$

$$a_o = 2024 \text{ mm}^2; d_o = 50.77 \text{ mm}$$

$$a_c = a_o \left(\frac{1}{1 - \varepsilon_1} \right) = \frac{2024}{1 - 0.0258} = 2077 \text{ mm}^2 \text{ (Corrected specimen area)}$$

2 Membranes used: Yellow + Blue

1. YELLOW MEMBRANE:

From Equation [5] (Larochelle *et al.* 1988):

$$\sigma_{1m} = \frac{\pi d_o M \varepsilon}{a_c} = \frac{\pi (50.77 \text{ mm})(7.19 \text{ N/cm} \cdot 1 \text{ cm}/10 \text{ mm} \cdot 2)(0.0258)}{2077 \text{ mm}^2} \\ = 0.00284 \text{ N/mm}^2 = 2.82 \text{ kPa}$$

where

d_o = diameter of specimen at E.O.C.

M = Modulus (Extension) of Membrane (N/cm)

= [ASTM D4767-88, Henkel and Gilbert, 1965]

= 1345 kPa @ $\varepsilon = 43.2\% \equiv 7.19 \text{ N/cm}$

(See calculation shown later)

Assume 2×7.19 to estimate M at low strain $\varepsilon_1 = 0.0258$

$$a_c = 2077$$

From Equation [4]: (Larochelle *et al.* 1988)

$$\sigma_{om} = 2M_i \left[\frac{d_o - d_{im}}{d_o d_{im}} \right] = 2(14.38 \cdot 1 \text{ cm}/10 \text{ mm}) \cdot \frac{50.77 - 49.24}{(50.77)(49.24)} \\ = 0.00176 \text{ N/cm} = 1.76 \text{ kPa}$$

where

$$d_{im} = \text{initial diameter membrane} = 49.24 \text{ mm}$$

$$M_i = \text{initial tangent modulus (1 %) of Membrane}$$

(Assume $2xM = 14.38 \text{ N/cm}$; conservative estimate)

calculate the correction to q is the sum of

$$\begin{aligned}\Delta q &= p_{om} + \sigma_{1m} \\ &= 1.76 + 2.82 = 4.58 \text{ kPa}\end{aligned}$$

similarly

2. BLUE MEMBRANE:

Equation [5]:

$$\sigma_{1m} = 1.41 \text{ kPa}$$

where

$$M = 11.1 \text{ N/cm}$$

Equation [4]:

$$p_{om} = 6.88$$

where

$$d_o = \text{Specimen + Membrane} = 50.77 + 2.5 = 53.27 \text{ mm}$$

$$d_{im} = 49.24$$

calculate the correction to q

$$\begin{aligned}\Delta q &= p_{om} + \sigma_{1m} \\ &= 6.88 + 1.41 = 8.29 \text{ kPa}\end{aligned}$$

3. YELLOW + BLUE

$$\Delta q = 4.59 + 8.29 = 12.88 \text{ kPa}$$

$$\Delta q/q_{peak} = 12.88/1600 = 0.80 \%$$

NOTE: 1. Correction will be smaller if buckling occurs, therefore the initial assumption is conservative

2. The correction will be larger for 2 blue membranes

B. Method: ASTM D4767-88 (1988)

Apply corrections only if Δq exceeds $q_{\text{peak}} \times 5\%$

YELLOW:

$$\Delta q = \Delta(\sigma_1 - \sigma_3) = \frac{4 \cdot E_m t_m \epsilon_1}{D_e} = \frac{4(2 \times 1345 \text{ kPa})(1.25 \text{ mm})(0.0258)}{50.77 \text{ mm}}$$

$$= 6.83 \text{ kPa}$$

BLUE:

$$\Delta q = \frac{4(2 \times 2052)(1.25)(0.0258)}{50.77} = 10.43 \text{ kPa}$$

YELLOW + BLUE:

$$\Delta q = 6.83 + 10.43 = 17.26 \text{ kPa}$$

$$\Delta q/q_{\text{peak}} = 1.07\%$$

- NOTE: 1. $5\% \times q_{\text{peak}} = 80 \text{ kPa}$ therefore no correction required
 2. $17.26 \text{ (ASTM)} > 12.88 \text{ (Larochelle)}$

II. FINAL DEVIATOR STRESS (END OF TEST), q_{eot} :

A. Method: Larochelle *et al.* (1988)

Assume buckling occurs

From Equation [6]:

$$\sigma_{3m} = p_{om} = 0.75 \cdot \frac{M\sqrt{\epsilon}}{d_o}$$

From T1228:

$$\epsilon_{\text{eot}} = 7.0\%$$

$$q_{\text{eot}} = 1.48 \text{ MPa}$$

YELLOW + BLUE MEMBRANE:

$$p_{om} = 1.76 + 6.88 = 8.64 \text{ kPa}$$

$$\sigma_{3m} = 8.64 + \frac{0.75(M_Y(27\%) + M_B(47\%))\sqrt{\epsilon}}{d_o}$$

$$= 8.64 + \frac{0.75(1345 + 2052)\sqrt{0.07}}{50.77}$$

$$= 21.91 \text{ kPa}$$

$$\Delta q/q_{\text{eot}} = 1.4\%$$

B. Method: ASTM D4767-88

No correction specified

III. CALCULATION OF M ($=E_m$):

ASTM D4767-88 uses Henkel and Gilbert's method for computing the extension modulus, E_m . This is assumed to be equivalent to Young's modulus. It is also assumed that the modulus is the same in tension and compression. Basically the load required to stretch a section of membrane (band) is measured.

$$E_m = M = \frac{F / A_m}{\Delta L / L} \text{ (kPa)}$$

where

E_m = Young's modulus, psi (kPa)

F = Force to stretch a band, lbf (kN)

L = Unstretched length of the band, inches (mm)

ΔL = Change in length of the band, inches (mm)

A_m = Area of band = $2xt_m \cdot W_s \text{ in}^2$ (mm^2)

t_m = band thickness

w_s = width of band

This can be converted to N/cm by multiplying E_m by the membrane thickness, t .

APPENDIX B: Moisture Content Data

TABLE B1: Specimen Preparation and Moisture Content Data

TEST NO. ²	Start Consolidation					End-of-Test				
	T (°C)	w _o [%]	γ_d (Mg/m ³)	S _o [%]	V _{co} (S=S _o)	ϵ_v [meas]	w _f [%]	V _{cf} ¹ [calc]	V _{cf} ¹ [meas]	ΔV_{cf}
						(%)	(%)	(S=1)	(S=1)	
T1204	26	22.5	1.65	94.8	2.306	-0.38	22.2	2.250	2.221	0.0289
T1205	65	28.2	1.51	96.2	2.613	3.80	23.3	2.415	2.282	0.1332
T1206 ³										
T1207	26	23.5	1.63	96.5	2.340	3.00	20.4	2.193	2.122	0.0706
T1208	26	20.9	1.66	90.4	2.271	-7.50	24.9	2.388	2.369	0.0195
T1209	65	22.2	1.64	93.2	2.310	4.24	20.0	2.083	2.100	-0.0170
T1210 ³	63									
T1211	65	21.6	1.66	93.6	2.269	6.17	20.7	1.989	2.139	-0.1490
T1212	26	22.7	1.64	94.8	2.317	-4.38	24.4	2.392	2.342	0.0504
T1213	52	23.5	1.64	98.2	2.316	6.20	15.0	2.086	1.825	0.2611
T1214	65	22.5	1.63	92.5	2.338	4.78	19.5	2.081	2.073	0.0085
T1215	26	21.5	1.65	90.8	2.302	-2.67	22.0	2.268	2.210	0.0585
T1216	62	22.7	1.63	93.7	2.332	-4.40	24.4	2.393	2.342	0.0511
T1217	24	21.9	1.64	91.9	2.310	0.64	21.1	2.184	2.161	0.0233
T1218	27	21.8	1.64	91.7	2.307	-4.23	23.0	2.336	2.265	0.0709
T1219	63	22.3	1.64	92.7	2.323	-3.20	21.3	2.331	2.172	0.1594
T1220	65	21.3	1.69	95.5	2.227	-0.47	21.3	2.187	2.172	0.0151
T1221	26	22.4	1.67	97.8	2.259	-4.40	22.1	2.376	2.216	0.1603
T1222 ⁴	65					0.05				
T1223	65	22.0	1.67	95.7	2.265	3.82	19.9	2.086	2.095	-0.0090
T1224 ⁴	65					-2.66				
T1225	65	22.3	1.67	97.5	2.258	-1.66	23.3	2.281	2.282	-0.0008
T1226	100	23.5	1.66	101.4	2.274	0.26	17.6	2.284	1.968	0.3158
T1227	100	21.8	1.68	96.8	2.238	4.39	17.2	2.057	1.946	0.1109
T1228	100	21.7	1.69	97.7	2.221	4.23	17.6	2.057	1.968	0.0888

T1229	65	21.4	1.70	98.4	2.196	8.00	18.2	1.920	2.001	-0.0810
T1230	100	22.2	1.67	97.1	2.257	2.41	19.0	2.142	2.045	0.0975
T1231 ⁴	100					1.50				
T1232	100	22.1	1.67	96.1	2.265	3.25	24.1	2.110	2.326	-0.2160
T1233	100	22.5	1.66	96.3	2.285	-13.50	24.0	2.680	2.320	0.3596
T1234	100	21.8	1.67	95.8	2.251	-10.00	30.1	2.523	2.656	-0.1330
T1235	100	21.9	1.66	94.8	2.272	5.32	16.3	2.033	1.895	0.1382
T1236	65	21.7	1.67	95.2	2.255	6.84	16.7	1.975	1.916	0.0583
Avg.		22.1	1.65	95.2						0.0598
Std.Dev.		0.6	0.01	2.5						0.1243

- NOTE:
1. $V_o = \text{Initial specific volume} = 1 + e_o$
 - $V_{co} = \text{Initial clay specific volume} = 1 + e_{co}$
 - $V_c = \text{Specific volume (after Saadat 1989)} = 0.491V_c + 0.509$
 - $V_{cf}[\text{calc}] = \text{Calculated final clay specific volume}$
 $= V_{co} - \epsilon_v \cdot (1.037 + V_{co})$
 - $V_{cf}[\text{meas}] = \text{Measured final clay specific volume}$
 $= 1 + 5.5(w_f/S_f); S_f = 1.0$
 - $S_o = \text{Initial saturation} = w_o \cdot \gamma_d \cdot G_s / (G_s - \gamma_d)$
 2. Missing test numbers are tests that were preliminary, quality control, or in which leaks, etc. developed. These tests will not be included in the data analysis.
 3. Equipment failure, no test results
 4. Dummy specimen

APPENDIX C: Compaction Data

TABLE C1: Summary of Compaction Data.

	Compaction				Post-Compaction		
	σ_g (psi)		σ_v (kPa)		w_o (%)	V_{co} (S=1)	p'_{cons} (kPa)
	last lift	avg lift	last lift	avg lift			
T1204					22.5	2.238	1300
T1205					28.2	2.551	1400
T1207	900	900	4464	4464	23.5	2.293	3000
T1208	900	900	4464	4464	20.9	2.150	500
T1209	1000	800	4960	3968	22.2	2.221	1400
T1210	900	900	4464	4464			1600
T1211	1100	900	5456	4464	21.6	2.188	3000
T1212	900	900	4464	4464	22.7	2.249	600
T1213	1500	1300	7440	6448	23.5	2.293	1600
T1214	900	800	4464	3968	22.5	2.238	2200
T1215	800	750	3968	3720	21.5	2.183	1500
T1216	900	800	4464	3968	22.7	2.249	600
T1217	800	750	3968	3720	21.9	2.205	3000
T1218	850	750	4216	3720	21.8	2.199	1000
T1219	850	750	4216	3720	22.3	2.227	1000
T1220	5000	3700	24800	18352	21.3	2.172	1000
T1221	3500	2200	17360	10912	22.4	2.232	1000
T1223	5000	4300	24800	21328	22.0	2.210	3000
T1225	5100	3980	25296	19741	22.3	2.227	600
T1226	5300	4500	26288	22320	23.5	2.293	3000
T1227	4400	3400	21824	16864	21.8	2.199	1500
T1228	4600	2900	22816	14384	21.7	2.194	2200
T1229	3100	1920	15376	9523	21.4	2.177	7000
T1230	5200	4000	25792	19840	22.2	2.221	2200
T1232	5300	4680	26288	23213	22.1	2.216	500
T1233	5000	4640	24800	23014	22.5	2.238	600

NOTE:1. σ_g = gauge pressure; σ_v = vertical pressure

APPENDIX D: Membrane Types

TABLE D1: Types of Membranes used in HITEP Tests: Yellow 5026 A/B (Y), Blue 5050 A/B (B), Latex (L). Two membranes were used in most tests

Test No.	Temp. (°C)	Membranes Inner/Out	Thickness mm (inch)	Comments
T1204	26	L/L	1.40 (0.055)	
T1205	65	Y/B	1.25 (0.050)	
T1206				No test
T1207	26	L/L	0.25 (0.010)	
T1208	26	L	1.40 (0.055)	
T1209	65	Y/B	1.25 (0.050)	
T1210	63	Y	1.25 (0.050)	DW Apparatus
T1211	65	Y/B	1.25 (0.050)	
T1212	26	L	1.25 (0.050)	
T1213	52	B	1.25 (0.050)	DW Apparatus
T1214	65	Y/B	1.25 (0.050)	Photo ¹
T1215	26	L	2.54 (0.100)	
T1216	62	Y/B	1.25 (0.050)	
T1217	24	L	1.40 (0.055)	
T1218	27	L	1.40 (0.055)	Photo
T1219	63	Y/B	1.25 (0.050)	Photo
T1220	65	Y/B	1.25 (0.050)	
T1221	26	L	1.40 (0.055)	
T1222	65	Y/B	1.25 (0.050)	Photo
T1223	65	Y/B	1.25 (0.050)	
T1224	65	Y/B	1.25 (0.050)	Photo
T1225	65	Y/B	1.25 (0.050)	Photo
T1226	100	Y/Y	1.25 (0.050)	Out of B
T1227	100	Y/B	1.25 (0.050)	
T1228	100	Y/B	1.25 (0.050)	

T1229	65	Y/B	1.25 (0.050)
T1230	100	B/B	1.25 (0.050)
T1231	100	Y/B	1.25 (0.050)
T1232	100	B/B	1.25 (0.050)
T1233	100	B/B	1.25 (0.050)
T1234	100	B/B	1.25 (0.050)
T1235	100	B/B	1.25 (0.050)
T1236	65	B/B	1.25 (0.050)

NOTE: 1. From photograph

APPENDIX E: LEAKAGE AND DIFFUSION TESTS

Leakage tests have been carried out in two different apparatuses: (1) HITEP cells; and (2) low pressure triaxial cells. Three tests were carried out using dummy specimens in the HITEP cells (T1222, T1224, T1231). The results for these tests are discussed in Chapter 5. Five tests were carried out in the low pressure triaxial cells (SML1-SML5). The results for two of these tests (SML3, SML4) were summarized in Table 5.6. The instantaneous volume change rates for these tests are given in Figure E.1 and E.2. The volume change rate reaches equilibrium after 1 day. Clearly, the average rate is 0.1 %/day for SML3 and about 0.02 %/day for SML4.

Membrane diffusion tests were carried out in the diffusion apparatus described in Chapter 3. Tests were performed at 26°C and 65°C, but tests at elevated temperature were not successful. Net diffusion rates for tests at 26°C (MD1, MDAL2) were given in Table 5.7. The results of calibration volume change tests are summarized in Table E.1. Here, diffusion and leakage rates are given in units of ml/day. Net diffusion is calculated by subtracting system volume change from measured volume change.

$$[E.1] \quad (\Delta \dot{V})_{\text{Net}} = (\Delta \dot{V})_{\text{Diffusion}} - (\Delta \dot{V})_{\text{System}}$$

The tests were conducted at the same effective stress, temperature and duration. Similar calculations can be done for different pressures.

TABLE E.1: Summary of Membrane Diffusion/Leakage Results from the Diffusion Apparatus at 0.6 MPa effective stress. Membrane diffusion area is 1/20 of triaxial membranes. A single silicone membrane of thickness 1.2 mm was used. Isotropic stress conditions were used with silicone oil as cell fluid.

Test No.	B.P. (MPa)	p' (MPa)	ΔV (ml/day)	T (°C)	t (day)	Test Type
MDAL1	1.6	-	0.01	26	4.0	Burette Leak ¹
MDAL2	1.0	0.6	-0.01	26	4.0	System Leak ²
MD1	1.0	0.6	0.006	26	4.0	Memb Diffuse ³
	1.0	0.6	0.016	26	4.0	Net Diffusion

NOTE: 1. Burette was isolated for the Burette Leak test
 2. A metal cover plate was placed over the membrane to prevent diffusion. A single O-ring was used in the pedestal of the apparatus. The membrane was clamped with an aluminum ring.
 3. Metal cover removed; Results include all system leakage effects

The results of a multistage system leakage test (MDAL2) for the diffusion apparatus are summarized in Table E.2. The results of a multistage diffusion test are summarized in Table E.3. Figure E.3 shows a comparison of the rates. Generally, the diffusion rates were less than the system compliance. The apparatus was capable of applying a larger pressure on the water-membrane interface than the oil-membrane interface which resulted in a negative value of effective stress. This was a severe test to check leakage of the membrane clamping system. Test MD1-1 is shown in Figure E. 4. Test MD1-2 is shown in Figure E.5. Test MDAL2 is shown in Figure E.6.

TABLE E.2: Summary of Results from a Multistage System Leakage Test on the Diffusion Apparatus. Membrane diffusion area is 1/20 of triaxial membranes. A single membrane (RTV 5050 A/B) with a thickness of 1.2 mm was used. Silicone oil (CSL cP 500) was used for cell fluid.

Test No.	p' (MPa)	$\Delta \dot{V}$ (ml/day)	T (°C)	t (day)	Test Type	Comments
MDAL2-A	-1.7	0.096	26	0.5	Leak	Non-Equilibrium
MDAL2-B	0.6	-0.010	26	4.0	"	SS after 2 days
MDAL2-C	3.0	0.052	26	2.0	"	SS after 0 days
MDAL2-D	7.0	0.001	26	6.0	"	SS after 0.5 days
MDAL2-E	9.0	-0.0005	26	2.0	"	SS after 0.5 days

Note: 1. SS = steady state

TABLE E.3: Summary of Results from a Multistage Diffusion Test (MD1) from the Membrane Diffusion Apparatus. Membrane diffusion area is 1/20 of triaxial membranes. A single membrane (RTV 5050 A/B) of thickness 1.2 mm was used. Silicone oil (CSL cP 500) was used for cell fluid.

Test No.	p' (MPa)	$\Delta \dot{V}$ (ml/day)	T (°C)	t (day)	Test Type	Comments
MD1-1	0.6	-0.006	26	4.0	Diff	SS after 1 day
MD1-2	3.0	0.027	26	4.5	"	SS after 0 day
MD1-3	9.0	-0.005	26	5.0	"	SS after 1.0 day

TABLE E.4: Summary of Membrane Diffusion and Leakage Results from Yarechewski (1993) and Lingnau (1993). Results are from triaxial and diffusion apparatuses.

Test No.	B.P. (MPa)	p' (MPa)	ΔV (ml/day)	T (°C)	t (day)	Comments
Multistage Diffusion Test (Yarechewski 1993)¹: Diffusion Apparatus						
1	1.0	0.6	0.08	26	6	New Memb.Seal & Ped
2	"	1.5	0.22	26	3	"
3	"	3.0	0.26	26	2	"
4	"	6.0	0.30	26	3	"
5	"	9.0	0.30	26	2	"
6	"	0.6	0.16	65	5	"
7	"	1.5	0.40	65	2	"
8	"	3.0	0.60	65	2	"
9	"	0.6	0.10	100	8	"
10	"	1.5	0.60	100	2	"
11	"	3.0	0.88	100	3	"
12	"	0.6	0.10	26	3	"
Diffusion Tests (Lingnau 1993)²: Diffusion Apparatus						
MDAL1	1.0	0.6	0.32	26	4	1/20 Area
MDAL2	1.0	3.0	-50	26	4	"
MDAL3	1.0	9.0	0.11	26	4	"
Leakage Tests (Lingnau 1993)³: Low pressure triaxial cell						
SML1						
SML2						
SML3	0.5	1.0	0.10	26	5	Sil/Sil/Dummy
SML4	0.5	1.0	0.02	26	40	Water/Sil/Dummy
SML5						
Leakage Tests (Lingnau 1993)⁴: HITEP Apparatus						
Leak#1	1.0	-	-02	65	5	Burr/Lines
Leak#1	1.0	2.0	-05	65	10	Burr/Lines/Pedestal

T1222	1.5	3.0	0.012	65	32	
T1224	1.0	1.0	-.225	65	40	
T1231	1.0	0.6	-.06	100	26	
Leakage Tests (Saadat 1989) ⁵ : High pressure TX cell						
1.	0.3	1.5	0.01	26	14	Sil/Latex/Dummy
2.	0.3	3.0	0.01	26	13	Sil/Latex/Dummy
3.	7.0	3.0	0.01	26	4	Sil/Latex/Dummy
Leakage Tests (Leroueil <i>et al.</i> 1988): Triaxial cell						
1.			0.006			Sil/Latex/Dummy
2.			0.207			Glycerin/Latex/Dum
3.			?			

-
- Note:
1. New method of sealing membrane used. Single full size membrane 1.2 mm thick used. Silicone cell fluid. New pedestal seals
 2. Single layer of silicone membrane coupon (RTV 5050 A/B) 1.2 mm thick used. Area of coupon is 1/20 of full size membrane. Silicone oil cell fluid used (CSL 500 cP). Single O-ring used in pedestal. Values of ΔV are net (measured - system compliance).
 3. Single layer of membrane used. Latex and silicone membranes tested. Two different cell fluids tested: de-aired water and silicone oil. System compliance negligible.
 4. Double silicone membranes used. Full size 1.2 mm thick. Silicone cell fluid used. Test Leak#1 shows compliance of lines and pedestal
 5. Double latex membranes 0.64mm thick were used for the first two tests. A single latex membrane 1.27mm thick was used

APPENDIX F: Thermal Expansion Coefficients

This Appendix shows the methods for calculating: (1) thermal volumetric compliance, ΔV_{app} of the HITEP apparatus; (2) thermal expansion coefficients for the mineral solids, β_s ; (3) thermal expansion coefficient, β_{cw} , for the pore water and bulk water, β_w ; (4) pressure dependency of β_w ; and (5) temperature dependency of β_w .

I. Estimate Thermal Volume Change of Water in the HITEP Apparatus:

Consider the Porous Stones, Drainage lines, and Transducer Housing.

Assume:

- (1) Pressure dependency of thermal expansion coefficient of bulk water, β_w , is negligible. (See Pressure dependency calculation later)
- (2) Operating temperature of porous stones, drainage lines and transducer are the same for all. Actually, the transducer temperature is 10°C to 20°C cooler than the cell
- (3) $\beta_w = 923 \times 10^{-6} \text{ } 1/\text{ }^\circ\text{C}$ at 65°C; and 1162×10^{-6} at 100°C (Baldi *et al.* 1991)

The following has been measured in the current test program:

- (a) Volume of water in drainage lines at room temperature, $V_{DL} = 2.8 \text{ ml}$
- (b) Volume of water in porous stones at room temperature, $V_{ST} = 6.0 \text{ ml/each}$
- (c) Volume of water in transducer at room temperature, $V_{TR} = 5.7 \text{ ml}$

The total volume of water in the system is then $2.8 + 6.0 \times 2 + 5.7 = 20.5 \text{ ml}$

Therefore the thermal expansion of the apparatus water, ΔV_{app} , is:

$$[F.1] \quad \Delta V_{app} = \beta_w (V_{DL} + V_{ST} + V_{TR})$$

The apparent thermal volumetric strain produced by thermal expansion of the apparatus water, ϵ_v , is:

$$[F.2] \quad \epsilon_v = \Delta V_{app}/V_o$$

where V_o is the volume of a dummy specimen = 203 ml

The volume change, ΔV_{app} , is calculated for 65°C and 100°C and compared with triaxial test results on dummy specimens as a check in Table F.1:

Table F.1: Comparison of calculated and measured thermal expansion of apparatus water.

TEST	Pres. (MPa)	Temp. (°C)	V_w (ml)	ΔT (°C)	$\beta_w \times 10^{-6} \Delta V$ (1/°C)	ϵ_v (ml)	ϵ_v [meas] (%)	Diff (%)
T1222	1.0-3.0	65	14.5	40	923	0.535	0.26	0.26
T1224	1.5	65	20.5	40	923	0.757	0.37	-0.75
T1231	0.6	100	20.5	75	1162	1.786	0.89	1.50
LEAK#1	2.2	65	20.5	40	923	0.757	0.37	0.12

NOTE: 1. T1224 had a membrane leakage problem
2. T1222 had drainage only at the bottom

Clearly this calculation provides a rough estimate of thermal expansion of the apparatus water. The discrepancies shown in Table F.1 are due to factors which can not be accounted for. These include compression of seals, and mechanical expansion of the system at different pressures.

As a final check, the calculations are checked against test results from Yarechewski (1992) in Table F.2:

Table F.2: Comparison of calculated and measured values (average) of thermal expansion of apparatus water.

Temp. (°C)	ϵ_v [calc] (%)	ϵ_v [meas] (%)	ϵ_v [meas] (%)
(Lingnau) (Yarechewski 1992)			
65	0.37	0.20	0.30
100	0.89	1.50	0.70

The following conclusions may be drawn:

- (1) The calculated thermal expansion of the apparatus water, ΔV_{app} is of the same order of magnitude as the measured system thermal compliance.
- (2) Dixon's coefficient of thermal expansion for bulk water, β_w can be considered accurate.

II. Check Dixon's estimate of thermal expansion of Montmorillonite:

McKinstry (1965) used X-ray diffraction techniques to measure the thermal expansion coefficients of several dry clays parallel ($\bar{\alpha}_1$) and perpendicular ($\bar{\alpha}_2$) to the layers of clay particles. The linear expansion coefficients mentioned are average values for a given temperature range, hence the superscript bar. Several points are worth noting:

- (1) He found that the coefficient for active clays was always greater perpendicular to the clay particles.
- (2) He studied only reversible expansion behavior, that is, below temperatures at which mineralogical changes occur.
- (3) He used powdered, dry samples presumably at atmospheric pressure

Table F.3 summarizes some of his results:

**Table F.3: Linear coefficients of thermal expansion for minerals, α_1 , α_2 .
(after McKinstry 1965).**

Mineral	$\bar{\alpha}_1 \times 10^{-6}$ (1/°C)	$\bar{\alpha}_2 \times 10^{-6}$ (1/°C)	Temp. Range (°C)
Kaolinite	18.6 ± 1.3	5.2 ± 1.7	25 - 400
Pyrophyllite	14.9 ± 1.8	12.2 ± 0.7	25 - 400

The volumetric coefficient of thermal expansion can be calculated as follows for an isotropic material (Haliday and Resnick 1970):

$$[F.3] \quad \beta = \left[\frac{1}{V} \cdot \frac{\Delta V}{\Delta T} \right] = \left[\frac{1}{V} \cdot \frac{3\alpha V \Delta T}{\Delta T} \right] = 3\alpha$$

By averaging the linear coefficients, the volumetric coefficient can be obtained.

Table F.4 shows the calculated volumetric coefficients for mineral solids, β_s :

Table F.4: Volumetric coefficient of thermal expansion for minerals, β_s .

Mineral	$\beta_s \times 10^6$ (1/°C)	Temp. Range (°C)
Kaolinite	29.0	25 - 400
Pyrophyllite	39.3	25 - 400

These values agree with Dixon's estimates (Baldi *et al.* 1991).

McKinstry (1965) observed that dioctahedral and trioctahedral structures appear to have essentially similar expansion coefficients, α .

III. Dixon's calculation of thermal expansion coefficient, β_{cw}

Dixon established β_{cw} for water in contact with different minerals (Baldi *et al.* 1991). Most of his tests were carried out at 2.0 MPa pressure. He used a rigid walled cell which prevented changes in the dimensions of the specimen. His test method is relevant to calculating thermo-elastic (pore water) expansion because it is probable that skeletal deformation of the specimen was minimal.

He also attempted to evaluate the quantities of the four types of water in soil-water systems using soil suction measurement techniques but the results were not conclusive.

IV. Check the pressure dependency of β_w :

Using standard steam tables for pure liquid water the author found that the pressure dependency of β_w for bulk water was of the same order as the expansion coefficient for clay minerals. An example calculation is given below:

PRESSURE DEPENDENCY OF β_w AT 100°C:

Choose two similar temperatures close to 100°C with a convenient increment, say 100°C and 120°C. At Saturation Pressure (Approximately 0.1 MPa at 100°C) from Table 4 (Keenan *et al.* 1969):

$$[F.4] \quad T_1 = 100^\circ\text{C}; v_1 = 1.0436 \times 10^{-3}; \rho_1 = 958.221$$

$$[F.5] \quad T_2 = 120^\circ\text{C}; v_2 = 1.0604 \times 10^{-3}; \rho_2 = 943.040$$

where v is the specific volume of fluid and ρ is the density of the fluid. The specific volume is the inverse of density. Calculating differences:

$$[F.6] \quad \Delta\rho = -15.18$$

$$[F.7] \Delta T = +20^\circ C$$

$$[F.8] \rho_{avg} = 950.63$$

The laws of thermodynamics provide the following relationship for the volumetric thermal expansion coefficient:

$$[F.9] \beta = -\frac{1}{\rho} \left(\frac{\partial \rho}{\partial T} \right)_P \quad (\text{Incropera and DeWitt, 1981})$$

where β is the volumetric thermal expansion coefficient, ρ is density, T is temperature and P is pressure. Substituting F.6, F.7, and F.8 into F.9 gives:

$$[F.10] \beta = 798 \times 10^{-6} (1/\text{C})$$

CHECK β AT SATURATION:

From Table A.6 of Incropera and DeWitt (1981)"

$$[F.11] T_1 = 373.15^\circ K; P_1 = 1.0133 \text{ bars (0.10133 MPa)}; v_1 = 1.044 \times 10^{-3}; \beta = 750.1 \times 10^{-6}$$

$$[F.12] T_2 = 390.00^\circ K; P_2 = 1.7940 \text{ bars (0.1794 MPa)}; v_2 = 1.058 \times 10^{-3}; \beta = 841.0 \times 10^{-6}$$

$$[F.13] \Delta T = 20^\circ K; P_{avg} \cong \text{above}; v_{avg} \cong \text{above}; \beta_{avg} = 796$$

Since $\beta_{avg} \cong \beta$, the fluid is saturated. Similar Computations have been performed at 2.5 MPa and 10.0 MPa pressure and at 65°C.

Figure 6.12 summarizes the calculations. From the slopes of the curves in Figure 6.12a and 6.12b, the pressure dependency is:

$$[F.14] \left(\frac{\partial \beta}{\partial P} \right)_{100^\circ C} = 1.313 \times 10^{-6} (1/\text{C/MPa})$$

which is small compared to β .

V. Calculate the Temperature Variation of β :

$$[F.15] \left[\frac{\partial \beta}{\partial T} \right]_{0.1 \text{ MPa}} = 6.20 \times 10^{-6} \text{ (1/}^{\circ}\text{C/}^{\circ}\text{C)}$$

$$[F.16] \left[\frac{\partial \beta}{\partial T} \right]_{2.5 \text{ MPa}} = 6.14 \times 10^{-6} \text{ (1/}^{\circ}\text{C/}^{\circ}\text{C)}$$

$$[F.17] \left[\frac{\partial \beta}{\partial T} \right]_{10 \text{ MPa}} = 5.82 \times 10^{-6} \text{ (1/}^{\circ}\text{C/}^{\circ}\text{C)}$$

which are significant considering the range of temperatures in the current test program.

Baldi *et al.* (1991) derived a coefficient of thermal expansion α as a function of pressure and temperature:

$$[F.18] \frac{\partial \alpha}{\partial T} = 6.744 \times 10^{-6} - 3.664 \times 10^{-9} \kappa + 5.328 \times 10^{-13} \kappa^2$$

where κ is the pressure (bars). Applying equation [F.18] to the current test program:

$$[F.19] \left[\frac{\partial \alpha}{\partial T} \right]_{0.1 \text{ MPa}} = 7.74 \times 10^{-6} \text{ (1/}^{\circ}\text{C/}^{\circ}\text{C)}$$

$$[F.20] \left[\frac{\partial \alpha}{\partial T} \right]_{2.5 \text{ MPa}} = 6.74 \times 10^{-6} \text{ (1/}^{\circ}\text{C/}^{\circ}\text{C)}$$

$$[F.21] \left[\frac{\partial \alpha}{\partial T} \right]_{10 \text{ MPa}} = 6.74 \times 10^{-6} \text{ (1/}^{\circ}\text{C/}^{\circ}\text{C)}$$

Clearly, Hueckel's equation is insensitive to pressures over 1.0 MPa. His values at low pressures are approximately equal to the author's computations from Standard Steam Tables. The author's values will be used throughout the thesis.

APPENDIX G: Thermal Expansion Calculations

This Appendix deals with calculation of the change in volume of the clay structure with temperature (see Section 6.3). The structural volume change coefficient, β_{st} is calculated using two methods: (1) a forward calculation; and (2) a back calculation.

I. Forward Calculation

Use V_{co} and ϵ_v from the start of any given test and thermal expansion coefficients. Thermo-elasto-plastic theory tells us that combined heating and mechanical consolidation gives the following:

$$[G.1] \quad \epsilon_v = (\epsilon_v^{te} + \epsilon_v^{tp}) + (\epsilon_v^{se} + \epsilon_v^{sp})$$

where ϵ_v is the total volumetric strain, ϵ_v^{te} is the thermo-elastic strain, ϵ_v^{tp} is the thermo-plastic strain, ϵ_v^{se} is the stress dependent elastic strain, ϵ_v^{sp} is the stress dependent plastic strains. These are shown in Figure 6.15. In the case of the current test program, path 1-2-3 is relevant. The strain ϵ_v represents the volume of pore fluid drained from the specimen after consolidation at 65°C is complete. The first term on the RHS of equation G.1 is calculated from thermal expansion coefficients and represents the vertical separation between the NCL's at different temperatures in Figure 6.15. The second term is measured from consolidation tests at 26°C.

Rearranging equation G.1:

$$[G.2] \quad \epsilon_v - (\epsilon_v^{te} + \epsilon_v^{tp}) = (\epsilon_v^{se} + \epsilon_v^{sp})$$

Equation G.2 means that subtracting the calculated thermal volume change of the

clay plus water system from the total measured volume change at elevated temperature should give the stress dependent volume change, that is the volume change due to consolidation at room temperature. In other words, if the coefficients are correct, then equation G.2 should predict the 26°C NCL using the elevated temperature data.

Using the theory from Kosar (1989):

$$[G.3] \quad (\varepsilon_v^{te} + \varepsilon_v^{tp}) = \frac{1}{V_{to}} \left[\beta_{cw} V_w \Delta T - \beta_s (V_t - V_s) \Delta T - \beta_{st} V_t \Delta T \right]$$

where β_{cw} is the coefficient of thermal expansion of the pore water, β_s is the coefficient of thermal expansion for the mineral solids, β_{st} is the coefficient of thermal expansion for the soil skeleton, V_{to} is the initial specimen volume, V_w is the volume of water, V_t is the total specimen volume, V_s is the volume of mineral solids, and ΔT is the temperature change. The terms on the RHS represent thermal expansion of the water, voids, and skeleton, respectively. For the current test program, the following is true:

$$[G.4] \quad \varepsilon_v = (\varepsilon_v)_{meas} - (\varepsilon_v)_{app}$$

where $(\varepsilon_v)_{meas}$ is the total system and specimen volume change. $(\varepsilon_v)_{app}$ is the thermal volumetric apparatus compliance. This has been measured from tests LEAK#1, T1222, T1224, T1231. Combining equations G.1, G.3, and G.4 the following is true:

$$[G.5] \quad \left[(\varepsilon_v)_{meas} - (\varepsilon_v)_{app} \right] - \frac{1}{V_{to}} \left[\beta_{cw} V_w \Delta T - \beta_s (V_t - V_s) \Delta T - \beta_{st} V_t \Delta T \right] = (\varepsilon_v^{se} + \varepsilon_v^{sp})$$

For the purposes of discussion, $\beta_{cw} V_w \Delta T$ and $\beta_s (V_t - V_s) \Delta T$ may be thought of as thermo-elastic volume change, and $\beta_{st} V_t \Delta T$ may be thought of as the thermo-plastic volume change resulting from particle rearrangement in the soil skeleton. Choosing an elevated test temperature of 65°C, let:

$$[G.6] \quad (\epsilon_v)_{\text{meas}} = (\Delta V_d^{65})/V_o$$

$$[G.7] \quad (\epsilon_v)_{\text{app}} = (\Delta V_{\text{app}}^{65})/V_o$$

where (ΔV_d^{65}) and $(\Delta V_{\text{app}}^{65})$ are the total volume change and apparatus compliance due to a temperature change from 26°C to 65°C. Substituting equations G.6 and G.7 into G.5 gives:

$$[G.8] \quad \left[\Delta V_d^{65} - \Delta V_{\text{app}}^{65} \right] - \left[\beta_{\text{cw}} V_w \Delta T - \beta_s (V_t - V_s) \Delta T - \beta_{\text{st}} V_t \Delta T \right] = V_{t0} (\epsilon_v^{se} + \epsilon_v^{sp})$$

rearranging equation G.8 gives:

$$[G.9] \quad \beta_{\text{st}} = - \frac{1}{V_t \Delta T} \left[\Delta V_d^{65} - \Delta V_{\text{app}}^{65} - \beta_{\text{cw}} V_w \Delta T + \beta_s (V_t - V_s) \Delta T - V_{t0} (\epsilon_v^{se} + \epsilon_v^{sp}) \right]$$

The following was derived for buffer:

$$[G.10] \quad V_{cf} = V_{co} - \epsilon_v (1.037 + V_{co})$$

which can be rearranged:

$$[G.11] \quad \epsilon_v = \left[\frac{V_{co} - V_{cf}}{1.037 + V_{co}} \right]$$

knowing that $V_{co} = 2.252$ for buffer with saturation, $S=1$, and $\gamma_d = 1.67 \text{ Mg/m}^3$

and $V_o = 202 \text{ ml.}$:

$$[G.12] \quad \Delta V_d^{26} = 202 \left[\frac{2.252 - V_{cf}}{1.037 + 2.252} \right]$$

where

$$[G.13] \quad \Delta V_d^{26} = V_o \cdot \epsilon_v^{26}$$

The regression for the 26°C data gives the following hardening line:

$$[G.14] \quad V_{cf} = 3.102 - 0.278 * \log(p')$$

Combining G.14 and G.12 gives

$$[G.15] \quad \Delta V_d^{26} = 17.074 * \log(p') - 52.204$$

where p' is in MPa.

By definition:

$$[G.16] \quad V_o (\epsilon_v^{se} + \epsilon_v^{sp}) = \Delta V_d^{26} = 17.074 * \log(p') - 52.204$$

Combining G.16 and G.9 gives:

$$[G.17] \beta_{st}^{65} = -\frac{1}{V_t \Delta T} \left[\Delta V_d^{65} - \Delta V_{app}^{65} - \beta_{cw} V_w \Delta T + \beta_s (V_t - V_s) \Delta T - (17.074 * \log(p') - 52.204) \right]$$

A similar equation can be written for β_{st}^{100} where

$$[G.18] \beta_{cw} = 923 \times 10^{-6} (1/\text{C}) \text{ at } 65^\circ\text{C} \quad (\text{Hueckel et al. 1991})$$

$$[G.19] \beta_{cw} = 1162 \times 10^{-6} (1/\text{C}) \text{ at } 100^\circ\text{C} \quad (\text{Hueckel et al. 1991})$$

$$[G.20] \beta_s = 39 \times 10^{-6} (1/\text{C}) \text{ at } 65^\circ\text{C, } 100^\circ\text{C} \quad (\text{McKinstry 1965})$$

$$[G.21] \Delta V_{app}^{65} = 0.757 \text{ CC at } 65^\circ\text{C} \quad (\text{Graham et al. 1992})$$

$$[G.22] \Delta V_{app}^{100} = 1.787 \text{ CC at } 100^\circ\text{C} \quad (\text{Graham et al. 1992})$$

where p' is in MPa, ΔV_d^{65} , V_w , V_t , and V_s are measured for the current test.

Forward and back calculations of β_{st} for buffer at 65°C and 100°C are summarized in

Table 6.3.

NOTE:

1. Independent calculations by the author (Appendix G.2) using standard steam tables has confirmed Dixon's findings that β_{cw} is independent of the range of effective confining pressure used in the current program (0.6 to 10.0 MPa). Hueckel et al. (1991) showed that β_s has an even smaller pressure dependency.
2. Hueckel et al. (1991) showed that the pore water in dense buffer has a thermal expansion coefficient similar to bulk water at temperatures 100°C when the dry density is greater than 1.2 Mg/m³. A constant volume cell was used for their tests. If no particle slippage occurred then their value of β_{cw} would indeed be only thermo-elastic response. It is possible with the electrochemical nature of montmorillonite that even if slippage did occur, it may be reversible.

II. Back Calculation:

Use β_{st} from V_{cf} , and thermal expansion coefficients. From equation G.3 we know that the separation of the NCL's at elevated temperature defines the thermal-elasto-plastic volume change of the specimens:

$$[G.3] \quad (\varepsilon_v^{te} + \varepsilon_v^{tp}) = \frac{1}{V_{to}} \left[\beta_{cw} V_w \Delta T - \beta_s (V_t - V_s) \Delta T - \beta_{st} V_t \Delta T \right]$$

Rearranging:

$$[G.23] \quad \beta_{st} = -\frac{1}{V_t \Delta T} \left[V_{to} (\varepsilon_v^{te} + \varepsilon_v^{tp}) - \beta_{cw} V_w \Delta T + \beta_s (V_t - V_s) \Delta T \right]$$

This is the same basic equation as G.9 derived from initial conditions

The distance between NCL's is:

$$[G.24] \quad \Delta V_{cf} = \left[V_{co}^{26} \cdot \varepsilon_v^{26} (1.037 + V_{co}^{26}) \right] - \left[V_{co}^{65} \cdot \varepsilon_v^{65} (1.037 + V_{co}^{65}) \right]$$

where $V_{co}^{26} = V_{co}^{65}$ therefore:

$$[G.25] \quad \Delta V_{cf} = \left[1.037 + V_{co}^{26} \right] \left[\varepsilon_v^{65} - \varepsilon_v^{26} \right]$$

from which:

$$[G.26] \quad \left[\varepsilon_v^{65} - \varepsilon_v^{26} \right] = \frac{\Delta V_{cf}}{\left[1.037 + V_{co}^{26} \right]} = (\varepsilon_v^{te} + \varepsilon_v^{tp})$$

but as before $V_{co}^{26} = 2.252$ for $\gamma_d = 1.67 \text{ Mg/m}^3$, $S=1$, and $w_o = 22.75\%$

Also :

$$[G.27] \quad \Delta V_c^T = \left[N^{65} \cdot \lambda^{65} \ln(p') \right] - \left[N^{26} \cdot \lambda^{26} \ln(p') \right] = N^{65} - N^{26}$$

from which

$$[G.28] \quad \Delta V_c^T = 3.102 - 3.050 = 0.052 \text{ (for the range } 26^\circ\text{C to } 65^\circ\text{C)}$$

$$[G.29] \quad \Delta V_c^T = 3.102 - 2.950 = 0.152 \text{ (for the range } 26^\circ\text{C to } 100^\circ\text{C)}$$

Substitute V_{co}^{26} and ΔV_c^T into G.26 gives:

$$[G.30] \quad (\varepsilon_v^{te} + \varepsilon_v^{tp}) = 0.0158 \text{ (for the range } 26^\circ\text{C to } 65^\circ\text{C)}$$

$$[G.31] \quad (\varepsilon_v^{te} + \varepsilon_v^{tp}) = 0.0462 \text{ (for the range } 26^\circ\text{C to } 100^\circ\text{C)}$$

Substitute G.30 and G.31 into G.23 gives:

$$[G.32] \quad \beta_{st}^{65} = -\frac{1}{V_t \Delta T} \left[0.0158 \cdot V_{to} - \beta_{cw} V_w \Delta T + \beta_s (V_t - V_s) \Delta T \right]$$

and

$$[G.33] \quad \beta_{st}^{100} = -\frac{1}{V_t \Delta T} \left[0.0462 \cdot V_{to} - \beta_{cw} V_w \Delta T + \beta_s (V_t - V_s) \Delta T \right]$$

NOTE:

1. If theory and coefficients are correct then β_{st} calculated from the initial specimen conditions should equal β_{st} calculated from the final moisture content. However, there is some discrepancy between the measured and calculated final specific volume at 26°C. This discrepancy will introduce an error in the comparison of β_{st} .
2. If the specimens are H-OC, then it is possible that all thermal deformation is elastic. In other words, β_{st} will be negligible compared to β_{cw} and β_s .

III. Estimate the Thermo-elasto-plastic component of volume change ($\varepsilon_v^{te} + \varepsilon_v^{tp}$)

It is possible to substitute the average β_{st} (from the forward calculation) into equation G.3 to predict the thermo-elasto-plastic component of volume change

IV. Predict the 26°C NCL using β_{st} and Measured final water contents:

It is possible to substitute the average β_{st} (backward calculation) into equation G.3 to calculate the thermo-elasto-plastic volume change. Subtracting this volume change from volume changes measured in individual elevated tests should give net volume changes corresponding to the 26°C NCL

APPENDIX H: Diffusion in Polymers

In order to assess the true volume change of buffer specimens due to expulsion of water, it was necessary to estimate the amount of diffusion of oil and/or water across the silicone membranes (polymeric elastomer). The first approach was to set up a triaxial environment similar to actual test pressure and temperature conditions using a flat coupon of silicone membrane with an nominal surface area. This produced ambiguous results because the apparatus was limited by the accuracy to measure diffusion rates across the small coupon area. The second approach was to test with brass dummy specimen and membrane identical in size and configuration to actual buffer triaxial specimens. These tests, carried out by Yarechewski (unpublished), are different than the results reported in Chapter 5. Yarechewski's results showed net diffusion rates of 0.16 to 0.60 ml/day inward. A third approach was a simple theoretical prediction of outward diffusion of specimen water. This provided a relative basis of comparison for assessing the need for corrections to specimen volume changes.

The following is a discussion of the third approach. Basic theory is given and eight factors influencing diffusion are considered, but calculations include only the most important factors (the first, fifth, and seventh factors). It should be appreciated that the diffusion process is a complicated one and the presence of not one, but two diffusants (water and silicone oil) adds complexity. Simplifying assumptions were made as necessary without invalidating the prediction.

(1) Consider a simple system where only water diffuses through a silicone rubber membrane. The water is adsorbed on the inner surface and diffuses through the membrane as vapour and is desorbed on the outer surface in a condensed form (H. Gesser, personal communication). The driving potential is provided by differential

vapour pressure across the membrane. Vapour pressure on the inside varies with temperature, applied back pressure, and solution chemistry, but is independent of applied effective stress. Values of vapour pressure are given at standard temperature (0°C) and pressure (75 cm Hg) (STP) up to 1 Atm. by Perry *et al.*(1984). These can also be calculated using the following equation (Perry *et al.* 1984):

$$[H.1] \frac{\partial p}{\partial T} = \frac{H - H'}{RT^2}$$

where p is vapour pressure, T is temperature, H is enthalpy of the gas mixture, H' is the residual enthalpy, and R is the ideal gas constant. Residual enthalpy depends on interactions between molecules. Since the ideal gas model presumes the absence of molecular interactions, deviations from ideality are measured by the residual enthalpy.

A better known form of this equation is the Clausius-Clapeyron equation which is as follows (Mortimer 1975):

$$[H.2] \log\left(\frac{p_2}{p_1}\right) = \frac{\Delta H_v}{2.303R} \left[\frac{T_2 - T_1}{T_1 \cdot T_2} \right]$$

where ΔH_v is the molar heat of vaporization (cal/mol or J/mol), R is the gas constant (1.987 cal/°K·mol, or 8.314 J/°K·mol), T is the absolute temperature (°K), and p is the vapour pressure of the liquid (atm). The vapour pressure on the outside of the membrane is assumed zero for all time, but will increase with time. The change from zero has not been quantified.

In general, diffusion in one dimension is governed by Fick's law of diffusion (Crank and Park 1968) as follows:

$$[H.3] \frac{\partial C}{\partial t} = \frac{\partial}{\partial x} \left[D \cdot \frac{\partial C}{\partial x} \right]$$

where C is the concentration of the diffusing substance (g diffusant/ml polymer), x is the space co-ordinate measured normal to the section, and D is called the diffusion coefficient. If steady state conditions govern then the concentration remains constant at all points in the material. Assuming also that the diffusion coefficient, D is constant these laws reduce to the following

$$[H.4] \frac{\partial^2 C}{\partial x^2} = 0$$

from which it can be shown that the rate of transfer, F of diffusant is the same across all sections and is given by

$$[H.5] F = -D \cdot \frac{dC}{dx}$$

For systems where gas diffuses through a membrane, the vapour pressure on each side is often known but the concentrations are not known. If there is a linear relationship between the external vapour pressure and the corresponding concentration just within the surface of the sheet (i.e. the sorption isotherm is linear) then the following is true

$$[H.6] C = S \cdot p$$

from which it can be shown

$$[H.7] F = P_r \cdot \frac{dp}{dx}$$

where

$$[H.8] P_r = D \cdot S \left[\frac{\text{cc gas (STP) cm (thick)}}{\text{cm}^2(\text{memb}) \cdot \text{sec} \cdot \text{cm Hg} (\Delta p)} \right]$$

P_r is the permeability in units given here as $\text{cm}^2/(\text{sec} \cdot \text{cm Hg})$, D is the diffusion coefficient (cm^2/sec) and S is the solubility coefficient ($\text{cc(RTP)}/\text{cc} \cdot \text{cm Hg}$).

Clearly, the rate of diffusion is a function of diffusivity and solubility.

The following equation is used to calculate the diffusion, Q (flow rate, ml/sec) of water vapour through the silicone membranes:

$$[H.9] Q = 75P_r \cdot \frac{dp}{dx} \cdot A$$

where A is the area of the membrane (cm^2). Note that this equation gives flow rate of water vapour. The constant 75 is used to convert units of cm Hg to units of atm. The ideal gas law was used to convert the volume of gas to an equivalent mass assuming $18\text{g H}_2\text{O}/\text{mole}$:

$$[H.10] pV = nRT$$

where p is the vapour pressure (atm.), V is the volume of vapour (ml), n is the moles of gas per litre volume, R is the universal gas constant ($0.082 \text{l}\cdot\text{atm./}^\circ\text{K}\cdot\text{mole}$), and T is temperature ($^\circ\text{K}$). Steady state flow and conservation of mass are assumed. Then the volume of liquid water in ml is equal to the mass in grams.

It is of interest that the equation governing diffusion (Equation H.3) is of the same form as the one-dimensional consolidation equation first solved by Terzaghi. The equation governing flow rates (Equation H.7) is equivalent to Darcy's law.

The time lag involved in reaching steady state conditions may be calculated from the following equation assuming constant D (Crank and Park 1968):

$$[H.11] Q_t = \frac{DC_1}{l} \left[t - \frac{l^2}{6D} \right]$$

where Q_t is the amount of diffusant, C_1 is the concentration, t is time, and l is the thickness of the membrane.

$$[H.12] L = \frac{l^2}{6D} = \text{Time lag}$$

For diffusion of water through two silicone membranes, the calculated time lag is 137 seconds. The time to reach steady state conditions for the oil-membrane-water system may be much longer. It is known that the initial rate is zero and increases non-linearly with time and concentration varies non-linearly with position until saturation is achieved. Assuming steady state conditions gives an upper bound solution. It is obvious from the above that diffusion is both a kinetic and thermodynamic process.

The membranes used in our program are polydimethylsiloxane. With 25% silica filler, this type of polymer has published permeability to water vapour of 3600×10^{-9} cm/(sec·cm Hg) at RTP (Robb 1965). Crank and Park (1968) give values of 4300×10^{-9} at 35°C, and 3280×10^{-9} at 65°C at STP.

Using $P_r = 3600 \times 10^{-9}$, the diffusion of water (liquid) over a period of one month was 0.007 ml at 26°C (vapour pressure = 0.0332 atm.); 0.34 ml at 65°C (vapour pressure = 0.247 atm.); and 5.04 ml at 100°C (vapour pressure = 1.0 atm.). The diffusion of water increases by 3 orders of magnitude by increasing the temperature from 26°C to 100°C.

Increases in back pressure of the pore water cause increases in vapour pressure of the water, according to the Clausius-Clapeyron equation (Mortimer 1975). Equation [H.2] was used to account for the effect of back pressure of 1.0 MPa (10 atm). The vapour pressure increased 2.5% at 26°C and increased 17.4% at 100°C. Therefore the diffusion rates increase by these amounts.

(2) Consider a system where silicone oil at a nominal pressure provides confinement to the outside of the membrane and the inside is saturated with liquid water at a nominal pressure (oil-membrane-water). The silicone oil causes physical expansion of the membrane. Expansion increases the oil diffusion rates and has an

unknown effect upon water vapour diffusion rates. It is thought that the presence of oil decreases the net diffusion rate because of its molecular size. Expansion increases with temperature.

(3) Silicone oil diffuses in the opposite direction to the water vapour, that is inwards towards the specimen. The presence of oil which is always seen on the inside of both membranes after completion of testing confirms this prediction. Triaxial tests on dummy specimens by Yarechewski (in progress) and Lingnau show an apparent positive volume change, which implies net inflow across the membrane. The buffer has an affinity for the silicone oil and may provide an additional driving potential in actual tests. The result is that the opposing diffusion processes tend to cancel each other in terms of the externally observed volume change in the buffer.

(4) The effect of molecular interaction between water and silicone oil on permeability is not known. Theoretical relations exist for simultaneous diffusion of gases (Crank and Park 1968), but this is beyond the scope of this investigation. Published information suggests that the effect can be reasonably assumed to produce negligible changes in permeability.

(5) Consider the effects of increased temperature. Increasing the temperatures from 35°C to 65°C reduces the permeability of the membrane to water vapour by 24% (Crank and Park 1968). On the other hand, increasing the temperature from 25°C to 100°C appears to increase the amount of diffusion to silicone oil (observed qualitatively from actual buffer tests). This may be due to increased flexibility of the polymer structure.

(6) Self diffusion of silicone fluids with molecules containing three Si atoms are about the same as for CO₂ (McCall *et al.* 1961). CO₂ has a permeability

of 325×10^9 compared to 3600×10^9 for water vapour at RTP. Under these conditions silicone oil permeability is an order of magnitude less than water vapour, but considering that much larger silicone molecules likely exist, the permeability to oil is likely to be even less. However, because the vapour pressure of the oil depends on the applied cell pressure, the pressure potential driving the silicone oil can be up to one order larger than the pressure potential driving the water in the opposite direction..

(7) The thickness of the membrane will influence the concentration gradient. A thick membrane (100 mils) will produce lower average concentrations of water vapour at steady state, but diffusivity is higher at lower concentrations. The net result appears to be similar diffusion rates at steady state, but longer times to reach steady state.

(8) The influence of silica filler is to decrease the permeability of the rubber by increasing the tortuosity of the flow path. Robb (1965) found that increasing the filler content from 0 to 60% decreased the permeability of polydimethylsiloxane to O_2 by about 50%. Similar effects may be expected for water.

Earlier, three chemistry based approaches to obtaining diffusion rates of the oil-membrane-water system were discussed. A fourth approach would be to cover a container of water with a membrane leaving an air space for vapour pressure to equilibrate and place it in a desiccator or drying chamber. The weight of the container could be recorded with time to give the diffusion rate. In a second container silicone oil could be placed on top of a membrane covering the same amount of air and water. Comparing results, the relative influence of the silicone oil on net diffusion could be determined. This work has not yet been undertaken.

We will now examine laboratory tests that have provided diffusion rates. A high pressure consolidation cell was modified to measure diffusion in a triaxial environment equivalent to the buffer triaxial test. A full sized dummy specimen was used. An oil-membrane-water interface was provided with a confining stress on the outside and a constant back pressure of 1.0 MPa on the inside. The measured diffusion rates (Yarechewski 1993) are given in Table 6.5. The data are also shown in Figure 6.16. Theoretical rates of water diffusion and measured net diffusion rates have been plotted with the same sign for comparison purposes.

It is evident from the measured diffusion rates that the process of diffusion is pressure and temperature dependent. There appears to be a logarithmic relationship between the incremental diffusion rate and pressure. In a low stress range, below 1 MPa, doubling the effective stress doubles the diffusion rate. Above 6.0 MPa pressure has little effect (Figure 6.16). The relationship of diffusion with temperature is not entirely clear because only two temperatures are reported. On average the net diffusion rate from the experiments may be expressed as:

$$[H.13] \quad \dot{\epsilon}_v^{PT} = (0.2963 + 0.2727 \cdot \ln p') \left[\frac{\Delta T}{39} \cdot \frac{1}{2} \right] \quad ; 26^\circ C < T < 65^\circ C \quad ; R^2 = 0.9996$$

where p' is in MPa and ΔT is in $^\circ C$.

A comparison of observed and theoretical predictions of diffusion are made in the following concluding remarks. The observed net diffusion rate in our diffusion apparatus using the dummy specimen was 0.16 to 0.60 ml/day inwards towards the specimen at $65^\circ C$ for effective stresses from 0.6 to 3.0 MPa, respectively. This equals an apparent volume change of 5 to 18 ml (2.5% to 9.0%) in one month. Theory predicts an outwards diffusion rate of water of -0.922 ml/day at $65^\circ C$, independent of effective stress. The observed net inwards diffusion rate

at 26°C was 0.08 to 0.24 ml/day at effective stresses of 0.6 to 3.0 MPa, respectively, and in this case, theory predicts a diffusion rate of water of -0.92 ml/day.

The measured diffusion rates are for net diffusion and offer no insight into the relative diffusion rates of water and oil. However, if the predicted diffusion rate of water is assumed correct, then the cross diffusion of oil toward the specimen must be of the same order of magnitude as the outward diffusion of water. Predictions above 65°C appear to be an order of magnitude too high. Triaxial tests on buffer specimens show much smaller volume strain rates. It is believed that actual diffusion rates of water at 100°C are approximately an order of magnitude less than those predicted in Table 6.5

The measured net diffusion rate at steady state is of the same order as the end-of-consolidation strain rate criterion assumed to be 0.1% per day. The observed diffusion rates reached steady state in 3 days, which is much longer time than theory would suggest for water vapour diffusion. In actual buffer tests two membranes are used, and therefore diffusion rates should take much longer to reach steady state than indicated here.

The theory and assumptions in the previous paragraphs account for the effects of changes in back pressure, but not effective stress across the membrane. Robb (1965) reported permeability to CO₂ is constant within \pm 10% for pressure differentials from 0.2 to 500 psi (1.4 to 3500 kPa.).